

University of Alberta

Capillary Collapse and Adhesion of a Micro Double Cantilever Beam

by

Shawn Lavoie

A thesis submitted to the Faculty of Graduate Studies and Research
in partial fulfillment of the requirements for the degree of

Master of Science

Mechanical Engineering

©Shawn Lavoie
Fall 2011
Edmonton, Alberta

Permission is hereby granted to the University of Alberta Libraries to reproduce single copies of this thesis and to lend or sell such copies for private, scholarly or scientific research purposes only. Where the thesis is converted to, or otherwise made available in digital form, the University of Alberta will advise potential users of the thesis of these terms.

The author reserves all other publication and other rights in association with the copyright in the thesis and, except as herein before provided, neither the thesis nor any substantial portion thereof may be printed or otherwise reproduced in any material form whatsoever without the author's prior written permission.

Abstract

High aspect ratio microelectromechanical structures have been found, in the literature, to collapse due to capillary forces of liquids. In this dissertation, mathematical models are developed to study (i) the collapse of a microstructure represented by a double cantilevered beam (DCB) with a free end liquid droplet, and (ii) post-collapse DCB adhesion. Formulations are presented using the classical Bernoulli-Euler beam theory as well as an analysis that accounts for geometrical nonlinearity. The models introduce rigorous coupling between the DCB deformation, the capillary forces and meniscus position, and have predicted interesting nonlinear behaviours that previous models could not. Parameters governing the capillary collapse and adhesion of the DCB are identified and their influence is discussed. A single dimensionless number that controls the condition for collapse is proposed. Comparison between the linear and nonlinear beam analyses shows that linear analysis generally suffices in description of capillary collapse and adhesion of microelectromechanical systems.

Acknowledgements

Support from Alberta Scholarship programs and the Natural Science and Engineering Research Council (NSERC).

Table of Contents

CHAPTER 1	INTRODUCTION	1
CHAPTER 2	THEORETICAL BACKGROUND.....	15
2.1	QUANTITIES DESCRIBING CAPILLARY FORCES	15
2.1.1	<i>Surface Tension</i>	<i>15</i>
2.1.2	<i>Contact Angle and Wetting.....</i>	<i>16</i>
2.1.3	<i>Capillary Pressure.....</i>	<i>18</i>
2.1.4	<i>An Example.....</i>	<i>19</i>
2.1.5	<i>Dupré Equation</i>	<i>28</i>
2.2	BERNOULLI-EULER BEAM THEORY.....	29
2.2.1	<i>Bernoulli-Euler Kinematic Assumption</i>	<i>29</i>
2.2.2	<i>Constitutive Assumption</i>	<i>32</i>
2.2.3	<i>Reference Coordinate System and Infinitesimal Strain</i>	<i>33</i>
2.2.4	<i>Equilibrium.....</i>	<i>35</i>
2.2.5	<i>Discontinuity Functions.....</i>	<i>38</i>
2.2.6	<i>Strain Energy.....</i>	<i>39</i>
2.2.7	<i>Bernoulli- Euler Derivation Summary.....</i>	<i>40</i>
CHAPTER 3	LINEAR BEAM FORMULATION	41
3.1	UNCOLLAPSED CONFIGURATION	45
3.2	ADHERED CONFIGURATION	54
3.3	ENERGY CONSIDERATIONS	59
CHAPTER 4	NONLINEAR FORMULATION	62
4.1	UNCOLLAPSED CONFIGURATION	64
4.2	ADHERED CONFIGURATION	70
4.3	ENERGY CONSIDERATIONS	73
CHAPTER 5	RESULTS FROM LINEAR BEAM FORMULATION	74
5.1	RANGE OF GOVERNING PARAMETERS	74
5.2	PRELIMINARY CONSIDERATIONS ON THE ROLE OF THE 4 GOVERNING PARAMETERS... 76	76
5.2.1	<i>Discussion Neglecting Nonlinear Deflection Coupling Effects</i>	<i>78</i>
5.2.2	<i>Importance of Nonlinear Deflection Coupling</i>	<i>84</i>
5.3	MODERATE CONTACT ANGLE	88
5.3.1	<i>Collapse at moderate contact angles and low β.....</i>	<i>89</i>
5.3.2	<i>DCB Collapse at moderate contact angles and high β.....</i>	<i>102</i>
5.4	HIGH CONTACT ANGLE.....	115
5.5	LOW CONTACT ANGLE.....	128
5.5.1	<i>General Low Contact Angle Collapse Behaviour.....</i>	<i>129</i>
5.5.2	<i>Influence of Liquid Displaced by Menisci</i>	<i>131</i>
5.5.3	<i>Role of surface tension forces at low θ_c.....</i>	<i>135</i>
5.6	DISCONTINUITY IN DEFLECTION CONTOURS AT LOW V^*	139
5.7	SUMMARY	154
CHAPTER 6	RESULTS ON UNCOLLAPSED CONFIGURATION FROM NONLINEAR FORMULATION.....	157
6.1	SUMMARY OF GOVERNING EQUATIONS	157
6.2	IMPORTANCE OF NONLINEAR GEOMETRY	158
6.3	INFLUENCE OF B ON COLLAPSE.....	160
6.4	COLLAPSE CORRELATION EQUATION.....	165
6.5	COMPARISON WITH PREVIOUS WORKS.....	172
6.6	SUMMARY	175
CHAPTER 7	RESULTS ON ADHERED CONFIGURATION.....	176

7.1	SUMMARY OF GOVERNING EQUATIONS	177
7.2	BASIC CONSIDERATIONS.....	179
7.3	EFFECT OF Λ_{SL}	189
7.4	DISCREPANCY BETWEEN THE LINEAR AND NONLINEAR MODELS	194
7.5	COMPARISON WITH PREVIOUS WORKS.....	195
7.6	SUMMARY	199
CHAPTER 8 CONCLUSIONS AND FUTURE WORK		200
BIBLIOGRAPHY		203
APPENDIX A DETAILS OF MODIFIED NEWTON-RAPHSON METHOD.....		206
APPENDIX B DETAILS OF RUNGE-KUTTA SHOOTING METHOD.....		207
APPENDIX C ANALYTICAL RESULT FOR NONLINEAR BEAM THEORY		210
APPENDIX D MDISP NONLINEAR DEFLECTION COUPLING ($\Theta_c = 0$).....		212
APPENDIX E DCB BRANCHING		219
APPENDIX F AXISYMMETRIC MENISCUS CALCULATION		226

List of Tables

<i>Table 1: List of symbols</i>	<i>xiv</i>
<i>Table 2: List of normalized quantities</i>	<i>xvi</i>
<i>Table 3: Selected Surface tension values for 20-25° C [30]</i>	<i>15</i>
<i>Table 4: Selected Advancing contact angles (deg) for 20-25° C [30]</i>	<i>17</i>
<i>Table 5: Quantities required for the “J Integral”</i>	<i>56</i>
<i>Table 6: Range for governing parameters</i>	<i>76</i>
<i>Table 7: Maximum discrepancy between linear and nonlinear beam theories. For a range of θ_c and V^*. β is fixed at 0.1 to give maximum error</i>	<i>160</i>
<i>Table 8: Change in l_1^* for $V^* = 0.1$ as deflection increases from $w_2^* = 0.6$ to collapse</i>	<i>214</i>

List of Figures

<i>Figure 1.1: Schematic of the DCB to be studied in this work (shown from side).</i>	12
<i>Figure 1.2: Schematic of the s-shaped adhered DCB to be studied in this work (shown from side).</i>	13
<i>Figure 2.1: Equilibrium of 3-phase contact line</i>	17
<i>Figure 2.2: Equilibrium of a solid plate subjected to pressure forces</i>	19
<i>Figure 2.3: Schematic for plate drop example</i>	20
<i>Figure 2.4: Total energy of spring-plate-liquid system for a range of liquid drop sizes</i>	23
<i>Figure 2.5: Branching and energy diagrams for spring-plate-liquid system for 3 values of η</i>	27
<i>Figure 2.6: Separating a cohesively bonded solid in a liquid [28]</i>	28
<i>Figure 2.7: Bernoulli-Euler beam theory derivation path</i>	29
<i>Figure 2.8: Bernoulli-Euler beam theory kinematic assumption</i>	30
<i>Figure 2.9: Equilibrium of an infinitesimal beam section showing internal reactions in positive sense for sign convention for this work</i>	36
<i>Figure 3.1: FBD of a section of a linear beam for obtaining internal reactions $M(x)$ and $Q(x)$</i>	42
<i>Figure 3.2: Schematic of the uncollapsed DCB problem to be solved</i>	45
<i>Figure 3.3: FBD of a linear beam in the uncollapsed case for obtaining base reactions from equilibrium</i>	46
<i>Figure 3.4: Angle diagrams at the base meniscus</i>	49
<i>Figure 3.5: Angle diagrams at the free end meniscus</i>	51
<i>Figure 3.6: Schematic of the adhered DCB problem to be solved</i>	55
<i>Figure 3.7: FBD of a linear beam in the adhered case for obtaining base reactions from equilibrium</i>	55
<i>Figure 3.8: Integration path for “J-integral”</i>	56
<i>Figure 4.1: FBD of a section of a nonlinear beam for obtaining internal reaction $M(s)$</i>	62
<i>Figure 4.2: FBD of a nonlinear beam in the uncollapsed case for obtaining base reactions</i>	65
<i>Figure 4.3: Solution algorithm</i>	69
<i>Figure 4.4: FBD of a nonlinear beam in the adhered case for obtaining base reactions</i>	70
<i>Figure 5.1: MVF minimum V^* factor for a range of contact angles</i>	76
<i>Figure 5.2: Dependency of deflection on the Governing Parameters neglecting nonlinear effects of deflection (w, ϕ) in constraint equations</i>	80
<i>Figure 5.3: Effect of θ_c on meniscus geometry factor and the appearance of the meniscus</i>	82
<i>Figure 5.4: Meniscus displacement factor (MDF) for complete range of l^*</i>	83

<i>Figure 5.5: Solution dependence on governing parameters, including nonlinear coupling</i>	85
<i>Figure 5.6: Contours for the free end deflection (w_2^*). The contours are plotted with varying Λ and V^*. The other two governing parameters are fixed at $\theta_c = 45^\circ$ and $\beta = 0.025$.</i>	91
<i>Figure 5.7: Elastic curve and meniscus location for $V^* = 0.15$ and $V^* = 0.55$. The other three governing parameters are fixed at $\beta = 0.025$, $\Lambda = 0.0045$, $\theta_c = 45^\circ$.</i>	93
<i>Figure 5.8: Contours for the normalized meniscus radius (α). The contours are plotted with varying Λ and V^*. The other two governing parameters are fixed at $\theta_c = 45^\circ$ and $\beta = 0.025$.</i>	93
<i>Figure 5.9: Contours for the Base meniscus deflection (w_1^*). The contours are plotted with varying Λ and V^*. The other two governing parameters are fixed at $\theta_c = 45^\circ$ and $\beta = 0.025$.</i>	96
<i>Figure 5.10: Contours for the Base meniscus location (x_1^*). The contours are plotted with varying Λ and V^*. The other two governing parameters are fixed at $\theta_c = 45^\circ$ and $\beta = 0.025$.</i>	97
<i>Figure 5.11: Changes in x_1^*, w_1^*, α with increases in free end deflection (w_2^*) for $V^* = 0.15$. Λ is increased to create the increase in w_2^*. The other two governing parameters are fixed at $\beta = 0.025$ and $\theta_c = 45^\circ$.</i>	97
<i>Figure 5.12: Contours for the fraction of reaction moment due to the surface tension forces. The contours are plotted with varying Λ and V^*. The other two governing parameters are fixed at $\theta_c = 45^\circ$ and $\beta = 0.025$.</i>	101
<i>Figure 5.13: Contours for the normalized volume of liquid displaced by menisci (MDISP). The contours are plotted with varying Λ and V^*. The other two governing parameters are fixed at $\theta_c = 45^\circ$ and $\beta = 0.025$.</i>	101
<i>Figure 5.14: Contours for the free end deflection (w_2^*). The contours are plotted with varying Λ and V^*. The other two governing parameters are fixed at $\theta_c = 45^\circ$ and $\beta = 0.1$.</i>	103
<i>Figure 5.15: Contours for the normalized meniscus radius (α). The contours are plotted with varying Λ and V^*. The other two governing parameters are fixed at $\theta_c = 45^\circ$ and $\beta = 0.1$.</i>	104
<i>Figure 5.16: Contours for the base meniscus deflection (w_1^*). The contours are plotted with varying Λ and V^*. The other two governing parameters are fixed at $\theta_c = 45^\circ$ and $\beta = 0.1$.</i>	105
<i>Figure 5.17: Contours for base meniscus geometry factor (l_1^*). The contours are plotted with varying Λ and V^*. The other two governing parameters are fixed at $\theta_c = 45^\circ$ and $\beta = 0.1$.</i>	106
<i>Figure 5.18: Changes in x_1^*, w_1^*, ϕ_1, α with increases in free end deflection (w_2^*) for $V^* = 0.55$. Λ is increased to create the increase in w_2^*. The other two governing parameters are fixed at $\beta = 0.1$ and $\theta_c = 45^\circ$.</i>	108
<i>Figure 5.19: Contours for the base meniscus location (x_1^*). The contours are plotted with varying Λ and V^*. The other two governing parameters are fixed at $\theta_c = 45^\circ$ and $\beta = 0.1$.</i>	110
<i>Figure 5.20: Contours for the fraction of reaction moment due to the surface tension forces. The contours are plotted with varying Λ and V^*. The other two governing parameters are fixed at $\theta_c = 45^\circ$ and $\beta = 0.1$.</i>	112
<i>Figure 5.21: Bending moment diagram with governing parameters V^* and Λ chosen to give a free end deflections close to collapse. The other two governing parameters are fixed at $\theta_c = 45^\circ$, and $\beta = 0.1$. Arrows indicate location of meniscus.</i>	113

Figure 5.22: Contours for the reaction moment (M_R^*). The contours are plotted with varying Λ and V^* . The other two governing parameters are fixed at $\theta_c = 45^\circ$ and $\beta = 0.1$	114
Figure 5.23: Contours for the free end deflection (w_2^*). The contours are plotted with varying Λ and V^* . The other two governing parameters are fixed at $\theta_c = 80^\circ$ and $\beta = 0.1$	117
Figure 5.24: Contours for the normalized meniscus radius (α). The contours are plotted with varying Λ and V^* . The other two governing parameters are fixed at $\theta_c = 80^\circ$ and $\beta = 0.1$	118
Figure 5.25: Contours for the base meniscus deflection (w_1^*). The contours are plotted with varying Λ and V^* . The other two governing parameters are fixed at $\theta_c = 80^\circ$ and $\beta = 0.1$	119
Figure 5.26: Contours for base meniscus geometry factor (l_1^*). The contours are plotted with varying Λ and V^* . The other two governing parameters are fixed at $\theta_c = 80^\circ$ and $\beta = 0.1$	120
Figure 5.27: Contours for the fraction of reaction moment due to the surface tension forces. The contours are plotted with varying Λ and V^* . The other two governing parameters are fixed at $\theta_c = 80^\circ$ and $\beta = 0.1$	122
Figure 5.28: Contours for the reaction moment (M_R^*). The contours are plotted with varying Λ and V^* . The other two governing parameters are fixed at $\theta_c = 80^\circ$ and $\beta = 0.1$	122
Figure 5.29: Contours for the Sum of the surface tension forces at the two menisci (F_{ST}^*). The contours are plotted with varying Λ and V^* . The other two governing parameters are fixed at $\theta_c = 80^\circ$ and $\beta = 0.1$	124
Figure 5.30: Contours for the base meniscus location (x_1^*). The contours are plotted with varying Λ and V^* . The other two governing parameters are fixed at $\theta_c = 80^\circ$ and $\beta = 0.1$	124
Figure 5.31: Contours for the moment about base due to surface tension forces (M_{ST}^*). The contours are plotted with varying Λ and V^* . The other two governing parameters are fixed at $\theta_c = 80^\circ$ and $\beta = 0.1$	125
Figure 5.32: Contours for the force due to pressure (F_p^*). The contours are plotted with varying Λ and V^* . The other two governing parameters are fixed at $\theta_c = 80^\circ$ and $\beta = 0.1$	126
Figure 5.33: Contours for the Moment about base due to Laplace pressure (M_p^*). The contours are plotted with varying Λ and V^* . The other two governing parameters are fixed at $\theta_c = 80^\circ$ and $\beta = 0.1$	127
Figure 5.34: Contours for the free end deflection (w_2^*). The contours are plotted with varying Λ and V^* . The other two governing parameters are fixed at $\theta_c = 0^\circ$ and $\beta = 0.1$	130
Figure 5.35: Contours for the Reaction moment (M_R^*). The contours are plotted with varying Λ and V^* . The other two governing parameters are fixed at $\theta_c = 0^\circ$ and $\beta = 0.1$	130
Figure 5.36: Contours for the base meniscus location (x_1^*). The contours are plotted with varying Λ and V^* . The other two governing parameters are fixed at $\theta_c = 0^\circ$ and $\beta = 0.1$	131
Figure 5.37: Contours for fraction of displaced liquid due to meniscus curvature. The contours are plotted with varying Λ and V^* . The other two governing parameters are fixed at $\theta_c = 0^\circ$ and $\beta = 0.1$	133
Figure 5.38: Contours for ratio of displaced liquid due to meniscus curvature to drop volume ($MDISP/V^*$). The contours are plotted with varying Λ and V^* . The other two governing parameters are fixed at $\theta_c = 0^\circ$ and $\beta = 0.1$	133

<i>Figure 5.39: Changes in x_1^*, MDISP, and liquid displaced by DCB deflection with increases in free end deflection (w_2^*) for $V^* = 0.1$ and $V^* = 0.5$. Λ is increased to create the increase in w_2^*. The other two governing parameters are fixed at $\beta = 0.1$ and $\theta_c = 0^\circ$.</i>	134
<i>Figure 5.40: Contours for the Moment about base due to surface tension forces (M_{ST}^*). The contours are plotted with varying Λ and V^*. The other two governing parameters are fixed at $\theta_c = 0^\circ$ and $\beta = 0.1$.</i>	136
<i>Figure 5.41: Contours for the moment about base due to pressure forces (M_P^*). The contours are plotted with varying Λ and V^*. The other two governing parameters are fixed at $\theta_c = 0^\circ$ and $\beta = 0.1$.</i>	138
<i>Figure 5.42: Contours for the fraction of reaction moment due to the surface tension forces. The contours are plotted with varying Λ and V^*. The other two governing parameters are fixed at $\theta_c = 0^\circ$ and $\beta = 0.1$.</i>	138
<i>Figure 5.43: Contours for the free end deflection (w_2^*) focusing on a discontinuity. The contours are plotted with varying Λ and V^*. The other two governing parameters are fixed at $\theta_c = 45^\circ$ and $\beta = 0.025$. Generated by increasing Λ.</i>	141
<i>Figure 5.44: Changes in free end deflection w_2^*, with increases in Λ for $V^* = 0.1$. The other two governing parameters are fixed at $\beta = 0.025$ and $\theta_c = 45^\circ$.</i>	141
<i>Figure 5.45: Elastic curve and meniscus location for $V^* = 0.0975$ and $V^* = 0.1025$ (on either side of discontinuity). The other three governing parameters are fixed at $\beta = 0.025$, $\Lambda = 0.0046$, $\theta_c = 45^\circ$.</i>	143
<i>Figure 5.46: Changes in x_1^*, w_1^*, α with increases in Λ for $V^* = 0.1$ (showing discontinuity). The other two governing parameters are fixed at $\beta = 0.025$ and $\theta_c = 45^\circ$.</i>	143
<i>Figure 5.47: Changes in total potential energy, surface energy, and strain energy of DCB system, with increases in Λ for $V^* = 0.1$. The other two governing parameters are fixed at $\beta = 0.025$ and $\theta_c = 45^\circ$.</i>	145
<i>Figure 5.48: Branching (a,c,e) and energy (b,d,f) diagrams of DCB for different values of the elastocapillary number. Arrows indicate the path that the DCB would follow as a drop with initial volume of $V^* = 1$ is evaporated.</i>	147
<i>Figure 5.49: DCB branching diagrams for different values of the elastocapillary number.</i>	150
<i>Figure 5.50: Contours for the free end deflection (w_2^*) focusing on a discontinuity. The contours are plotted with varying Λ and V^*. The other two governing parameters are fixed at $\theta_c = 45^\circ$ and $\beta = 0.025$. Generated by decreasing V^*.</i>	153
<i>Figure 6.1: Contours for the discrepancy between linear and nonlinear beam theories. The contours are plotted with varying Λ and β. The other two governing parameters are fixed at $\theta_c = 45^\circ$ and $V^* = 0.3$.</i>	160
<i>Figure 6.2: Contours for the base meniscus position (s_1^*). The contours are plotted with varying Λ and β. The other two governing parameters are fixed at $\theta_c = 45^\circ$ and $V^* = 0.3$.</i>	161
<i>Figure 6.3: Contours for the free end deflection (w_2^*). The contours are plotted with varying β and V^*. The other two governing parameters are fixed at $\theta_c = 45^\circ$ and $\Lambda = 0.05$.</i>	163
<i>Figure 6.4: Contours for the reaction moment (M_R^*). The contours are plotted with varying β and V^*. The other two governing parameters are fixed at $\theta_c = 45^\circ$ and $\Lambda = 0.05$.</i>	165

Figure 6.5: Contours for the reaction moment (M_R^*) at collapse. The contours are plotted with varying β and V^* and increasing Λ to create collapse ($w_2^* = 1$). The contact angle is fixed at $\theta_c = 45^\circ$	166
Figure 6.6: Contours for the nondimensional number N for comparison with free end deflection (w_2^*). Ideally the 1 contours of each would be coincident. The contours are plotted with varying Λ and V^* . The other two governing parameters are fixed at $\theta_c = 45^\circ$ and $\beta = 0.1$	168
Figure 6.7 Contours for the nondimensional number N for comparison with free end deflection (w_2^*). Ideally the 1 contours of each would be coincident. The contours are plotted with varying Λ and V^* . The other two governing parameters are fixed at $\theta_c = 45^\circ$ and $\beta = 0.1$	171
Figure 6.8: Contours for the nondimensional number N for comparison with free end deflection (w_2^*). Ideally the 1 contours of each would be coincident. The contours are plotted with varying Λ and V^* . The other two governing parameters are fixed at $\theta_c=45^\circ$ and $\beta=0.025$	171
Figure 6.9 Contours for the nondimensional number N for comparison with free end deflection (w_2^*). Ideally the 1 contours of each would be coincident. The contours are plotted with varying Λ and V^* . The other two governing parameters are fixed at $\theta_c = 0^\circ$ and $\beta=0.1$	172
Figure 6.10 Contours for the nondimensional number N for comparison with free end deflection (w_2^*). Ideally the 1 contours of each would be coincident. The contours are plotted with varying Λ and V^* . The other two governing parameters are fixed at $\theta_c = 80^\circ$ and $\beta = 0.1$	172
Figure 6.11: Comparison of free end deflection (w_2^*) with completely filled DCB models [4],[6] using data from [6].....	174
Figure 6.12: Comparison of free end deflection (w_2^*) with completely filled DCB models [4],[6] using data from [6] with contact angle changed to 50°	175
Figure 7.1: Elastic curve and meniscus location for $V^* = 0.2$. The other four governing parameters are fixed at $\theta_c = 30^\circ$, $\Lambda = 0.01$, $\Lambda_{SL} = 0.01$, $\beta = 0.02$	179
Figure 7.2: Contours for the normalized length of DCB not in contact (s_2^*). The contours are plotted with varying β and V^* . The other three governing parameters are fixed at $\theta_c = 45^\circ$ $\Lambda = 0.02$, and $\Lambda_{SL} = 0$	180
Figure 7.3: Contours for the normalized base meniscus position (s_1^*). The contours are plotted with varying β and V^* . The other three governing parameters are fixed at $\theta_c = 45^\circ$ $\Lambda = 0.02$, and $\Lambda_{SL} = 0$	183
Figure 7.4: Contours for the normalized meniscus radius (a) contours. The contours are plotted with varying β and V^* . The other three governing parameters are fixed at $\theta_c = 45^\circ$, $\Lambda = 0.02$, and $\Lambda_{SL} = 0$	183
Figure 7.5: Contours for the pressure moment (M_p^*) contours. The contours are plotted with varying β and V^* . The other three governing parameters are fixed at $\theta_c = 45^\circ$ $\Lambda = 0.02$, and $\Lambda_{SL} = 0$	186
Figure 7.6: Contours for the ratio G of normalized shear reaction at adhered end to base (Q_2^*/Q_R^*). The contours are plotted with varying β and V^* . The other three governing parameters are fixed at $\theta_c = 45^\circ$ $\Lambda = 0.02$, and $\Lambda_{SL} = 0$	186

Figure 7.7: Contours for the normalized shear reaction at adhered end of DCB (Q_2^*). The contours are plotted with varying β and V^* . The other three governing parameters are fixed at $\theta_c = 45^\circ$ $\Lambda = 0.02$, and $\Lambda_{SL} = 0$.	188
Figure 7.8: Contours for the normalized Laplace pressure ($F_P^*/(x_2^* - x_1^*)$). The contours are plotted with varying β and V^* . The other three governing parameters are fixed at $\theta_c = 45^\circ$ $\Lambda = 0.02$, and $\Lambda_{SL} = 0$.	188
Figure 7.9: Contours for the normalized shear reaction at adhered end of DCB (Q_2^*). The contours are plotted with varying β and V^* . The other three governing parameters are fixed at $\theta_c = 45^\circ$ $\Lambda = 0.02$, and $\Lambda_{SL} = 0.01$.	192
Figure 7.10: Contours for the normalized shear reaction at adhered end of DCB (Q_2^*). The contours are plotted with varying β and V^* . The other three governing parameters are fixed at $\theta_c = 45^\circ$ $\Lambda = 0.02$, and $\Lambda_{SL} = \Lambda \cos \theta_c = 0.01414$.	193
Figure 7.11: Comparing bending moment diagrams for $\Lambda_{SL} = 0.01$ $\beta = 0.02$, and for $\Lambda_{SL} = 0$, $\beta = 0.01$. With governing parameters $V^* = 0.2$, $\theta_c = 30^\circ$, and $\Lambda = 0.01$.	194
Figure 7.12: Contours for the discrepancy between linear and nonlinear beam theories. The contours are plotted with varying β and V^* . The other three governing parameters are fixed at $\theta_c = 45^\circ$ $\Lambda = 0.02$, and $\Lambda_{SL} = \Lambda \cos \theta_c = 0.01414$.	195
Figure 7.13: Comparison of s_1^* and s_2^* with results from Lui et al. [25]. β varied the other four governing parameters are fixed at $\theta_c = 0^\circ$, $\Lambda = 0.2685$, $\Lambda_{SL} = 0.2685$, $V^* = 0.02$.	198
Figure 7.14: Elastic curve and meniscus location of s-shaped adhered hair for $V^* = 0.02$. The other four governing parameters are fixed at $\theta_c = 0^\circ$, $\Lambda = 0.2685$, $\Lambda_{SL} = 0.2685$, $\beta = 0.06$.	198
Figure B.1: Free end deflection convergence	209
Figure B.2: Strain energy convergence	209
Figure D.1: Contours of normalized volume of liquid displaced by menisci (MDISP). The contours are plotted with varying Λ and V^* . The other two governing parameters are fixed at $\theta_c = 0^\circ$ and $\beta = 0.1$.	212
Figure D.2: Influence of MDISP on x_1^* . $V^* = 0.1$ with $\theta_c = 0^\circ$, $\beta = 0.1$.	213
Figure D.3: Contours of base meniscus geometry factor (l_1^*). The contours are plotted with varying Λ and V^* . The other two governing parameters are fixed at $\theta_c = 0^\circ$ and $\beta = 0.1$.	214
Figure D.4: Contours of free end meniscus geometry factor (l_2^*). Contours are plotted with varying Λ and V^* . The other governing parameters are fixed at $\theta_c = 0^\circ$ and $\beta = 0.1$.	216
Figure D.5: Contours of sum of meniscus displacement factors (SMDF). Contours are plotted with varying Λ and V^* . The other governing parameters are fixed at $\theta_c = 0^\circ$ and $\beta = 0.1$.	217
Figure D.6: Contours for the normalized meniscus radius (a). The contours are plotted with varying Λ and V^* . The other governing parameters are fixed at $\theta_c = 0^\circ$ and $\beta = 0.1$.	218
Figure E.1: Variation of the function g with x_1^* . Maximum value gives N_T .	221
Figure E.2: DCB branch and energy diagrams showing equilibrium path of a quasistatic evaporation process a) Branch diagram $N_{EC} = 0.9$ b) Branch diagram $N_{EC} = 1$ c) Branch diagram $N_{EC} = 1.1$ d) Energy diagram $N_{EC} = 0.9$ e) Energy diagram $N_{EC} = 1$ f) Energy diagram $N_{EC} = 1.1$	225

<i>Figure F.1: Schematic of axisymmetric drop</i>	228
<i>Figure F.2: An example of an axisymmetric equilibrium surface. Meniscus is shown in blue plate is shown in red</i>	232
<i>Figure F.3: a) Variation in each principal curvature with position along meniscus. Also shown are the mean curvature and the value obtained using the method of Mastrangelo et al. [3] b) Variation of equilibrium surface shape (z^* vs. r^*) with V_L^* c) Variation of equilibrium surface shape (z^* vs. r^*) with θ_c * d) Variation of equilibrium surface shape (z^* vs. r^*) with ζ.</i>	233
<i>Figure F.4: Dependency of q^* and r_i^* on ζ, θ_c, and V_L^*. r_o^* and r_{ii}^* are also shown in b),d), f). a) q^* vs. ζ b) r_i^* vs. ζ c) q^* vs. V_L^* d) r_i^* vs. V_L^* e) q^* vs. θ_c f) r_i^* vs. θ_c</i>	237
<i>Figure F.5 Dependency of U^* and F^* on ζ, θ_c, and V_L^*. In a) c) e) contributions from the wetted plate U_{SL}^* and meniscus U_{LA}^* are also shown along with the energy obtained using the method of Mastrangelo et al. [3] U_{lit}^*. In b), d), f) contributions from the pressure force F_p^* and surface tension force F_{ST}^* are also shown along with the force obtained using the method of Mastrangelo et al. [3] F_{lit}^*. a) U^* vs. ζ b) U^* vs. ζ c) U^* vs. V_L^* d) F^* vs. V_L^* e) F^* vs. θ_c f) F^* vs. θ_c</i>	239

Nomenclature

Table 1: List of symbols

Symbol	Description	Dimension (F,L,T)
U_S	Surface energy	FL
$\gamma_{LA}, \gamma_{SA}, \gamma_{SL}$	Surface tensions of Liquid-Air, Solid-Air, and Solid-Liquid Interfaces	FL ⁻¹
θ_c	Equilibrium contact angle	-
ΔP_{lap}	Laplace pressure difference	FL ⁻²
R_1, R_2	Principal radii of curvature of meniscus	L
W_{SS}, W_{LL}	Work of Cohesion between solid-solid and liquid-liquid interfaces respectively	FL ⁻¹
W_{SL}	Work of Adhesion between solid-liquid interface	FL ⁻¹
ε	strain	-
ρ	Beam radius of curvature	L
κ	curvature	L ⁻¹
s, y, ξ	Position within beam coordinate system: arc length, binormal direction and transverse direction	L
σ	Stress	FL ⁻²
E	Young's Modulus	FL ⁻²
I	Moment of inertia	L ⁴
M	Bending moment	FL
ν	Poisson's ratio	-
E^*	Wide beam modified Young's Modulus	FL ⁻²
x, y, z	Position within Cartesian coordinate system	L
ϕ	Deflection angle (positive x-axis to beam)	-
Q, T	Beam internal shear and axial forces respectively	F
f, q	Distributed transverse and axial loading	FL ⁻¹
m	Distributed moment	F
u, v, w	Components of displacement vector (w corresponds to beam deflection)	L
U_{SE}	Strain energy	FL
W	Strain Energy density	FL ⁻²
s_1, s_2	Location of base and free end menisci	L
x_1, x_2	x -position of base and free end menisci	L
w_1, w_2	z -deflection at base and free end menisci	L
ϕ_1, ϕ_2	Deflection angle at base and free end menisci	-
D	Depth of beam	L

Symbol	Description	Dimension (F,L,T)
M_R	Reaction moment at base	FL
Q_R, T_R	Shear and axial reactions at base	F
$R_1 = R, R_2 = \infty$	Principal radii of curvature of meniscus for 2-D model	L
l_1, l_2	Meniscus geometry factor (complementary to cap height)	L
h	Half width (between beams)	L
θ_2	Angle between free end meniscus and beam	-
θ_{m1}, θ_{m2}	Angle from positive x -axis to base and free end menisci at beam intersection respectively	-
V	Drop volume	L^3
Q_2	Contact force at crack tip	F
$A_{SA}, A_{LA}, A_{LS}, A_{SS}$	Areas of solid-air, liquid-air, liquid-solid, and solid-solid interfaces respectively	L^2
$M_{ST}(s)$	Portion of beam internal moment caused by surface tension forces	FL
$M_P(s)$	Portion of beam internal moment caused by Laplace Pressure	FL
M_{ST}	Net moment on entire beam about base due to surface tension forces	FL
M_P	Net moment on entire beam about base due to Laplace Pressure	FL
M_2	Moment at s_2	FL

Table 2: List of normalized quantities

Normalized Quantity and Definition	Description
$s^* = \frac{s}{L}$	Normalized position along beam
$x^* = \frac{x}{L}$	Normalized position
$w^* = \frac{w}{h}$	Normalized deflection
$M^* = \frac{ML}{EI}$	Normalized moment
$Q^* = \frac{Q L^2}{EI}$	Normalized shear force
$T^* = \frac{T L^2}{EI}$	Normalized axial force
$\beta = \frac{h}{L}$	Ratio of beam half spacing to length
$\alpha = \frac{R}{h}$	Normalized meniscus radius
$l_i^* = \frac{l_i}{R}$	Normalized meniscus geometry factor
$V^* = \frac{V}{2LDh}$	Normalized drop volume
$\Lambda = \frac{\gamma_{LA} L^2 D}{EI}$	Normalized surface tension force
$\Lambda_{SL} = \frac{\gamma_{SL} DL^2}{EI}$	Normalized interfacial energy of cohesive solid-solid bond in liquid
$U^* = \frac{U L}{EI}$	Normalized potential energy

Chapter 1 Introduction

Capillary forces result from the presence of a liquid surface or a meniscus. There are familiar examples of these forces at work in our every day lives from capillary forces causing water to form droplets to drawing wet hair together to form clumps. Most scientists are likely familiar with the capillary rise experiment where capillary forces draw water up a tube against gravity. While these phenomena are all visible at the macroscopic scale, at microscopic and lower length scales capillary forces become increasingly important and even dominant. The reason for this is that capillary forces scale linearly with the length scale whereas body forces, such as gravity, scale with volume or the cube of the length scale. As a result at the length scales of many micro-electromechanical systems (MEMS) and nano-electromechanical systems (NEMS) capillary forces are sufficient to deform solid structures [1]. Examples include capillary forces creating cellular or ‘tepee’ structures from an array of ZnO or Si nanowires, or capillary forces collapsing carbon nanotubes partially filled with liquid [1].

MEMS devices are widely used in data transduction applications as sensors, and actuators [2], such as pressure and acceleration sensors [3], ultrafine lithographic photoresist patterns [4], and Radio frequency (RF) switches [5]. Often to obtain high performance these devices are designed to be tightly spaced and have large surface areas [3]. In lithographic photoresist patterns, for example, there is a constant drive towards narrower resist patterns¹ while at the same time device performance requires the resist to have some thickness which results in

¹ Consider for example the new line of INTEL® processors released in 2011 have 32nm lithography. Two years prior INTEL® first released processors with 45nm lithography.

high aspect ratio patterns, for example a pattern of 1000nm thickness and 200nm spacing was investigated by Kotera et al [6]. Furthermore, these patterns are often made of polymers with relatively low stiffness [12]. These characteristics result in low device stiffness and make MEMS devices susceptible to capillary forces. In fact many surface micromachined and lithographic structures are formed using wet etching of sacrificial layers [3]. When the rinse liquid is gradually removed strong capillary forces are created which may bring patterns into contact at the tips [4]. Similarly the same process can cause a MEMS structure to adhere to a substrate [7], [8]. Furthermore, capillary forces may cause suspended or moving structures to adhere to a substrate during operation [9]. Once these structures come into contact they will often permanently adhere; this type of device failure is known as “stiction” [2]. Although, ordinarily capillary forces and stiction cause manufacturing problems, they have been used in advantageous ways to self assemble microstructures that are locked in place to a substrate by stiction [10].

Basic theory for predicting collapse of microstructures due to capillary forces has been developed by Mastrangelo and Hsu [3]. This formulation looked at energy and developed approximate conditions for collapse, involving the so-called elastocapillary number and the associated pull-in length defined as the maximum length beyond which the beam will contact the substrate [3]. This analysis was performed for a doubly clamped beam using both linear and non linear beam theories, and was extended to plates; in each case the Ritz method was used with approximate test function for the beams deflection [3]. Capillary forces have been experimentally identified as the mechanism of resist pattern

collapse in the work of Tanaka *et al.* [4]. This phenomenon was subsequently modeled [4] by a double cantilevered beam (DCB) with fluid completely filling the gap between the two beams; using this model the critical values of Young's modulus that would lead to collapse, as well as the critical aspect ratios (length/spacing) were determined for limiting values of contact angle. Subsequent studies used this model to visualize collapsed configurations for larger 2-D and 3-D patterns of beams, and compared these with existing experimental images [11], [6]. Extensions have been made to different materials by incorporating an elastic-perfectly plastic constitutive model [12], as well as to collapse of resist patterns with alternating smaller and larger spacing [13]. Tanaka's model has also been modified to include surface tension forces [43]. Abe *et al.* studied the drying process and observed that for long beams a droplet can be formed which moves to the free end of the beam [7]. Simulations for a cantilever beam partially filled with liquid do exist with linear [9] and nonlinear beam models [8]. Numerous procedures for preventing contact have been proposed, examples include freeze drying, supercritical drying, dry etching, liquid bridge cleavage, hydrophobic coatings, external force release [2], antistiction tabs [7], and specialized rinse processes [17].

As mentioned above, there are typically two aspects of capillary force induced MEMS failure: capillary forces cause the collapse of the structures but stiction keeps them in that position. In the hope of determining the work of adhesion Mastrangelo *et al.* devised an experiment in which an array of cantilever beams of increasing length were brought into contact with a substrate using

capillary forces and the detachment lengths, length of longest beam that remains detached after the liquid dries, were measured [14]. These experiments were accompanied by a theoretical model which related the strain energy of the cantilever beam to the adhesion energy [14]. This analysis was subsequently extended using linear and nonlinear theories to doubly clamped beams and plates by the same authors [15]. In the extension the analysis initially included liquid in the derivation however it was later removed in a limiting process to obtain the peel number that predicts whether the microstructure will remain attached [15]. The problem of the doubly clamped beam differs from that of the cantilever in that the doubly clamped beam has additional elongation requirements and the cantilever may experience a shear deformation at the tip if the adhered length is short [14], [15]. The doubly clamped formulation was subsequently used by Wu *et al.* to estimate the detachment length for a micro-stereolithography application [16]. O Raccurt *et al.* again used the approach of [15] to estimate the work of adhesion however it was shown that the existing model was deficient in that the obtained value was greatly dependent on the last liquid used before drying [17]. The previous techniques measuring the detachment length of an array of cantilevers assumed an arc shaped beam in which only the tip makes contact, de Boer *et al.* argues that for such a configuration it is difficult to know the area of contact which can lead to error in the measurement of work of adhesion [18]. Furthermore, in the same work the argument is made that an s-shaped configuration, in which the adhered portion of the beam is parallel to the substrate, would be preferable due to larger contact area and well of energy;

fracture mechanics methods can be applied to this case [18]. Some analysis into the length required for arc and s-shaped configurations has been done [18], and the transition from arc to s-shaped collapse has been modelled [8]. Subsequently the strain energy release rate from both arc and s-shaped stiction failed cantilevers was measured by Leseman *et al.* and used to obtain adhesion energies [19].

Naturally there has also been significant accompanying research interest into adhesion mechanisms responsible for stiction, one particular study attributed stiction of hydrophobic surfaces to van der Waals forces, and stiction of hydrophilic surfaces to hydrogen bridging [20]. Tas *et al.* discussed four potential sources of adhesion, namely hydrogen bridging, van der Waals forces, electrostatic forces, and capillary forces with added attention given to the effect of capillary condensation [21]. Because contact and subsequent stiction of devices during operation was a concern anti stiction devices such as bumps, spacers, increasing surface roughness, and weakly adhesive coatings used to decrease adhesion energy have been discussed [21]. Furthermore the influence of surface roughness and environmental conditions, such as temperature and relative humidity, on stiction has been investigated [22]. Delrio *et al.* used electrostatic forces to bring a microcantilever into an s-shaped stiction failure thus eliminating capillary forces at the interface. The resulting measurements indicated that adhesion was due primarily to van der Waals forces [23]. Additional methods for reducing intersolid adhesion include, textured surfaces and posts, low-energy monolayer coatings, and fluorinated coatings [2].

Another active area of research involving capillary forces and adhesion is the capillary adhesion of “hairs”. Here “hairs” are a model consisting of lamella of wetted slender cantilever beams used to represent things such as MEMS devices, nanotube carpets, and bundles of hair [24]. These investigations illustrate the interplay between elasticity and surface tension forces and often define a length scale, the elastocapillary length, which compares bending stiffness and surface tension [1]. Bico *et al.* performed an experimental investigation and scaling analysis of elastocapillary coalescence in wet hair (why wet hair clumps into bundles) [24]. The analysis of Bico includes both a pair of hairs, and multiple pairs. A more detailed analysis of this problem at the microcantilever level has been performed in which the energy method is used to analyze 2, 3, 4 and even a hierarchy of hairs [25]. Nonlinear geometrical effects in the beam model were subsequently investigated in the problem of two hairs [26]. Typically these investigations look to find the length of the beam that is adhered.

There are numerous deficiencies in the works that study the collapse of microstructures due to capillary forces. Most notably there are two forms of loading created by the presence of liquid, the Laplace pressure and the direct surface tension force applied at the contact line. Of works previously cited only [43] accounted for the surface tension force at the contact line in beam loading; all of the partial drop works neglected this force. Roman *et al.* discussed this force but only in the context of deforming a solid surface but not the bending of a microstructure [1]. It is apparent from a force balance of interfacial tensions normal to a solid surface that unless the liquid is perfectly wetting it will exert a

force on the solid. Numerous works [4], [6], [7], [11], [12], [13] obtained the beam deflection from equilibrium differential equations using known formula for the capillary or Laplace pressure; in each case no consideration was given to the surface tension force applied at the contact line. These works may have assumed it to be negligible but no work was done to support such an assumption. Furthermore, those who used energy methods to obtain beam loading simplified or neglected the contribution of the liquid-air interface to the total surface energy without performing any work to support this simplification [3], [5], [8], [9]. Often these areas are neglected because they are typically smaller, however doing so removes some of the physics of the problem because the phenomena of wetting is driven by minimizing the surface energy of a drop by adjusting the amount of surface area involved in air-liquid interfaces and solid-liquid interfaces (for example a drop of water wets glass however a drop of mercury placed on glass forms a bead because the energy of the mercury-glass interface is higher than the mercury-air interface). As will be shown in this work by means of a simple example retaining these energy terms allows the energy method to give surface tension forces as well as capillary pressure. The discussion in [43] compares deflections given from the model of Tanaka *et al.* [4] which only considers capillary pressure with their model that also considers surface tension. The comparisons were made when the beam was nearly undeflected and significant discrepancies were reported. However, in these models the capillary pressure increases with deflection so if the comparison were made closer to collapse there would be a smaller discrepancy. In the model to be presented here the change in

capillary pressure with deflection is nonmonotonic which creates greater potential for surface tension forces to impact collapse.

Several works consider liquid for the entire length of the beam [4], [6], [11], [12], [13]; however it has also been observed experimentally that during the drying process isolated droplets may form which move to the free end of a cantilever [7]. Because it adds additional complication modeling of these partial drops seems to lead to considerably more confusion. The first common modelling error encountered pertains to the pressure within the drop. Several works [5], [8], [9] propose mathematical models in which the capillary pressure is obtained at each point along the beam and thus varies within the drop. These models are all flawed since they all look for an equilibrium solution however basic fluid mechanics tells us that a pressure gradient is a driving force for fluid motion [27]; thus the drop must be isobaric as has been expressed by Abe *et al.* [7]. So the Laplace pressure must be determined only using the deflection at the meniscus. However, for the partial drops there is more than one meniscus which requires a constraint to ensure the same pressure is obtained from each. In addition several works [8], [9] performed their formulation for an arbitrary drop position along the beam and then proceeded to conduct analysis only for specialized cases, without justification for why they were chosen. In fact the physical justification for these cases should come from requiring the Laplace pressure calculated from each meniscus to be equal, as will be elucidated later in this work.

Further issues in the literature exist regarding the use of test functions and approximate analytical solutions. Mastrangelo *et al.* used simple polynomial test

functions [3] however there was no convergence analysis in which different forms or higher order polynomials were used. The work of Mastrangelo was scrutinised for these reasons by Ouakad *et al.* [8], who subsequently used multiple forms and studied convergence. However, because there are areas on the beam with and without liquid the form of the test function physically should have been piecewise continuous as used in the solution presented by Peng *et al.* [9]. Probably the biggest shortcoming of many of the prior works is the over simplification of discussion on collapse. For the works which considered the microstructure completely filled with liquid [4], [6], [11], [12], [13], the discussion is relatively straight forward since there are less governing parameters. However, for works that considered the microstructure only partially filled with liquid the existing discussion available in the literature does not allow one to understand how each parameter influences collapse. Some works avoided having to discuss multiple parameters by restricting the discussion to a perfectly wetting liquid, or not allowing the meniscus to move during beam deflection [8], or avoided discussion of results almost entirely [9]. In other works the focus of the discussion is often centered on the elastocapillary number and the associated pull-in length [3]. The approximate elastocapillary number brings together geometry, contact angle and surface tension to describe if there is an entrapped volume of liquid that will cause the structure to collapse [3]. In reality this problem depends on many variables (the gap between beams, beam length, moment of inertia, surface tension, contact angle, drop volume, Young's modulus for the beam etc.) and detailed discussion on how each parameter can influence collapse is nonexistent. Furthermore,

although some models do account for larger strain [3] only one model explores nonlinear geometrical effects [8] on the deflection of a cantilever; in addition, the discussion in [8] is limited to the collapse of a cantilever 80 times longer than the distance from the beam to the substrate so it is not surprising that nonlinear geometry was found to be negligible. On the other hand, it has been documented in the literature that collapse can be a problem when the length of a double cantilever beam is five times the spacing between beams [4], [6]; such geometry would result in larger beam slopes and make geometric nonlinearity more important.

There are also issues with previous works studying adhesion of beams. Several works presented formulations for the adhered beam deflection with the presence of liquid [15], [16], [17]. Each of these works then proceeded to take the limit as the liquid disappears and used the result to evaluate the work of adhesion. However, in each case before the limit is taken the adhered portion of beam is surrounded by water. As a result if a small area of the adhered solid surfaces separates, the interface will be filled with liquid rather than be exposed to air. In other words, the energy to “fracture” a unit area of the adhered solid surfaces is not the standard solid-solid work of adhesion [28]. Furthermore, as previously noted the experimental values were found to depend on the last liquid used [17] indicating that the adhesion energy depends on more than the solid-solid work of adhesion. The likely reason is the presence of liquid in the pores or other imperfections between the solid surfaces in contact, adding capillary adhesion [21]. This type of adhesion has been modeled as thin layer of liquid between the

two adhered solid surfaces in an s-shaped beam [21]. This same approach was taken in the adhesion of hairs models [24], [25]. The obvious question with these models is whether or not it is appropriate to neglect the solid-solid adhesion, and model the problem as though liquid completely fills the space between the beams. Finally, in the study of adhesion of beams, there also exist problems of neglecting surface tension force, allowing for pressure gradients in the liquid droplet [20], neglecting geometrical nonlinearity [14], [16]-[22], and lack of exact solution for the beam deflection (assumed form of deflection) [15], [16], [20], [24], [26].

In this work, the above deficiencies are removed by formulating the capillary collapse and adhesion of a system in a rigorous manner and obtaining the exact solution for the deformation. In particular, the following effects not consistently incorporated in previous partial drop works are considered: (1) loading due to both the Laplace pressure and the surface tension force; (2) consistent coupling between the deformation of the DCB and the capillary forces (3) possible movement of the menisci as the DCB deflect. In addition the need to consider geometrical nonlinearity will be investigated. Finally, how each governing parameter influences collapse will be thoroughly discussed.

Two specific problems are studied in this work, the first being the collapse of a DCB partially filled with a liquid droplet at the free end. Figure 1.1 is a schematic of the DCB shown from the side. Here L is the length of each beam, h is the half spacing between the beams, and the depth of the beams in to the page will be denoted as D . For this analysis D is assumed to be much greater than the spacing between the beams, $2h$. The base of each beam at $x = 0$ is clamped so that

it will have zero slope and deflection. x_1 is the location of the meniscus closer to the base, which will be referred to as the base meniscus. The second meniscus is located at the free end or $x = x_2 = L$. The liquid will form contact angle θ_c with the solid surface and liquid-air and have surface tension of γ_{LA} . The system is assumed to be symmetrical about line O_1O_2 so only half needs to be considered. Unlike in [8], we allow one of the menisci to move in order to maintain a constant liquid volume. The isobaric drop condition from [7] will be rigorously enforced which provides a constraint equation that can be used to explain why one meniscus pinned at the free end is under consideration. In addition, we consider both Laplace pressure and surface tension force from the liquid as functions of beam deformation and solve the coupled problem consistently. Both linear and nonlinear beam models will be used to evaluate the need for using a nonlinear analysis. Through this work, we identify four dimensionless parameters that govern the collapse of the DCB and discuss in detail how each parameter contributes to collapse.

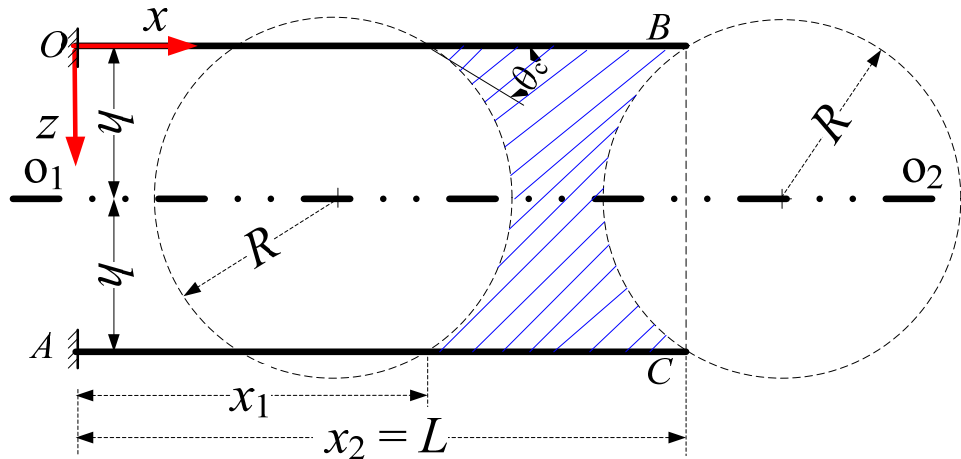


Figure 1.1: Schematic of the DCB to be studied in this work (shown from side).

The second problem studied in this work is the adhesion of the two beams in the DCB in an s-shaped configuration. The schematic for this problem is shown in Figure 1.2; here the beams come into contact at point B where $x = x_2$. This investigation will differ from those in the past in several ways. Most notably we will consider liquid in the unadhered space between the beams. This allows the study of behaviour the previous models could not. For example it has been documented in the literature that beams are often pulled in to contact by evaporating a liquid drop [19]. This model will be able to predict how the adhered length of the DCB changes as the liquid volume decreases. As before this model will account for both Laplace pressure and surface tension loading, and will allow for the meniscus position to change with beam deflection. Finally the analysis will be performed using both linear and nonlinear beam models to evaluate the necessity of using a nonlinear analysis.

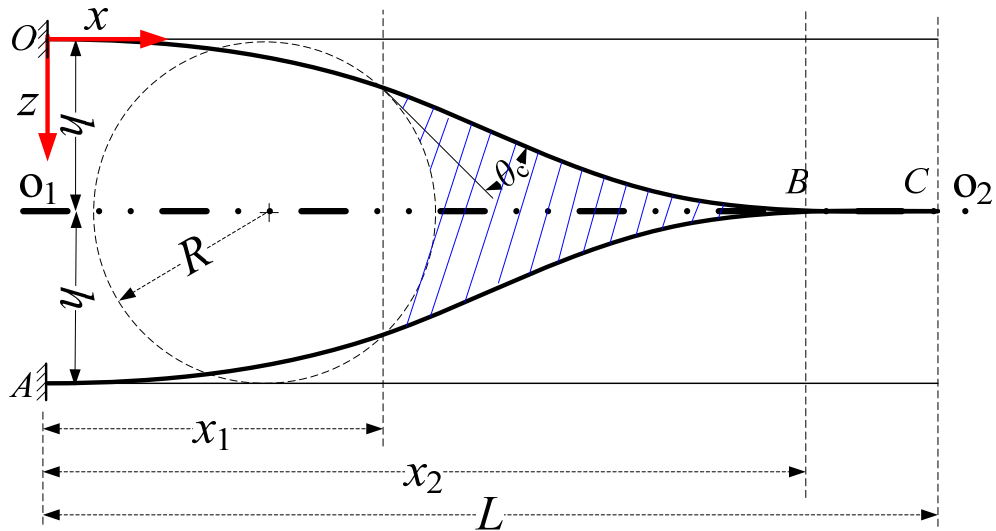


Figure 1.2: Schematic of the s-shaped adhered DCB to be studied in this work (shown from side).

The structure of the dissertation is as follows. In Chapter 2 the basic theory needed will be presented. Chapter 3 and Chapter 4 present the formulation of the

linear and nonlinear models respectively, the latter accounts for geometric nonlinearity. DCB collapse results from the linear theory are presented and discussed in Chapter 5. These discussions will be primarily qualitative and will focus on how each governing parameter influences collapse. In Chapter 6, the results of the nonlinear theory are compared with those obtained from the linear theory. This chapter also compares results with those from existing models in the literature, as well as proposes an empirical relationship to predict collapse. The results of both the linear and nonlinear theories for the adhered case are presented in Chapter 7. Finally, conclusions and future work are discussed in Chapter 8.

Chapter 2 Theoretical Background

In this chapter, the background theories describing capillary forces and beam deformation pertinent to this work will be presented.

2.1 Quantities describing capillary forces

This section will introduce some quantities that are commonly used to describe liquid-air and liquid-solid interfaces. It will also be discussed how capillary forces arise and why they are significant at small length scales.

2.1.1 Surface Tension

To cause an increase dA_s in the surface area of a liquid drop, work has to be done and this work increases the potential energy of the surface by dU_s as follows [29]

$$dU_s = \gamma dA_s \quad (2.1)$$

where the proportionality constant γ is called the surface tension. The surface tension depends on the properties of the liquid and the vapour as well as temperature and pressure. Some representative values of surface tension are shown in Table 3. The dimension of γ is force per unit length or equivalently energy per unit area. The potential energy U_s of a surface can be defined by integrating Eq. (2.1) and letting U_s be zero when $A_s = 0$, to give

$$U_s = \gamma A_s. \quad (2.2)$$

Table 3: Selected Surface tension values for 20-25° C [30]

Liquid	Surface Tension (mN/m)	Liquid	Surface Tension (mN/m)
Water	72	Benzene	28
Mercury	484	n-Propanol	23
Formamide	58		

2.1.2 Contact Angle and Wetting

The wetting phenomenon is of interest when a small amount of liquid is placed on a solid surface; the liquid may establish a contact angle, θ_c as shown in Figure 2.1, or spread on the surface completely ($\theta_c = 0^\circ$). The former case is shown in Figure 2.1 where the three phases form a contact line, here the contact line is perpendicular to the plane and goes through the intersection point of the three vectors representing the three interfacial tensions γ_{LA} , γ_{SA} and γ_{SL} . Equilibrium of the three tensions acting on the contact line gives Young's Equation [29]

$$\gamma_{SA} = \gamma_{LS} + \gamma_{LA} \cos \theta_c. \quad (2.3)$$

A liquid is said to be completely wetting if $\theta_c = 0^\circ$, partially wetting if $0^\circ < \theta_c < 90^\circ$ and non wetting if $\theta_c > 90^\circ$. If the liquid is water then a surface is hydrophilic if $\theta_c < 90^\circ$ and hydrophobic if $\theta_c > 90^\circ$. The value of the contact angle depends on the energetics of forming solid-air, liquid-air, and solid-liquid interfaces. For example if solid-liquid interface has a high energy then larger contact angles $\theta_c > 90^\circ$ are favourable in order to minimize the total energy. The contact angle also depends on ambient temperature and pressure, and surface geometry such as roughness. Finally, because the solid surfaces are never perfectly smooth if the drop is in motion the contact angle can show hysteresis depending on whether the drop is advancing or receding; for this reason, advancing and receding contact angles are typically tabulated, and some representative advancing contact angles are shown in Table 4. Because contact

angle hysteresis is not the focus of this work, the contact angle considered here should be interpreted as the equilibrium or static contact angle.

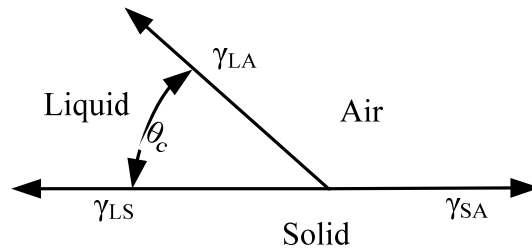


Figure 2.1: Equilibrium of 3-phase contact line

In light of Figure 2.1, Young's equation represents equilibrium in the direction tangential to the solid surface. However, a portion of the liquid-air interface surface tension acts in the direction normal to the solid surface and this force must be balanced by a reaction from the solid. This resultant force, when applied on a flexible structure such as on a micro cantilever beam, can cause deformation of the structure.

Table 4: Selected Advancing contact angles (deg) for 20-25° C [30]

Solids	Liquids				
	Water	Mercury	Formamide	Benzene	n-Propanol
Paraffin	110			0	22
n-Hexatriacontane	111			42	
Teflon	108-112	150		46	43
Polyethylene	103		75		7
Graphite	86			0	
Platinum	40				
Glass	small	128-148			
Polytetrafluoroethylene-co-hexafluoropropylene	108		92		
Polyethylene terephthalate	79.1		61		
Polymethylmethacrylate	59.3		50		
Talc	78.3		67.1		

2.1.3 Capillary Pressure

If an equilibrium liquid surface is curved there is a pressure difference across it, which is given by the Young-Laplace equation [29]

$$\Delta P_{lap} = \gamma_{LA} \left(\frac{1}{R_1} + \frac{1}{R_2} \right), \quad (2.4)$$

where R_1 and R_2 are the principal radii of curvature of the meniscus. This work will consider liquid drop in air and will use the following sign convention for the pressure change across the meniscus

$$\Delta P_{lap} = P_L - P_A = P_{Lg}, \quad (2.5)$$

where P_L , P_A , P_{Lg} are respectively the absolute pressure in the liquid, the atmospheric pressure and the gage pressure in the liquid.

A dimensionless quantity often used for liquids is the bond number defined by [27],

$$Bo = \frac{g(\rho_L - \rho_A)L^2}{\gamma_{LA}} \quad (2.6)$$

which represents the ratio of gravitational forces to surface tension forces. Here g , ρ_L , ρ_A and L are gravitational acceleration, density of the liquid, density of the gas, and a length scale respectively. Clearly when L is small gravitational effects can be neglected. In the case of water and air the Bond number is less than 1 for length scales smaller than about 2cm, which is much larger than the length scales in MEMS and NEMS applications. Therefore it is reasonable to neglect gravitational effects. Neglecting gravitational effects implies that there is negligible variation in both atmospheric and hydrostatic pressures within a liquid droplet; therefore, the jump in Laplace pressure across a meniscus, given by Eq. (2.4), must be constant at all locations along the meniscus. In addition, if a liquid

drop is in equilibrium it must be isobaric (i.e., constant pressure everywhere in the liquid), since pressure gradients are a driving force for fluid motion [27]. As a result if a liquid droplet possesses multiple menisci ΔP_{lap} must be the same across each meniscus. As previously mentioned several works had models in which the capillary pressure varied within the droplet since ΔP_{lap} was calculated based on local beam deflection [5], [8], [9], [20], rather than only at each meniscus with a constraint on their equality. This is a violation of the isobaric condition.

The Laplace pressure exerts a load on the solid surface in contact with the liquid. Since gravitational forces have been neglected P_A is constant and acts on all sides of the solid; therefore, if P_A is subtracted a uniform pressure load of magnitude $\Delta P_{lap} = P_{Lg}$ pushes on the solid surface. This can be seen in Figure 2.2, where the absolute pressures are shown on the left, and the net pressure loading is shown on the right.

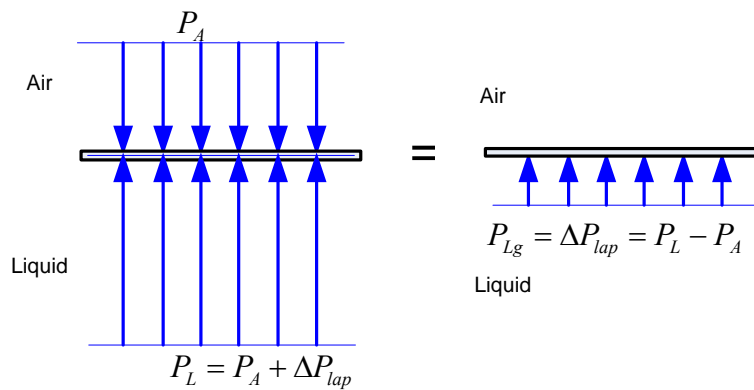


Figure 2.2: Equilibrium of a solid plate subjected to pressure forces

2.1.4 An Example

To help link the previous sections together and tie the results to mechanics consider the example of an incompressible liquid droplet sandwiched

symmetrically between two identical plates. For simplicity assume that the system is 2-dimensional (one radius of meniscus curvature is infinite). A quarter of the system is shown in Figure 2.3. The objective of the analysis is to determine the force F required to hold the plates separated by a distance $2z$. A similar analysis has been conducted in several works [3], [5].

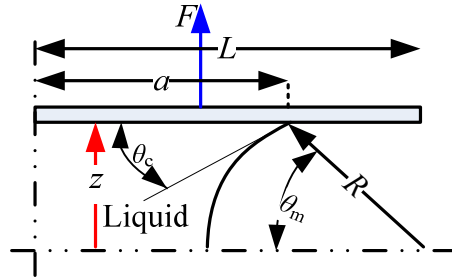


Figure 2.3: Schematic for plate drop example

Using Eq. (2.2) the potential energy of all the surfaces is given by

$$U_S = \gamma_{LA}A_{LA} + \gamma_{SA}A_{SA} + \gamma_{SL}A_{SL} \quad (2.7)$$

where A_{LA} , A_{SA} , A_{SL} are the areas of the liquid-air, solid-air and solid-liquid interfaces respectively. Using Young's Equation, Eq. (2.3), to eliminate γ_{SL} , U_S can be expressed as

$$U_S = \gamma_{LA}(A_{LA} - A_{SL} \cos \theta_c) + \gamma_{SA}(A_{SA} + A_{SL}). \quad (2.8)$$

Note that $A_{SA} + A_{SL}$ is a constant (surface area of the plate) thus the second term is a constant, denote U_{S_0} . From the geometry shown in Figure 2.3, the following relationships can be obtained

$$\begin{aligned} A_{SL} &= aD, & A_{LA} &= DR\theta_m, \\ \theta_m &= \sin^{-1}(z/R), & R &= z/\cos \theta_c, \end{aligned} \quad (2.9)$$

where a , z , R , and θ_m are geometric quantities shown in Figure 2.3 and D is the depth of the plate into the page. Substituting Eq. (2.9) into Eq. (2.8) gives

$$U_S = U_{S_0} + \gamma_{LA} D \left(\frac{z}{\cos \theta_c} \sin^{-1}(\cos \theta_c) - a \cos \theta_c \right). \quad (2.10)$$

Since the liquid is assumed to be incompressible and not leaking we require the volume of the drop given by

$$V = aDz - D \left(\frac{R^2}{2} \sin^{-1}(z/R) - \frac{z}{2} \sqrt{R^2 - z^2} \right) \quad (2.11)$$

to be constant. Here the second term represents the liquid displaced by the meniscus (circular cap). This term along with A_{LA} are neglected in previous formulations [3], [5]. Using Eq. (2.9) to simplify Eq. (2.11) gives

$$V = aDz - \frac{z^2 D}{2 \cos \theta_c} \left(\frac{\sin^{-1}(\cos \theta_c)}{\cos \theta_c} - \sin \theta_c \right) = aDz - \frac{z^2 D}{2 \cos \theta_c} \zeta \quad (2.12)$$

where the term in the brackets has been denoted by $\zeta(\theta_c)$ for simplicity. If the position of the plate z changes so will the wetted length of the plate, a , therefore applying the constant volume constraint gives

$$dV = \frac{\partial V}{\partial z} dz + \frac{\partial V}{\partial a} da = 0 = D \left(a - \frac{z \zeta}{\cos \theta_c} \right) dz + Dz da, \quad (2.13)$$

which can be rearranged to give a relationship between the liquid spreading width $2a$ and the plate spacing $2z$

$$\frac{da}{dz} = -\frac{a}{z} + \frac{\zeta}{\cos \theta_c}. \quad (2.14)$$

The force acting on the 1/2 of one plate can be obtained by differentiating the potential energy with respect to z as follows

$$F = \frac{dU_S}{dz} = \frac{\partial U_S}{\partial z} + \frac{\partial U_S}{\partial a} \frac{da}{dz}. \quad (2.15)$$

Introducing Eq. (2.10) and Eq. (2.14) gives, after simplification

$$F = \frac{\gamma_{LA} \cos \theta_c}{z} Da + \gamma_{LA} D \sin \theta_c . \quad (2.16)$$

Finally using the definition of R in Eq. (2.9) gives

$$F = \frac{\gamma_{LA}}{R} Da + \gamma_{LA} D \sin \theta_c . \quad (2.17)$$

The first term in Eq. (2.17) is the Laplace pressure, given by Eq. (2.4) with one radius being infinite since the meniscus was assumed to be 2-D, multiplied by the area on which it acts. The second term is the portion of the liquid-air surface tension that acts normal to the plate. This result could have been obtained directly by applying the results of sections 2.1.2 and 2.1.3. However, in the literature when the energetic approach is taken for similar problems the area of the meniscus and the liquid displaced by the meniscus are often assumed to be small and hence neglected [3], [5]. As a result the second term in Eq. (2.17), owing to the surface tension force, is not obtained. When this is a good assumption will be addressed in the discussion by looking at the contributions from each component.

In the analysis above, the half contact width a is a variable that depends on the plate separation z through the constant volume condition. In other words, the meniscus is allowed to adjust its location. We note that some previous studies apply the Laplace pressure (2.4) but force the meniscus locations to be fixed to simplify the analysis [8]. Following the approach of this section but constraining the meniscus in such a way would not give rise to the desired Laplace pressure loads in Eq. (2.17).

Let us expand this example by attaching a linear spring of stiffness k to each plates as is done in [2], [3]. Assume that the spring is unstretched when $z = h$, then after eliminating a using Eq. (2.12) the energy of the system is

$$U_T = \frac{1}{2}k(z-h)^2 + U_{So} - \frac{\gamma_{LA}V}{z} \cos \theta_c + \frac{\gamma_{LA}Dz}{2} \left(\frac{\sin^{-1}(\cos \theta_c)}{\cos \theta_c} + \sin \theta_c \right). \quad (2.18)$$

Differentiating Eq. (2.18) with respect to z gives the net force on the system which must be zero for equilibrium, i.e.,

$$0 = k(z-h) + \gamma_{LA} \cos \theta_c \left(\frac{V}{z^2} \right) + \frac{\gamma_{LA}}{2} D \left(\frac{\sin^{-1}(\cos \theta_c)}{\cos \theta_c} + \sin \theta_c \right). \quad (2.19)$$

It is convenient to introduce the following normalized parameters

$$z^* = \frac{z}{h}, V_L^* = \frac{V}{LDh}, \eta = \frac{kh}{\gamma_{LA}D}, \beta = \frac{h}{L}, U_T^* = \frac{U_T}{\gamma_{LA}DL \cos \theta_c}, \quad (2.20)$$

which are respectively normalized plate position, normalized liquid volume, ratio of spring forces to capillary forces, the ratio of plate length to spacing, and normalized energy. Introducing these parameters into Eq. (2.19) and rearranging the terms gives

$$V_L^* = \frac{\beta z^{*2}}{2 \cos \theta_c} \left(2\eta(1-z^*) - \left(\frac{\sin^{-1}(\cos \theta_c)}{\cos \theta_c} + \sin \theta_c \right) \right). \quad (2.21)$$

Similarly introducing the normalized parameters into Eq. (2.18) gives

$$U_T^* = \frac{\eta \beta}{2 \cos \theta_c} (z^* - 1)^2 + U_{So}^* - \frac{V_L^*}{z^*} + \frac{z^* \beta}{2 \cos \theta_c} \left(\frac{\sin^{-1}(\cos \theta_c)}{\cos \theta_c} + \sin \theta_c \right). \quad (2.22)$$

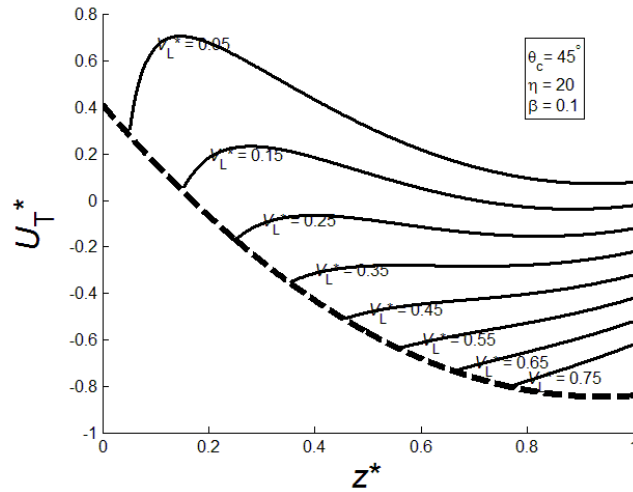


Figure 2.4: Total energy of spring-plate-liquid system for a range of liquid drop sizes.

The total energy given by Eq. (2.22) is plotted against z^* in Figure 2.4. The solid black curves represent U_T^* at various values of V_L^* , and the dashed line represents U_T^* when $a = L$ or when the liquid completely fills the gap between the plates. The system attains z^* that minimizes U_T^* , which may occur either at $a = L$ or at a local minimum of U_T^* given by a solution of Eq. (2.21). Note that for larger drops $V_L^* > 0.4$, U_T^* has no local minimum while for smaller drops there is both a local minimum and a local maximum. The maximum separates a minimum at $a = L$ from the local minimum; it may act as an energy barrier and prevent the solution from attaining a global minimum energy. As a result there may be multiple solutions to this problem for smaller drops in which case the solution will depend on the initial condition. To see this consider the branching and energy diagrams showing in Figure 2.5 for three increasing values of η , which could correspond to a soft, moderate and stiff spring respectively. We consider a quasi-static process in which the liquid initially fills the entire gap ($a = L$), and is very slowly evaporated till $V_L^* \rightarrow 0$. The path that the system will follow as the drop evaporates is represented by the red arrows in Figure 2.5. In the branching diagrams Figure 2.5a), c), e), V_L^* is plotted against z^* . In each of these subfigures, the dashed line represents the system in the configuration where $a = L$. To focus on demonstrating the concept and simplify the analysis, the liquid volume displaced by the menisci has been neglected, which results in the approximation of $V_L^* \approx z^*$ when the gap is filled with the liquid. The solid line in each of these subfigures represents the system in a configuration given by a solution to Eq.

(2.21). Note that for larger drops there is no solution to Eq. (2.21) which was also observed in the energy graph Figure 2.4 in that there are no local minima or maxima. In addition if Figure 2.5a), c), e) are compared with their associated energy diagrams Figure 2.5b), d), f) it is clear that the portion of the solid line in Figure 2.5a), c), e) (solution to Eq. (2.21)) to the left of its maxima corresponds to a maximum in U_T^* whereas the portion of the line to the right of the maxima corresponds to a minimum in U_T^* . Physically the system can only stably exist in a configuration that minimizes energy U_T^* , so in Figure 2.5a), c), e) the system will never follow a path on the portion of the solid line to the left of its maxima. Now consider what happens for a soft spring shown in Figure 2.5a), as the drop volume decreases. Initially, $V_L^* = 1$ the space between plates is completely filled with liquid, the spring is undeformed and the system is at point A. As the drop volume decreases the plates move closer together and the system moves to point B. After this point there also exist local minima in U_T^* , however as can be seen in Figure 2.5b), this minima is not reachable due to the energy barrier. Therefore, as the liquid volume continues to decrease the system proceeds to point H. Physically, this means that the contact lines are pinned at the edges of the plates during the entire evaporation process. The two plates approach each other during the evaporation and eventually the gap between them reduces to zero. What happens for a spring of moderate stiffness, shown in Figure 2.5c), as the drop volume decreases is different. Again the system cannot move to the local minimum at point B due to the energy barrier, however as the liquid volume decreases to point D the energy maximum becomes extraneous because it occurs at z^* less than that

of the $a = L$ configuration; thus from Figure 2.5d) the system comes to an equilibrium at the local energy minimum point E. This transition corresponds to an abrupt jump in plate position z^* . As the drop volume continues to decrease to point F a local maximum appears again making the energy of the $a = L$ configuration, at point G, a local minimum; however, point G is not reachable due to the energy barrier so the system instead proceeds to point H as the volume of the liquid droplet is further increased. Physically, the jump in z^* separates the motion of the liquid/plates system into two regimes. Before the jump, the contact lines are pinned at the edges of the plates, and the plates move closer as the liquid is evaporated. At the jump, the plates experience a sudden increase in separation. After the jump, the contact lines move inward during the evaporation and continue to increase the separation between the two plates. The third case, for a stiff spring, is shown in Figure 2.5e), where as the drop volume is decreased the system proceeds following A-D-H. The difference in this case is that the local maxima which makes the energy of the $a = L$ configuration (Point G again not reachable due to energy barrier) a minimum does not occur until the system is at point F. Therefore when a local minimum first occurs at point D, it coincides with the $a = L$ configuration and there is no jump in the separation z^* .

If the above quasi-static evaporation process does not start with a gap-filling liquid volume, but rather with a small drop, then the system may attain a different solution. For example in Figure 2.5a), if the initial state was instead $V_L^* = 0.3$ and $z^* = 1$, when released the system would come to equilibrium on the curve CI, representing a solution to Eq. (2.21), and would instead proceed to point I rather

than point H (as previously described for initial state of $V_L^* = 1$ and $z^* = 1$) as $V_L^* \rightarrow 0$. Mastrangelo *et al.* [3] presented this analysis for the spring plate system as well as for a doubly clamped beam and it was found that the behaviour of the beam system shared many of the same characteristics as the simpler spring plate system.

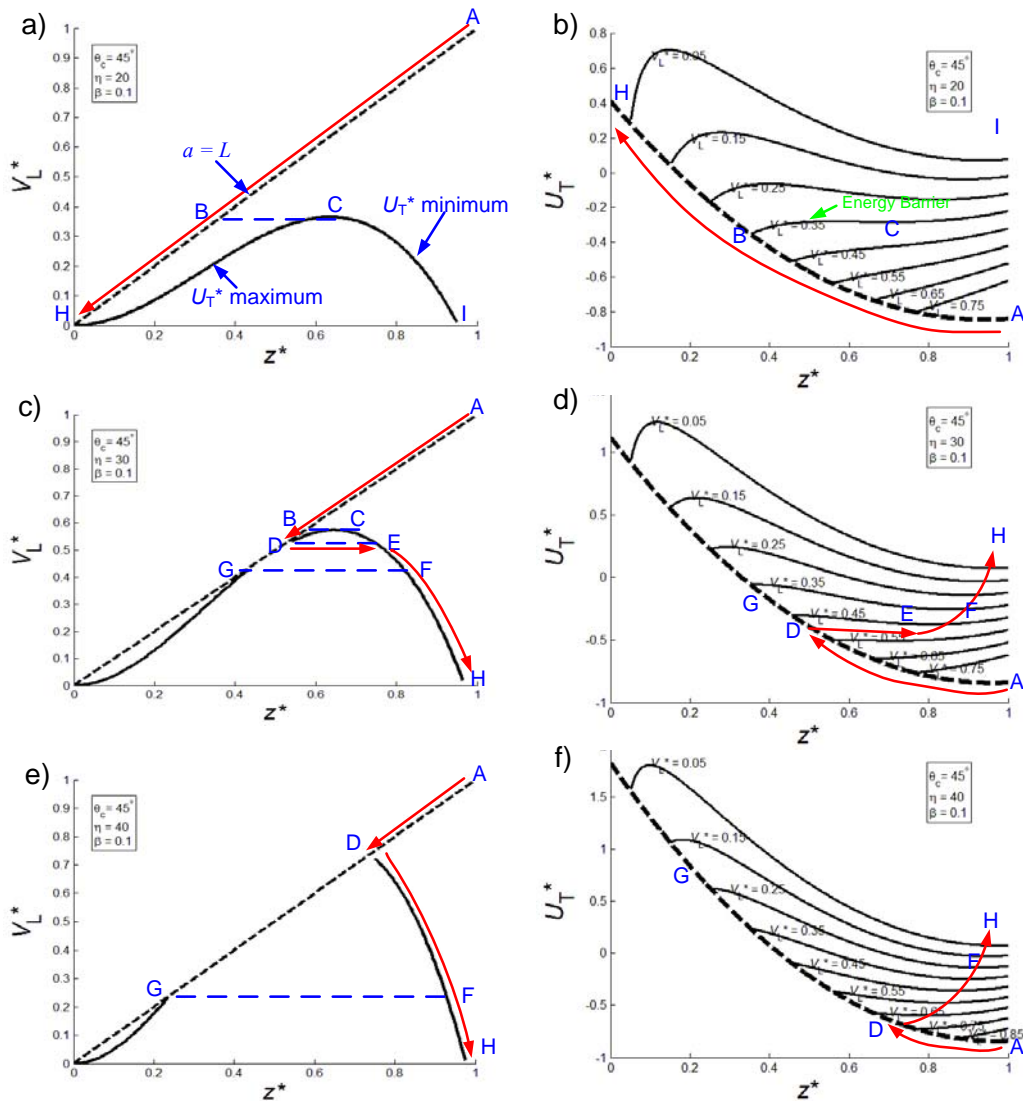


Figure 2.5: Branching and energy diagrams for spring-plate-liquid system for 3 values of η

2.1.5 Dupré Equation

Since one of the objectives of this work is to study s-shaped adhesion of a DCB we also need to look at adhesion energies. Consider the process of separating two solid surfaces joined cohesively within a liquid, shown in Figure 2.6, to create two liquid-solid interfaces. The energetics can be understood by considering the two-step process: (I) separating $\frac{1}{2}$ unit area of the solid-solid interface, the result of which is a unit area of the solid in contact with vacuum and a unit area of the liquid in contact with vacuum, and (II) bringing the solid and the liquid into contact to form a unit area of solid-liquid interface. This is captured by the Dupré equation [28]

$$\gamma_{SL} = \frac{1}{2}W_{SS} + \frac{1}{2}W_{LL} - W_{SL} = \gamma_S + \gamma_L - W_{SL}. \quad (2.23)$$

where γ_S, γ_L , are the equivalent of γ_{SA}, γ_{LA} in vacuum, W_{SS} and W_{LL} are works of cohesion of the solid and liquid respectively and W_{SL} is the work of adhesion between the solid and the liquid. In the literature the work of cohesion (γ_S) between solid and solid has been mistakenly used in place of γ_{SL} for situation shown in Figure 2.6 [15],[17].

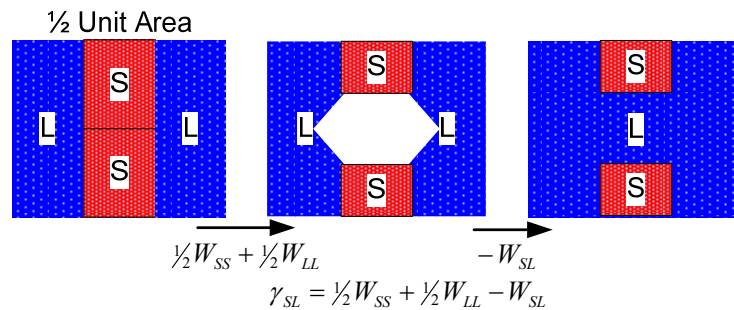


Figure 2.6: Separating a cohesively bonded solid in a liquid [28]

2.2 Bernoulli-Euler Beam Theory

The linear Bernoulli-Euler beam theory should be well known to most mechanical engineers. However, the many assumptions used to obtain the theory are not as commonly known. Essential elements in the derivation of the theory will be presented following the flowchart shown in Figure 2.7. The key purpose will be to identify the assumptions associated with this theory. A nonlinear version of the theory will also be presented that removes some of the assumptions by allowing for nonlinear geometrical effects.

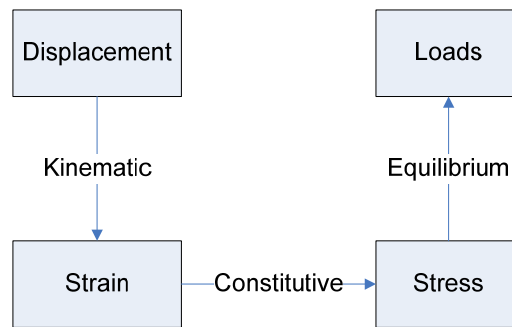


Figure 2.7: Bernoulli-Euler beam theory derivation path

2.2.1 Bernoulli-Euler Kinematic Assumption

Bernoulli-Euler beam theory makes the following kinematic assumption about the deflected shape of the beam: plane sections remain plane and normal to the axis of the beam. This assumption requires that the beam's deformation be caused solely by internal bending moments. Deformation caused by internal shear or axial forces are neglected. If the beam length is much greater than its height deformations caused by bending will be much greater than deformations caused by shear forces [31], hence the Bernoulli-Euler assumption is valid for thin beams. Typically beam loading is transverse so neglecting deformation caused by axial forces is reasonable and the beams behave as though they are inextensible. The Bernoulli-Euler kinematic assumption can be used to obtain a relationship for

the beam's strain. Figure 2.8a) shows an infinitesimal section of a beam that has been deformed by an internal moment M . Both cross sections remain planes and the extensions of these planes intersect at the center of curvature, point O . The radius of curvature ρ represents the distance from the center of curvature to the neutral axis (NA) of the beam. The NA is defined as the location on the cross section where there is no strain; any point on the cross section at a distance ξ from the NA is subjected to a normal strain given by [31]

$$\varepsilon = -\xi / \rho = -\kappa \xi \quad (2.24)$$

where κ is the beam curvature at this section. The strain expressed in Eq. (2.24) is the infinitesimal strain because it neglects second order terms that occur in the finite strain theory [41].

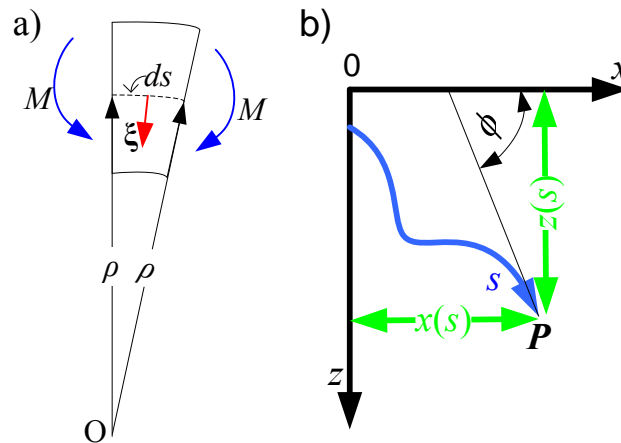


Figure 2.8: Bernoulli-Euler beam theory kinematic assumption

Relationships for curvature κ are readily available in calculus texts [32]. Let ϕ be the angle of inclination of the tangent line at a point P of a curve, the curvature κ at P is the rate of change of ϕ with respect to arc length s , and is defined as

$$\kappa = \frac{d\phi}{ds} \quad (2.25)$$

If the curve is given parametrically by $x = x(s)$, $z = z(s)$, as shown in Figure 2.8b), an alternate form of Eq. (2.25) can be derived by noting that $\phi = \tan^{-1}(dz/dx)$ and applying the chain rule to obtain

$$\kappa = \frac{\frac{dx}{ds} \frac{d^2z}{ds^2} - \frac{d^2x}{ds^2} \frac{dz}{ds}}{\left[\left(\frac{dx}{ds} \right)^2 + \left(\frac{dz}{ds} \right)^2 \right]^{3/2}}. \quad (2.26)$$

Although Eq. (2.26) is difficult to use, for parametric curves of the form $x = x$, $z = z(x)$ it reduces to

$$\kappa = \frac{\frac{d^2z}{dx^2}}{\left[1 + \left(\frac{dz}{dx} \right)^2 \right]^{3/2}}. \quad (2.27)$$

Finally if the higher order term $(dz/dx)^2$ in Eq. (2.27) is neglected the following approximate relationship for curvature is obtained

$$\kappa \approx \frac{d^2z}{dx^2}. \quad (2.28)$$

Neglecting the higher order term in Eq. (2.27) requires slopes to be small. For large slopes, it is more appropriate to consider the geometrical nonlinearity and use Eq. (2.25) coupled with the following two relationships,

$$\begin{aligned} \frac{dx}{ds} &= \cos \phi, \\ \frac{dz}{ds} &= \sin \phi. \end{aligned} \quad (2.29)$$

Eq. (2.25) and Eq. (2.29) have previously been used to model larger deflections of carbon nanotubes [33], [34]. It should be noted that if $\phi \ll 1$, then $\cos \phi \approx 1$, $\sin \phi \approx \phi$, i.e., s and x coincide, and Eq. (2.26) reduces to the linear relation, Eq. (2.28). Using these curvature relationships together with moment-curvature relationships allow the location of the beam's neutral-axis to be determined.

2.2.2 Constitutive Assumption

If the material is homogeneous, isotropic, and behaves in a linear elastic manner then 1-D Hooke's law can be used to give normal stress σ from the assumed strain

$$\sigma = E\varepsilon, \quad (2.30)$$

where E is Young's Modulus. The internal moment, M shown in Figure 2.8, can be obtained from the stress distribution

$$M = -\int_A \xi \sigma dA = \kappa E \int_A \xi^2 \sigma dA = \kappa EI. \quad (2.31)$$

where I is the area moment of inertia of the cross section. Rearranging Eq. (2.31) gives a relationship between internal moment and beam curvature

$$\kappa = \frac{1}{\rho} = \frac{M}{EI}. \quad (2.32)$$

Eq. (2.32) can be used to determine the beam's deflected shape based on the internal moment and flexural rigidity, once an appropriate curvature equation is adopted. Finally, Eqs. (2.24)-(2.32) can be combined to give the flexure formula for the stress distribution on the beam's cross section due to pure bending

$$\sigma = -M\xi/I. \quad (2.33)$$

Because the Bernoulli-Euler kinematic assumption assumes only one component of strain, only a one dimensional constitutive law, Eq. (2.30), is used. There are several repercussions of this simplification that should be discussed. First the Bernoulli-Euler theory neglects transverse normal stress that would accompany any transverse load. However, this stress will generally be negligible if the beam's length is much greater than its height [35]. Secondly, the theory neglects the Poisson effect which would cause the vertical sides of the beam's cross section to rotate due to the distribution of stress shown in Eq. (2.33). Physically

the top and bottom surfaces of the beam would become saddle-shaped or anticlastic [36]; this effect is small when the beam height is comparable with its depth [36]. But, for wide beams the following substitution is recommended [36]

$$E^* = E / (1 - \nu^2) \quad (2.34)$$

Where ν is Poisson's Ratio. Eq. (2.34) is a usual swap of material constants used in elasticity to transform plane stress solutions into plane strain solutions.

2.2.3 Reference Coordinate System and Infinitesimal Strain

The main body of the Bernoulli-Euler beam theory is in place however it is prudent to introduce some definitions. For instance to determine the displacement of a point on the beam requires that a coordinate system and a reference configuration be defined. In section 2.2.1 we discussed infinitesimal strain, however, this was only one component of the infinitesimal strain tensor which can be defined in terms of the displacement.

First to define positions of points on the beam two coordinate systems are utilized. The regular Cartesian coordinate system (x, y, z) , where x and z are shown in Figure 1.1 and y is directed perpendicular to the page, and a curvilinear coordinate system (s, y, ξ) . In the latter s is the arc length along the neutral axis (NA) from the base of the beam and ξ is directed transverse to the NA (Figure 2.8); since the beam is assumed to be inextensible the coordinates of points on the beam in this coordinate system do not change with deflection. Now consider a point on a beam that before deflection is located at position (x_o, y_o, z_o) . If after deflection this point is located a position (x_f, y_f, z_f) the displacement vector is

$$\underline{u} = u\underline{i} + v\underline{j} + w\underline{k} = (x_f - x_o)\underline{i} + (y_f - y_o)\underline{j} + (z_f - z_o)\underline{k} \quad (2.35)$$

where \underline{i} , \underline{j} , \underline{k} are unit vectors. In general the displacement is measured against a known reference state. In this work the undeflected state where the beam is unstrained will be taken as the reference configuration. In this configuration Cartesian and curvilinear coordinate systems coincide and the beam's neutral axis coincides with the positive x -axis.

With the displacement vector we can now define the infinitesimal strain tensor as follows

$$\underline{\varepsilon} = \frac{1}{2}(\nabla\underline{u} + (\nabla\underline{u})^T). \quad (2.36)$$

As mentioned in section 2.2.1 the infinitesimal strain omits the higher order terms so it is valid for small strains. However only one component of the strain tensor, $\varepsilon = \varepsilon_x$, was previously discussed since the kinematics of the theory assume that all other components are zero. It then follows from Eqs. (2.24) and (2.32) that[35]

$$\begin{aligned} \varepsilon_x &= \frac{\partial u}{\partial x} = -\frac{M\xi}{EI} & \varepsilon_y &= \frac{\partial v}{\partial y} = 0 & \varepsilon_z &= \frac{\partial w}{\partial z} = 0 \\ \varepsilon_{xy} &= \frac{1}{2}\left(\frac{\partial v}{\partial x} + \frac{\partial u}{\partial y}\right) = 0 & \varepsilon_{xz} &= \frac{1}{2}\left(\frac{\partial w}{\partial x} + \frac{\partial u}{\partial z}\right) = 0 & \varepsilon_{yz} &= \frac{1}{2}\left(\frac{\partial v}{\partial z} + \frac{\partial w}{\partial y}\right) = 0 \end{aligned} \quad (2.37)$$

Note that transverse shear would cause ε_{xz} to be non-zero and transverse normal stress would cause ε_z to be non-zero. Both have been assumed to be negligible in the Bernoulli-Euler theory.

The moment-curvature relationship Eq. (2.32) combined with an appropriate definition of curvature allow for solution of the position of the NA after deflection. Points not on the NA can then be located using the kinematic

assumption Eq. (2.24). If after deflection a point on the NA ($s, y, 0$) is located at position (x, y, z) , then the components of its displacement vector are

$$u = x - s, \quad v = 0, \quad w = z, \quad (2.38)$$

since before deformation x and s coincide. Furthermore in the linearized version of the theory x is assumed to coincide with s even after deflection. In this case $u = 0$. Throughout the rest of the dissertation, unless otherwise specified, w will be used to denote the z -component of the displacement, or the deflection, of the NA.

2.2.4 Equilibrium

In the following, equations describing equilibrium are first presented with full consideration of geometrical nonlinearity, based on the formulation presented in Love *et al.* [36]. These equations are then linearized for the case of small deflection to give the relationships typically presented in undergraduate mechanics of materials textbooks such as [31].

Consider an infinitesimal section of length ds from a deflected beam shown in Figure 2.9. This figure shows the internal shear Q , axial force T , and bending moment M in their positive directions for this work. To maintain generality assume that this section is also subjected to the following distributed loading: a transverse traction q per unit length in the direction of ζ , an axial traction f per unit length in the direction of ds , and a clockwise bending moment m , per unit length. Since the section is infinitesimal the following simplifications apply.

$$\kappa = \frac{1}{\rho} = \frac{d\phi}{ds}, \quad \cos(d\phi) = 1, \quad \sin(d\phi) = d\phi \quad (2.39)$$

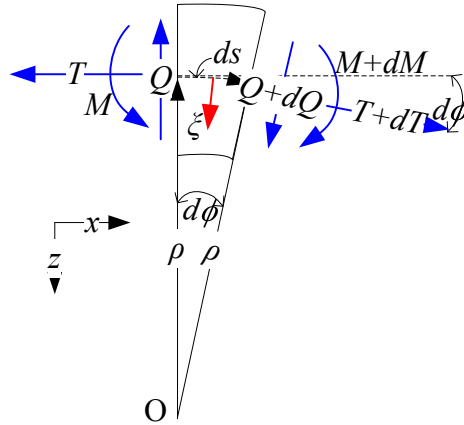


Figure 2.9: Equilibrium of an infinitesimal beam section showing internal reactions in positive sense for sign convention for this work

Force equilibrium in the x and z directions as well as moment equilibrium can be used to obtain three differential equations. Applying force equilibrium in the x -direction gives, after cancelation, division by ds and substitution of Eq. (2.25)

$$\frac{dT}{ds} - \kappa Q + f = 0. \quad (2.40)$$

Similarly, force equilibrium in z direction gives

$$\frac{dQ}{ds} + \kappa T + q = 0. \quad (2.41)$$

Finally, making use of Eq. (2.40), moment equilibrium about center of curvature O gives

$$\frac{dM}{ds} + Q + m = 0. \quad (2.42)$$

These three differential equations can be rearranged to isolate each internal force for use in applying natural boundary conditions. For the internal moment combining Eq. (2.32) and Eq. (2.25) gives

$$M = EI \frac{d\phi}{ds} \quad (2.43)$$

which is the primary differential equation that will be used to obtain the deflection in the nonlinear case. For the internal shear Q combining Eq. (2.42) with Eq. (2.43) gives

$$Q = -EI \frac{d^2\phi}{ds^2} - m. \quad (2.44)$$

Finally for the internal axial force combining Eq. (2.41) and Eq. (2.44) gives

$$T = \frac{1}{d\phi/ds} \left(EI \frac{d^3\phi}{ds^3} + \frac{dm}{ds} - q \right), \quad (2.45)$$

Due to its complexity Eq. (2.45) is difficult to implement and alternatives will be discussed in Chapter 4 when the nonlinear mathematical model is formulated.

The preceding results can be linearized for small slopes as follows. Applying the small slope approximation ($x \rightarrow s$ from Eq. (2.29)) to the differential equations (2.40) (2.41) and (2.42), and substituting in Eq. (2.28), recognizing that $w = z(x)$ for the NA, gives

$$\begin{aligned} \frac{dT}{dx} - Q \frac{d^2w}{dx^2} + f &= 0 \\ \frac{dQ}{dx} + T \frac{d^2w}{dx^2} + q &= 0. \\ \frac{dM}{dx} + Q + m &= 0 \end{aligned} \quad (2.46)$$

It then follows from Eqs. (2.32), (2.28) and (2.46) that each internal force is related to the deflection $w(x)$ by

$$\begin{aligned}
M &= EI \frac{d^2 w}{dx^2} \\
Q &= -EI \frac{d^3 w}{dx^3} - m \\
T &= \frac{1}{\frac{d^2 w}{dx^2}} \left(EI \frac{d^4 w}{dx^4} + \frac{dm}{dx} - q \right)
\end{aligned} \tag{2.47}$$

Finally, if $T = 0$ and $m = \text{constant}$, combining the last two equations in (2.46) gives

$$\frac{d^2 M}{dx^2} = q, \tag{2.48}$$

which can be combined with the first equation in (2.47) to give, for the case of constant flexural rigidity EI ,

$$EI \frac{d^4 w}{dx^4} = q. \tag{2.49}$$

This equation is commonly associated with Bernoulli-Euler beam theory. However, it will not be used in this work because the internal moment can easily be obtained by summation; hence the first equation in Eq. (2.47) would be preferred as it is only of second order. Furthermore, Eq. (2.49) requires the additional assumption of $T = 0$, which is not necessarily true in presence of the surface tension force.

2.2.5 Discontinuity Functions

If there are discontinuities in the beam's loading it is necessary to first solve the beam equations in multiple domains and subsequently determine the integration constants by matching the beam slope and deflection at the domain boundaries. This procedure can be tedious so it is desirable to express the loads, beam slopes and deflections using a single function. This can be accomplished using Macaulay Functions which are defined as follows [31]

$$\langle x-a \rangle^n = \begin{cases} 0 & \text{for } x < a \\ (x-a)^n & \text{for } x \geq a \end{cases} \quad n \geq 0. \quad (2.50)$$

With the exception of $n = 0$ or $\langle x-a \rangle^0$ which corresponds to the Heavyside unit step function, these Macaulay Functions are continuous. For $n > 0$ these functions are C^{n-1} continuous and their derivatives are as follows

$$\frac{d}{dx} \langle x-a \rangle^n = n \langle x-a \rangle^{n-1} \quad n > 0. \quad (2.51)$$

These functions also integrate like polynomials

$$\int \langle x-a \rangle^n dx = \frac{\langle x-a \rangle^{n+1}}{n+1} + C \quad n \geq 0. \quad (2.52)$$

Note that a similar class of “singularity functions” can be defined to accommodate point forces and moments for use with Eq. (2.49). However, since Eq. (2.49) will be avoided these “functions” will not be needed.

2.2.6 Strain Energy

Since considerable attention has been given to surface energy it is necessary to define the potential energy of strain or strain energy as follows

$$U_{SE} = \int_V \frac{1}{2} \underline{\sigma} : \underline{\varepsilon} dV. \quad (2.53)$$

Here the term within the integration is the strain energy per unit volume calculated by

$$W = \frac{1}{2} \underline{\sigma} : \underline{\varepsilon} = \frac{1}{2} \sigma_{ij} \varepsilon_{ij}, \quad (2.54)$$

where summation is implied over repeated indices. In the Bernoulli-Euler beam theory, the strain components are given in Eq. (2.37). From Eq. (2.33), and Eq. (2.30), the strain energy can be obtained as

$$U_{SE} = \int_l \frac{E}{2} \left(\frac{M}{EI} \right)^2 \int_A z^2 dA ds = \int_l \frac{M^2}{2EI} ds. \quad (2.55)$$

2.2.7 Bernoulli- Euler Derivation Summary

Although most of the results of this section are well known, they were explained in considerable detail to highlight the numerous assumptions that were made in obtaining Bernoulli-Euler beam theory. In particular the version of the theory that accounts for nonlinear deflection (large displacement) makes the following assumptions:

1. Neglect effect of transverse shear on strains
2. Neglect effect of axial normal stress (caused by axial forces) on strains (inextensible)
3. Neglect effect of transverse normal stress on strains
4. Small strain
5. Require homogenous, linear elastic, isotropic material
6. Neglect anticlastic curvature caused by Poisson effect

The linearized version makes several additional assumptions. Firstly, the expression for curvature was linearized by assuming small slopes. Secondly, as will be seen in a later section the geometrically nonlinear effects of beam deflection are ignored when obtaining an expression for the internal moment M .

Chapter 3 Linear Beam Formulation

The preceding theory will be applied to obtain a mathematical model for the capillary collapse and adhesion of the DCB. This chapter will focus on using the linear beam theory, and the formulation with nonlinear beam theory will be presented in Chapter 4. For each case the governing parameters and a system of equations to be solved will be identified, as well as the numerical algorithm used to solve these equations.

Two different cases will be presented in this chapter: one where the beams are separated (Figure 1.1) and we wish to predict contact at the free ends; and the other where the beams are in s-shaped adhesion (Figure 1.2). Formulation applicable to both cases is presented first below and the differences will be addressed in separate subsections later. Note that due to symmetry the formulation will focus only on the upper beam. For the linear theory the moment-curvature relationship is given by the first equation in Eq. (2.47)

$$M = EI \frac{d^2 w}{dx^2}. \quad (3.1)$$

Here the moment $M(x)$ can be determined by considering equilibrium of a section shown in Figure 3.1. The loadings that contribute to $M(x)$ are M_R the reaction moment at the base, Q_R the shear moment at the base, the surface tension force which acts at the meniscus (described in section 2.1.2), and the Laplace pressure force which acts on the section of the beam in contact with the drop (described in section 2.1.3). Note that in the linear case the beam's deflection is assumed to be so small that it does not affect the evaluation of $M(x)$. In reality the deflection will change the moment and this effect will be addressed in the nonlinear formulation.

Using Macaulay Functions (Eq. (2.50)) the internal moment $M(x)$ determined from moment equilibrium of Figure 3.1 can be written as follows

$$M = M_R - Q_R x - \frac{\Delta P_{lap} D}{2} \langle x - x_1 \rangle^2 + \gamma_{LA} D \sin \theta_c \langle x - x_1 \rangle^1, \quad 0 \leq x < x_2 \quad (3.2)$$

where x_1 , and D are respectively the location of the base meniscus, and the depth of the beam into the page shown in Figure 3.1. The third term in Eq. (3.2) represents the moment due to the Laplace pressure, and the fourth term represents the moment due to the surface tension force. x_2 should be interpreted as the free end ($x_2 = L$) in the uncollapsed case and the point of contact of the two beams (Figure 1.2) in the adhesion case. Note that in deriving Eq. (3.2) the couple moments associated with transferring the surface tension forces to the beam's NA have been neglected. This is a good assumption for thin beams where height is considerably smaller than length. Also, attractive forces between the beams, such as the Casimir effect, are ignored which is a generally a good assumption when capillary forces are present [37]. The reactions M_R and Q_R can be obtained from global beam equilibrium or boundary conditions; however they will differ for the two scenarios we are considering and therefore will be presented separately in sections 3.1 and 3.2.

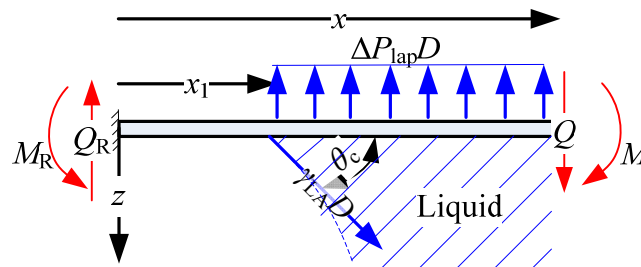


Figure 3.1: FBD of a section of a linear beam for obtaining internal reactions $M(x)$ and $Q(x)$

Several assumptions about the meniscus geometry have been made in formulating Eq. (3.2). Recall ΔP_{lap} is given by the Young-Laplace equation, Eq. (2.4), and can be related to the principal radii of curvature of the meniscus. Because D , the out of plane dimension of the beam, is much greater than the spacing between the beams, $2h$ (see Figure 1.1) the meniscus can be treated as two-dimensional [18], i.e., one of the principal radii $R_2 = \infty$. In addition since the droplet must be isobaric the menisci have a constant radius of curvature at all locations. In other words, each meniscus is part of a circular cylinder, as shown in Figure 1.1. In the following, we denote this radius as R , which leads to

$$\Delta P_{lap} = \gamma_{LA} / R \quad (3.3)$$

Furthermore, the sign convention (2.5) combined with the Young-Laplace equation (2.4) establish a sign convention for R ; negative R corresponds to a concave meniscus as is shown in Figure 1.1 whereas a positive R corresponds to a convex meniscus with contact angle greater than 90° . It should be noted that R is not a known quantity and needs to be determined from the equilibrium of the beam and of the liquid.

Combining Eqs. (3.1), (3.2) and (3.3) gives a 2nd order differential equation for the deflected curve

$$\frac{d^2 w}{dx^2} = \frac{1}{EI} \left(M_R - Q_R x - \frac{\gamma_{LA} D}{2R} \langle x - x_1 \rangle^2 + \gamma_{LA} D \sin \theta_c \langle x - x_1 \rangle^1 \right). \quad (3.4)$$

This equation can be integrated to give the slope and the deflection of the beam.

To eliminate the constants of integration the boundary conditions corresponding to zero deflection and slope at the clamped end are used, i.e.,

$$w(0) = 0, \quad \frac{dw(0)}{dx} = 0. \quad (3.5)$$

The expressions for the slope and the deflection are respectively given by

$$\tan(\phi) = \frac{dw}{dx} = \frac{1}{EI} \left(M_R x - \frac{Q_R}{2} x^2 - \frac{\gamma_{LA} D}{6R} \langle x - x_1 \rangle^3 + \frac{\gamma_{LA} D \sin \theta_c}{2} \langle x - x_1 \rangle^2 \right) \quad (3.6)$$

$$w = \frac{1}{EI} \left(\frac{M_R}{2} x^2 - \frac{Q_R}{6} x^3 - \frac{\gamma_{LA} D}{24R} \langle x - x_1 \rangle^4 + \frac{\gamma_{LA} D \sin \theta_c}{6} \langle x - x_1 \rangle^3 \right) \quad (3.7)$$

where ϕ is the angle the deflected curve makes with the positive x -axis.

The preceding equations can be normalized by introducing the following nondimensional parameters

$$x^* = \frac{x}{L}, \quad w^* = \frac{w}{h}, \quad \Lambda = \frac{\gamma_{LA} L^2 D}{EI}, \quad \beta = \frac{h}{L}, \quad \alpha = \frac{R}{h}, \quad M^* = \frac{ML}{EI}, \quad Q^* = \frac{Q L^2}{EI}. \quad (3.8)$$

These parameters correspond to normalized position, deflection, surface tension, spacing, meniscus radius, moment, and shear force. Introducing these parameters into the Eq. (3.4) gives

$$\beta \frac{d^2 w^*}{dx^{*2}} = M^* - Q^* x^* - \frac{\Lambda}{2\alpha\beta} \langle x^* - x_1^* \rangle^2 + \Lambda \sin \theta_c \langle x^* - x_1^* \rangle^1. \quad (3.9)$$

Similarly, introducing the parameters into the Eqs. (3.6) and Eq. (3.7) gives expressions for normalized slope and deflection

$$\tan(\phi) = \beta \frac{dw^*}{dx^*} = M^* x^* - \frac{Q^*}{2} x^{*2} - \frac{\Lambda}{6\alpha\beta} \langle x^* - x_1^* \rangle^3 + \frac{\Lambda \sin \theta_c}{2} \langle x^* - x_1^* \rangle^2, \quad (3.10)$$

$$\beta w^* = \frac{M^*}{2} x^{*2} - \frac{Q^*}{6} x^{*3} - \frac{\Lambda}{24\alpha\beta} \langle x^* - x_1^* \rangle^4 + \frac{\Lambda \sin \theta_c}{6} \langle x^* - x_1^* \rangle^3. \quad (3.11)$$

Note that for the portion of the formulation presented thus far, once the geometry of the DCB and the material properties of the liquid and the solid are specified, Λ , β and θ_c are known governing parameters while α and x_1^* need to be determined along with the deflected curve.

3.1 Uncollapsed configuration

In the first case the two beams in the DCB are separated, a schematic is shown in Figure 3.2. Here the lines AB and OC represent the undeflected beams and the lines AB' , and OC' represent the deflected beams. Since the droplet is at the free end $x_2 = L$. As mentioned above each meniscus is part of a circular cylinder with radius R , represented by the dashed circles in Figure 3.2. l_1 , l_2 measure the distance from x_1 and x_2 to the center of each respective circle; these parameters are defined to have the same sign as R ; the negative direction is shown in Figure 3.2. Finally, as will be explained in detail later, without contact angle hysteresis, a droplet sandwiched between the deflected DCB can only be in equilibrium if one of its menisci is pinned at the free end, resulting in the angle θ_2 differing from the contact angle. This is also physical as the corner of the beam at the free end cannot be perfectly sharp. In total, there are five unknown parameters that have been introduced: R , l_1 , l_2 , θ_2 , and x_1 , which must be determined as part of the solution.

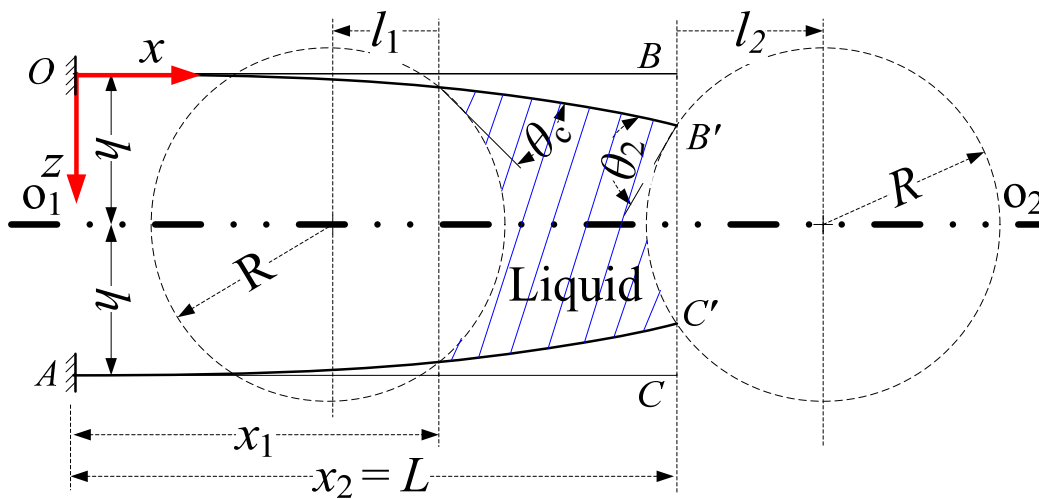


Figure 3.2: Schematic of the uncollapsed DCB problem to be solved

In Eq. (3.10) and (3.11), the reactions M_R^* and Q_R^* must be obtained to determine the beam deflection. A free body diagram (FBD) of the beam is shown in Figure 3.3. To obtain the reactions utilize Eq. (2.47) and note the following natural boundary conditions at the free end of the beam

$$-EI \frac{d^3 w(L)}{dx^3} = \gamma_{LA} D \sin \theta_2, \quad EI \frac{d^2 w(L)}{dx^2} = 0. \quad (3.12)$$

The first equation corresponds to the shear force due to the surface tension force at the free end. The second equation states that there is no applied moment at the free end. Either utilization of the boundary conditions Eq. (3.12) (with Eq. (3.4), and the derivative of this equation) or direct application of force balance in the z -direction and moment balance to Figure 3.3 gives

$$\begin{aligned} Q_R &= -\Delta P_{lap} D (x_2 - x_1) + \gamma_{LA} D (\sin \theta_c + \sin \theta_2) \\ M_R &= -\frac{\Delta P_{lap} D}{2} (x_2^2 - x_1^2) + \gamma_{LA} D (\sin \theta_c x_1 + \sin \theta_2 x_2). \end{aligned} \quad (3.13)$$

Using the parameters from Eq. (3.8), Eq. (3.13) can be normalized to give

$$\begin{aligned} M_R^* &= \frac{M_R L}{EI} = -\frac{\Lambda}{2\alpha\beta} (x_2^{*2} - x_1^{*2}) + \Lambda (\sin \theta_c x_1^* + \sin \theta_2 x_2^*) \\ Q_R^* &= \frac{Q_R L^2}{EI} = -\frac{\Lambda}{\alpha\beta} (x_2^* - x_1^*) + \Lambda (\sin \theta_c + \sin \theta_2). \end{aligned} \quad (3.14)$$

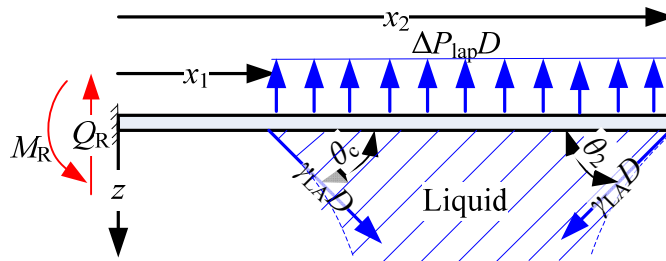


Figure 3.3: FBD of a linear beam in the uncollapsed case for obtaining base reactions from equilibrium.

Recall that five unknown parameters have been introduced in Figure 3.2: R , l_1 , l_2 , θ_2 , and x_1 . These parameters must be obtained as part of the solution and will require five additional constraint equations to be solved coupled with the beam's deflection Eq. (3.11). In addition, Figure 3.2 also raises several questions: why consider only the droplet pinned at the free end and why is it necessary to introduce the angle θ_2 at the free end? The answers to these questions will be addressed when the constraint equations are formulated.

Starting with the equations of the circles shown in Figure 3.2

$$R^2 = (x - x_1 - l_1)^2 + (z - h)^2 = (x - x_2 + l_2)^2 + (z - h)^2. \quad (3.15)$$

To ensure that the isobaric droplet condition is satisfied the two menisci have been constrained to have the same radius of curvature. The first two constraint equations arise by requiring the contact points between the menisci and the beams to lie on the meniscus circle. For the base meniscus the condition is

$$R^2 = l_1^2 + (w(x_1) - h)^2, \quad (3.16)$$

where $w(x_1)$ is the beam deflection at the base meniscus. The equivalent condition for the free end meniscus is

$$R^2 = l_2^2 + (w(x_2) - h)^2 \quad (3.17)$$

where $w(x_2)$ is the beam deflection at the free end.

A third constraint equation can be derived by requiring the angle between the deflected beam and the left meniscus curve to be the contact angle. The angle from the positive x -axis to the upper deflected beam at the left meniscus measured clockwise is $\phi_1 = \tan^{-1}(dw(x_1)/dx)$. Similarly the clockwise angle from the positive x -axis to the base meniscus is given by

$$\begin{aligned} \theta_{m1} &= \sin^{-1}\left(\frac{l_1}{R}\right) & \theta_c < 90^\circ \\ \theta_{m1} &= 180^\circ - \sin^{-1}\left(\frac{l_1}{R}\right) & \theta_c > 90^\circ \end{aligned} \quad (3.18)$$

In Eq. (3.18) two expressions are given in two regimes separated by contact angle $\theta_c=90^\circ$. Different expressions are needed because R can take positive and negative signs. Before the deflection, it is clear that $\theta_c < 90^\circ$ corresponds to $R < 0$, and $\theta_c > 90^\circ$ corresponds to $R > 0$. However, when θ_c is near 90° , deflection could cause the sign of R to change. Therefore strictly speaking, $\theta_c=90^\circ$ may not be the exact boundary to separate the $R < 0$ and $R > 0$ regimes. However, Eq. (3.18) only becomes invalid for cases in which the magnitude of the meniscus radius is very large. In these cases, from Eq. (3.3), the Laplace pressure becomes negligible making it difficult for the DCB to collapse; hence these limiting cases will not be of interest to the current discussion. In addition, a change in the sign of R corresponds to a change between the meniscus being concave and convex. During this change the meniscus becomes linear or $R = \infty$, which is difficult to handle numerically. For these reasons Eq. (3.18) suffices in describing the angle associated with the base meniscus in this discussion. To express the third constraint equation consider the angle diagrams shown in Figure 3.4. This figure shows the 4 combinations of signs of the beam deflection and meniscus radius. In each case enforcing the angle constraint results in the following relationship

$$\theta_{m1} = \theta_c + \phi_1. \quad (3.19)$$

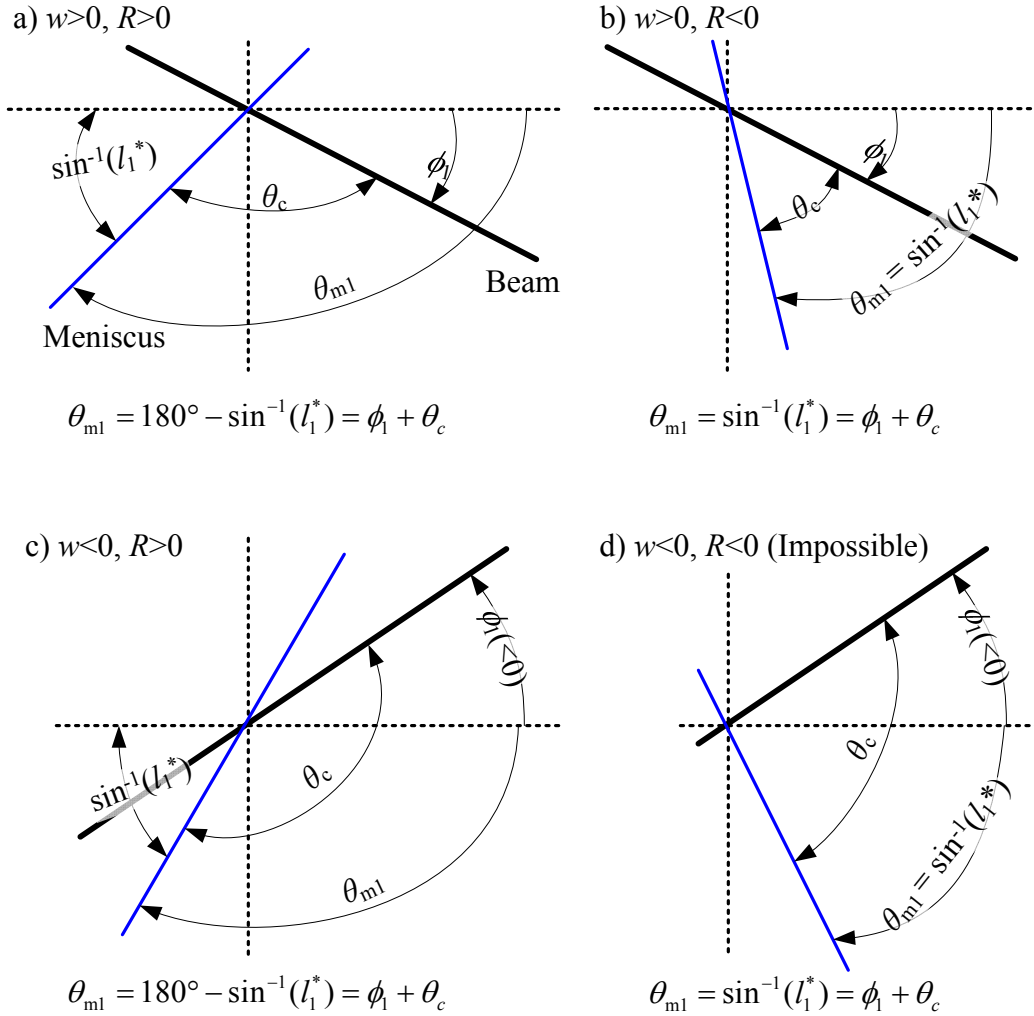


Figure 3.4: Angle diagrams at the base meniscus.

One may wonder whether a similar constraint should be placed for the right meniscus. Mathematically, such a constraint combined with the requirement for the two menisci radius to be equal would over constrain the problem and prohibit an equilibrium solution. This may seem troubling since physically Young's equation requires such a constraint. However, Consider the case of a drop of wetting liquid ($\theta_c < 90^\circ$) placed somewhere in the middle of the beam. In this case enforce a constraint similar to Eq. (3.19) for the right meniscus and consider what happens when the beam deflects. Because the contact angle is the same at

the two menisci, higher deflection at the right meniscus would lead to a smaller radius of curvature and thus a lower absolute pressure on the right side of the droplet—violating the isobaric condition. Because of the resulting pressure gradient the liquid droplet is no longer in equilibrium and will be driven towards the free end. This behaviour has been observed experimentally [7] and is a motivating factor for choosing to study the case of a drop pinned at the free end $x_2 = L$, as shown in Figure 3.2. Physically, the corners of the free ends cannot be perfectly sharp. This allows the angles θ_2 between the beams' longitudinal axes and the right meniscus to differ from the contact angle once the drop reaches the free end. As before let the angle from the positive x -axis to the deflected beam at the free end, measured clockwise, be $\phi_2 = \tan^{-1}(dw(x_2)/dx)$. The clockwise angle from the positive x -axis to the free end meniscus is given by

$$\begin{aligned} \theta_{m2} &= 180^\circ - \sin^{-1}\left(\frac{l_2}{R}\right) & \theta_C < 90^\circ \\ \theta_{m2} &= \sin^{-1}\left(\frac{l_2}{R}\right) & \theta_C > 90^\circ \end{aligned} \quad (3.20)$$

The angle diagrams in Figure 3.5 show the four combinations of signs of the beam slope and meniscus radius. In each case enforcing the angle constraint results in the fourth constraint equation

$$180^\circ - \theta_{m2} = \theta_2 - \phi_2. \quad (3.21)$$

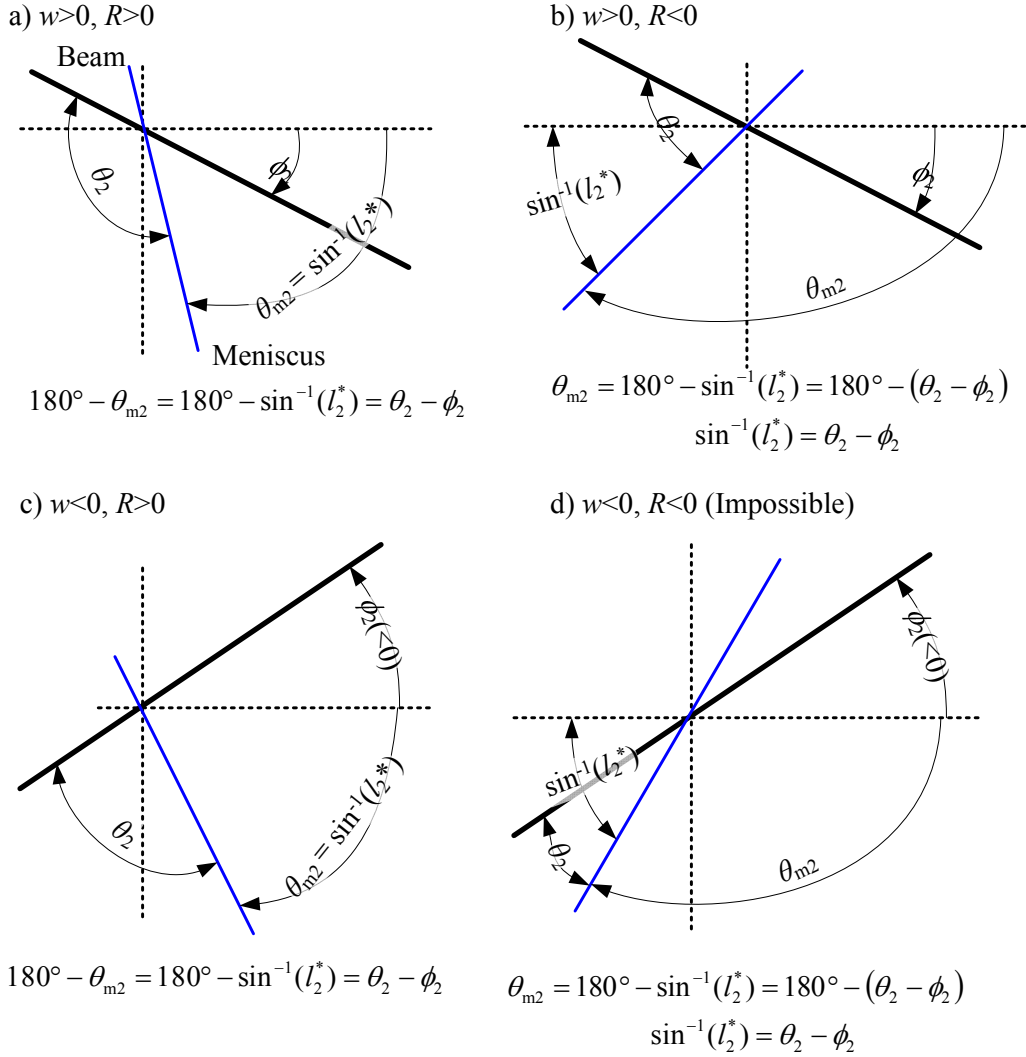


Figure 3.5: Angle diagrams at the free end meniscus.

The final constraint equation is the assumption that the incompressible liquid does not leak during beam deflection, i.e.,

$$V = D \left[2 \int_{x_1}^{x_2} (h - w(x)) dx + \sum_{i=1}^2 \left(R^2 \cos^{-1} \left(\frac{l_i}{R} \right) \text{sign}(R) - l_i \sqrt{R^2 - l_i^2} \right) \right], \quad (3.22)$$

where the term in the summation represent the area of each meniscus cap (negative). Eqs.(3.16), (3.17), (3.19), (3.21), and (3.22) are five equations for the five additional unknowns R , l_1 , l_2 , x_1 , and θ_2 , which allows the complete determination of the beam deflection.

As before it is desirable to normalize these equations and it is necessary to introduce additional normalized parameters as follows

$$V^* = \frac{V}{2LDh}, \quad l_i^* = \frac{l_i}{R}, \quad (3.23)$$

where V^* is the normalized drop volume, and l_i^* will be referred to as the meniscus geometry factors. Introducing these parameters along with existing parameters from Eq. (3.8) into Eqs. (3.16) and (3.17) gives

$$1 = l_1^{*2} + \alpha^{-2}(w^*(x_1^*) - 1)^2. \quad (3.24)$$

$$1 = l_2^{*2} + \alpha^{-2}(w^*(x_2^*) - 1)^2 \quad (3.25)$$

where $x_2^* = 1$. Combining Eq. (3.18) with Eq. (3.19) gives, after normalization

$$l_1^* = \sin(\theta_c + \phi(x_1^*)). \quad (3.26)$$

Note that normalized slopes are transformed to physical slopes through

$$\phi(x^*) = \tan^{-1}\left(\beta \frac{dw^*}{dx^*}\right). \quad (3.27)$$

Combining Eq. (3.20) with Eq. (3.21) gives after normalization

$$l_2^* = \sin(\theta_2 - \phi(x_2^*)). \quad (3.28)$$

Finally Eq. (3.22) is normalized to be

$$V^* = \int_{x_1^*}^{x_2^*} (1 - w^*(x^*)) dx^* + \frac{\alpha^2 \beta}{2} \text{sign}(\alpha) \sum_{i=1}^2 \left(\cos^{-1}(l_i^*) - l_i^* \sqrt{1 - l_i^{*2}} \right). \quad (3.29)$$

After normalization, the dimensionless parameters governing the deformation of the DCB are V^* , β , A , θ_c , which are respectively normalized liquid volume, normalized spacing, normalized surface tension, and contact angle. The objective of the analysis will be to study what combinations of the governing parameters result in DCB collapse defined as $w_2^* = w^*(1) = 1$. This represents contact between the free ends of the beams. The deflected curve and slope are

given by Eq. (3.11) and Eq. (3.10) respectively where M_R^* , and Q_R^* are given by Eq. (3.14). However in these equations α , x_1^* , θ_2 are not known a priori and must be guessed. The calculated beam deflection is then substituted into the five constraint equations, (3.24), (3.25), (3.26), (3.28), and (3.29) to obtain α , x_1^* , θ_2 as well as the two intermediate variables l_1^* , and l_2^* in an iterative fashion. The constraint equations are solved primarily using the Newton-Raphson method [42] with relaxation. Because all of the variables have physical bounds and the Newton-Raphson method often converges in an oscillatory fashion, a slight modification was necessary, as an unphysical value during the iteration (e.g. $l_1^* > 1$) can cause the solution to fail. The modifications are as follows. If a Newton-Raphson iteration gives an unphysical value for a variable, that variable would be recalculated using the Gauss-Seidel method [42]. Newton-Raphson typically converges faster, whereas the Gauss-Seidel method tends to be more stable. A brief overview of the algorithm and convergence criteria used is given in Appendix A.

At this point it is prudent to discuss what may seem to be an inconsistency in the preceding formulation. In the beam theory the effects of slope and angle were neglected both in the definition of curvature (see derivation of Eq. (2.28)) and in the determination of the internal moment from equilibrium (see derivation of Eq. (3.4)). However, these effects are included in the constraint equations. There are several reasons for this. First the effect of slope was of second order when neglected to obtain curvature relationship Eq. (2.28) but may not be negligible in other places. Secondly, in the discussion of Chapter 5 it will be

shown that the influence of angles in the constraint equations can be important and even dominant in certain situations; whereas, the effect of nonlinear geometry in the beam equations (formulation to be presented in Chapter 4 and results in Chapter 6) will be shown to be negligible for the range of governing parameters of interest. Therefore, by neglecting nonlinear geometrical effects in the beam equations we can obtain an analytic expression for the deflection (Eq. (3.11)), which in turn allows us to investigate the effect of the governing parameters in a clear way with the added benefit of less computational time. Although, for any given V^* , β , A , θ_c a solution can be obtained quickly with either Eq. (3.11) or evaluating the beam deflection numerically as is needed in the nonlinear beam theory, we wish to study many different combinations of the four governing parameters so the significantly decreased computational time offered by the linear model is an advantage.

3.2 Adhered configuration

In the second case the DCB beams are joined at the free end, as shown in Figure 3.6. The objective is to predict when this configuration is possible i.e. satisfying $x_2 < L$. In Figure 3.6, the lines AB and OB represent the deflected beams while the line BC represents the portion of the beams that are adhered. Because of the similarity of the adhered configuration to a crack, we shall from now on refer to the point of contact (B) as the crack tip with the area ABO representing the “crack”. Because the adhered beam length is not known a priori, x_2 is an unknown to be determined by the solution. Furthermore there may be a contact force between the beams. Due to assumption of DCB symmetry about line

O_1O_2 the contact force can only be in the transverse direction, so there is no need to consider midplane stretching of the DCB as was done by Ouakad *et al.* when studying adhesion of a cantilever to a substrate [8].

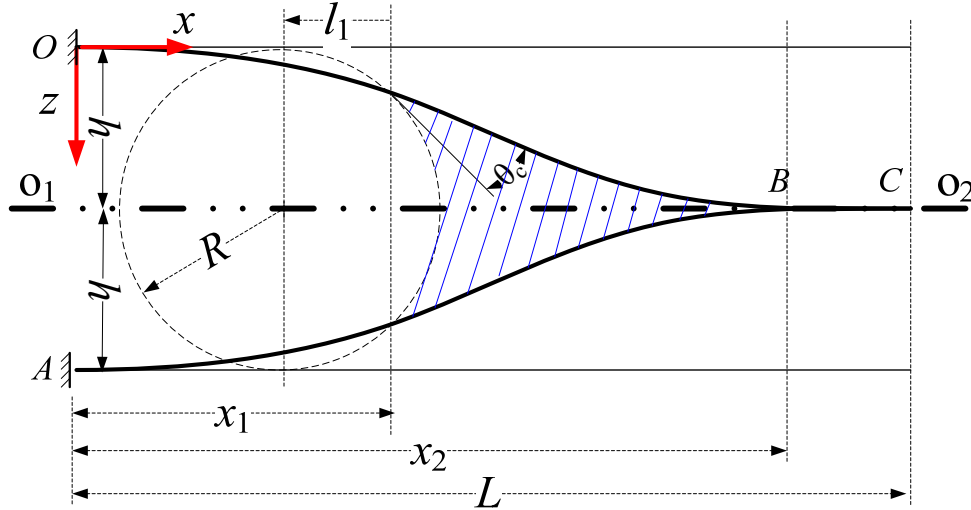


Figure 3.6: Schematic of the adhered DCB problem to be solved

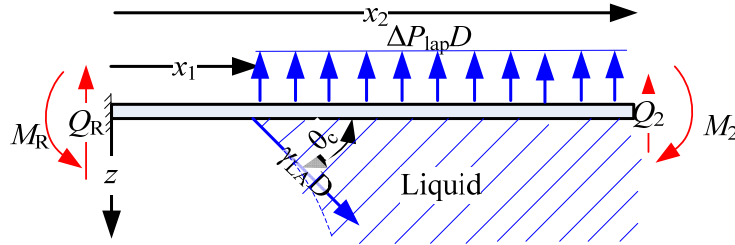


Figure 3.7: FBD of a linear beam in the adhered case for obtaining base reactions from equilibrium

To obtain the reactions M_R^* and Q_R^* in the beam deflection equation, a FBD of the beam is shown in Figure 3.7. First the contact force between the two beams can be used to obtain a natural boundary condition on the beam's shear force at x_2 as follows

$$EI \frac{d^3 w(x_2)}{dx^3} = Q_2. \quad (3.30)$$

The moment natural boundary condition is not as easy. Glassmaker *et al.* obtained a moment boundary condition using the “J-integral” when they studied self-

adhesion of nanotubes [33]. This approach can be repeated but with two modifications. Firstly, in the current work, there are two deforming beams that must be accounted for. Secondly, the current problem involves the interfacial energy, γ_{SL} , of two solids joined cohesively that when separated will be bridged by liquid (Eq. (2.23)), rather than the solid-solid work of adhesion. In the literature there have been issues with determining work of adhesion for microbeam structures because the rinse liquid often remains in the pores of the solid and contributes capillary adhesion [17],[21]. In such situation, γ_{SL} should be interpreted as an effective interfacial energy that accounts for partially wetted solid-solid interface prior to separation. The “J-integral” is defined as [38]

$$J = \int_{\Gamma} \left(W n_1 - \sigma_{ij} n_j \frac{du_i}{dx} \right) d\Gamma, \quad i, j = 1 \dots 2. \quad (3.31)$$

where W is the strain energy given by Eq. (2.54), u_i are displacement components (see Eq. (2.35)), and n_i are components of the normal to path Γ which is shown in Figure 3.8. For quasi-static crack propagation in a linear elastic solid, J has been shown to be equal to $2\gamma_{SL}$, the energy required to advance a unit area of crack.

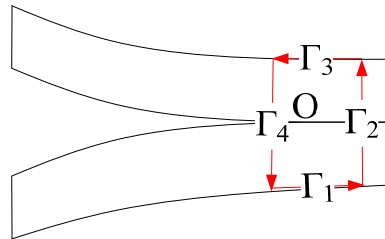


Figure 3.8: Integration path for “J-integral”

Table 5: Quantities required for the “J Integral”

	n_1	n_2	σ_{ij}	ε_{ij}	$\sigma_{ij} n_j$
Γ_1	0	-1	N/A	N/A	0
Γ_2	1	0	0	0	0
Γ_3	0	1	N/A	N/A	0
Γ_4	-1	0	Eq. (2.33)	Eq. (2.30)	0

Some of the quantities for the integral in Eq. (3.31) are given in Table 5 which reveals that the only nonzero contributions will come from the path Γ_4 . Note that on this path $du_1/dx = \varepsilon_{11}$, so if Eq. (3.31) is simplified and rewritten for opening a crack of length dx between the beams of width D the result is

$$2\gamma_{SL}Ddx = \int_{\Gamma_4} \left(-\frac{1}{2} \sigma_{ij} \varepsilon_{ij} n_1 - \sigma_{11} n_1 \varepsilon_{11} \right) Dd\Gamma dx = \int_{\Gamma_4} W D d\Gamma dx = 2 \left(\frac{M^2}{2EI} \right) dx \quad (3.32)$$

where M is the moment in the beam at the tip of the crack. Eq. (3.32) implies that the energy required to separate a length dx of the adhered beams and allow the liquid to fill the opening is equal to the strain energies of the two beams for length dx at the clamped end (see Eq. (2.55)). Rearranging Eq. (3.32) gives an equation for the moment at x_2 in the direction shown in Figure 3.7

$$M_2 = -\sqrt{2\gamma_{SL}DEI}. \quad (3.33)$$

Now the following boundary condition can be written at x_2

$$EI \frac{d^2 w(x_2)}{dx^2} = M_2. \quad (3.34)$$

Either utilizing the boundary conditions Eqs. (3.30) and (3.34) in Eq. (3.4) or direct application of force balance in the z -direction and moment balance to Figure 3.7 gives

$$\begin{aligned} Q_R &= -\Delta P_{lap} D(x_2 - x_1) + \gamma_{LA} D \sin \theta_c - Q_2 \\ M_R &= -\frac{\Delta P_{lap} D}{2} (x_2^2 - x_1^2) + \gamma_{LA} D \sin \theta_c x_1 + M_2 - Q_2 x_2 \end{aligned} \quad (3.35)$$

Again it is desirable to normalize these relationships using Eq. (3.8) however it is necessary to introduce the following additional dimensionless parameter

$$\Lambda_{SL} = \gamma_{SL} DL^2 / EI, \quad (3.36)$$

which has the same form as Λ except that it uses a different interfacial energy.

Now the normalized moment at x_2 becomes

$$M_2^* = M_2 L / EI = -\sqrt{2\Lambda_{SL}}, \quad (3.37)$$

and the normalized reactions are

$$Q_R^* = \frac{Q_R L^2}{EI} = -\frac{\Lambda}{\alpha\beta} (x_2^* - x_1^*) + \Lambda \sin\theta_c - Q_2^* \quad (3.38)$$

$$M_R^* = \frac{M_R L}{EI} = -\frac{\Lambda}{2\alpha\beta} (x_2^{*2} - x_1^{*2}) + \Lambda (\sin\theta_c x_1^*) - \sqrt{2\Lambda_{SL}} - Q_2^* x_2^*.$$

In the above equations, α , x_1^* , x_2^* , and Q_2^* are unknown and have to be obtained from the solution. To determine these unknowns, two additional essential boundary conditions can be written at $x = x_2$. They are

$$w(x_2) = h, \quad \frac{dw(x_2)}{dx} = 0. \quad (3.39)$$

The first condition requires deformation symmetry about the line O_1O_2 in Figure 3.6. The second condition is that the slope of the beam at x_2 is zero; this would typically be true unless the length AB is short in which case there may be a shear deformation [14]. With the normalization introduced earlier, Eq. (3.39) becomes

$$w^*(x_2^*) = 1, \quad \frac{dw^*(x_2^*)}{dx^*} = 0. \quad (3.40)$$

Additional constraint equations can be obtained from the uncollapsed case. Meniscus and beam deflection compatibility Eq. (3.24) and angle matching Eq. (3.26) for the base meniscus are still valid here. So is the constant incompressible liquid volume constraint Eq. (3.22). However, since there is only one meniscus in this case this equation is modified to

$$V^* = \int_{x_1^*}^{x_2^*} (1 - w^*(x^*)) dx^* + \frac{\alpha^2 \beta}{2} \text{sign}(\alpha) \left(\cos^{-1}(l_1^*) - l_1^* \sqrt{1 - l_1^{*2}} \right). \quad (3.41)$$

These five constraint equations will be solved simultaneously with the beam equation to obtain α , x_1^* , x_2^* , l_1^* , and Q_2^* , which are respectively the normalized meniscus radius, base meniscus location, length of the non-contact part of the

beam, base meniscus geometry factor, and the contact force between the two beams.

After normalization, the dimensionless parameters governing the deformation of the adhered DCB are V^* , β , Λ , θ_c , and Λ_{SL} . The objective of the analysis will be to study what combinations of the governing parameters result in the adhered configuration being possible, i.e. $x_2^* < 1$. Of particular interest is the influence of the interfacial energy Λ_{SL} on the solution. The solution procedure is similar to the uncollapsed case. The deflection and slope are given by Eq. (3.11) and Eq. (3.10) respectively where M_R^* , and Q_R^* are given by Eq. (3.38). In these equations α , x_1^* , x_2^* , Q_2^* are not known a priori and must be guessed. The resulting beam deflection is then substituted into the five constraint equations, (3.24), (3.26), (3.38), and (3.41) to iteratively solve for α , x_1^* , x_2^* , Q_2^* as well as the intermediate variable l_1^* . The numerical procedure is the same as for the uncollapsed case. However, in the adhered case it can be much more difficult for the solution to converge, the reason being that in the uncollapsed case one can always start with parameters that give a small beam deflection and gradually change them to the desired level. This is not possible in the adhered case because if the load is too low such a configuration does not exist in equilibrium, which makes the numerical solution very sensitive to the initial guess.

3.3 Energy Considerations

Although energy methods are not used to obtain the solutions looking at energy can often help with interpreting the results. For these reasons expressions for strain energy and surface energy will be developed for the problem under

consideration. To be consistent with the rest of the formulation symmetry will be used to only focus on the top half of the system. Strain energy is given by Eq. (2.55) which can be normalized using the parameters from Eq. (3.8) as follows

$$U_{SE}^* = \frac{U_{SE}L}{EI} = \int_0^{x_2^*} \frac{M^{*2}}{2} dx^* . \quad (3.42)$$

The moment is given by Eq. (3.9) and the result of the integration is

$$\begin{aligned} 2U_{SE}^* = & M_R^{*2} x_2^* - M_R^* Q_R^* x_2^{*2} + \frac{Q_R^{*2}}{3} x_2^{*3} \\ & + \left(\frac{\Lambda}{2\alpha\beta} \right)^2 \frac{(x_2^* - x_1^*)^5}{5} + \frac{\Lambda}{\alpha\beta} (Q_R^* - \Lambda \sin(\theta_c)) \frac{(x_2^* - x_1^*)^4}{4} \\ & + \left(\Lambda \sin(\theta_c) (\Lambda \sin(\theta_c) - 2Q_R^*) + \frac{\Lambda}{\alpha\beta} (Q_R^* x_1^* - M_R^*) \right) \frac{(x_2^* - x_1^*)^3}{3} \\ & + 2\Lambda \sin(\theta_c) (M_R^* - Q_R^* x_1^*) \frac{(x_2^* - x_1^*)^2}{2} . \end{aligned} \quad (3.43)$$

Using Eq. (2.2) the surface energy of the system is

$$U_S = \gamma_{LA} A_{LA} + \gamma_{SA} A_{SA} + \gamma_{SL} A_{SL} . \quad (3.44)$$

Since γ_{LA} , and γ_{SL} are both parameters used in the solution γ_{SA} will be eliminated using Young's Equation Eq. (2.3) to give

$$U_S = \gamma_{LA} (A_{LA} + A_{SA} \cos \theta_c) + \gamma_{SL} (A_{SL} + A_{SA}) . \quad (3.45)$$

The total area of the beam, defined as $A_T = A_{SS} + A_{SL} + A_{SA}$, when introduced into

Eq. (3.45) gives the following result

$$U_S = U_{So} + \gamma_{LA} (A_{LA} + A_{SA} \cos \theta_c) - \gamma_{SL} A_{SS} , \quad (3.46)$$

where $U_{So} = \gamma_{SL} A_T$ is a constant. The remaining areas can be calculated as follows

$$\begin{aligned}
A_{SA} &= x_1 D, \\
A_{LA} &= |R| D \left(\sin^{-1} \left(\frac{l_1}{R} \right) + \sin^{-1} \left(\frac{l_2}{R} \right) \right), \\
A_{SS} &= (1 - x_2) D
\end{aligned} \tag{3.47}$$

Substituting Eq. (3.47) into Eq. (3.46) gives

$$U_S = U_{So} + \gamma_{LA} D \left(|R| \left(\sin^{-1} \left(\frac{l_1}{R} \right) + \sin^{-1} \left(\frac{l_2}{R} \right) \right) + x_1 \cos \theta_c \right) - \gamma_{SL} D (L - x_2). \tag{3.48}$$

Normalizing this equation in the same way as strain energy gives

$$U_S^* = \frac{U_S L}{EI} = U_{So}^* + \Lambda \left(-\alpha \beta \left(\sin^{-1} (l_1^*) + \sin^{-1} (l_2^*) \right) + x_1^* \cos \theta_c \right) - \Lambda_{SL} (1 - x_2^*). \tag{3.49}$$

Note that the last term is the interfacial energy of separating the two adhered solid surfaces and filling the space with liquid and is also given by

$$U_{IE}^* = \Lambda_{SL} (1 - x_2^*) = \frac{M_2^{*2}}{2} (1 - x_2^*). \tag{3.50}$$

The above energy formulation is valid for both uncollapsed and adhered cases.

The former corresponds to $x_2^* = 1$ whereas the latter corresponds to $l_2^* = 0$.

The above energy expressions will be used, together with the example from section 2.1.4, to understand some of the results to be presented in Section 5.6.

Chapter 4 Nonlinear Formulation

In this chapter formulation will be provided for the deformation of the beam considering geometrical nonlinearity. Again two scenarios will be considered: the non-collapsed configuration and the adhered configuration. For each case, the set of governing equations, boundary conditions and constraint equations will be specified, as well as the numerical procedure used to solve these equations.

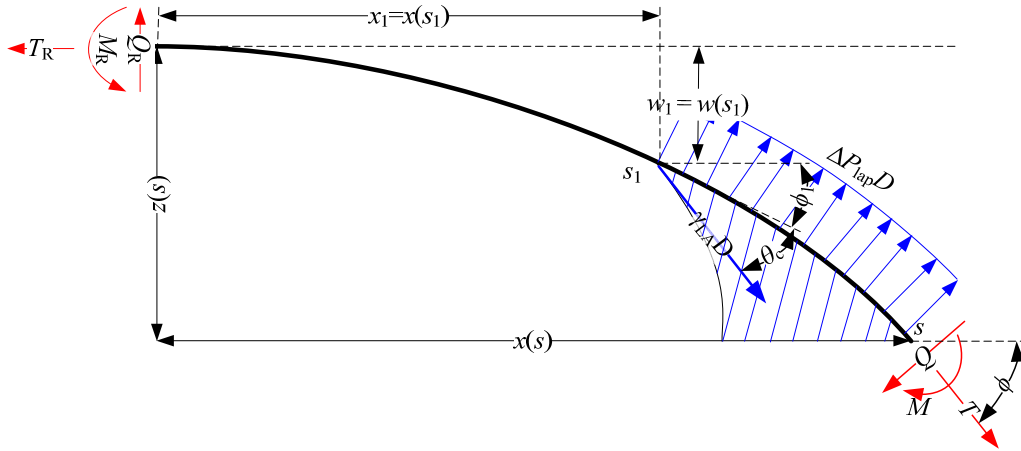


Figure 4.1: FBD of a section of a nonlinear beam for obtaining internal reaction $M(s)$

As in Chapter 3, equations applicable to both scenarios are first presented. In the nonlinear analysis, the moment curvature relationship is given by the first equation in Eq. (2.43) whereas positions of points on the parametric curve defining the NA are given by Eq. (2.29). Combining these relationships gives

$$\begin{aligned}
 M &= E^* I \frac{d\phi}{ds}, \\
 \frac{dx}{ds} &= \cos \phi, \\
 \frac{dw}{ds} &= \sin \phi,
 \end{aligned} \tag{4.1}$$

where $x(s)$ and $w(s)$ are respectively the horizontal and vertical positions of an arbitrary point s on the NA, and $\phi(s)$ is the angle between x -axis and tangent of the

deflected NA (see Figure 4.1). These three equations are accompanied by the boundary conditions related to the clamped end at $s = 0$

$$\phi(0) = 0, \quad x(0) = 0, \quad w(0) = 0. \quad (4.2)$$

In Eq. (4.1) the moment $M(s)$ can be determined by considering equilibrium of a section shown in Figure 4.1. Unlike in the linear case the effect of beam deflection on moment will now be considered i.e. $M(s) = M(s, x(s), w(s), \phi(s))$. Using Macaulay Functions (Eq. (2.50)) a single function for the internal moment can be written as follows

$$M(s) = M_R - Q_R x(s) + T_R w(s) + M_{ST}(s) + M_P(s) \quad (4.3)$$

where M_R , Q_R , and T_R are the reactions at the base shown in Figure 4.1. M_{ST} is the moment due to the surface tension force given by

$$M_{ST}(s) = \gamma_{LA} D (\sin(\phi(s_1) + \theta_c) \langle x(s) - x(s_1) \rangle - \cos(\phi(s_1) + \theta_c) \langle w(s) - w(s_1) \rangle). \quad (4.4)$$

Finally M_P , is the moment caused by the Laplace pressure. This moment is the most difficult to evaluate since the Laplace pressure acts normally to the deflected beam surface as shown in Figure 4.1. Nevertheless, there are two ways to evaluate it: directly integrating from s_1 to s , or using methods for determining hydrostatic forces on curved surfaces by considering equilibrium of the liquid [27]. Either approach gives the following result

$$M_P(s) = -\frac{\gamma_{LA} D}{2R} (\langle x(s) - x(s_1) \rangle^2 + \langle w(s) - w(s_1) \rangle^2). \quad (4.5)$$

The preceding equations can be normalized by introducing the following nondimensional parameters

$$s^* = \frac{s}{L}, \quad x^* = \frac{x}{L}, \quad w^* = \frac{w}{h}, \quad M^* = \frac{ML}{EI}, \quad T^* = \frac{T L^2}{EI}, \quad Q^* = \frac{QL^2}{EI}, \quad (4.6)$$

$$\Lambda = \frac{\gamma_{LA} L^2 D}{EI}, \quad \alpha = \frac{R}{h}, \quad \beta = \frac{h}{L}.$$

The above normalized parameters are the same as in Eq. (3.8) with the addition of normalized arc length s^* , and axial force T^* . Introducing these parameters into the first equation in Eq. (4.1) as well as Eqs. (4.3), (4.4) and (4.5) gives

$$\begin{aligned} \frac{d\phi}{ds^*} &= M_R^* - Q_R^* x^* + T_R^* \beta w^* + M_{ST}^*(s^*) + M_P^*(s^*) \\ M_{ST}^*(s^*) &= \Lambda \left(\sin(\phi(s_1^*) + \theta_c) \langle x^*(s^*) - x^*(s_1^*) \rangle - \beta \cos(\phi(s_1^*) + \theta_c) \langle w^*(s^*) - w^*(s_1^*) \rangle \right) \\ M_P^*(s^*) &= \frac{-\Lambda}{2\alpha\beta} \left(\langle x^*(s^*) - x^*(s_1^*) \rangle^2 + \beta^2 \langle w^*(s^*) - w^*(s_1^*) \rangle^2 \right). \end{aligned} \quad (4.7)$$

Similarly the last two equations in Eq. (4.1) after normalization become

$$\begin{aligned} \frac{dx^*}{ds^*} &= \cos \phi, \\ \frac{dw^*}{ds^*} &= \frac{\sin \phi}{\beta}. \end{aligned} \quad (4.8)$$

Finally the normalized base boundary conditions Eq. (4.2) are

$$\phi(0) = 0, \quad x^*(0) = 0, \quad w^*(0) = 0. \quad (4.9)$$

In the nonlinear case the deflection cannot be expressed analytically and must be obtained numerically. It is expected that in the case of small deflection, the above equations should reduce to those presented in the linear formulation (Chapter 3). This can be confirmed by making the following approximations: $w^* \approx 0$, $\phi \approx 0$, $\sin \phi \approx \phi$ and $\cos \phi \approx 1$ which lead to $dx^*/ds^* = 1$ and $x^* = s^*$. Furthermore, combining Eqs. (4.8) gives $\beta dw^*/dx^* = \tan \phi$. Introducing these simplifications reduces Eq. (4.7) to the linear version Eq. (3.9).

4.1 Uncollapsed configuration

The schematic is the same as in the linear case Figure 3.2, but when formulating the constraint equations and reactions nonlinear geometry must be

considered. To evaluate the reactions consider the beam FBD shown in Figure 4.2 and note that internal reactions take on the following values at the free end

$$\begin{aligned} Q(s_2 = L) &= \gamma_{LA} D \sin \theta_2 \\ T(s_2 = L) &= -\gamma_{LA} D \cos \theta_2 \\ M(s_2 = L) &= 0. \end{aligned} \quad (4.10)$$

In the nonlinear case directly applying the boundary conditions using Eqs. (2.43), (2.44), and (2.45) to obtain Q_R , T_R and M_R is undesirable for several reasons. First, the deflection will be obtained numerically at discrete points so its derivatives would need to be evaluated numerically. Since as high as a 3rd derivative is needed for the axial force, applying boundary conditions in such a way would require a dense mesh along the beam to accurately approximate the derivatives. The second reason is that Eq. (2.45) is also nonlinear which makes it more difficult to apply. For these reasons the reactions will be obtained through application of global equilibrium to the beam shown in Figure 4.2.

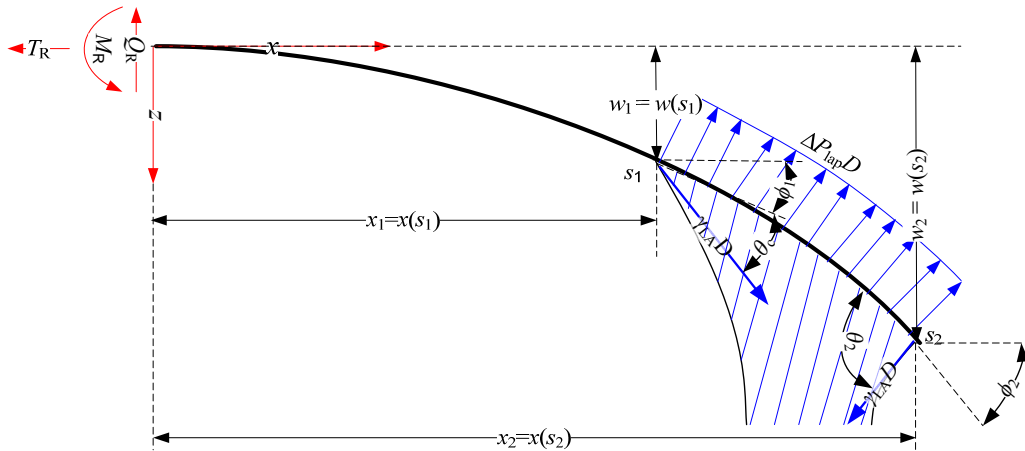


Figure 4.2: FBD of a nonlinear beam in the uncollapsed case for obtaining base reactions.

Equilibrium of forces in the x -direction gives, after using Eq. (3.3) to replace the Laplace pressure, the reaction tension at the base

$$T_R = \frac{\gamma_{LA}D}{R} [w(s_2) - w(s_1)] + \gamma_{LA}D(\cos(\theta_c + \phi(s_1)) - \cos(\theta_2 - \phi(s_2))). \quad (4.11)$$

In the linear case this tension does not appear in Eq. (3.2) because the effect of beam deflection on the calculation of moment is neglected. It however must be considered with the inclusion of geometrical nonlinearity. Similarly equilibrium in the z -direction and substitution of Eq. (3.3) gives the reaction shear force

$$Q_R = -\frac{\gamma_{LA}D}{R} [x(s_2) - x(s_1)] + \gamma_{LA}D(\sin(\theta_c + \phi(s_1)) + \sin(\theta_2 - \phi(s_2))). \quad (4.12)$$

Finally moment equilibrium about the base and substitution of Eq. (3.3) gives the reaction moment

$$\begin{aligned} M_R = & \gamma_{LA}D(\sin(\theta_c + \phi(s_1))x(s_1) - \cos(\theta_c + \phi(s_1))w(s_1)) \\ & + \gamma_{LA}D(\sin(\theta_2 - \phi(s_2))x(s_2) + \cos(\theta_2 - \phi(s_2))w(s_2)) \\ & - \frac{\gamma_{LA}D}{2R} ((w(s_2)^2 - w(s_1)^2) + (x(s_2)^2 - x(s_1)^2)). \end{aligned} \quad (4.13)$$

Again it is desirable to normalize these equations using the parameters in Eq.

(4.6). After normalization Eqs. (4.11), (4.12) and (4.13) become

$$T_R^* = \Lambda \left[\frac{1}{\alpha} [w^*(1) - w^*(s_1^*)] + (\cos(\theta_c + \phi(s_1^*)) - \cos(\theta_2 - \phi(1))) \right]. \quad (4.14)$$

$$Q_R^* = \Lambda \left[-\frac{1}{\alpha\beta} [x^*(1) - x^*(s_1^*)] + (\sin(\theta_c + \phi(s_1^*)) + \sin(\theta_2 - \phi(1))) \right] \quad (4.15)$$

$$\begin{aligned} M_R^* = & \Lambda (\sin(\theta_c + \phi(s_1^*))x^*(s_1^*) - \beta \cos(\theta_c + \phi(s_1^*))w^*(s_1^*)) \\ & + \Lambda (\sin(\theta_2 - \phi(1))x^*(1) + \beta \cos(\theta_2 - \phi(1))w^*(1)) \\ & - \frac{\Lambda}{2\alpha\beta} (\beta^2 (w^*(1)^2 - w^*(s_1^*)^2) + (x^*(1)^2 - x^*(s_1^*)^2)). \end{aligned} \quad (4.16)$$

Now compare Eqs. (4.15) and (4.16) with their counterparts in the linear case, Eq. (3.14). Clearly if the terms involving ϕ and w due to the nonlinear consideration are removed the equations coalesce. Furthermore, it can be shown that the even with nonlinear geometry the reaction T_R^* is zero; specifically, substituting Eq.

(3.26) into Eq. (3.24), and Eq. (3.28) into Eq. (3.25) gives, after rearrangement and application of trigonometric identities

$$\cos(\theta_c + \phi_1) = \alpha^{-1}(w^*(s_1^*) - 1) \quad (4.17)$$

$$\cos(\theta_2 - \phi_2) = \alpha^{-1}(w^*(s_2^*) - 1). \quad (4.18)$$

Subtracting Eq. (4.17) from Eq. (4.18) gives

$$w^*(s_2^*) - w^*(s_1^*) = \alpha(\cos(\theta_2 - \phi_2) - \cos(\theta_c + \phi_1)) \quad (4.19)$$

Finally substituting Eq. (4.19) into Eq. (4.14) results in $T_R^* = 0$.

The influence of the beam's deflection and slope on the meniscus geometry has been accurately captured in Figure 3.2, so the constraint equations pertaining to meniscus geometry Eqs. (3.24), (3.25), (3.26) and (3.28) also apply to the nonlinear case. However in the nonlinear case arc length s^* is the independent variable rather than x^* so values at each meniscus should be evaluated in terms of s^* . For example $w^*(x_1^*)$ would become $w^*(s_1^*)$ etc. Furthermore, it is desirable to change the integration in the last constraint equation Eq. (3.29) to

$$\int_{x_1^*}^{x_2^*} (1 - w^*(x^*)) dx^* = \int_{s_1^*}^{s_2^*} (1 - w^*(s^*)) \frac{dx^*}{ds^*} ds^* = \int_{s_1^*}^{s_2^*} (1 - w^*(s^*)) \cos(\phi(s^*)) ds^*, \quad (4.20)$$

where the condition of the drop being at the end of the beam is now $s_2^* = 1$.

Substituting this result into Eq. (3.29) gives

$$V^* = \int_{s_1^*}^{s_2^*=1} (1 - w^*(s^*)) \cos(\phi(s^*)) ds^* + \frac{\alpha^2 \beta}{2} \text{sign}(\alpha) \sum_{i=1}^2 \left[\cos^{-1}(l_i^*) - l_i^* \sqrt{1 - l_i^{*2}} \right]. \quad (4.21)$$

Eq. (4.21) completes the set of constraint equations.

As in the linear case it is necessary to guess $\alpha, s_1^*, l_2^*, l_1^*$, and θ_2 then iteratively solve for the final values using the modified Newton-Raphson method previously described. However in this case the beam equations cannot be

integrated explicitly so the procedure will use a shooting method as follows. Guess M_R^* , Q_R^* and calculate the beam deflection using the 4th order Runge-Kutta method (RK4) for Eqs. (4.7) and (4.8) with the initial condition Eq. (4.9). The obtained solution is checked against Eq. (4.15) and Eq. (4.16). If these two equations are not satisfied, then secant interpolation is used to calculate a new guess for M_R^* , Q_R^* . The procedure is repeated until Eq. (4.15) and Eq. (4.16) are satisfied to a desired accuracy. Having obtained $x_1^*, x_2^*, w_1^*, w_2^*, \phi_1, \phi_2$ and evaluating numerically the integration needed for Eq. (4.21) from the RK4 solution these values can be substituted into the constraint equations which are iteratively solved for $\alpha, s_1^*, l_2^*, l_1^*$, and θ_2 . For each iteration of Newton-Raphson it is necessary to repeat the iterative RK4 shooting method calculation. The algorithm followed is also shown schematically in Figure 4.3. Basic details of the RK4 scheme used for this problem such as convergence criteria and mesh sensitivity analysis are given in Appendix B.

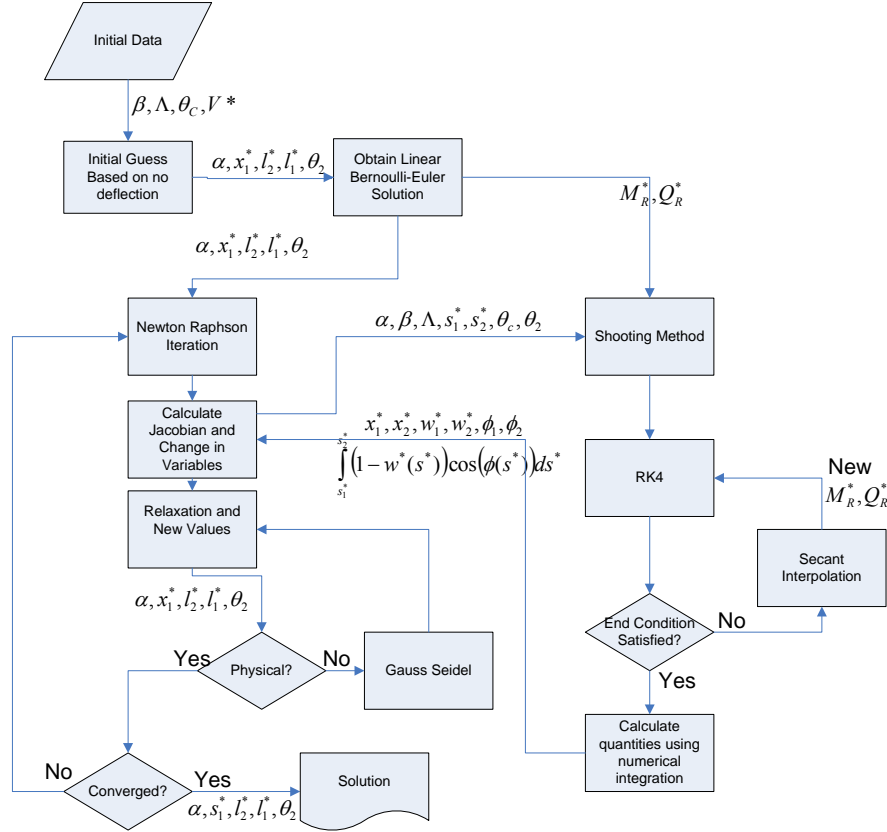


Figure 4.3: Solution algorithm

Some analytical results can be obtained from the governing equations that will be useful to our understanding of collapse. As can be seen in Appendix C at collapse ($w^*(s_2^*) = 1$) the following result can be obtained

$$\frac{1}{2} \left((M_2^*)^2 - (M_R^*)^2 \right) = -Q_R^* \sin(\phi(s_2^*)) + \Lambda \left[\sin(\phi(s_1^*) + \theta_c) \sin(\phi(s_2^*)) - \cos(\theta_c) \right] - \frac{\Lambda}{\alpha\beta} \left(x^*(s_2^*) - x^*(s_1^*) \right) \sin(\phi(s_2^*)), (\text{at collapse}) \quad (4.22)$$

where M_2^* is the reaction at $s^* = s_2^*$. Eq. (4.22) can be simplified by noting that there is no moment at the free end, i.e., $M_2^* = 0$. Furthermore Q_R^* , given by Eq. (4.15), can also be simplified when considering $w^*(s_2^*) = 1$. From Eq. (3.28) the last term in Eq. (4.15) is $l_2^* = l_2 / R = \sin(\theta_2 - \phi(1))$ but from Figure 3.2 it is apparent that at collapse $l_2 = R$ or

$$l_2^* = 1 \text{ (at collapse)}. \quad (4.23)$$

Substituting the simplified Eq. (4.15) into Eq. (4.22) gives

$$M_R^* = \sqrt{2\Lambda(\sin(\phi(s_2^*)) + \cos \theta_c)} \text{ (at collapse)}. \quad (4.24)$$

Eq. (4.24) is exact however, $\phi(s_2^*)$ is unknown without solving the problem. If we estimate $\phi(s_2^*)$ then we obtain an approximate analytical result for collapse M_R^* . Since most of the beams of interest are slender it is possible to obtain an good estimate for $\phi(s_2^*)$. As will be shown in Chapter 5 and Chapter 6 there is a strong correlation between M_R^* and collapse, as a result Eq. (4.24), which can be thought of as the moment available to the beam at collapse, is invaluable for understanding how the governing parameters affect collapse which is a primary objective of this study.

4.2 Adhered configuration

The schematic is the same as in the linear case (Figure 3.6) but when formulating the constraint equations and reactions nonlinear geometry must be considered.

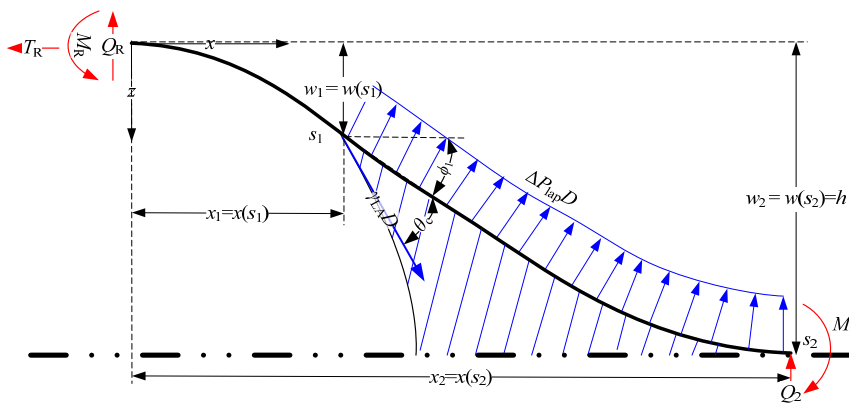


Figure 4.4: FBD of a nonlinear beam in the adhered case for obtaining base reactions.

To evaluate the reactions consider the beam FBD shown in Figure 4.4 and note the following natural boundary conditions at s_2^* from Eqs. (3.37) and (3.30)

$$\begin{aligned} M^*(s_2^*) &= M_2^* = -\sqrt{2\Lambda_{SL}} \\ Q^*(s_2^*) &= -Q_2^*. \end{aligned} \quad (4.25)$$

As in Section 4.1 it is undesirable to apply the boundary conditions directly, rather global equilibrium of the beam shown in Figure 4.4 will be used as follows. Because of symmetry there cannot be a reaction force in the x -direction at the contact point. Equilibrium of forces in the x -direction gives, after using Eq. (3.3) to replace the Laplace pressure

$$T_R = \frac{\gamma_{LA}D}{R} [w(s_2) - w(s_1)] + \gamma_{LA}D \cos(\theta_c + \phi(s_1)). \quad (4.26)$$

Equilibrium in the z -direction and substitution of Eq. (3.3) gives

$$Q_R = -\frac{\gamma_{LA}D}{R} [x(s_2) - x(s_1)] + \gamma_{LA}D \sin(\theta_c + \phi(s_1)) - Q_2 \quad (4.27)$$

Finally, moment equilibrium about the base and substitution of Eq. (3.3) gives

$$\begin{aligned} M_R &= \gamma_{LA}D (\sin(\theta_c + \phi(s_1))x(s_1) - \cos(\theta_c + \phi(s_1))w(s_1)) \\ &\quad - \frac{\gamma_{LA}D}{2R} ((w(s_2)^2 - w(s_1)^2) + (x(s_2)^2 - x(s_1)^2)) - Q_2x(s_2) + M_2 \end{aligned} \quad (4.28)$$

After normalization using Eq. (4.6), Eqs. (4.26), (4.27) and (4.28) become

$$T_R^* = \Lambda \left[\frac{1}{\alpha} [w^*(s_2^*) - w^*(s_1^*)] + \cos(\theta_c + \phi(s_1^*)) \right] \quad (4.29)$$

$$Q_R^* = \Lambda \left[-\frac{1}{\alpha\beta} [x^*(s_2^*) - x^*(s_1^*)] + \sin(\theta_c + \phi(s_1^*)) \right] - Q_2^* \quad (4.30)$$

$$\begin{aligned} M_R^* &= \Lambda (\sin(\theta_c + \phi(s_1^*))x^*(s_1^*) - \beta \cos(\theta_c + \phi(s_1^*))w^*(s_1^*)) \\ &\quad - \frac{\Lambda}{2\alpha\beta} (\beta^2 (w^*(s_2^*)^2 - w^*(s_1^*)^2) + (x^*(s_2^*)^2 - x^*(s_1^*)^2)) - Q_2^*x^*(s_2^*) - \sqrt{2\Lambda_{SL}} \end{aligned} \quad (4.31)$$

As in Section 4.1, these results will coalesce with the linear case if the nonlinear terms involving ϕ , and w are removed. Furthermore, it can be shown, by substituting Eq. (4.17) into (4.29), that since $w^*(s_2^*) = 1$ the reaction $T_R^* = 0$ in the adhered configuration as well.

In Section 4.1 we were able to obtain an expression that can be used to estimate M_R^* at collapse. Interestingly, for the adhered configuration, similar

analysis yields an explicit formula M_R^* that only depends on Λ_{SL} , Λ and θ_c .

Specifically, Eq. (4.22) is also valid for the adhered case. Substituting in

$$M_2^* = -\sqrt{2\Lambda_{SL}}, \quad w^*(s_2^*) = 1 \quad \text{and} \quad \phi(s_2^*) = 0 \quad \text{yields}^2$$

$$M_R^* = \sqrt{2(\Lambda_{SL} + \Lambda \cos \theta_c)} \quad (4.32)$$

The constraint equations pertaining to meniscus geometry, Eqs. (3.24) and (3.26), and the essential boundary conditions at s_2^* , Eq. (3.39) apply to the nonlinear case. However, as in Section 4.1 functions will be evaluated in terms of s^* . The final constraint equation is given by introducing Eq. (4.20) into Eq. (3.41), resulting in

$$V^* = \int_{s_1^*}^{s_2^*} (1 - w^*(s^*)) \cos(\phi(s^*)) ds^* + \frac{\alpha^2 \beta}{2} \text{sign}(\alpha) \left(\cos^{-1}(l_1^*) - l_1^* \sqrt{1 - l_1^{*2}} \right). \quad (4.33)$$

Eq. (4.33) completes the set of constraint equations for this case.

To numerically solve the problem, it is necessary to guess $\alpha, s_1^*, s_2^*, l_1^*$, and Q_2^* then iteratively solve for the final values using the modified Newton-Raphson method previously described. Eq. (4.32) can be used to prescribe M_R^* , whereas Q_R^* will be guessed for use with the RK4 shooting method to calculate the deflected curve. It should be noted that there are four conditions at s_2^* , the essential boundary conditions Eq. (3.39) and the equilibrium equations (4.30) and (4.31). It is necessary to choose two conditions to use as boundary conditions in the shooting method to obtain the deflection, and the other two equations are used as constraint equations to be solved with the Newton-Raphson method. Here the

² Note that using Young's Equation (2.3), Eq. (4.32) can be rewritten as $M_R^* = \sqrt{2\Lambda_S}$, where $\Lambda_S = \gamma_{SA} DL^2 / EI$.

equilibrium relationships Eqs. (4.30) and (4.31) can be easily applied in either case; however the essential boundary conditions (3.39) do not work well in the Newton-Raphson method. This is because $\phi(s_2^*)$ and $w^*(s_2^*)$ are numerical values returned by the RK4 shooting method, the derivatives of Eq. (3.39) with respect to each variable $\alpha, s_1^*, s_2^*, l_1^*$, and Q_2^* , needed for the Newton-Raphson Jacobian, have to be approximated numerically (where possible). On the other hand, the variables α, s_1^*, s_2^* , and Q_2^* appear in the equilibrium relationships Eqs. (4.30) and (4.31) so derivatives of these two equations may be evaluated analytically if these relationships are used within the Newton-Raphson scheme, which results in less zeroes in the Jacobian and better conditioned numerics. Therefore, the essential boundary conditions, Eq. (3.39) will be used in the shooting method and the equilibrium relationships Eqs. (4.30) and (4.31) will be used in the Newton Raphson iteration.

4.3 Energy Considerations

The energy results from Section 3.3 can be replicated for the nonlinear case as follows. The normalized strain energy Eq. (3.42) becomes

$$U_{SE}^* = \frac{U_{SE}L}{EI} = \int_0^{s_2^*} \frac{M^{*2}}{2} ds^* , \quad (4.34)$$

where the integration must be performed numerically using the RK4 results. The normalized surface energy Eq. (3.49) becomes

$$U_S^* = \frac{U_S L}{EI} = U_{S_0}^* + \Lambda \left(\alpha |\beta (\sin^{-1}(l_1^*) + \sin^{-1}(l_2^*)) + s_1^* \cos \theta_c \right) - \Lambda_{SL} (1 - s_2^*) \quad (4.35)$$

This energy formulation is valid for both uncollapsed and adhered configurations.

The former corresponds to $s_2^* = 1$ whereas the latter corresponds to $l_2^* = 0$.

Chapter 5 Results from Linear Beam

Formulation

In this chapter, results obtained from the linear beam formulation (Chapter 3) pertaining to collapse are presented. The normalization of the governing equations revealed four governing parameters for DCB collapse: β , θ_c , V^* , and Λ . The condition governing the collapse of the DCB ($w_2^*=1$) is of the general form $f(\beta, \theta_c, V^*, \Lambda) = 0$, where f is a function of the four governing parameters. A parametric study was completed by holding two of the governing parameters fixed and varying the other two to create contour plots of the variables of interest. For example, by fixing the normalized gap β and the contact angle θ_c , a contour plot can be generated for the normalized maximum deflection w_2^* as a function of V^* and Λ . This will further allow us to determine what combination of V^* and Λ will cause collapse of the DCB, for this choice of β and θ_c . The discussion below will seek to describe and explain the trends observed in these contour plots, the physical interpretation of the results and the impact of each governing parameter on the solution. Note that the primary objective here is to study the condition for collapse ($w_2^*=1$) so we will not consider x^* as an independent variable, unless otherwise specified.

5.1 Range of Governing Parameters

Before proceeding to discuss any numerical results we must first establish the range of each governing parameter relevant to the study. The DCB structure

will be more prone to collapse when the beam length is long compared to the gap. In fact, $\beta = 0.1$ is the highest value for which collapse is usually a problem [4], so as previously mentioned $\beta \leq 0.1$ will be the focus. Furthermore, when the menisci of the beam are concave both surface tension forces and the Laplace pressure work to collapse the beam; since this case will be of the greatest relevance to collapse the contact angle will be limited to $\theta_c < 90^\circ$. The range of normalized drop volume V^* is more complicated. First the minimum value of V^* will be such that when there is no deflection the two menisci are touching. This constraint can be expressed as $\min(V^*) = \beta \times MVF$, where the minimum V^* factor (MVF) is a function of contact angle:

$$MVF = \frac{2}{\cos \theta_c} (1 - \sin \theta_c) - \frac{1}{\cos^2 \theta_c} (\cos^{-1}(\sin \theta_c) - \sin \theta_c \cos \theta_c). \quad (5.1)$$

A plot of MVF is shown in Figure 5.1. Here smaller contact angles require larger volume of liquid to prevent the two menisci from intersecting. Practically due to liquid bridge instability [39] the drop would need to be larger, so $V^* > \min(V^*)$ is a necessary but not sufficient condition for the stability of the liquid drop. Furthermore, the 2-D meniscus assumption breaks down for very small drops [43]. The maximum value of V^* is such that the base meniscus makes contact with the base at collapse. From our numerical calculations to be presented later, this typically occurs between $V^* = 0.5$ and $V^* = 0.6$ depending on the values of β and θ_c . The final governing parameter Λ , which is a ratio of surface tension forces to the beam's restoring forces, does not have similar bounds only $\Lambda > 0$; using the data from Kotera *et al.* $\Lambda \approx 0.02$ however scaling down the resist size results in

significantly larger Λ values . Therefore Λ in our numerical calculations will be adjusted to ensure that the plots display a meaningful range of deflection. The range of governing parameters pertinent to this study are summarized in Table 6.

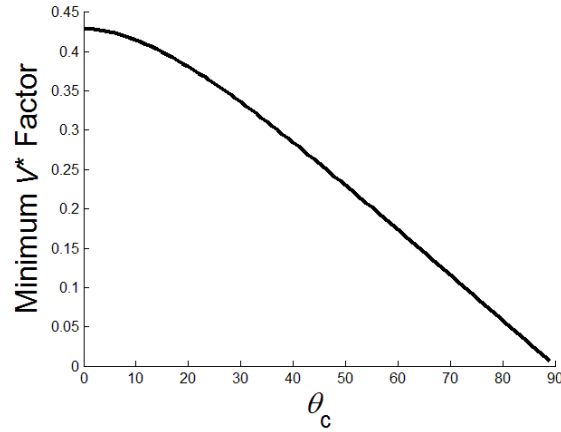


Figure 5.1: MVF minimum V^* factor for a range of contact angles

Table 6: Range for governing parameters

Governing Parameter	β	θ_c	V^*	Λ
Maximum	0.1	$<90^\circ$	0.5-0.55	(>0) adjust accordingly
Minimum	>0	0	$\beta \times MVF$	

5.2 Preliminary Considerations on the Role of the 4 Governing Parameters

To begin to understand how each governing parameter influences the solution, the system of governing equations for DCB deformation are revisited. Since our interest is in collapse the discussion will be limited to negative α which corresponds to concave menisci. When α is negative both the Laplace pressure and surface tension forces work to collapse the DCB. Due to numerical limitations described in Chapter 3 to obtain $\alpha < 0$ the contact angle range will be

limited to $\theta_c < 90^\circ$. The normalized equations from Chapter 3 pertinent to the discussion are listed below.

Dimensionless ODE relating moment and curvature:

$$\beta \frac{d^2 w^*}{dx^{*2}} = M^* = \Lambda \left(-\frac{\langle x^* - x_1^* \rangle^2}{2\alpha\beta} + \sin(\theta_c) \langle x^* - x_1^* \rangle \right) - Q_R^* x^* + M_R^*. \quad (5.2)$$

Dimensionless shear force and moment at the clamped end:

$$Q_R^* = \Lambda \left(-\frac{x_2^* - x_1^*}{\alpha\beta} + \sin(\theta_c) + \sin(\theta_2) \right),$$

$$M_R^* = M_P^* + M_{ST}^* = \Lambda \left(-\frac{x_2^{*2} - x_1^{*2}}{2\alpha\beta} + \sin(\theta_c)x_1^* + \sin(\theta_2)x_2^* \right), \quad (5.3)$$

$$M_P^* = -\Lambda \left(\frac{x_2^{*2} - x_1^{*2}}{2\alpha\beta} \right) \text{ (moment due to Laplace pressure),}$$

$$M_{ST}^* = \Lambda (\sin(\theta_c)x_1^* + \sin(\theta_2)x_2^*) \text{ (moment due to surface tension force).}$$

Deflection and slope at an arbitrary position x^* along the beam:

$$\beta w^*(x^*) = \Lambda \left(-\frac{\langle x^* - x_1^* \rangle^4}{24\alpha\beta} + \sin(\theta_c) \frac{\langle x^* - x_1^* \rangle^3}{6} \right) - \frac{Q_R^*}{6} x^{*3} + \frac{M_R^*}{2} x^{*2}, \quad (5.4)$$

$$\tan(\phi) = \beta \frac{dw^*}{dx^*} = \Lambda \left(-\frac{\langle x^* - x_1^* \rangle^3}{6\alpha\beta} + \sin(\theta_c) \frac{\langle x^* - x_1^* \rangle^2}{2} \right) - \frac{Q_R^*}{2} x^{*2} + M_R^* x^*.$$

Constant liquid volume constraint:

$$V^* = \int_{x_1^*}^{x_2^*} (1 - w^*(x^*)) dx^* - \frac{\alpha^2 \beta}{2} \sum_{i=1}^2 \left(\cos^{-1}(l_i^*) - l_i^* \sqrt{1 - l_i^{*2}} \right). \quad (5.5)$$

Deflection conditions at the menisci:

$$1 = l_1^{*2} + \alpha^{-2} (w^*(x_1^*) - 1)^2, \quad (5.6)$$

$$1 = l_2^{*2} + \alpha^{-2} (w^*(x_2^*) - 1)^2. \quad (5.7)$$

Conditions for the slopes at the locations of the menisci:

$$l_1^* = \sin(\theta_c + \phi(x_1^*)), \quad (5.8)$$

$$l_2^* = \sin(\theta_2 - \phi(x_2^*)).$$

In the following we conduct a preliminary discussion on how the governing parameters β , θ_c , V^* , and Λ might affect the maximum deflection based on the above system of equations. As demonstrated earlier in the formulation, the

loads on the beam (See Eq. (5.3)) depend on α , x_1^* , and θ_2 . However, these variables depend on the deflection of the beam and the subsequent displacement of the liquid, which introduces a nonlinear coupling. Specifically, the deflections of the beam can change the curvature or even the location of the menisci, which in turn can change the loading on the beam. Such effects will be subsequently referred to as the “nonlinear deflection coupling effects”. With every governing equation depending nonlinearly on the deflection of the beam it is easy to become lost in the minutiae when trying to determine how the governing parameters will influence the beam’s deflection. To elucidate this nonlinear coupling, the discussion will be carried out in two steps. First in section 5.2.1 the role of each governing parameter will be investigated using the governing equations; however, nonlinear coupling will be temporarily neglected, i.e., terms in the governing equations that involve $w^*(x_1^*)$, ϕ_2 etc. will be ignored. Afterwards in section 5.2.2 a brief discussion will be provided demonstrating how these terms play an important role on the behaviour of the beam’s deflection. With this foundation we will then proceed to discuss the numerical results from several parametric studies.

5.2.1 Discussion Neglecting Nonlinear Deflection Coupling Effects

Based upon the equations in section 5.2, a flow chart, shown in Figure 5.2, can be constructed illustrating how changing each governing parameter will influence the maximum deflection, if the nonlinear effects of deflection (w^* , ϕ) on the constraint equations (Eq. (5.5) - Eq. (5.8)) are neglected. Discussions will be given in the subsections below in accordance to Figure 5.2. In Figure 5.2, the

leftmost column shows the four governing parameters. The second column shows the five normalized variables that must be obtained from the constraint equations as part of the solution, from top to bottom, the magnitude of the meniscus radius, the base meniscus geometry factor, the free end meniscus geometry factor, angle between free end meniscus and positive x -axis, and the position of the base meniscus. M_{ST}^* and M_p^* in the third column are respectively the total moments on the beam in Eq. (5.3) due to surface tension forces and Laplace pressure. The rightmost column shows the output, the resulting beam deflection; if the maximum deflection w_2^* exceeds one, collapse occurs. Each solid blue arrow in Figure 5.2 indicates an increase in the variable it point towards and each dashed red arrow indicates a decrease. Since variables can often have competing inputs, all output arrows are for an increase in that variable. For example, consider x_1^* : increasing α and β both decrease x_1^* while increasing l_1^* and l_2^* both increase x_1^* . An increase in x_1^* both decreases M_p^* and increases M_{ST}^* .

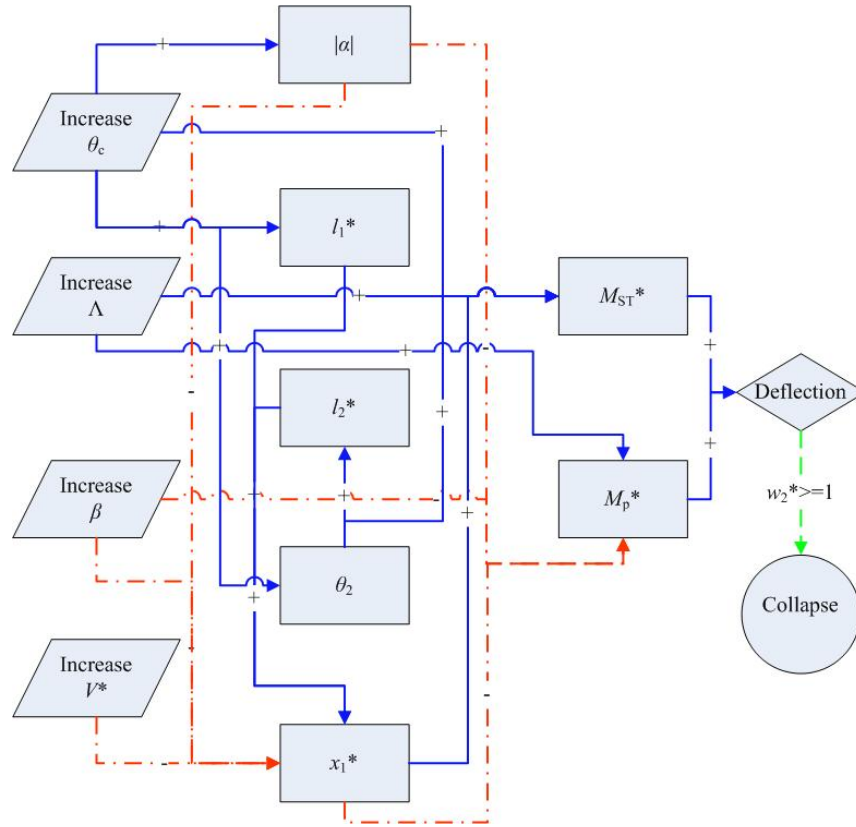


Figure 5.2: Dependency of deflection on the Governing Parameters neglecting nonlinear effects of deflection (w , ϕ) in constraint equations.

5.2.1.1 β

β is defined as $\beta = h/L$, the ratio of the gap at the clamped ends to the beam length. In Eq. (5.3), β appears in the denominator of M_p^* , which represents the total moment due to the Laplace Pressure. Therefore, increasing β decreases M_p^* and causes the beam deflection to decrease. Furthermore, the second term on the RHS of Eq. (5.5), which represents the volume of liquid displaced by the meniscus geometry, is directly proportional to β . This implies that increasing β will increase the amount of liquid displaced by the menisci, hence to compensate for this effect and satisfy the constant volume constraint the base meniscus must move closer to the base, i.e., x_1^* will be decreased. Both of these trends are

reflected in Figure 5.2. Because in terms of collapse, the range of $\beta \leq 0.1$ is of greatest practical interest [4], the influence of β on M_p^* tends to be more significant than on x_1^* . This is because $M_p^* \propto \beta^{-1}$ while the volume displaced by the menisci $\propto \beta$. Clearly the former is more sensitive to variations in β for $\beta \ll 1$.

5.2.1.2 θ_c

The contact angle, θ_c , is the angle between the liquid meniscus and the beam. It affects the deflection of the beam in several ways. Following Figure 5.2, θ_c affects the deflection by directly influencing M_{ST}^* and indirectly influencing M_p^* through α , l_1^* , and l_2^* . As θ_c is increased from 0° to 90° the surface tension force changes from axial to transverse resulting in larger M_{ST}^* . To see the influence of contact angle on the curvature of the meniscus, α substitution of Eq. (5.8) in to Eq. (5.6) yields

$$\alpha = \frac{w_1^* - 1}{\cos(\theta_c + \phi_1)}. \quad (5.9)$$

From this relation larger contact angles are expected to result in larger meniscus radii and thus smaller Laplace pressure and smaller M_p^* . In fact as θ_c approaches 90° , α approaches negative infinity and the pressure load disappears ($M_p^* = 0$).

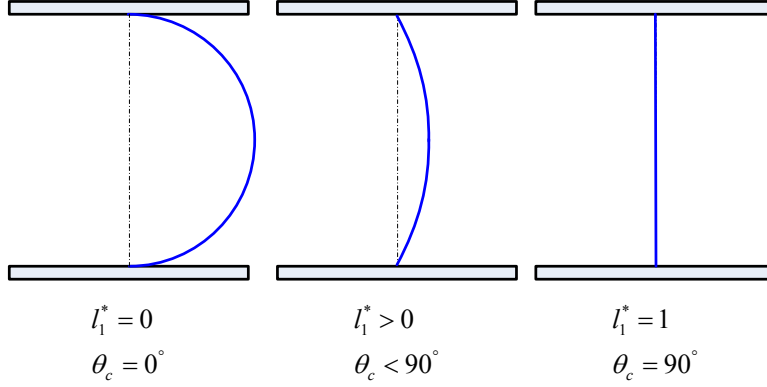


Figure 5.3: Effect of θ_c on meniscus geometry factor and the appearance of the meniscus

From Figure 5.2 the contact angle also influences l_1^* directly and l_2^* indirectly through θ_2 . These parameters (l_i^*) are meniscus geometry factors as shown in Figure 3.2. In particular, when $l_i^* = 0$ the corresponding meniscus is a semicircle, for $l_i^* > 0$ the meniscus is a circular cap and as l_i^* increases the cap height decreases. The case of $l_i^* = 1$ corresponds to zero cap height which can only be accomplished by a meniscus with an infinite radius of curvature; i.e., a straight line. Clearly from Eq. (5.8), θ_c affects l_1^* , which consequently affects the amount of liquid displaced by the meniscus, as shown in the second term on the RHS of Eq. (5.5). It can be seen from Figure 5.3 that smaller θ_c gives smaller l_1^* and larger cap height, which should displace more liquid. Since the volume of liquid is required to be constant, smaller θ_c results in the left meniscus being closer to the base. To see this relationship more directly consider the constant volume constraint Eq. (5.5), and define the term within the summation as the meniscus displacement factor (MDF)

$$MDF = \cos^{-1}(l_i^*) - l_i^* \sqrt{1 - l_i^{*2}} . \quad (5.10)$$

The value of MDF is plotted in Figure 5.4, which is a monotonically decreasing function of l_i^* . Hence, higher l_i^* which can result from larger contact angles displace less liquid, and result in larger x_1^* . Following Figure 5.2 this increase in x_1^* decreases M_p^* and increases M_{ST}^* , which in turn influences the beam's deflection.

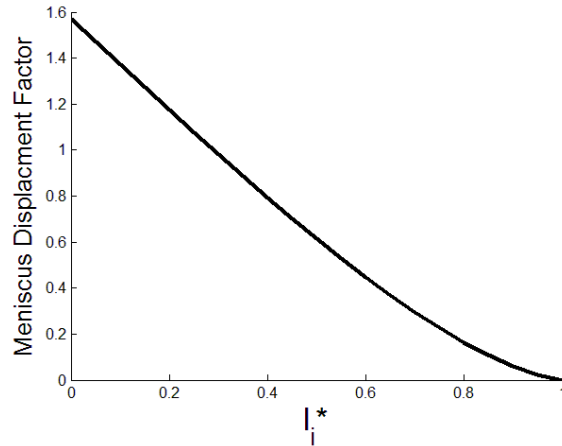


Figure 5.4: Meniscus displacement factor (MDF) for complete range of l^*

5.2.1.3 V^*

$V^* = V/2LDh$ is the fraction of the volume between the two beams occupied by the liquid. A first glance at Eq. (5.5) seems to indicate that for higher V^* , x_1^* will need to be smaller and as a result the Laplace pressure acts over a larger area; it would then be expected that the DCB would have a higher deflection for higher V^* . On the other hand, since the Laplace pressure acts over a smaller area for smaller V^* it would be expected that the surface tension force would play a more important role for the smaller drops. This behaviour is represented in Figure 5.2, through the relationship between V^* and the moments (M_{ST}^* and M_p^*) via x_1^* .

5.2.1.4 Λ

Λ defined as $\Lambda = \gamma_{LA} DL^2 / EI$, is a ratio of surface tension force to elastic restoring force. Using Eq. (5.3), it is clear from Eq. (5.2) that the internal moment is directly proportional to Λ ; as a result so is the beam deflection shown in Eq. (5.4). Therefore, increasing Λ is expected to increase the deflection, as shown in Figure 5.2. Furthermore, Figure 5.2 shows that unlike the other governing parameters, Λ 's influence bypasses the intermediate variables (α , x_1^* , l_1^* , l_2^* and θ_2) and directly applies to the moments. For this reason increasing Λ creates a predictable increase in the maximum deflection.

5.2.2 Importance of Nonlinear Deflection Coupling

In Section 5.2.1 we began to discuss how each of the governing parameters would affect the solution of the problem. However, nonlinear deflection coupling effects were ignored, if they are added the new flow chart is shown in Figure 5.5. Here the results of the deflection discussed in 5.2.1 feedback into intermediate variables α , l_i^* , x_1^* , θ_2 , which describe the geometry of the deformed liquid drop. Among the four governing parameters, Λ and to a lesser degree β , skip past these intermediate variables and directly influence the moments. For this reason, the influences of the contact angle (θ_c) and normalized drop volume (V^*) are more intimately coupled with the beam deflection, and have the greatest potential to cause behaviour that may not conform to our expectations based on section 5.2.1. Coupling to the degree shown in Figure 5.5 is absent from previous works. Specifically, the influence of deflection w^* on Laplace pressure was taken into account whereas the effect of slope ϕ was often neglected [3], [8], [9] or

approximated in terms of w^* [4], [6], [11]. In addition the analysis of Ouakad *et al.* [8] held the meniscus position fixed, which essentially removed all of the output arrows from x_1^* shown in Figure 5.5; furthermore, existing models which allow the meniscus position to move [3], [9] neglected the liquid displaced by the meniscus curvature (second term of RHS of Eq. (5.5)) in which case ϕ does not influence the meniscus position x_1^* .

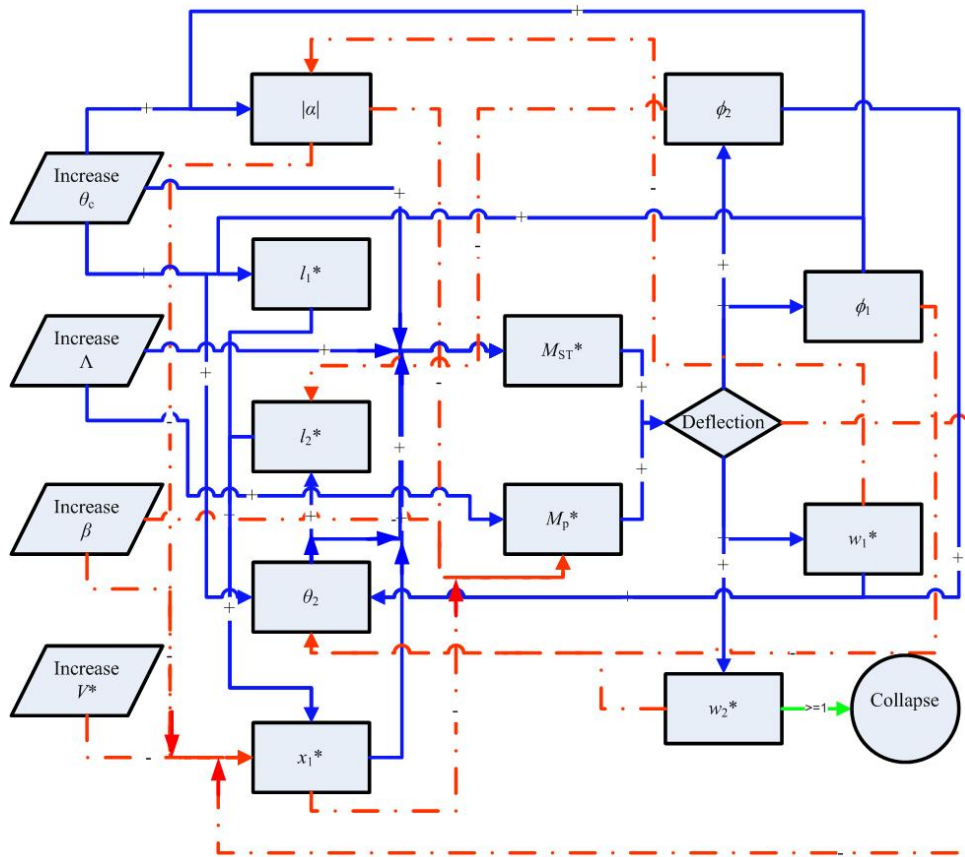


Figure 5.5: Solution dependence on governing parameters, including nonlinear coupling

Let us discuss some of the effects shown in Figure 5.5 to get a sense of the importance of the nonlinear deflection coupling. Recall that when this coupling is neglected in section 5.2.1, it was reasoned that for larger V^* the Laplace pressure acts over a larger area so larger deflections were expected for larger V^* , especially

for low contact angles where the surface tension force acts nearly axially. However, in Figure 5.5 it is shown that an increase in the deflection w_1^* at the base meniscus causes $|\alpha|$ to decrease. To explain, consider Eq. (5.9). Here the normalized meniscus radius α , which directly influences the Laplace pressure, depends on w_1^* . If for example the deflection causes w_1^* to increase from 0 to 0.5 then the magnitude of the Laplace pressure would double. For small V^* , the base meniscus is located closer to the free end so given the same free end deflection (w_2^*), w_1^* will be larger for smaller V^* . As a result smaller drops may have a larger Laplace pressure magnitude. Furthermore, for drop sizes close to the maximum indicated in Table 6, the base meniscus will be located very close to the clamped end where both slope and deflection are zero. In this case the nonlinear deflection coupling effects are negligible and the Laplace pressure hardly increases with the beam's deflection. From these discussions, it is not apparent for what drop size collapse will occur more easily.

Next it is shown in Figure 5.5 that deflection causes a decrease in x_1^* . This is clear from the constant volume constraint Eq. (5.5), which requires the base meniscus to move towards the base as liquid is displaced by the deflected beam. As a result the total area on which the Laplace pressure acts will increase upon deflection.

Finally it is shown in Figure 5.5 that increases in ϕ_1 , the angle at the base meniscus, cause an increase in l_1^* and in $|\alpha|$. The increase in $|\alpha|$ is evident from Eq. (5.9); for slender beams, where slopes are small, the influence of w_1^* in this

equation would in general overshadow that of ϕ_1 . However, if the contact angle θ_c is close to 90° , then ϕ_1 will play an important role since the denominator of Eq. (5.9) is close to zero and the magnitude of α can increase drastically from a small increase in ϕ_1 . This effect is amplified by the fact that the cosine function, which appears in the denominator of Eq. (5.9), has its largest rate of change when its argument is close to 90° . The increase in l_1^* caused by an increase in ϕ_1 can be seen from Eq. (5.8). As a result the MDF (Figure 5.4) decreases and by Eq. (5.5) the meniscus moves away from the base because less liquid is displaced by meniscus curvature. This is shown in Figure 5.5 by an increase in x_1^* . This effect is augmented when contact angle θ_c is close to 0° due to the rapid change of the sine function with its argument near zero (see Eq. (5.8)).

Clearly, the above preliminary discussion on only a few of the nonlinear deflection coupling effects shows that these effects are crucial to the collapse of the DCB. Furthermore, these effects can vary considerably based upon drop size and contact angle. In fact there are several regimes of contact angle where the solution will take on significantly different behaviour, some of which cannot be explained using the simple analysis presented in 5.2.1. For this reason the ensuing discussion will be separated into three regimes: low, moderate and high contact angles. Note that these regimes cannot be defined precisely in terms of exact contact angle values, but rather they are based on the behaviour of the solution to the system of governing equations. The key characteristics of the high contact angle regime are significant influence of ϕ_1 on the Laplace pressure, and maximum importance of surface tension forces. The key characteristics of the low

contact angle regime are increased influence of ϕ_1 and ϕ_2 on the base meniscus position, and minimal importance of surface tension forces. The moderate contact angle regime encompasses everything between these two extremes. The range of θ_c for each regime also depends on β (low β will extend the moderate range).

Although Figure 5.5 summarizes the influences of the governing parameters on DCB collapse and the nonlinear deflection coupling effects, it gives no indication of the relative importance of each effect. In addition, these effects form a feedback loop and therefore interact with each other, further convoluting the situation. Whether these effects contribute significantly to collapse must also be addressed. In order to address these issues we will now proceed to a more detailed analysis for each of the above mentioned contact angle regimes, using numerical solutions to the governing equations. Although there are also different behavioural regimes for V^* , these will be addressed within each θ_c section.

5.3 Moderate Contact Angle

The moderate contact angle regime includes contact angles for most wetting liquids (representative values shown in Table 4). Within this regime both surface tension and Laplace pressure forces contribute to the deflection of the DCB. The goal is to study how the governing parameters influence collapse so our interest will be focused on analysing contours plots of the free end deflection. From the discussion of Figure 5.5 V^* was deemed to have a significant effect on the nonlinear deflection coupling, it is desirable to have V^* as one of the parameters to be varied to create the contour plots. Increasing Λ causes a controllable increase in deflection; hence Λ will be used as the other variable to generate each

contour plot. Throughout this section θ_c will be fixed at 45° , which represents a moderate contact angle. From Table 4 this angle is close to that of benzene on Teflon. However the characteristics to be discussed should be applicable to other moderate contact angles.

Now the only governing parameter that needs to be specified is β . Recall that the relationship between the angle ϕ the deflected beam makes with the x -axis and the dimensionless slope is given by $\tan \phi = \beta dw^* / dx^*$, i.e., the range of possible deflection angles is scaled with β . Thus if β is small then ϕ is small at all positions, and the effects in Figure 5.5 pertaining to ϕ_1 and ϕ_2 may be ignored. In other words, for this case the nonlinear deflection coupling will be due primarily to w^* . Therefore, first choosing a “low β ” allows us to separate the coupling effect of w^* from that of ϕ . For this purpose, the first part of the discussion will be conducted with $\beta = 0.025$. Afterwards β will be increased to the maximum value (0.1) shown in Table 6 to study the complete effect of the nonlinear deflection coupling, especially from angle ϕ . Because β is a governing parameter and influences the Laplace pressure and the amount of liquid displaced by the meniscus, as mentioned in section 5.2.1.1, by changing its value we are also studying its influence on collapse.

5.3.1 Collapse at moderate contact angles and low β

Having a low value of β , in this case $\beta = 0.025$, provides numerous simplifications. As previously mentioned, from Eq. (5.4), normalized slopes are

transformed into physical slopes by multiplication with β . As a result if $\beta \ll 1$ all deflection angles ϕ will be small and have a negligible impact on the problem. This allows for ϕ to be ignored when analyzing the constraint equations. For example Eq. (5.8) simplifies to $l_1^* \approx \sin \theta_c$, which for this analysis is nearly a constant. Physically this means that the “shape” (see Figure 5.3) and hence MDF of the left meniscus remains approximately constant as the beam deflects but the meniscus radius α will change. Furthermore, as $\phi \rightarrow 0$ the expression for the dimensionless menisci radius simplifies to $\alpha \approx (w_1^* - 1) / \cos \theta_c$, which no longer depends on the slope at the left meniscus ϕ_1 .

For these parameters ($\theta_c = 45^\circ$ and $\beta = 0.025$) the resulting contour plot of the free end deflection w_2^* is shown in Figure 5.6, as a function of V^* and Λ . At a given V^* , deflection increases gradually as Λ is increased until collapse ($w_2^* = 1$) which occurs at the top of the figure. At the bottom of Figure 5.6, where deflections are small, the contours have negative slope as V^* increases; this means that for a given Λ the beam deflection increases for a larger drop (V^*). This is the behaviour that was expected in section 5.2.1 since larger liquid volume was expected to result in larger capillary forces as the Laplace pressure would be acting over a greater area. At higher values of Λ (near the middle of Figure 5.6, $\Lambda = 0.0035-0.0045$) the deflection pattern changes. In particular, with respect to V^* , the deflection contours first slope down, attain a minimum, and then slope up; this indicates that in this area there is a value of V^* that maximizes the deflection for each value of Λ . As Λ is further increased the contours slope up with respect to V^* indicating the DCB collapses more easily for smaller V^* . Furthermore, the

contours appear to converge for small V^* , whereas they remain somewhat parallel and equally spaced for larger V^* .

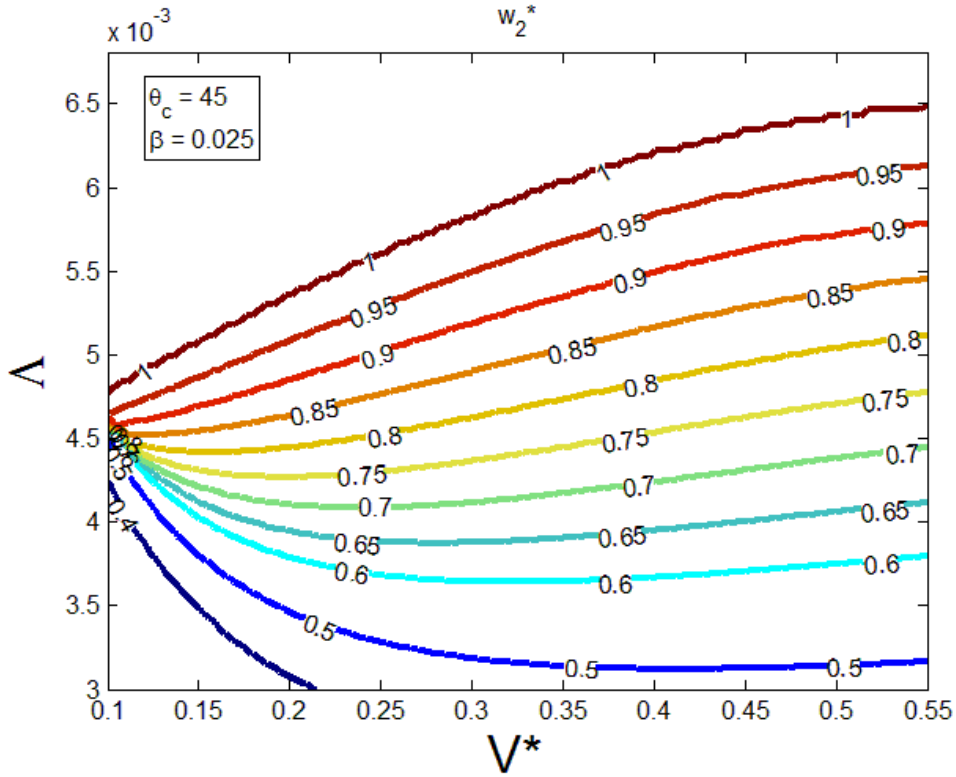


Figure 5.6: Contours for the free end deflection (w_2^*). The contours are plotted with varying Δ and V^* . The other two governing parameters are fixed at $\theta_c = 45^\circ$ and $\beta = 0.025$.

Clearly from Figure 5.6, there exists a reversal in the deflection trends: from deflecting more for larger drops at small deflections to deflecting more for smaller drops near collapse. Such reversal associated with increasing deflection must be caused by the nonlinear deflection coupling effects described in Section 5.2.2. To understand this trend consider Figure 5.7 which shows the deflection of two identical beams deformed by drops of different volume, one with $V^* = 0.15$ (red dashed curve) and the other with $V^* = 0.55$ (black solid curve). The location and shape of their base menisci are shown by blue solid curves. Note that for $\beta < 1$ the length scale is stretched in the vertical direction. The intersection of each

meniscus with its associated deflected beam gives the values of x_1^* on the horizontal axis and w_1^* on the vertical axis. Note that for the larger drop (solid black curve) the meniscus is closer to the base than for the smaller drop (dashed red curve). In Figure 5.7 $\Lambda = 0.003$ is shown on the left and $\Lambda = 0.0045$ is shown on the right. For $\Lambda = 0.003$ the beam with the larger drop has a higher deflection due to increased Laplace pressure area. However, the deflection at the base meniscus is less for the larger drop ($w_1^* \approx 0.05$) than for the smaller drop ($w_1^* \approx 0.2$). Recall that Eq. (5.9), the relationship between the dimensionless meniscus radius α and deflection at the base menisci w_1^* , simplified for small β , is $\alpha \approx (w_1^* - 1) / \cos \theta_c$. Since M_p^* , the net moment on the beam due to Laplace pressure, is inversely proportional to α (Eq. (5.3)), greater base meniscus deflection for smaller drop leads to smaller α magnitude and larger M_p^* . For $\Lambda = 0.0045$, the deflection contours in Figure 5.6 show the reversed trend because the increase in base meniscus deflection ($w_1^* \approx 0.025$ for larger drop and $w_1^* \approx 0.4$ the smaller drop) causes enough of an increase in Laplace pressure to cause the beam with the smaller drop to have a higher deflection. This explains why smaller drops were observed to collapse the DCB more easily in Figure 5.6.

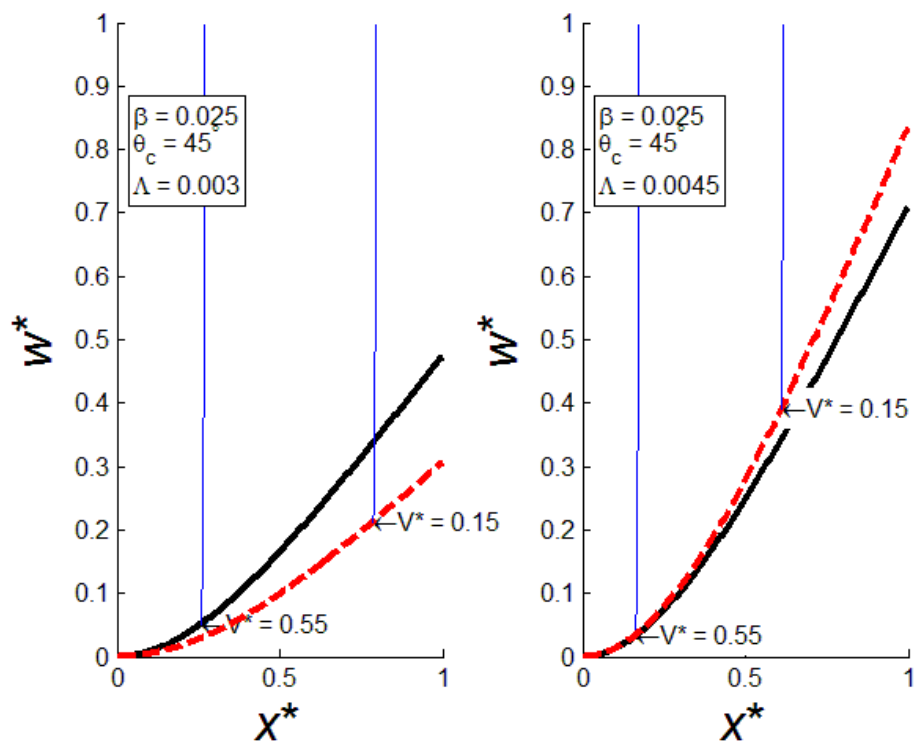


Figure 5.7: Elastic curve and meniscus location for $V^* = 0.15$ and $V^* = 0.55$. The other three governing parameters are fixed at $\beta = 0.025$, $\Lambda = 0.0045$, $\theta_c = 45^\circ$

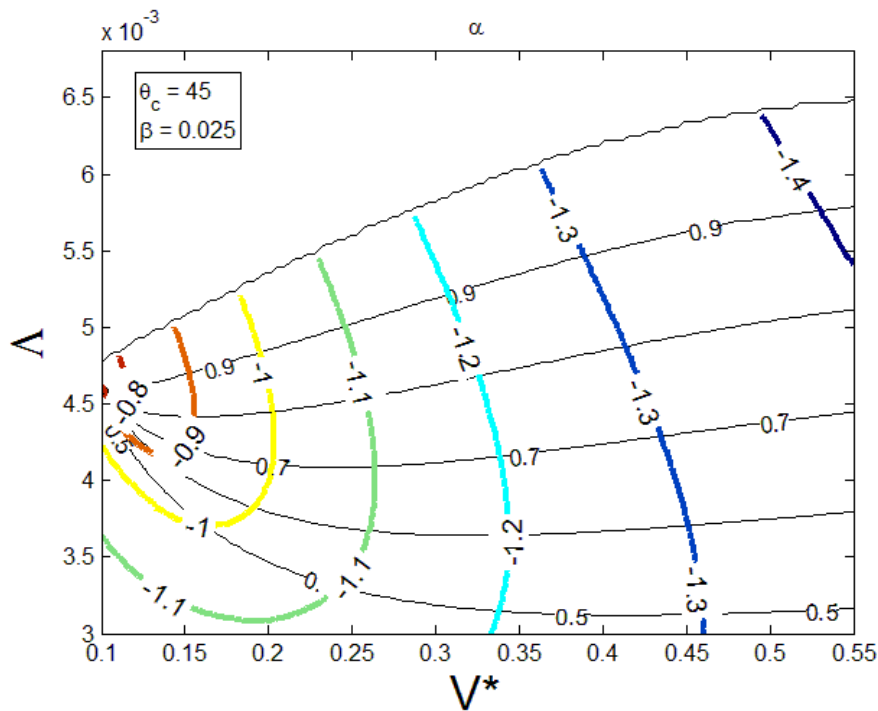


Figure 5.8: Contours for the normalized meniscus radius (α). The contours are plotted with varying Λ and V^* . The other two governing parameters are fixed at $\theta_c = 45^\circ$ and $\beta = 0.025$.

To systematically study how α changes with deflection, the corresponding contour plot for α is shown in Figure 5.8. In this figure contours of w_2^* are also plotted as black thin curves to allow comparison along lines of constant free end deflection. For example, following any line of constant w_2^* from $V^* = 0.1$ to $V^* = 0.55$ shows that $|\alpha|$ increases with V^* . This reinforces the prediction based on Figure 5.7 that for smaller drops, if w_2^* is similar, the base meniscus will be closer to the free end, causing larger w_1^* , smaller $|\alpha|$, and larger Laplace pressure. Another observation from Figure 5.8 is that the change of $|\alpha|$ with increasing Λ (and deflection) is greater at smaller V^* . As a result with increasing Λ , smaller drops experience a greater increase in M_p^* , and hence a greater increase in w_2^* . This gives rise to the converging behaviour of the w_2^* contours at small V^* observed in Figure 5.6. On the other hand, for very large V^* , it is expected that the final meniscus position is close to the base where deflection is zero. As a result $|\alpha|$ increases nearly to its undeflected value. Therefore, the free end deflection will be insensitive to the exact value of V^* when it is large, resulting in the levelling off of the contour lines for large V^* shown in Figure 5.6.

There is another interesting trend in Figure 5.8. Reading the plot at constant V^* ($V^* = 0.25$ for example), the same contour ($\alpha = -1.1$ in this case) is passed twice as deflection is increased to collapse; for larger drops such behaviour will also be seen in Figure 5.8 covers a broader range of w_2^* . This means that $|\alpha|$ first decreases with increasing w_2^* , attains a minimum and eventually begins to increase. The contours for the base meniscus deflection w_1^* shown in Figure 5.9

display the same non-monotonic pattern. Which is not surprising since for low values of β , α is determined primarily by w_1^* (see Eq. (5.9)). As the beam deflects, w_1^* first increases. However, deflection displaces liquid and because V^* is constant causes the base meniscus to move towards the clamped end where deflection is less. The associated contour plot for the base meniscus position is shown in Figure 5.10. Reading this plot along a curve of constant w_2^* from small V^* to large V^* , x_1^* is found to decrease as expected. Similarly reading the plot at a constant value of V^* , x_1^* again decreases as w_2^* is increased. Clearly as Λ is increased to cause more deformation there is a competition between two effects on the value of w_1^* : increased overall beam deflection, and meniscus movement towards the base where deflection is lower. Eventually the meniscus movement overtakes the increase in beam deflection, w_1^* attains a maximum and begins to decrease. This creates the non-monotonic changes in w_1^* with increasing deformation; an example is shown in Figure 5.11 for $V^* = 0.15$. Before the maximum when w_1^* increases, $|\alpha|$ decreases and the Laplace pressure increases, as a result the free end deflection w_2^* increases rapidly with increasing Λ . However, once the maxima is attained the Laplace pressure decreases with w_2^* , as a result much larger increases in Λ are required to increase w_2^* to collapse. This is reflected in the increased contour spacing after the maxima (easily seen in Figure 5.9 for $V^* = 0.175$). Contour spacing continues to increase with further deformation because w_1^* and hence the Laplace pressure continues to decrease.

From Figure 5.9 it can be seen the maximum w_1^* occurs at higher deflections for smaller V^* . Because for small V^* this maxima of w_1^* occurs at deflections close to collapse, the DCB collapses before a significant decrease in Laplace pressure is able to occur; hence the free end deflection contours near collapse are more closely spaced for smaller drops. To summarize, all drop sizes initially experience an increase in Laplace pressure due to the increase in w_1^* caused by deflection. However, w_1^* peaks due to meniscus movement towards the base. For larger drops this peak occurs at lower deflections allowing for most of the increase in Laplace pressure to be removed by the time the DCB reaches deflections near collapse. This a contributing factor to why smaller drops are able to collapse the DCB more easily.

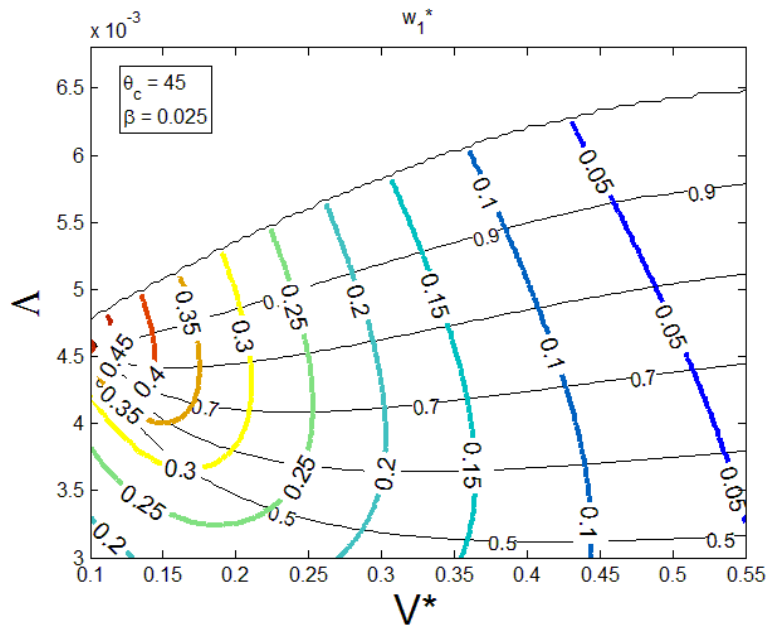


Figure 5.9: Contours for the Base meniscus deflection (w_1^*). The contours are plotted with varying Δ and V^* . The other two governing parameters are fixed at $\theta_c = 45^\circ$ and $\beta = 0.025$.

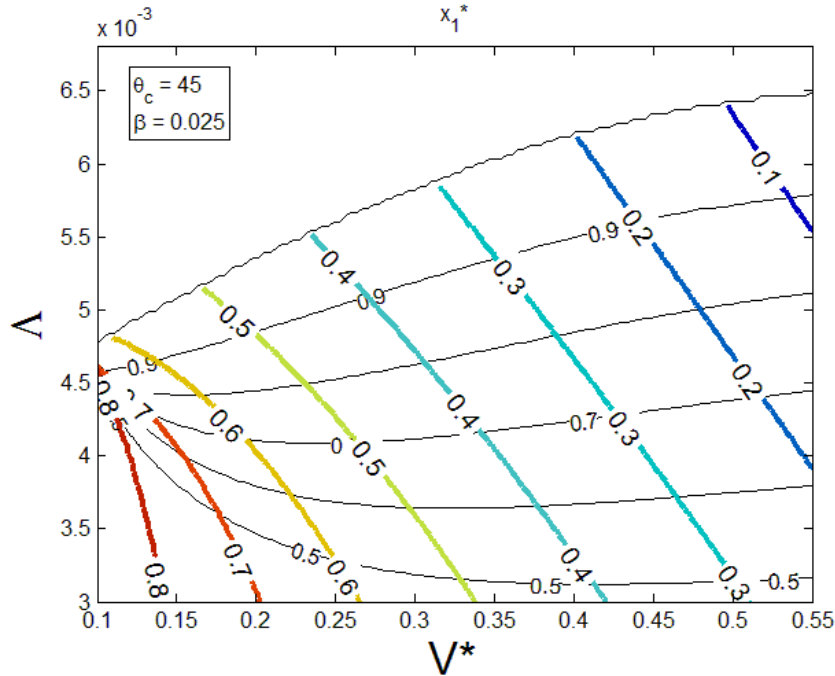


Figure 5.10: Contours for the Base meniscus location (x_1^*). The contours are plotted with varying Λ and V^* . The other two governing parameters are fixed at $\theta_c = 45^\circ$ and $\beta = 0.025$.

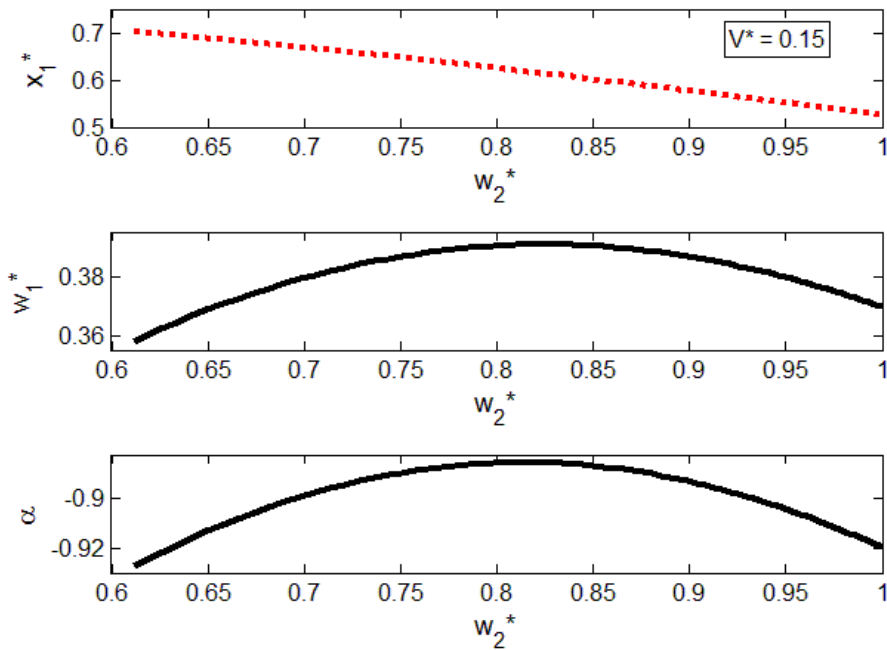


Figure 5.11: Changes in x_1^* , w_1^* , α with increases in free end deflection (w_2^*) for $V^* = 0.15$. Λ is increased to create the increase in w_2^* . The other two governing parameters are fixed at $\beta = 0.025$ and $\theta_c = 45^\circ$.

Having addressed the behaviour of α and hence the magnitude of the Laplace pressure we can return to the base meniscus position (x_1^*) contour plot, Figure 5.10, for further discussion. Besides the clear trend of x_1^* decreasing with increasing deflection and V^* , if Figure 5.10 is read carefully there is another important trend. Examining the contours at a constant value of w_2^* , it can be seen that they are closer together for smaller drops. For example at $w_2^* = 0.5$ the spacing between the $x_1^* = 0.7$ and $x_1^* = 0.6$ contours is 0.07 (measured in V^*) while the spacing between the $x_1^* = 0.4$ and $x_1^* = 0.3$ contours is approximately 0.09. To explain this, first note that the liquid volume displaced by beam deflection, $\int_{x_1^*}^{x_2^*} w^*(x^*) dx^*$, receives its largest contribution from liquid near the free end where deflection is largest. Consider a given curve $w^*(x^*)$ with two liquid drops of different volumes so that x_1^* and w_1^* are smaller for the larger drop. Now imagine adding liquid to each drop to cause a given decrease in x_1^* . Because w_1^* is less for the larger drop more space needs to be filled in order for x_1^* to decrease by a given amount; hence more liquid needs to be added. Now imagine the deflection-caused reduction in x_1^* for the two drops. Although, more liquid is displaced for the larger drop there is more room to fill so the decrease in x_1^* may actually be smaller for larger drops. This behaviour has an important repercussion on the area on which the Laplace pressure acts. Consider a numerical example where two drops having volumes of $V^* = 0.25$ and $V^* = 0.5$. Before deflection the Laplace pressure area for the larger drop nearly double that of the

smaller drop. However, at collapse $x_1^* = 0.4$ for the smaller drop, and $x_1^* = 0.1$ for the larger drop. Recognizing that the normalized area on which the Laplace pressure acts is $1-x_1^*$ (0.6 for the smaller drop and 0.9 for the larger drop), after deflection the Laplace pressure only acts on an area that is 50% larger for the $V^* = 0.5$ drop. That is, the beam's deflection causes a larger increase in the Laplace pressure area relative to the initial area for smaller drops, and further facilitates the collapse.

To summarize the results so far, for moderate contact angles and low β , small drops are observed to more easily collapse the DCB. Physically, this implies that if a pre-existing liquid drop is to be eliminated from a MEMS/NEMS structure through evaporation, collapse can occur during the evaporation process, which in turn facilitates stiction. Such an observation can be attributed to two mechanisms: (1) for smaller drops, beam deflection at the base meniscus is larger, resulting in larger Laplace pressure; and (2) beam deflection causes the base meniscus to move towards the clamped end, increasing the acting area of the Laplace pressure, and such increase is more pronounced for smaller drops. The first mechanism will not be revealed without considering coupling between the deformation of the beam and meniscus geometry, and the second mechanism will not be revealed if the meniscus is assumed to be pinned, as in the work of Ouakad *et al.* [8]. Assuming a pinned meniscus allows the liquid to leak, which is unphysical. Overall, our results demonstrate the necessity of modeling the detailed geometry of the liquid drop, and coupling it with the beam deflection.

The preceding discussion focussed primarily on the Laplace pressure, and in particular how it is coupled to the beam's deformation. However, this model also accounts for surface tension forces which have been neglected by prior models. Therefore, it is desirable to examine how important these forces are to collapse. Figure 5.12 plots the fraction of the total reaction moment due to surface tension forces, $M_{ST}^* / M_R^* = M_{ST}^* / (M_{ST}^* + M_P^*)$; here the thick curves are contours for M_{ST}^* / M_R^* whereas the black thin curves are contours for w_2^* . For small V^* and deflections (lower left corner of the plot), surface tension forces contribute to more than 22% of the total moment on the beam. However, at collapse (upper part of the plot) this contribution drops to less than 10%. Such drop is caused by an increase in the Laplace pressure moment M_P^* with deflection; although the change in Laplace pressure was with Λ non-monotonic there is an overall increase in Laplace pressure at collapse compared with no deflection. Furthermore, for larger drops (large V^*) surface tension plays an even smaller role, both because the Laplace pressure acts over a larger area and because the surface tension force at the base meniscus contributes a smaller moment as it acts closer to the base. Due to the small contribution of the surface tension force to collapse, the w_2^* behaviour seen in Figure 5.6 can be attributed primarily to Laplace pressure.

Finally, the normalized volume of liquid displaced by the two menisci, corresponding to the second term on the RHS of Eq. (5.5), is shown in Figure 5.13. For moderate contact angle and low β considered here, these values are more than one order of magnitude smaller than V^* so it is not a significant contributing

factor to x_1^* . That is, changes in x_1^* are determined primarily by liquid displacement due to beam deflection (first term on the RHS of Eq. (5.5)).

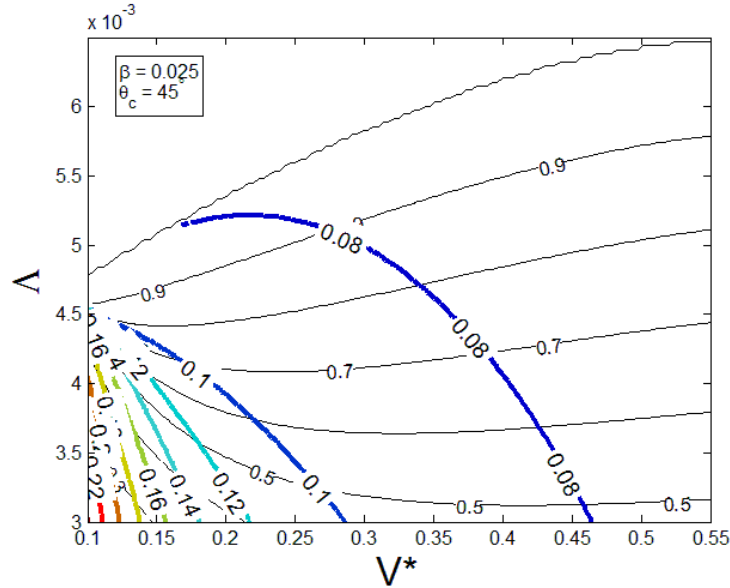


Figure 5.12: Contours for the fraction of reaction moment due to the surface tension forces. The contours are plotted with varying Δ and V^* . The other two governing parameters are fixed at $\theta_c = 45^\circ$ and $\beta = 0.025$

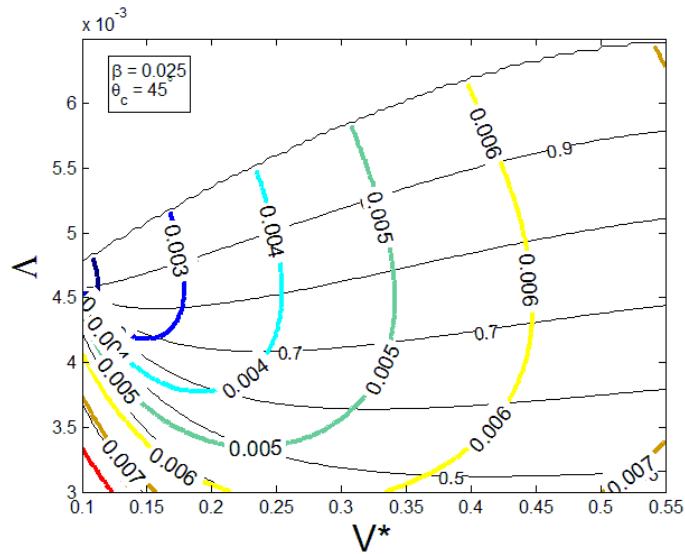


Figure 5.13: Contours for the normalized volume of liquid displaced by menisci (MDISP). The contours are plotted with varying Δ and V^* . The other two governing parameters are fixed at $\theta_c = 45^\circ$ and $\beta = 0.025$.

5.3.2 DCB Collapse at moderate contact angles and high β

Having the highest value of β of practical interest, 0.1, allows for maximum values of the deflection angle ϕ . As a result ϕ can play a larger role in the constraint equations Eq. (5.5)-(5.8). Specifically, from Figure 5.5, increases in ϕ_1 may counteract changes in α caused by increases in w_1^* , which can be seen in Eq. (5.9). Furthermore, ϕ_1 may now influence l_1^* (from Eq. (5.8)) and hence the meniscus position to a greater degree (Eq. (5.5)). In fact, as shown in Figure 5.5 and Eq. (5.5), this effect is amplified at higher β . Finally, from Figure 5.5 and Eq. (5.3), increasing β reduces the Laplace pressure moment, meaning the surface tension force can play a more important role compared with the low β case.

To begin, a free end deflection (w_2^*) contour plot as a function of Λ and V^* is again generated, but with $\beta = 0.1$. This is shown in Figure 5.14 which looks similar to Figure 5.6 for $\beta = 0.025$, but there are several noticeable differences. Firstly, at the same V^* , larger values of β require much larger Λ to collapse the DCB which is explained by the Laplace pressure in Eq. (5.2) being inversely proportional to β . Secondly, compared with Figure 5.6, the contours in Figure 5.14 are more spaced out in the vertical direction (note the difference in scale along the Λ axis). Thirdly, the curves at small V^* are flatter than in the small β case. Finally, in the high β plot as V^* is increased the contour for collapse ($w_2^* = 1$) first shows the same pattern as in Figure 5.6, i.e., easier collapse for smaller V^* ; however, as V^* is further increased the contour shows a more drastic levelling off pattern than in the low β case. In fact the trend even reverses and the DCB becomes easier to collapse again as V^* approaches 0.55. As was seen in the

low β case, changes in $|\alpha|$ caused by beam deflection played an important role on collapse, so to explain the differences observed in the w_2^* contours it is natural to first look at α .

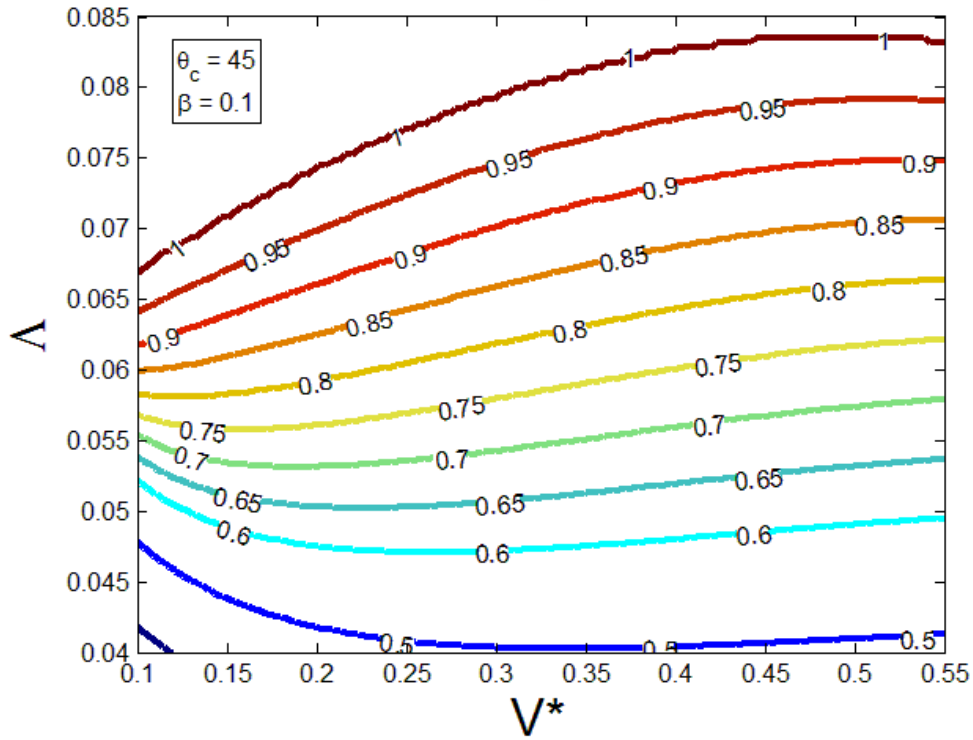


Figure 5.14: Contours for the free end deflection (w_2^*). The contours are plotted with varying Λ and V^* . The other two governing parameters are fixed at $\theta_c = 45^\circ$ and $\beta = 0.1$.

Comparing a contour plot of α shown in Figure 5.15 with the α contours from the low β case shown in Figure 5.8; there are several noticeable differences. First, the high β contours show higher $|\alpha|$ values throughout the entire plot. This increase in $|\alpha|$ is significant because it corresponds to a decrease in Laplace pressure. To understand why $|\alpha|$ was observed to be higher in Figure 5.15, recall the relationship for α in Eq. (5.9), $|\alpha| = (1 - w_1^*) / \cos(\theta_c + \phi_1)$. An increase in $|\alpha|$ could be caused by either a decrease in w_1^* or an increase in ϕ_1 . In the low β case, ϕ_1 was close to zero irrespective of the loading conditions, and hence the value of

the base meniscus deflection w_1^* determined $|\alpha|$. However, larger values of β lead to larger values of ϕ (see Eq. (5.4), $\tan \phi = \beta dw^*/dx^*$). As a result the cosine term in the denominator of Eq. (5.9), will have a smaller value and $|\alpha|$ will be larger. The other difference between Figure 5.8 and Figure 5.15 is that the high β contours appear to be stretched vertically which would imply less dependence on Λ . This stretching behaviour is consistent with the w_2^* contours being more spaced out (especially for low V^*), which are the black thin curves shown in Figure 5.15. To see whether w_1^* or ϕ_1 is the dominating contributor to the above observed differences, consider the w_1^* contours for the high β case shown in Figure 5.16. If read carefully at constant values of w_2^* and V^* , there are no significant differences in w_1^* for the high β case compared with the low β case (Figure 5.9), so the differences in α (and w_2^*) must be explained by ϕ_1 .

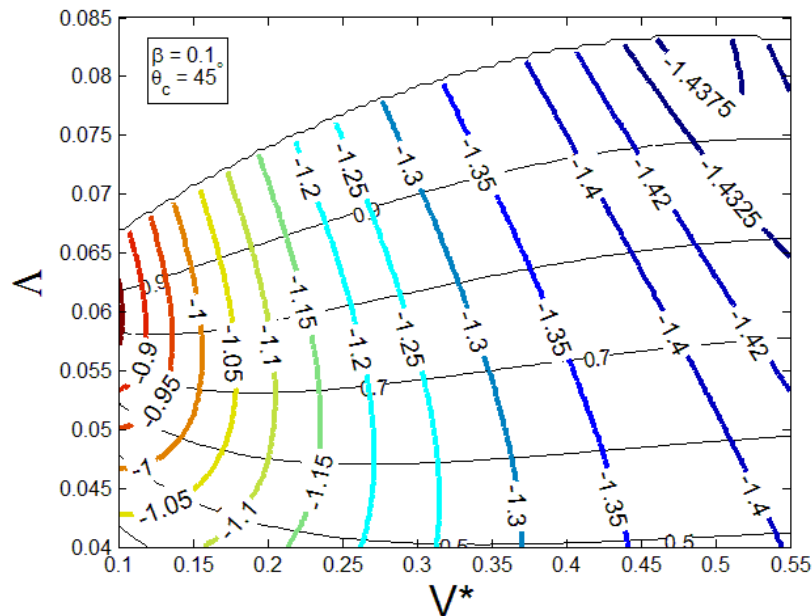


Figure 5.15: Contours for the normalized meniscus radius (α). The contours are plotted with varying Λ and V^* . The other two governing parameters are fixed at $\theta_c = 45^\circ$ and $\beta = 0.1$.

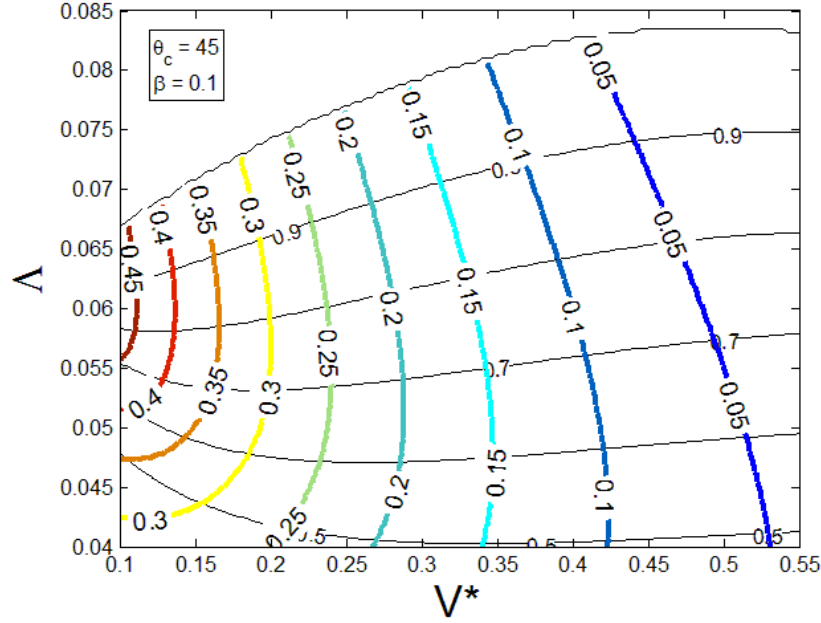


Figure 5.16: Contours for the base meniscus deflection (w_1^*). The contours are plotted with varying Λ and V^* . The other two governing parameters are fixed at $\theta_c = 45^\circ$ and $\beta = 0.1$.

Consulting Eq. (5.8), $l_1^* = \sin(\theta_c + \phi_1)$, l_1^* provides a measure of the angle ϕ_1 . Contours of l_1^* are shown in Figure 5.17. It can be seen that as Λ is increased at a fixed $V^* > 0.3$, l_1^* (therefore ϕ_1) first increases, attains a maximum and then begins to decrease with further deflection. Increasing deflection causes the base meniscus can move closer to the base where the slope is less. Competition between increased beam deformation and the relocation of the base meniscus cause the non-monotonic behaviour of l_1^* seen in Figure 5.17. Such non-monotonic behaviour is also seen for w_1^* in Figure 5.9 and Figure 5.16. However, for w_1^* this maxima occurs at deflection well before collapse which differs from the situation of l_1^* . It is clear from Figure 5.17 that for large V^* (>0.45) the l_1^* maximum occurs significantly before collapse; so near collapse l_1^* is decreasing with increasing w_2^* . On the contrary, for smaller V^* , l_1^* increases monotonically

with increasing w_2^* . With the knowledge of how the angle at the left meniscus changes with deflection we can now address the differences observed in the w_2^* contours with high β .

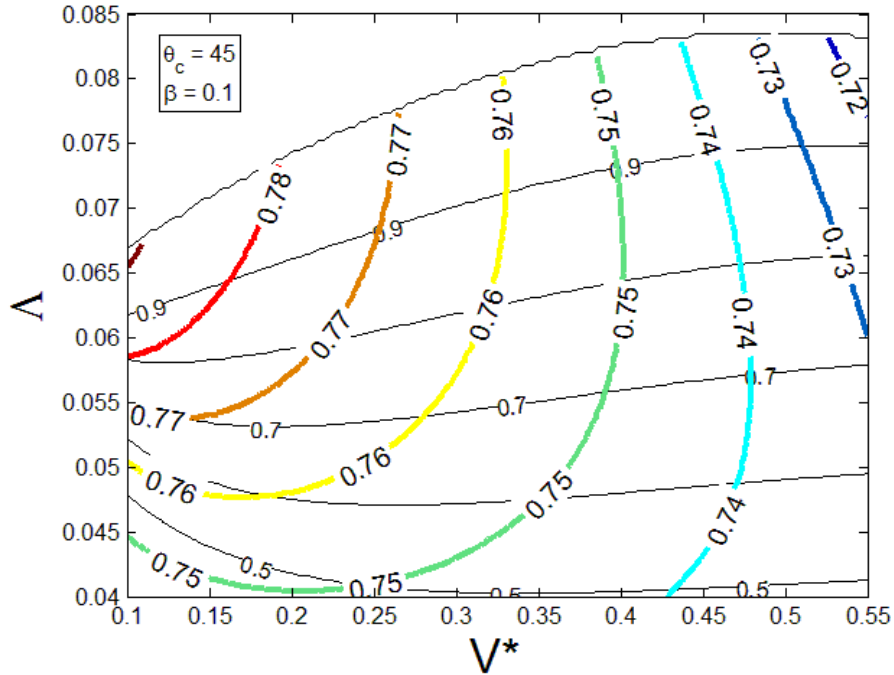


Figure 5.17: Contours for base meniscus geometry factor (l_1^*). The contours are plotted with varying Λ and V^* . The other two governing parameters are fixed at $\theta_c = 45^\circ$ and $\beta = 0.1$.

Recall that in the high β case the w_2^* contours, Figure 5.14, were flatter and more spaced at low V^* , and the collapse line levelled off and even reversed its trend for high V^* . The first observation can be explained by Figure 5.17 where at a fixed but small V^* , l_1^* increases monotonically with Λ , i.e., with deflection. This increase in l_1^* causes the denominator of Eq. (5.9) to decrease resulting in an increase in $|\alpha|$. On the other hand, nonmonotonic changes in w_1^* with deflection were the only driving force for $|\alpha|$ in the low β case. Therefore, in the high β case

the increase in ϕ_1 with deflection partly counteracts the increase in w_1^* with deflection resulting in increased contour spacing.

Levelling off and even reversal of the collapse curve trend for high V^* is due to a similar effect. Returning to the α contour plot, Figure 5.15, and focussing on $0.4 < V^* < 0.55$, α is restrained to a small range: $-1.45 < \alpha < -1.4$ and there exist subtle non monotonic changes in α within this range. The small variation in α and hence Laplace pressure is the main reason why the collapse curve levels off in the large V^* region. As a comparison, in the small β case, shown in Figure 5.8, a steady increase in $|\alpha|$ with increasing V^* occurred in this region. To explain why the variation in α is small for large V^* in the high β case, studying the w_1^* contours Figure 5.16, and the l_1^* contours Figure 5.17 in this range of V^* show that near collapse both w_1^* and l_1^* decrease with increasing deflection for constant V^* . Recall that from Eq. (5.9), decreasing w_1^* tends to increase $|\alpha|$, whereas decreasing l_1^* corresponds to decreasing ϕ_1 which tends to decrease $|\alpha|$. The competing effects of deflection and slope at the base meniscus results in the relatively small variation in α shown in Figure 5.15. However for larger drops near collapse both w_1^* and ϕ_1 become very small due to meniscus proximity to the clamped base; when this happens the decrease in ϕ_1 which occurs as the base meniscus moves closer to the base with beam deflection overpowers the simultaneous decrease in w_1^* ; this causes a slight decrease in $|\alpha|$ and in turn the trend reversal in the collapse line.

This trend reversal in α is shown more clearly for $V^* = 0.55$ in Figure 5.18. Initially both w_1^* and ϕ_1 increase as the beam deflects as described above, both eventually attain maximums and begin to decrease with further deflection; the w_1^* maximum occurs significantly before the ϕ_1 maximum. For $w_2^* < 0.8$ the behaviour of $|\alpha|$ mostly follows that of w_1^* . There are some differences such as the minimum $|\alpha|$ occurring before the maximum of w_1^* which is caused by the simultaneous increase in ϕ_1 (this was negligible for the low β case (Figure 5.11) and the maxima of w_1^* and minima of $|\alpha|$ occurred simultaneously). However, for $w_2^* > 0.8$, when w_1^* is small and decreases slowly, the decrease in ϕ_1 creates a small decrease in $|\alpha|$.

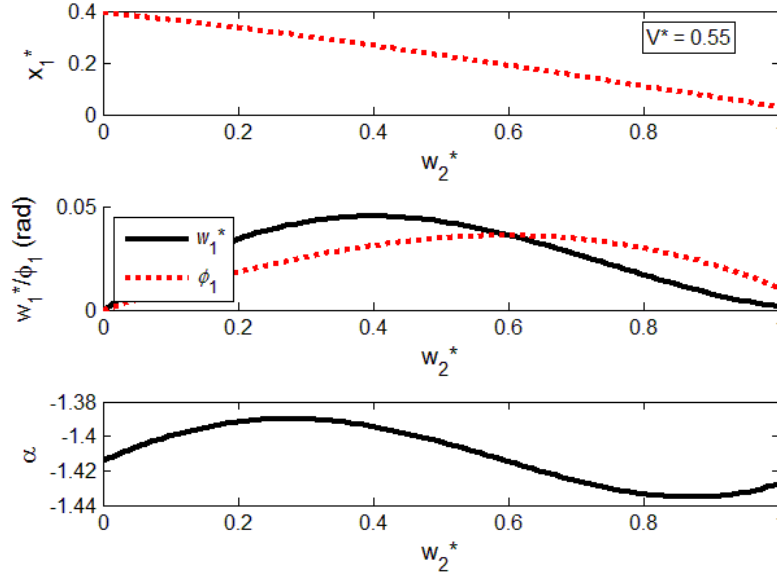


Figure 5.18: Changes in x_1^* , w_1^* , ϕ_1 , α with increases in free end deflection (w_2^*) for $V^* = 0.55$. Δ is increased to create the increase in w_2^* . The other two governing parameters are fixed at $\beta = 0.1$ and $\theta_c = 45^\circ$.

Referring to Figure 5.5 in the high β case slopes and angles may also influence x_1^* so it is desirable to see how this nonlinear deflection coupling influences collapse. Contours of base meniscus position are shown in Figure 5.19. Compared with the corresponding low β contours Figure 5.10 there does not appear to be any difference in the contour patterns. If in the high β regime the nonlinear deflection coupling of ϕ and x_1^* were strong, then larger ϕ associated with larger deflection would increase l_1^* and decrease the MDF (Figure 5.4) to cause an increase in x_1^* , which was not observed. Therefore, the nonlinear deflection coupling of ϕ and x_1^* is not important even in the high β regime. There is one subtle difference between the x_1^* contours for high β (Figure 5.19) and low β (Figure 5.10): at constant values of V^* and w_2^* , x_1^* is slightly smaller in the high β case. For example at $V^* = 0.5$ and collapse ($w_2^* = 1$), $x_1^* = 0.1$ in Figure 5.10 and $x_1^* = 0.08$ in Figure 5.19. In the constant volume constraint, Eq. (5.5) the amount of liquid displaced by the meniscus is proportional to β so with higher β , x_1^* will be slightly closer to the base. Physically this means that for a larger gap between the DCB, the meniscus curvature is able to displace more liquid in terms of the fraction of the total volume between the undeflected beams. Thus in the higher β case there is a minor contribution to collapse in that the increased β causes a slight increase in the area that the Laplace pressure acts on.

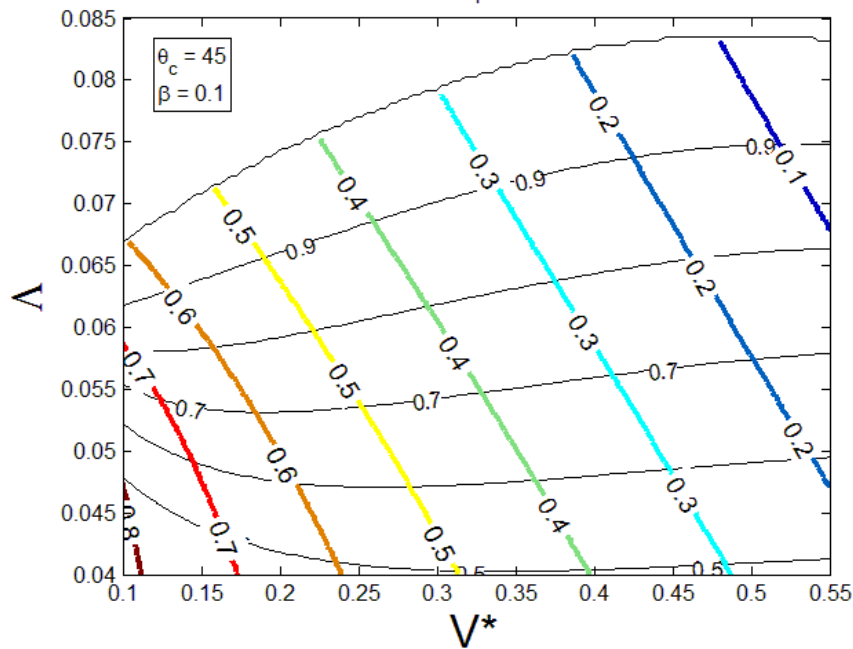


Figure 5.19: Contours for the base meniscus location (x_1^*). The contours are plotted with varying Λ and V^* . The other two governing parameters are fixed at $\theta_c = 45^\circ$ and $\beta = 0.1$.

To summarize, for moderate contact angles and high β , in general small drops are still observed to more easily collapse the DCB but it is less pronounced than in the low β case. Furthermore, compared with the low β case, the collapse condition becomes less sensitive to V^* when V^* exceeds 0.45. These changes are caused by the relatively large deflection angle ϕ that needs to be considered in the constraint equations when β is large. Essentially, ϕ counteracts the influence of deflection on the meniscus geometry. While the deflection results in larger Laplace pressure in smaller drops, ϕ reduces the difference. Because of the competition between deflection and angle, the characteristics for collapse differ from the low β case where deflection is the only driving force.

The preceding discussion has revolved around explaining differences in the low and high β deflection contours. Returning to Eq. (5.2) which governs the

beam's deformation, β appears in the denominator of the pressure term. Therefore, for larger β surface tension forces can become comparable to the Laplace pressure forces and should be investigated. Figure 5.20 plots the fraction of the reaction moment due to the surface tension forces $M_{ST}^* / M_R^* = M_{ST}^* / (M_{ST}^* + M_P^*)$. Comparing Figure 5.20 with Figure 5.12, the moment fraction contours exhibit similar characteristics for low and high β . However, quantitatively, the value of M_{ST}^* / M_R^* is significantly larger in the high β case, being as much as 45% for small deflection and V^* (lower left corner of Figure 5.20), and 25% for large deflection and V^* (upper right corner of Figure 5.20). Even along the collapse contour, M_{ST}^* / M_R^* is between 20% and 30% for all values of V^* , in contrast to less than 10% in the case of low β . Clearly, for high β , the surface tension force is a significant factor in determining collapse and cannot be ignored.

With M_{ST}^* being a non-negligible part of M_R^* , one may wonder whether M_{ST}^* is a main contributing factor to the differences observed between the collapse contours in the low β and high β cases on which much of the discussion of this section has focused. It is unlikely because as in Figure 5.12 the variation of M_{ST}^* / M_R^* in Figure 5.20 with respect to V^* is quite small along the collapse contour. Furthermore, increased M_{ST}^* / M_R^* in the high β case opposes the changes in free end deflection contours, Figure 5.14, observed for high β at collapse compared with low β , Figure 5.6. For example because M_{ST}^* is larger for smaller V^* , the increase in M_{ST}^* in the high β case would be expected to cause the collapse line to be steeper for small drops in the high β case compared with the

low β case. However, as previously described the collapse contours are flattened as β increases, and this is due to the influence of deflection angles. In addition, M_{ST}^* decreases as V^* is increased which should not cause the collapse curve to level off (beam becoming easier to collapse) as was observed in the large V^* regime. Again this trend can be attributed to the effect of angles on $|\alpha|$. To summarize, for moderate contact angles and high β , the surface tension force generates a significant portion of the net moment at collapse and should not be neglected, although it was found that surface tension was not the main contributor to the dependence of the collapse condition on V^* . As will be shown later, in the high contact angle regime to be described in Section 5.4 surface tension forces will be instrumental to determining the collapse condition and its dependence on V^* .

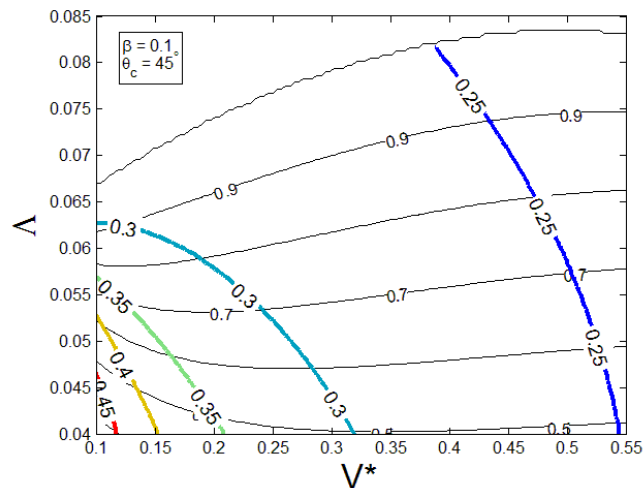


Figure 5.20: Contours for the fraction of reaction moment due to the surface tension forces. The contours are plotted with varying Δ and V^* . The other two governing parameters are fixed at $\theta_c = 45^\circ$ and $\beta = 0.1$.

It is prudent to point out that the bending moment distribution along the length of the beam is a monotonically decreasing function from M_R^* at the base to zero at the free end. This trend can be seen in a bending moment diagram of the

beam shown in Figure 5.21. Therefore, in light of Eq. (5.2), $\beta d^2 w^* / dx^{*2} = M^*$, the magnitude of M_R^* directly influences w_2^* and hence collapse. A contour plot of M_R^* is shown in Figure 5.22. There is some variation with V^* but there is a clear trend of higher M_R^* leading to higher w_2^* . In each contact angle regime we will consult M_R^* contours to see what value is required for collapse. Consider for example $V^* = 0.2$, for the given β , and θ_c , $M_R^* \approx 0.35$ is required to cause the DCB to collapse. In terms of the importance of the surface tension force, because $M_R^* = M_{ST}^* + M_P^*$, if M_{ST}^* were to be neglected in the analysis higher Λ would be needed to provide sufficient M_P^* and hence M_R^* to cause collapse. This point reinforces the need to consider the surface tension force when predicting collapse.

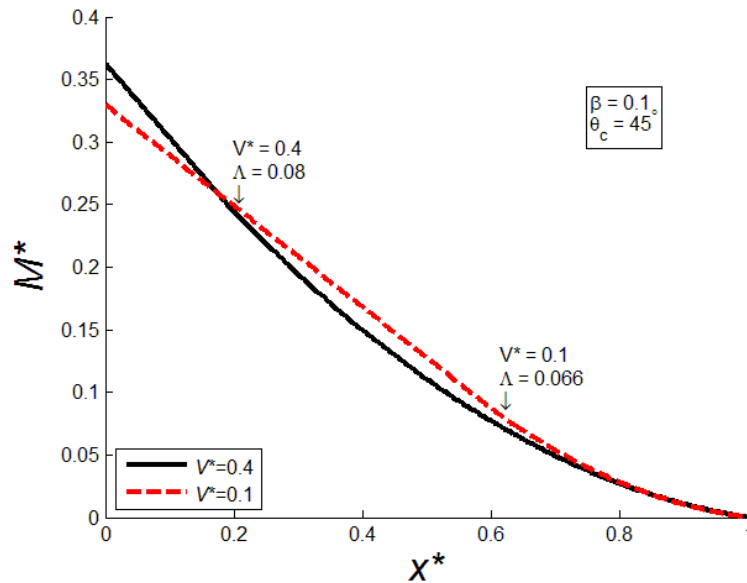


Figure 5.21: Bending moment diagram with governing parameters V^* and Λ chosen to give a free end deflections close to collapse. The other two governing parameters are fixed at $\theta_c = 45^\circ$, and $\beta = 0.1$. Arrows indicate location of meniscus.

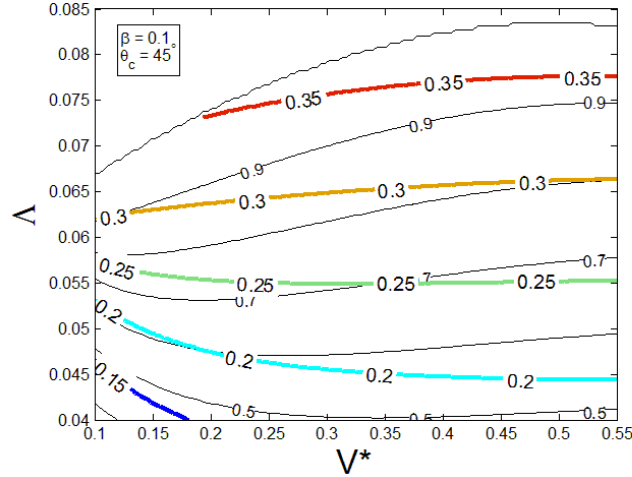


Figure 5.22: Contours for the reaction moment (M_R^*). The contours are plotted with varying Λ and V^* . The other two governing parameters are fixed at $\theta_c = 45^\circ$ and $\beta = 0.1$.

Before proceeding to discuss other contact angle regimes, an overall summary for the moderate contact angle regime results is provided below:

1. For low β , the nonlinear deflection coupling effects due to w_1^* cause a significant increase in the Laplace pressure as the beam deflects. This increase is larger for smaller V^* causing smaller drops to collapse the DCB more easily. In addition, upon deflection, the base meniscus moves closer to the base, i.e., x_1^* decreases. This effect creates a relative decrease in w_1^* which partially counteracts the increase in the Laplace pressure. However it also increases the area on which Laplace pressure applies. This increase is more pronounced for smaller drops, further facilitating the easier collapse of the DCB by smaller drops.
2. Larger β values create a decrease in M_p^* resulting in a significant increase in the Λ required for DCB collapse. In addition larger values of β introduce nonlinear coupling with ϕ_1 (shown in Figure 5.5), which competes with that of w_1^* resulting in a flatter collapse contour, i.e., less dependence of collapse

on the liquid volume V^* . However the dominant characteristics of the collapse contour still follow those observed in the low β case. In particular, the DCB still collapses more easily for smaller drops suggesting that in the moderate contact angle regime the nonlinear coupling effects of w^* are more important than those of ϕ . At the same time, as shown in Figure 5.5, increasing β lead to a decrease in x_1^* . However this decrease was small compared to the change in x_1^* due to liquid displacement by beam deflection.

3. At low β , M_{ST}^* at collapse makes only a small contribution to the total moment ($< 10\%$); therefore, for this case neglecting the surface tension force as was done in previous works would be valid. For large β , however, M_{ST}^* at collapse can be 30% of the total moment, it is significant for causing collapse, and hence strongly affects the dependence of collapse on Λ . However the V^* -dependence of the collapse condition is determined primarily by M_p^* .

5.4 High Contact Angle

In the high contact angle regime where $\theta_c + \phi_1 \rightarrow 90^\circ$, the magnitude of the menisci radii are expected to be large, and collapse is determined primarily by surface tension forces. Furthermore, since large menisci radii cause small Laplace pressure, much higher values of Λ will be needed for collapse. Although it was not shown, increasing the contact angle within the moderate contact angle range causes the low V^* contours to be flatter and eventually the behaviour of the plot changes significantly once the high contact angle regime is reached. For $\beta = 0.1$, a contact angle of $\theta_c = 80^\circ$ falls within this regime and will be used to demonstrate

high contact angle regime characteristics. In the moderate contact angle regime the discussion was divided into low and high β regimes. This division will not be performed for the high contact angle regime because in order to satisfy $\theta_c + \phi_1 \rightarrow 90^\circ$, decreasing β (and hence ϕ_1) is equivalent to increasing θ_c . Keeping with our goal of understanding how the governing parameters influence collapse, studying the high contact angle regime allows for a closer study of how surface tension forces influence collapse. As in the moderate contact angle case considerable discussion will be given to the behaviour of the nonlinear deflection coupling effects. In particular, as mentioned in section 5.2.2 it is expected that the deflection will be more sensitive to angles in this regime.

Consider the deformation of the DCB with $\beta = 0.1$ and $\theta_c = 80^\circ$. Contours for this case are shown in Figure 5.23. Near the bottom of the plot the contours are nearly linear and at a specific Λ , the deflection is higher for smaller V^* . This is different from the contours in the moderate contact angle regime (Figure 5.14) where for small Λ , larger V^* is found to cause larger deflection. More interestingly, at the top of Figure 5.23, near collapse, the curves show non-monotonic behaviour. In particular, at a specific Λ , the minimum deflection occurs between $V^* = 0.3$ and $V^* = 0.4$, and not at extremely low or high V^* values. This is clearly different from Figure 5.14 in the moderate contact angle regime, where the collapse contour ($w_2^* = 1$) first experiences a sharp increase as V^* increases, levels off for large V^* , and eventually has a slight drop near the maximum V^* . In the high contact angle case, Figure 5.23, the initial increase of the contour with V^* is more gradual, whereas the decline is more pronounced and

occurs at smaller V^* . Another two differences can be seen from comparing Figure 5.14 and Figure 5.23. First for a given V^* , the values of Λ required to cause collapse are much higher in the high contact angle case. Secondly, the behaviour at small V^* in the left part of the contour plot is also drastically different in the high contact angle case; no longer do the contours converge for small V^* . Recall that the contours converged in Figure 5.14 due to the increase of M_p^* with Λ for small drops caused by the beam's deflection.

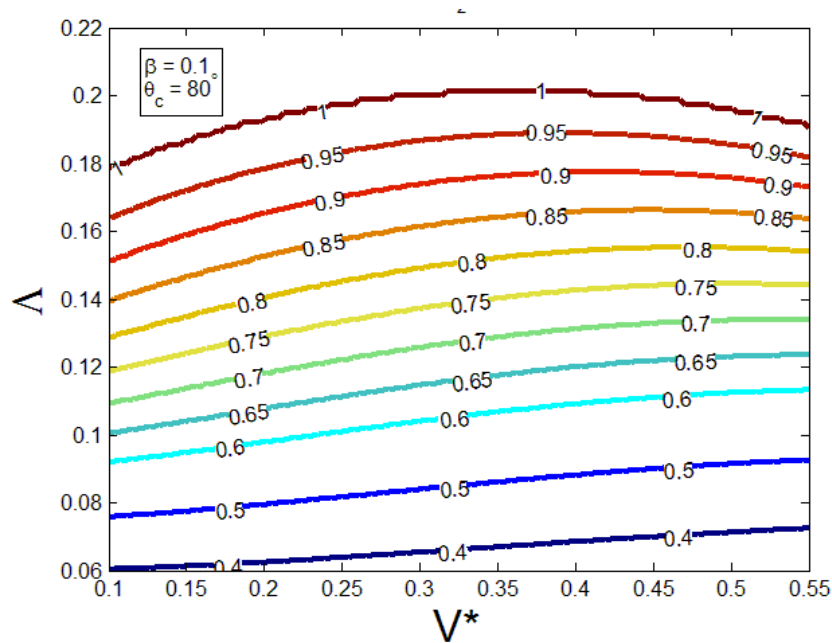


Figure 5.23: Contours for the free end deflection (w_2^*). The contours are plotted with varying Λ and V^* . The other two governing parameters are fixed at $\theta_c = 80^\circ$ and $\beta = 0.1$.

In section 5.3.1 nonlinear deflection coupling effects were observed to cause smaller drops to collapse the DCB more easily. One of the primary driving forces for this behaviour was changes in $|\alpha|$ caused by w_1^* . Although in section 5.3.2 it was shown that the effect of ϕ_1 counteracted the effect of w_1^* , the behaviour was still largely driven by w_1^* . Because α was observed to be sensitive to nonlinear deflection coupling and greatly influenced collapse, it is reasonable to investigate

α first for the high contact angle case. Contours for α are shown in Figure 5.24; the curve associated with highest $|\alpha|$ is in the top left corner and curves of decreasing magnitude expand outwards from this curve. This is in sharp contrast to the moderate θ_c regime (Figure 5.15), where the curve associated with lowest value of $|\alpha|$ was in the top left corner. This is an important observation because now at collapse the Laplace pressure is lower for smaller drops suggesting that collapse is no longer driven primarily by Laplace pressure. It also suggests that the behaviour of $|\alpha|$ is no longer driven primarily by w_1^* but rather by ϕ_1 . To verify this, consider the contour plot of w_1^* for the high contact angle case shown in Figure 5.25. Reading at constant w_2^* in Figure 5.25 shows the same patterns as in the moderate contact angle case (Figure 5.16). The important point is that the patterns in the contours of α (Figure 5.24) no longer follow from the contours of w_1^* (Figure 5.25) as Figure 5.15 did from Figure 5.16 in the moderate θ_c case. Based on this result the denominator in Eq. (5.9) must be driving the meniscus radius, and so it is necessary to look at ϕ_1 .

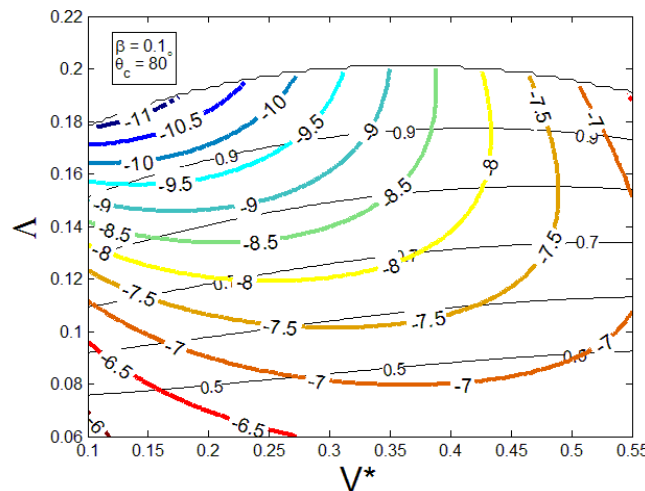


Figure 5.24: Contours for the normalized meniscus radius (α). The contours are plotted with varying Λ and V^* . The other two governing parameters are fixed at $\theta_c = 80^\circ$ and $\beta = 0.1$.

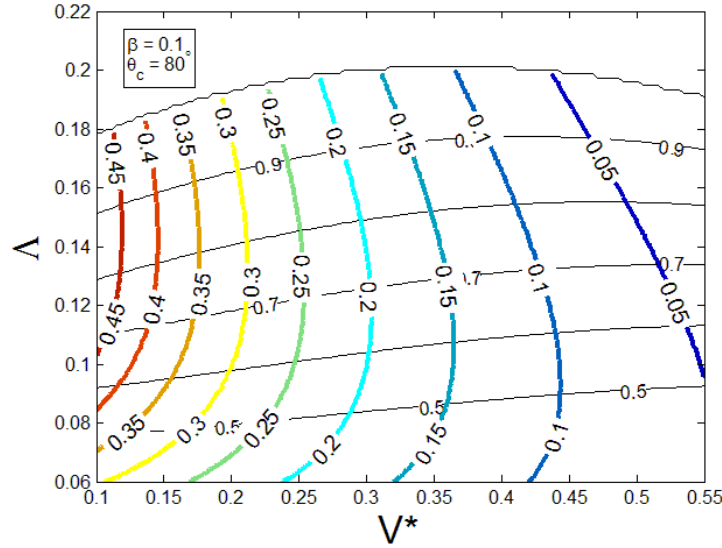


Figure 5.25: Contours for the base meniscus deflection (w_1^*). The contours are plotted with varying Λ and V^* . The other two governing parameters are fixed at $\theta_c = 80^\circ$ and $\beta = 0.1$.

To see the trends in ϕ_1 we will look at l_1^* since they are related by Eq. (5.8).

A contour plot of l_1^* is shown in Figure 5.26. Again comparing this plot with Figure 5.17 in the moderate contact angle case, we see the same basic patterns. However, the important difference is the magnitude of l_1^* in these curves. For the high contact angle regime l_1^* is close to 1. This is the fundamental characteristic of the high contact angle regime, since it was defined from $\theta_c + \phi_1$ being close to 90° . The significance of l_1^* approaching unity is that the denominator of Eq. (5.9) goes to 0, and $|\alpha|$ becomes infinite. Returning to the α contours Figure 5.24, l_1^* makes several important contributions. Firstly, since the denominator of Eq. (5.9) is small for large contact angles, it gives rise to the larger $|\alpha|$ values observed in Figure 5.24 compared with Figure 5.15, implying lower Laplace pressure and hence M_p^* . Secondly, the trends observed in α , Figure 5.24, follow the trends in l_1^* Figure 5.26. To explain this, note that at 90° the cosine function has the

greatest rate of change with respect to its argument. In addition the inverse function ($1/x$) has the greatest rate of change near zero. For these reasons Eq. (5.9) is most sensitive to changes in ϕ_1 when l_1^* is close to 1, and as a result in the high contact angle regime ϕ_1 rather than w_1^* drives the patterns observed in α and hence the Laplace pressure.

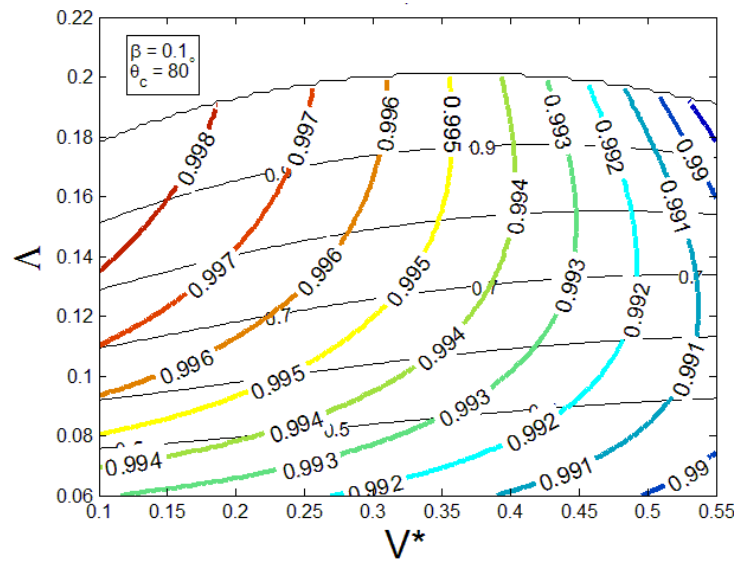


Figure 5.26: Contours for base meniscus geometry factor (l_1^*). The contours are plotted with varying Δ and V^* . The other two governing parameters are fixed at $\theta_c = 80^\circ$ and $\beta = 0.1$.

As previously discussed high contact angles result in large $|\alpha|$. Consequently, the Laplace pressure drops and surface tension forces become more important. The fraction of the reaction moment caused by the surface tension forces, M_{ST}^* / M_R^* , is shown in Figure 5.27. Comparing this plot with Figure 5.20 in the moderate contact angle regime, there are several differences. Firstly, the contours are more vertical at small V^* , indicating less dependency on V^* , because the Laplace pressure is dropping rather than increasing as deflection increases. Secondly and most importantly, the range of M_{ST}^* / M_R^* at collapse is now 60%-85%, rather than 25%-30% indicating that in the high contact angle regime

surface tension forces are the dominant cause of collapse. Because much higher values of Λ are required to cause collapse in the high contact angle regime (see Figure 5.14 and Figure 5.23), this implies that the surface tension forces are not as effective as the Laplace pressure in causing the collapse of the DCB since they do not increase with deflection as the Laplace pressure did in the moderate contact angle regime. This can be further verified by comparing the contour plots of the total reaction moment M_R^* , shown in Figure 5.28 for the high contact angle regime, and in Figure 5.22 for the moderate contact angle regime. The value of M_R^* at collapse appears to be nearly the same in both regimes. Consider for example $V^* = 0.2$, $M_R^* \approx 0.35$ is required to collapse the DCB in both cases. However, higher Λ is needed for the high contact angle case in order to reach this M_R^* and cause collapse. Note that M_R^* required to cause collapse is dependent on V^* as seen in both Figure 5.22 and Figure 5.28. The reason is that the bending moment distribution such as Figure 5.20 depends on the location of the base meniscus and shear reaction Q_R^* ; M^* decreases linearly (with slope Q_R^*) from M_R^* until x_1^* then decreases more slowly until $M^* = 0$ at the free end. Since smaller drops generally have lower Q_R^* and higher x_1^* they tend to collapse with lower M_R^* as seen in Figure 5.22 and Figure 5.28 (also see Figure 6.5).

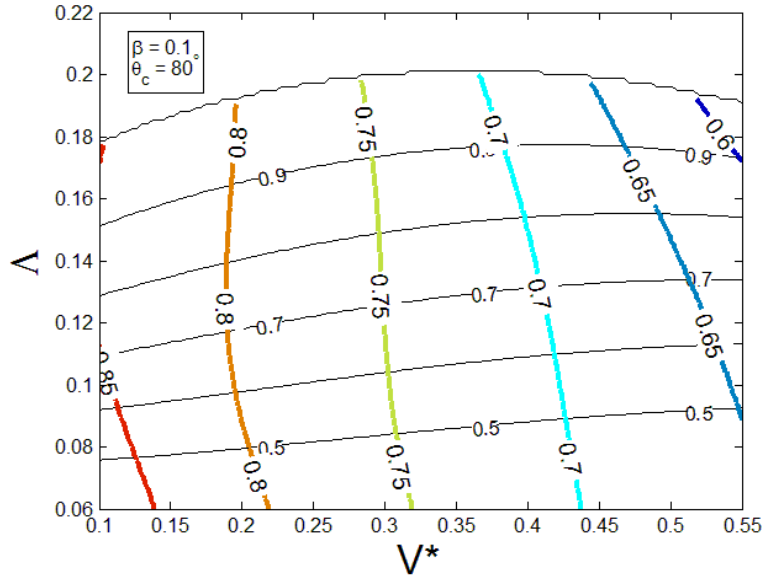


Figure 5.27: Contours for the fraction of reaction moment due to the surface tension forces. The contours are plotted with varying Δ and V^* . The other two governing parameters are fixed at $\theta_c = 80^\circ$ and $\beta = 0.1$.

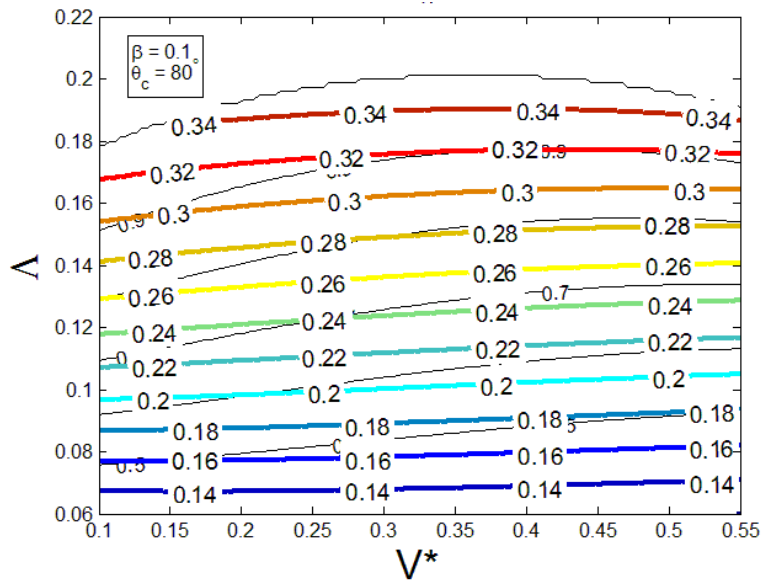


Figure 5.28: Contours for the reaction moment (M_R^*). The contours are plotted with varying Δ and V^* . The other two governing parameters are fixed at $\theta_c = 80^\circ$ and $\beta = 0.1$.

Till now, it remains to be a question why the collapse contour shown in Figure 5.23 exhibits non-monotonic changes with V^* . To answer this question, it is necessary to examine the two contributing moments M_{ST}^* and M_p^* in detail. Start with M_{ST}^* , whose expression is given in Eq. (5.3). Removing the moment

arms from this equation gives the net force caused by surface tension forces, $F_{ST}^* = \Lambda(\sin(\theta_c) + \sin(\theta_2))$; within the linear beam formulation the first term is the transverse force at the base meniscus and the second term is the transverse force at the free end meniscus. Contours of F_{ST}^* are shown in Figure 5.29, which are nearly horizontal, indicating that for this contact angle F_{ST}^* depends almost exclusively on Λ . Furthermore, because both θ_2 and θ_c are close to 90° , the difference between $\sin(\theta_c)$ and $\sin(\theta_2)$ is very small (less than 2%). As a result F_{ST}^* is split nearly evenly between the two menisci. Because the normalized moment arm of the surface tension force at the free end meniscus is $x_2^* = 1$, any variation of $M_{ST}^* \approx F_{ST}^*(x_1^* + 1)/2$ with V^* is essentially caused by the moment arm of the base meniscus, x_1^* . Contour plots of x_1^* and M_{ST}^* are respectively shown in Figure 5.30 and Figure 5.31. At a given Λ , M_{ST}^* decreases with V^* , which is attributed to the decrease in x_1^* with increasing V^* shown in Figure 5.30. The maximum value of M_{ST}^* occurs in the top left corner of Figure 5.31 for small drops near collapse. This explains why the DCB collapsed more easily for very small drops in Figure 5.23. However, it cannot explain why collapse becomes easier again for very large drops suggesting it is also necessary to examine M_p^* .

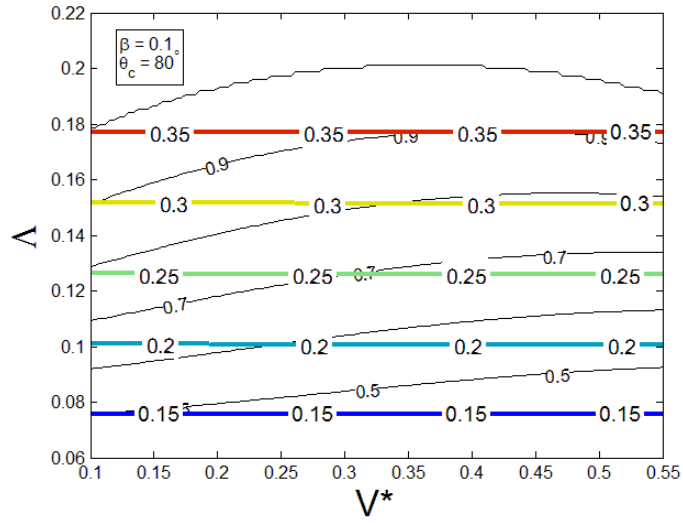


Figure 5.29: Contours for the Sum of the surface tension forces at the two menisci (F_{ST}^*). The contours are plotted with varying Δ and V^* . The other two governing parameters are fixed at $\theta_c = 80^\circ$ and $\beta = 0.1$.

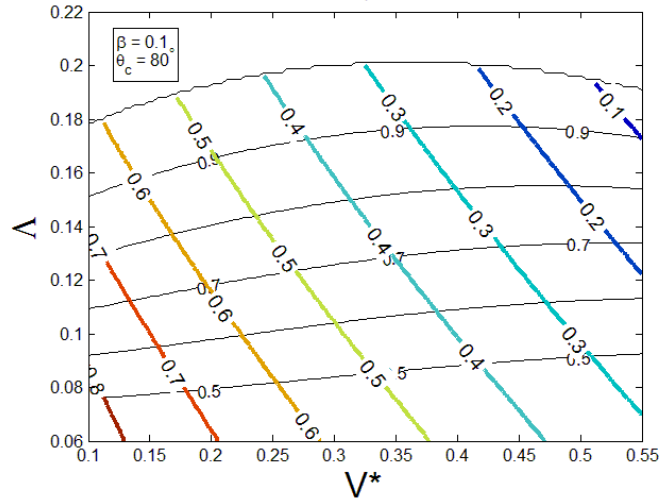


Figure 5.30: Contours for the base meniscus location (x_1^*). The contours are plotted with varying Δ and V^* . The other two governing parameters are fixed at $\theta_c = 80^\circ$ and $\beta = 0.1$.

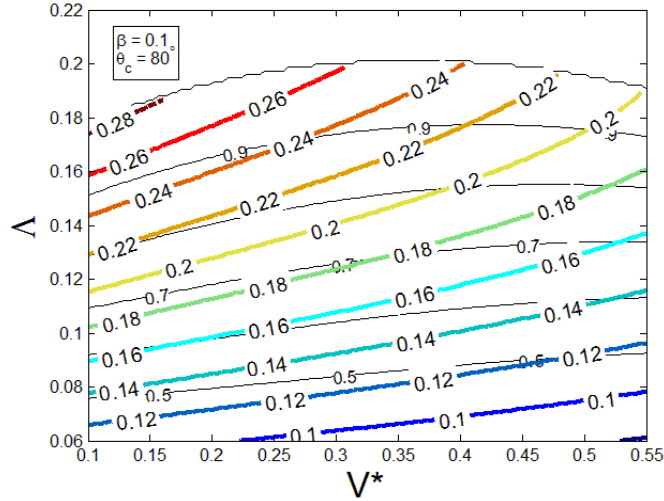


Figure 5.31: Contours for the moment about base due to surface tension forces (M_{ST}^*). The contours are plotted with varying Λ and V^* . The other two governing parameters are fixed at $\theta_c = 80^\circ$ and $\beta = 0.1$.

Contours of the Laplace pressure force acting on the beam, $F_p^* = -\Lambda(1 - x_1^*)/\alpha\beta$, are shown in Figure 5.32. Unlike the surface tension forces shown in Figure 5.26 which depended primarily on Λ , there is significant variation in F_p^* with V^* . In addition, the similarity in contour patterns between Figure 5.30 and Figure 5.32 indicates that there is a strong correlation between F_p^* and x_1^* . This is due to the fact that x_1^* directly influences the area the Laplace pressure acts over. For large V^* , x_1^* is small and the pressure acts over a larger area, which is consistent with the maximum F_p^* values occurring in the top right corner of Figure 5.32. Of course $|\alpha|$ also plays a role. In the high contact angle regime α is driven primarily by ϕ_1 . At low V^* , the increase in ϕ_1 with increasing Λ causes an increase in $|\alpha|$ which partially counteracts the increase in F_p^* from Λ . Whereas at high V^* , near collapse ϕ_1 was observed to decrease as Λ increases, resulting in a decrease of $|\alpha|$ which contributes to the increase of F_p^* from Λ . Consequently, the increase of F_p^* with Λ is slower for small V^* and faster for

large V^* , which results in the F_p^* contours being tightly spaced for high V^* , in the top right corner of Figure 5.32. With knowledge of F_p^* (Figure 5.32) and x_1^* (Figure 5.30), it is easy to understand the contour plot of M_p^* shown in Figure 5.33, as the moment arm is merely $(x_1^* + 1)/2$. Clearly the patterns are similar to that of F_p^* . In particular, at large V^* , the combination of increased Laplace pressure area and increased Laplace pressure due to lower ϕ_1 cause larger drops to have larger M_p^* . Figure 5.33, explains why in Figure 5.23 it was observed that increasing drop size beyond $V^* = 0.4$ made collapse easier even though M_{ST}^* would be smaller. In summary at collapse M_{ST}^* is maximized at low V^* while M_p^* is maximized at high V^* . These maxima result in the collapse curve in Figure 5.23 bending downwards (towards lower Λ) at extreme values of V^* .

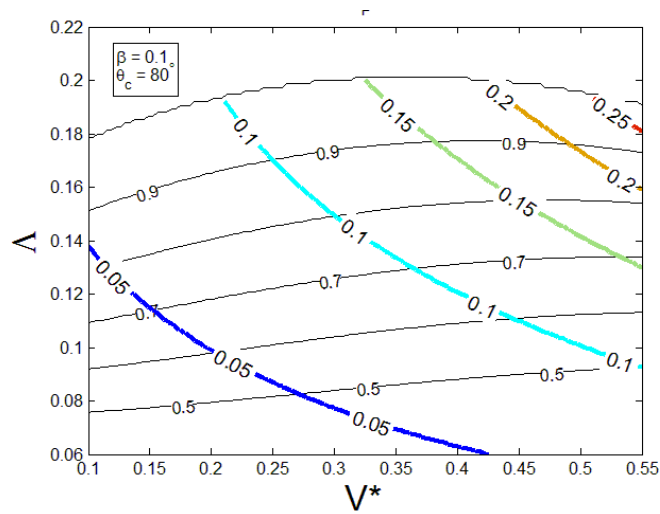


Figure 5.32: Contours for the force due to pressure (F_p^*). The contours are plotted with varying Λ and V^* . The other two governing parameters are fixed at $\theta_c = 80^\circ$ and $\beta = 0.1$.

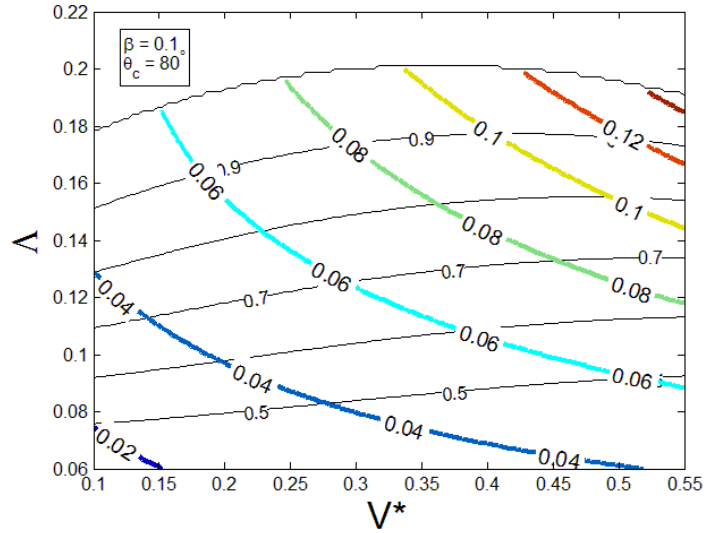


Figure 5.33: Contours for the Moment about base due to Laplace pressure (M_p^*). The contours are plotted with varying Δ and V^* . The other two governing parameters are fixed at $\theta_c = 80^\circ$ and $\beta = 0.1$.

To conclude, we summarize the important aspects of how the governing parameters influence collapse in the high contact angle regime. Unlike in the moderate contact regime, the nonlinear deflection coupling effects in the high contact angle regime are mainly controlled by ϕ_1 instead of w_1^* . Because of this, smaller drops have larger meniscus radius and smaller Laplace pressure. Surface tension forces were found to be a dominant contribution to collapse. This is especially true for small drops where not only is the Laplace pressure smaller but the moment arms for the surface tension forces are larger as well. Large M_{ST}^* for small drops and large M_p^* for large drops result in the collapse contour having a non-monotonic change with V^* : namely collapse is easiest for extremely large and extremely small drops.

5.5 Low Contact Angle

There are many combinations of liquids and solid surfaces that are perfectly wetting and belong to this regime. One common example would be water on glass for which the contact angle is close to 0° (see Table 4). Furthermore in many MEMS applications the contact angle of the rinse liquid is considered to be close to 0° [4], [6], [8]. For this reason we will use $\theta_c = 0^\circ$ in this section to demonstrate the typical characteristics of the low contact angle regime. Again we want to understand how the governing parameters influence collapse in this regime and the relative importance of the nonlinear deflection coupling effects. Based on Figure 5.5 and Eq. (5.9) decreasing θ_c tends to decrease $|\alpha|$ and thus increase the Laplace pressure. Furthermore, for small contact angles the surface tension force at the base meniscus acts nearly axially and gives a negligible contribution to beam deflection. However, the direction of the free end surface tension force changes from nearly axial before deformation to nearly transverse at collapse. So surface tension forces can still play a role and are highly coupled with the beam's deflection; this will be discussed in this section. Based on the discussion of Figure 5.5 and the governing equations in section 5.2.2, it was reasoned that for low contact angles the amount of liquid displaced by the menisci is more sensitive to changes in ϕ , which in turn can affect the location of the base meniscus. This will be another focus of the discussion in this section. These two features unique to the low contact angle regime have not been addressed in previous sections and it will be interesting to see the relative importance of these effects compared with those previously discussed.

5.5.1 General Low Contact Angle Collapse Behaviour

As always the analysis for collapse starts with looking at the free end deflection contours, shown in Figure 5.34. Surprisingly, despite the large difference in θ_c (0° vs. 45°), the pattern of these contours appears almost identical to that of Figure 5.14 for the moderate contact regime. This implies that the nonlinear deflection coupling effects discussed for the moderate contact angle regime also apply to the low contact angle regime. One subtle difference, the tighter contour spacing for small V^* in Figure 5.34 compared with Figure 5.14, can be explained by Eq. (5.9). For small contact angles the cosine function is less sensitive to changes in ϕ_1 so the nonlinear coupling of angles on the Laplace pressure, which opposed that of deflection, is dampened in the low contact angle regime. On the other hand, there are some quantitative differences between Figure 5.34 and Figure 5.14. The first difference is that for the same V^* collapse can be obtained at lower Λ in the low contact angle regime. This is due to the decrease of $|\alpha|$, and hence increase of the Laplace pressure, with lowering θ_c , as shown in Eq. (5.9). It is worth noting that the M_R^* required to cause collapse, shown in Figure 5.35, again appears to have the same value as the moderate contact angle regime (Figure 5.22). For example at $V^* = 0.2$, for the given β , $M_R^* \approx 0.35$ is required to cause the DCB to collapse in both Figure 5.22 and Figure 5.35.

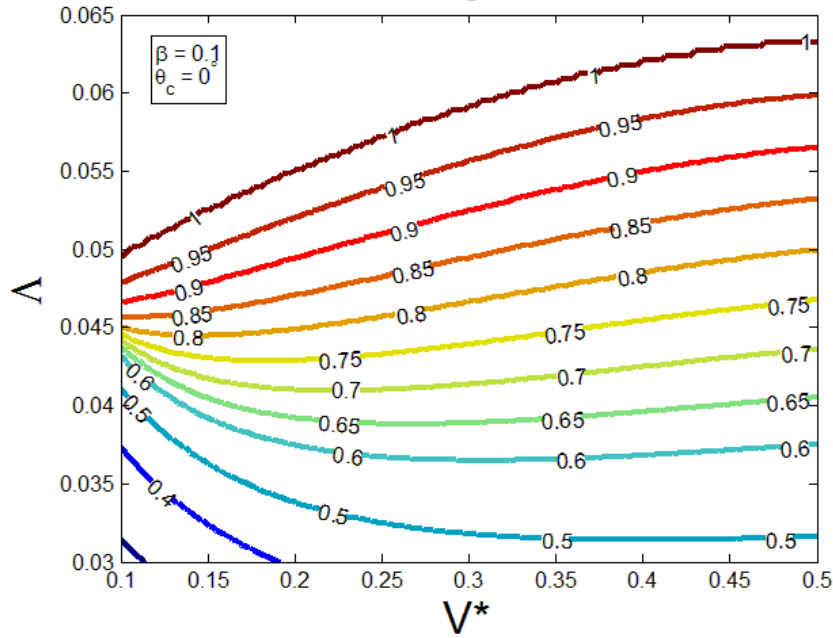


Figure 5.34: Contours for the free end deflection (w_2^*). The contours are plotted with varying Δ and V^* . The other two governing parameters are fixed at $\theta_c = 0^\circ$ and $\beta = 0.1$.

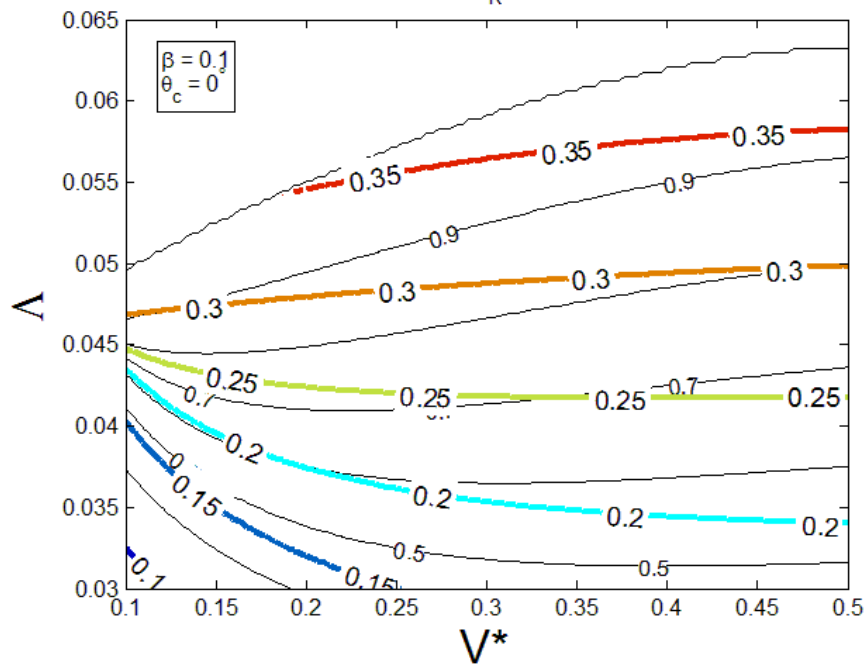


Figure 5.35: Contours for the Reaction moment (M_R^*). The contours are plotted with varying Δ and V^* . The other two governing parameters are fixed at $\theta_c = 0^\circ$ and $\beta = 0.1$.

5.5.2 Influence of Liquid Displaced by Menisci

Another quantitative difference between Figure 5.14 and Figure 5.34 is the range of V^* . The range can not be extended to $V^* = 0.55$ as it was in Figure 5.14 since it resulted in the base meniscus contacting the clamped end. This suggests that x_1^* in the low contact angle regime is smaller which can be confirmed by the low contact angle x_1^* contours shown in Figure 5.36. Compared with the moderate contact angle case (Figure 5.19), for a given w_2^* and V^* , x_1^* is lower in the low contact angle case. For example with $V^* = 0.3$ and at collapse, in the moderate contact angle case $x_1^* = 0.3$ while in the low contact angle case $x_1^* = 0.26$. This reduction in x_1^* results in larger acting area for the Laplace pressure and a relative decrease in Laplace pressure as described in section 5.3.1.

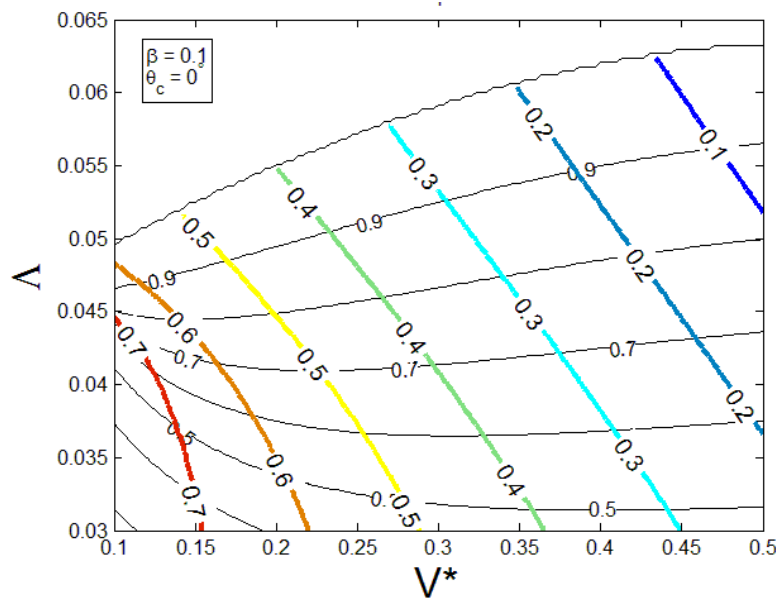


Figure 5.36: Contours for the base meniscus location (x_1^*). The contours are plotted with varying Δ and V^* . The other two governing parameters are fixed at $\theta_c = 0^\circ$ and $\beta = 0.1$.

In the preliminary discussion (Section 5.2) it was noted that in the low contact angle regime meniscus the displacement factors (MDF) would be larger.

Therefore, more liquid would be displaced by the menisci. The liquid volume displaced by the menisci is quantified by the dimensionless function MDISP. Specifically, the constant volume constraint (Eq. (5.5)) can be rearranged to give the following

$$x_1^* = 1 - V^* - \int_{x_1^*}^1 w^*(x^*) dx^* - \frac{\alpha^2 \beta}{2} \left(\cos^{-1}(l_1^*) - l_1^* \sqrt{1 - l_1^{*2}} \right) \quad (5.11)$$

where the integration represents the liquid displaced by the beams deflection and the last term represents MDISP. In the low β , moderate contact angle case, it has been shown that MDISP is considerably smaller than the liquid displaced by the beam's deflection, and therefore has negligible effect on the determination of x_1^* . Although $|\alpha|$ is larger in the moderate and high contact angle regimes, MDF is much smaller in these regimes, causing MDISP to have less impact on x_1^* than in the low contact angle regime. With a higher value of β and the contact angle closer to 0° MDISP has maximum impact on x_1^* . This impact can be seen in Figure 5.37, which shows the fraction MDISP contributes to the total liquid displaced (sum of last two terms in Eq. (5.11)). At collapse MDISP contributes to 10-20% of the liquid displaced; this contribution is larger for larger V^* because these drops will have a larger $|\alpha|$. Although the dominant influence on x_1^* is still due to liquid displaced by deflection MDISP is no longer negligible. This can also be seen in Figure 5.38, which plots the ratio of MDISP to the total liquid volume V^* . At collapse MDISP represents 15-25% of V^* . Based on Eq. (5.11), neglecting the liquid displaced by meniscus curvature as in [3], [9], results in a significant discrepancy in predicting x_1^* .

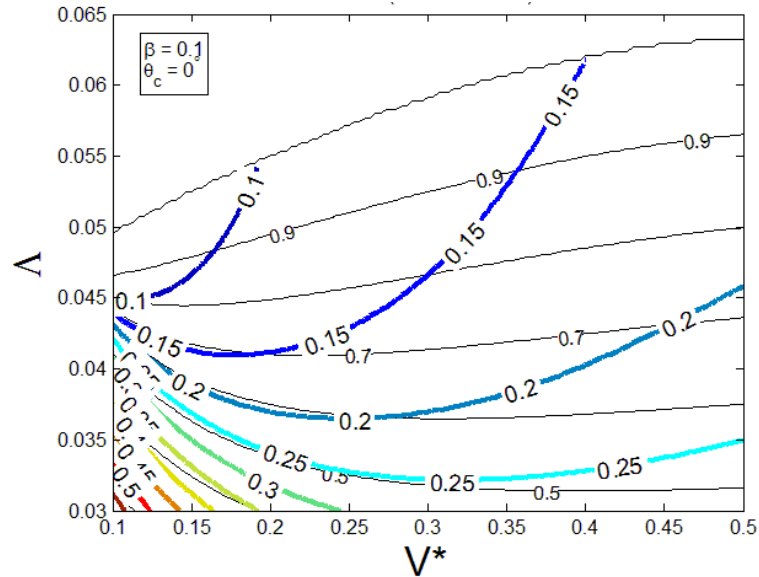


Figure 5.37: Contours for fraction of displaced liquid due to meniscus curvature. The contours are plotted with varying Δ and V^* . The other two governing parameters are fixed at $\theta_c = 0^\circ$ and $\beta = 0.1$.

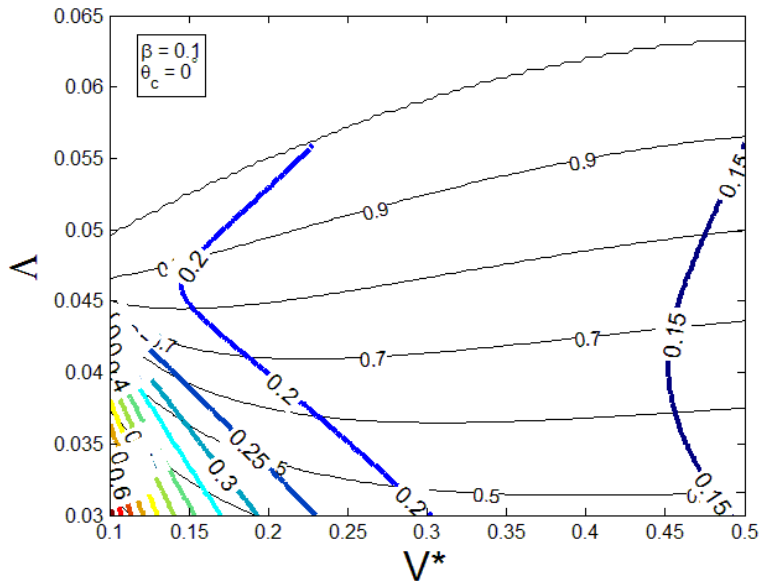


Figure 5.38: Contours for ratio of displaced liquid due to meniscus curvature to drop volume (MDISP/ V^*). The contours are plotted with varying Δ and V^* . The other two governing parameters are fixed at $\theta_c = 0^\circ$ and $\beta = 0.1$.

Changes in MDISP due to nonlinear deflection coupling may also impact x_1^* . This effect can be seen in Figure 5.39 which shows changes in x_1^* , MDISP, and the liquid displaced by the beams' deflection for $V^* = 0.1$ and $V^* = 0.5$ as

deflection is increased to collapse. In each case at small deflections there is a drop in MDISP which actually creates a slight increase in x_1^* . However, by the time deflection nears collapse MDISP levels off (to a different value depending on V^*) and changes in x_1^* are determined primarily by $\int_{x_1^*}^{x_2^*=1} w^*(x^*) dx^*$ which increases steadily for all levels of deflection. Although, the changes in MDISP from nonlinear deflection coupling can lead to some interesting behaviour these changes level off and are not important for deflections near collapse. Furthermore, the coupled behaviour is complicated so a discussion of what drives these changes in MDISP would detract from the objective of this section: collapse. Hence interested readers are directed to Appendix D for more detailed discussion.

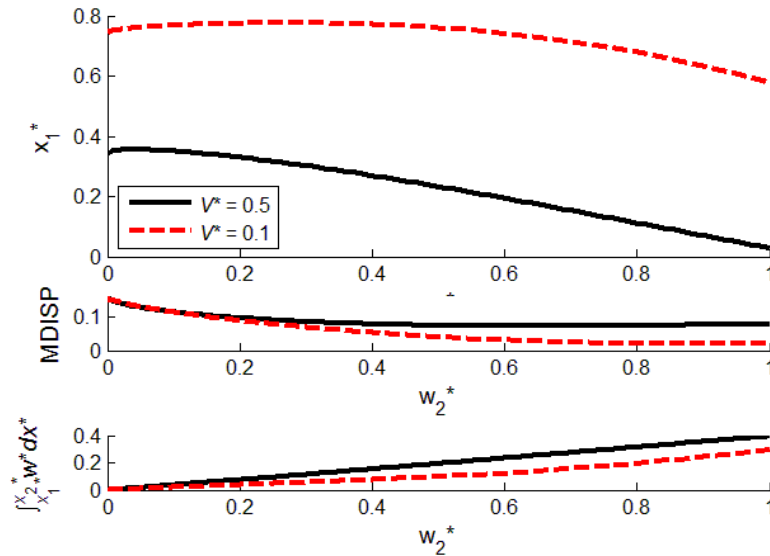


Figure 5.39: Changes in x_1^* , MDISP, and liquid displaced by DCB deflection with increases in free end deflection (w_2^*) for $V^* = 0.1$ and $V^* = 0.5$. Λ is increased to create the increase in w_2^* . The other two governing parameters are fixed at $\beta = 0.1$ and $\theta_c = 0^\circ$.

To conclude, in the low contact regime, MDISP is significant. It causes x_1^* to be smaller than in the moderate/high θ_c regimes. This has the combined effect of increasing the Laplace pressure area and creating a relative decrease in Laplace

pressure. In other words, MDISP influences the Λ -dependence of the collapse condition. However, this effect is not able to significantly change the V^* -dependence of the collapse behaviour and the qualitative characteristic of the collapse contour is similar to that the moderate θ_c case.

5.5.3 Role of surface tension forces at low θ_c

At low θ_c the surface tension force at the base meniscus acts axially and makes a negligible contribution to the moment M_{ST}^* . However, the surface tension force at the free end meniscus behaves differently. Before deflection this force also acts axially, however θ_2 increases with deflection causing this force to shift from axial to transverse as the beam deflects. The contours for M_{ST}^* are shown in Figure 5.40. These contours are nearly horizontal for high deflections, indicating dependence of M_{ST}^* only on Λ near collapse. Overall, at any V^* , there is a dependence of M_{ST}^* on the deflection, which is caused by the transition of the surface tension force at the free end meniscus from axial to transverse; this dependency is stronger at lower deflections. To see whether M_{ST}^* contributes significantly to the beams collapse it is necessary to compare its magnitude with that of the moment caused by the Laplace pressure, M_p^* .

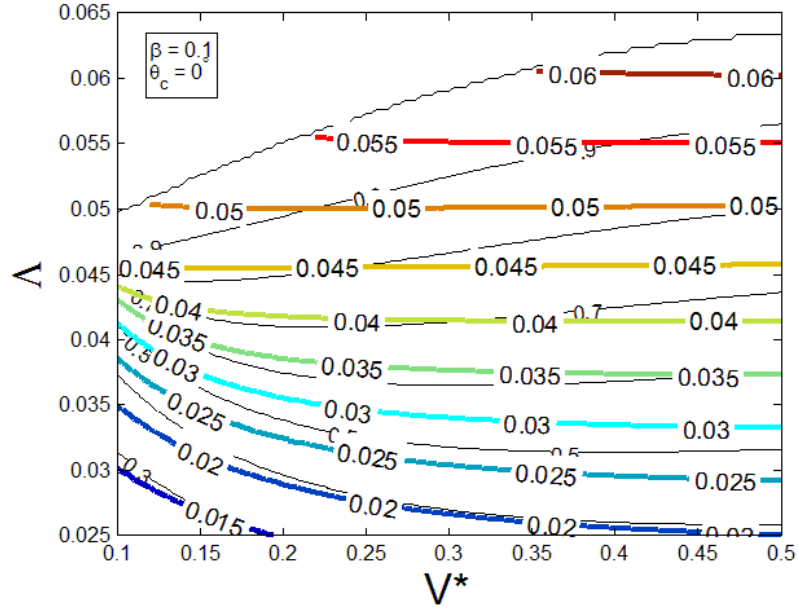


Figure 5.40: Contours for the Moment about base due to surface tension forces (M_{ST}^*). The contours are plotted with varying Λ and V^* . The other two governing parameters are fixed at $\theta_c = 0^\circ$ and $\beta = 0.1$.

The moment caused by the Laplace pressure, M_p^* , is shown in Figure 5.41. In this figure at low deflections M_p^* is clearly higher for larger drops, which is due to the larger area on which the pressure acts. However, for smaller V^* the contours are more tightly spaced, indicating that M_p^* rises much more rapidly with increasing Λ for smaller drops. This behaviour is due to nonlinear coupling between Laplace pressure and deflection as explained in section 5.3.1. For V^* at larger deflections, there is less nonlinear coupling and the contours become nearly horizontal, indicating that M_p^* depends primarily on Λ . To compare the relative significance of M_{ST}^* and M_p^* , contours of the fraction of the moment caused by surface tension forces are shown in Figure 5.42. Each corner of this figure appears to display a different behaviour. In the lower portion of the figure, M_{ST}^* / M_R^* increases with deflection because in this region M_{ST}^* increases both due to Λ and

nonlinear deflection coupling (surface tension force at free end changes direction with deflection). However for small V^* the M_p^* contours, Figure 5.41, become tightly spaced for $w_2^* > 0.5$, indicating a sharp increase in M_p^* with deflection. Because the magnitude of M_p^* is much greater than that of M_{ST}^* , this increase in M_p^* causes M_{ST}^* / M_R^* to begin to decrease with increasing deflection after passing $w_2^* = 0.5$, even though M_{ST}^* continues to increase. In the upper portion of the plot there is a different pattern. For larger V^* both M_{ST}^* and M_p^* have become primarily proportional to Λ ; therefore, in the top right corner the contours spacing is large which indicates only small changes in M_{ST}^* / M_R^* with deflection. For smaller V^* at high deflections M_p^* continues to increase with deflection at a faster rate compared with M_{ST}^* , resulting in the further decrease in M_{ST}^* / M_R^* . In the case of $\theta_c = 0^\circ$ because the base meniscus generates no moment, at collapse M_{ST}^* / M_R^* is actually higher for the larger drop; this contrasts the behaviour that was seen in the moderate and high contact angle cases. From Figure 5.42 at collapse M_{ST}^* contributes about 16% of the total moment, which is a much smaller percentage than in the moderate or high contact angle regimes. Furthermore, at collapse the variation in M_{ST}^* / M_R^* with V^* is less than 2%, so M_{ST}^* does not contribute to the V^* collapse dependency. However, M_{ST}^* has still a non-negligible contribution to the Λ -dependence of the collapse condition.

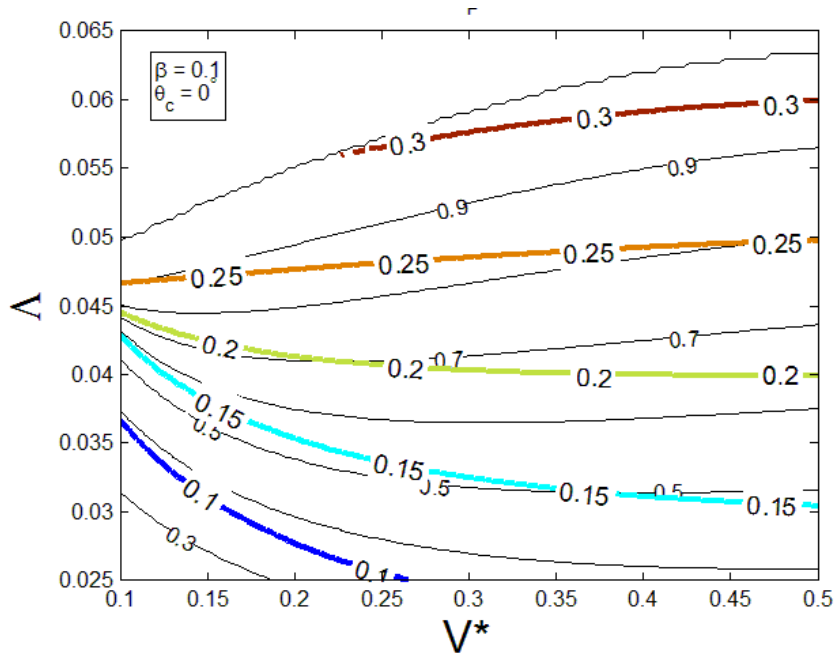


Figure 5.41: Contours for the moment about base due to pressure forces (M_p^*). The contours are plotted with varying Δ and V^* . The other two governing parameters are fixed at $\theta_c = 0^\circ$ and $\beta = 0.1$.

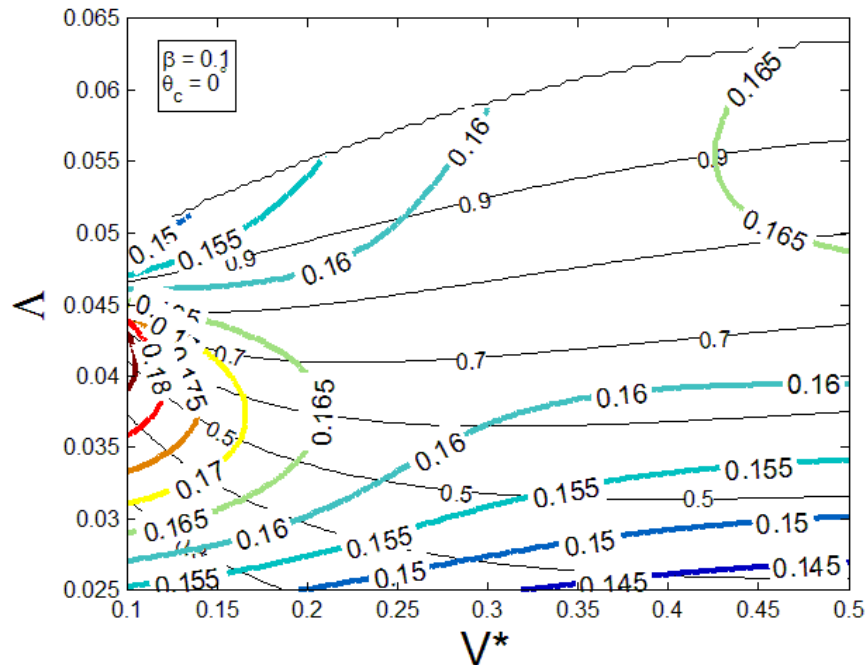


Figure 5.42: Contours for the fraction of reaction moment due to the surface tension forces. The contours are plotted with varying Δ and V^* . The other two governing parameters are fixed at $\theta_c = 0^\circ$ and $\beta = 0.1$.

With the discussions on low contact angle regime completed we seek to summarize the important findings as they pertain to understanding how the governing parameters influence collapse and the relative importance of the nonlinear deflection coupling effects. Qualitatively, the characteristics in the low contact angle regime mimic what has been obtained for the moderate contact angle regime. However, the much smaller contact angle results in larger Laplace pressure as well as larger area of its action. Because of this, for the same liquid volume and DCB spacing, liquid with smaller contact angle is found to be able to collapse the DCB at smaller Λ . Due to the nonlinear deflection coupling effects, as the beam deflects, the surface tension force at the free end shifts its direction from axial to transverse, and hence the moment due to the surface tension forces still constitutes a non-negligible part of the total moment. The liquid volume displaced by the menisci in the low contact angle regime is significant and contributes to the base meniscus position being closer to the clamped end.

5.6 Discontinuity in Deflection Contours at Low V^*

In previous sections the free end deflection contours, for example in Figure 5.6, were observed to converge for very small V^* . This decrease in contour spacing was attributed to the rapid increase of M_p^* with the beam's deflection due to nonlinear coupling. It is desirable to look more closely at the region of converging contours because closely spaced contours imply that large changes in deflection can occur for small changes in a governing parameter (Λ here). This type of solution behaviour is unstable numerically in that small numerical errors can cause large changes in the solution. Figure 5.43 shows the free end deflection

contours from Figure 5.6, zoomed in on the region of converging contours. This figure reveals some surprising behaviour: not only do the contours converge but there is also a discontinuity in free end deflection across which the behaviour of the contours completely changes. Within this narrow band of free end deflection discontinuity (dark black “line”) the solution will not converge numerically. Furthermore, across the discontinuity there are drastic changes in the solutions behaviour which can be seen more clearly in a plot of free end deflection w_2^* vs. Λ , shown in Figure 5.44 for $V^* = 0.1$. Here w_2^* first increases as Λ is increased, but begins to increase more rapidly as the discontinuity is approached, which is located at about $w_2^* = 0.6$ or $\Lambda \approx 4.57 \times 10^{-3}$. This is followed by a very small window of Λ ($\Lambda \approx 4.57 \times 10^{-3} - 4.58 \times 10^{-3}$) where a converged solution cannot be obtained numerically. If Λ is increased slightly more to about $\Lambda \approx 4.58 \times 10^{-3}$ a convergent solution can be obtained with $w_2^* = 0.9$. In the region after the discontinuity the behaviour changes as the concavity of the curve is now negative. Note that the range of Λ for which converging numerical solutions do not exist ($\Lambda \approx 4.57 \times 10^{-3} - 4.58 \times 10^{-3}$) is very small. According to the definition $\Lambda = \gamma_{LA} L^2 D / EI$, if $\Lambda = 4.58 \times 10^{-3}$ corresponds to a beam with thickness of 200 nm as in Kotera et al [6], then $\Lambda = 4.57 \times 10^{-3}$ corresponds to a beam with thickness of 200.15 nm. That is, these two beams differ by at most one layer of atoms. In other words, physically, the values of $\Lambda = 4.57 \times 10^{-3}$ and $\Lambda = 4.58 \times 10^{-3}$ are indistinguishable and should be treated as one point. The

discontinuity separates the solution into two regimes and suggests the existence of two equilibrium configurations, one with a much larger deflection.

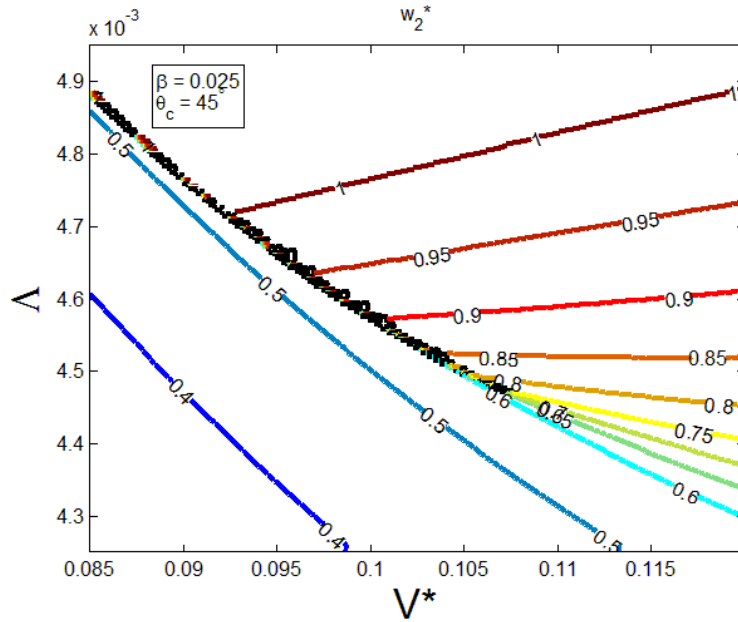


Figure 5.43: Contours for the free end deflection (w_2^*) focusing on a discontinuity. The contours are plotted with varying Λ and V^* . The other two governing parameters are fixed at $\theta_c = 45^\circ$ and $\beta = 0.025$. Generated by increasing Λ

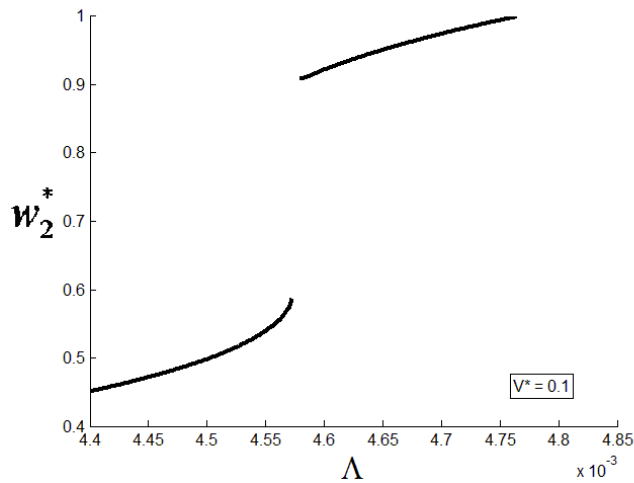


Figure 5.44: Changes in free end deflection w_2^* , with increases in Λ for $V^* = 0.1$. The other two governing parameters are fixed at $\beta = 0.025$ and $\theta_c = 45^\circ$.

To visualize such a jump in w_2^* , consider deflected beams from either side of the discontinuity, shown in Figure 5.45. For at $\Lambda = 0.0046$ the discontinuity is approximately at $V^* = 0.1$. The dashed red curve ($V^* = 0.975$) is from the left side

of the discontinuity and the solid black curve ($V^* = 0.1025$) is from the right side of the discontinuity. Ordinarily for such a small difference in V^* it would be expected that these two curves would be nearly coincidental. However, because of the discontinuity the deflection of the solid black curve is much higher. As a result for the solid black curve more liquid is displaced by beam deflection and the base meniscus (blue solid lines) is closer to the clamped end. In other words, associated with the jump in w_2^* , there is a jump in x_1^* . In fact, as shown in Figure 5.46, the jump increase in w_2^* also results in a simultaneous jump increase in w_1^* and a jump decrease in $|\alpha|$ which causes a jump increase in M_p^* . This increase in M_p^* counteracts the increase in the restoring force from the beam as a result of the jump increase in deflection, and the beam is able to reach a new equilibrium configuration with the jump. This explains why the discontinuity in the w_2^* contours is only observed for small V^* , since for large V^* if a jump increase in w_2^* occurred, it would push the base meniscus so close to the base that w_1^* would decrease instead of increasing; as a result $|\alpha|$ would increase and the Laplace pressure would decrease, making it impossible to counteract the increased restoring force and reach a new equilibrium configuration.

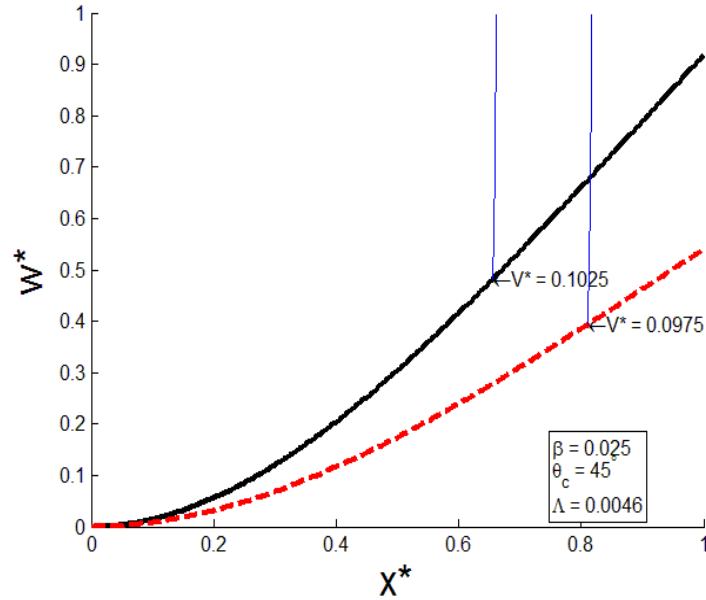


Figure 5.45: Elastic curve and meniscus location for $V^* = 0.0975$ and $V^* = 0.1025$ (on either side of discontinuity). The other three governing parameters are fixed at $\beta = 0.025$, $\Lambda = 0.0046$, $\theta_c = 45^\circ$.

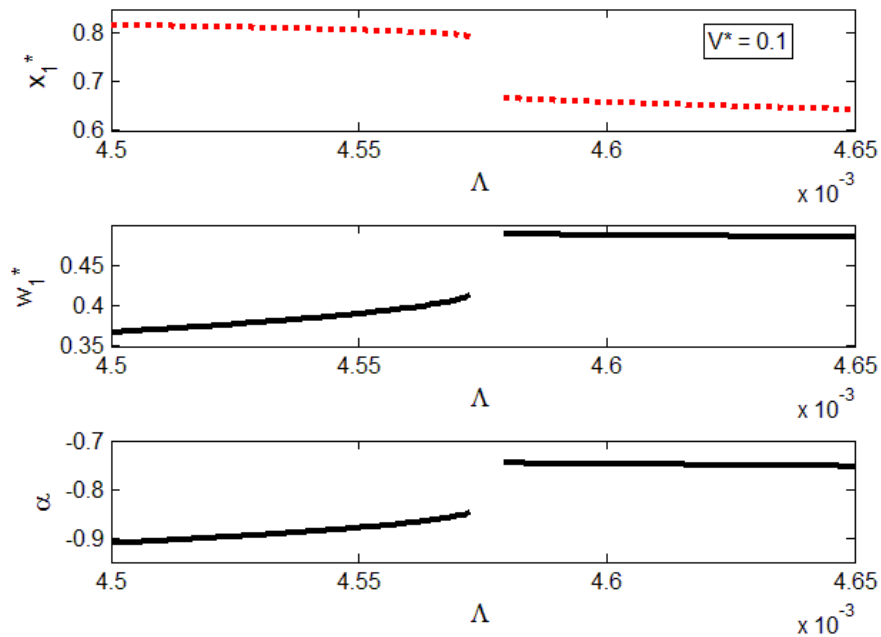


Figure 5.46: Changes in x_1^* , w_1^* , α with increases in Λ for $V^* = 0.1$ (showing discontinuity). The other two governing parameters are fixed at $\beta = 0.025$ and $\theta_c = 45^\circ$.

One may also consider the jump from an energy perspective. Energy has been given minimal attention in previous discussions since the governing

equations were derived from equilibrium rather than from the principle of minimum potential energy. If we consider the system that consists of the beams and the droplet then the total potential energy consists of the elastic strain energy of each beam, and the surface energy of the solid-gas, solid-liquid and liquid-gas interfaces. For this system there are no external forces, and hence no work of external forces. The potential energy is given by the sum of Eq. (3.42) and Eq. (3.49). The system is at equilibrium when its potential energy is at a minimum. The beams deflect because it decreases the liquid-air, and solid-air interfaces while increasing the solid-liquid interface; for the case of wetting liquid ($\theta_c < 90^\circ$) this results in lower surface energy. However, as the beams deflect their elastic strain energy also increases and competes with the reduction in surface energy. These energies for given values of V^* , β and θ_c are plotted against Λ in Figure 5.47. The dotted red curve is the strain energy, the dashed blue curve is the surface energy, and the solid black curve is the total potential energy. The reference values for these energies are from the undeflected configuration. In this figure the jump decrease in the surface energy is nearly equal to the jump increase in the strain energy and the total potential energy is nearly continuous across the jump in deflection.

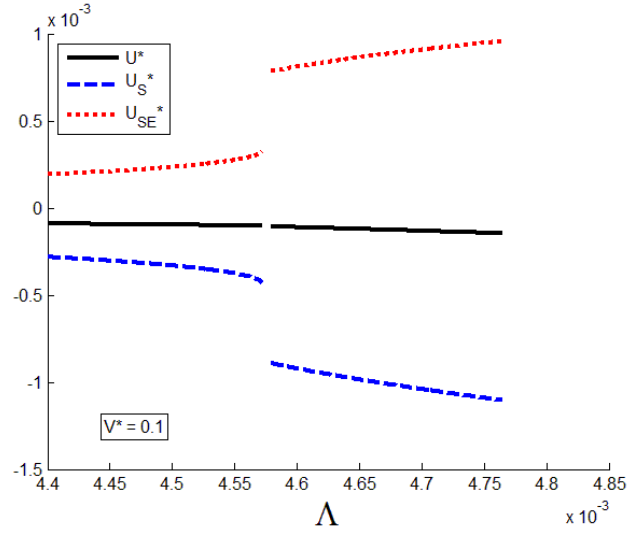


Figure 5.47: Changes in total potential energy, surface energy, and strain energy of DCB system, with increases in Λ for $V^* = 0.1$. The other two governing parameters are fixed at $\beta = 0.025$ and $\theta_c = 45^\circ$.

A similar jump in deflection was seen in Figure 2.5 c) and d), for the spring plate system where as the liquid volume decreased a local energy minimum appeared and eventually there was a discontinuous transition to this minimum. A similar branching diagram analysis exists in the literature for a doubly clamped beam [3]. The result of this analysis is the elastocapillary number N_{EC} which predicts that when the volume of the liquid tends to zero collapse will occur if $N_{EC} < 1$. For $N_{EC} = 1$, a discontinuous decrease in deflection as liquid dries is predicted [3], which prevents collapse. N_{EC} for a cantilever over a substrate was presented without formulation by Mastrangelo *et al* [3]. Here, to look at jump discontinuities that occur for a DCB, we adopted the same idea and carried out an energy formulation to obtain N_{EC} for a DCB, details shown in Appendix E. This analysis was simplified from the formulations in Chapter 3 and Chapter 4 by neglecting MDISP, surface tension forces and the influence of beam slopes on the Laplace pressure. These simplifying assumptions were shown in section 5.3.1 to

be reasonable in the low and moderate contact angle regimes when $\beta \ll 1$ which is the case demonstrated here. For comparison the governing equations for the simplified model are presented below:

Dimensionless ODE relating moment and curvature:

$$\beta \frac{d^2 w^*}{dx^{*2}} = M^* = -\Lambda \frac{\langle x^* - x_1^* \rangle^2}{2\alpha\beta} - Q_R^* x^* + M_R^*. \quad (5.12)$$

Dimensionless shear force and moment at the clamped end:

$$\begin{aligned} Q_R^* &= -\Lambda(x_2^* - x_1^*)/\alpha\beta, \\ M_R^* &= M_P^* = -\Lambda(x_2^{*2} - x_1^{*2})/2\alpha\beta. \end{aligned} \quad (5.13)$$

Constant liquid volume constraint:

$$V^* = \int_{x_1^*}^{x_2^*} (1 - w^*(x^*)) dx^*. \quad (5.14)$$

Normalized meniscus radius:

$$\alpha = \frac{w_1^* - 1}{\cos(\theta_c)}. \quad (5.15)$$

Furthermore, the branching diagram analysis follows the energy approach of Mastrangelo *et al.* for the doubly clamped beam [3] where the governing equations are approximately solved by assuming a 4th order polynomial test function to represent the deflection and using the Ritz method. From Appendix E the associated branching diagrams for three values of the elastocapillary number $N_{EC} = 5.504\beta^2/\Lambda\cos(\theta_c)$ are shown in Figure 5.48. The detailed branching analysis for a quasi-static evaporation process of the liquid is presented in Appendix E, similar to what is done for the spring-plate-liquid system presented in section 2.1.4. There is an important difference between the DCB solution in Figure 5.48 and the spring plate solution in Figure 2.5, namely that there are two equilibrium solutions in Figure 5.48 (represented by solid black line and dash-dot line in Figure 5.48 a) c) e)); although neither gives physical results for the entire range of V^* .

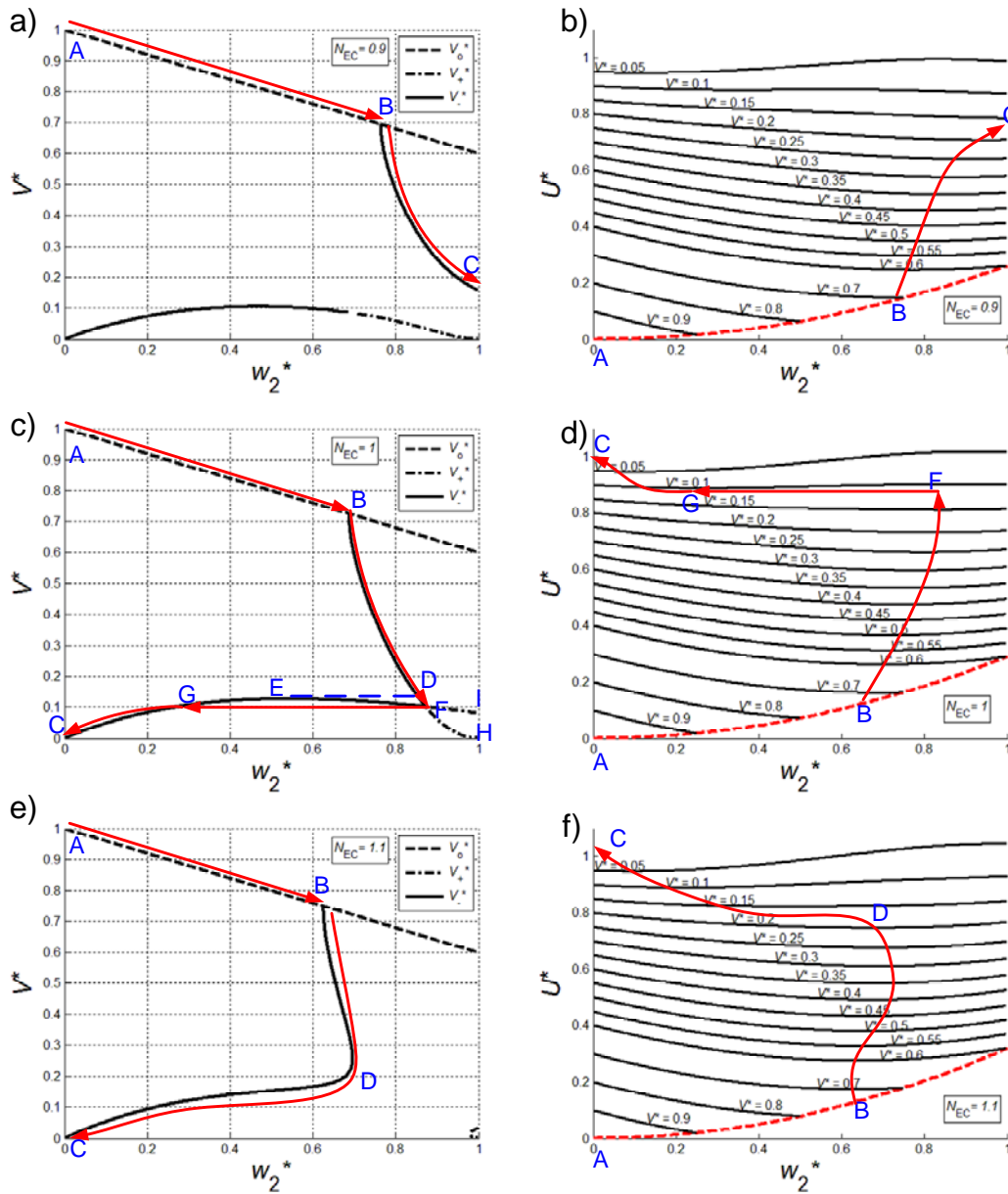


Figure 5.48: Branching (a,c,e) and energy (b,d,f) diagrams of DCB for different values of the elastocapillary number. Arrows indicate the path that the DCB would follow as a drop with initial volume of $V^* = 1$ is evaporated.

Although generated from a simplified model using an approximate energy approach, Figure 5.48 can be used to demonstrate the occurrence of the jump discontinuity observed in Figure 5.43. Clear from Figure 5.48 c), d) is the existence of multiple solutions for any given $V^* < 0.14$. Here curves EGC and

DFI represent energy minima separated by an energy maxima curve EFH. Curve BD also represents an energy minimum however, for these drop sizes the solution is unique. Furthermore the behaviour of the two energy minimizing solution curves EGC and BDFI corresponds to what was seen on the two sides of the discontinuity in Figure 5.43. In the bottom left of Figure 5.43 the deflection increases with increasing V^* as in curve EGC; in the top right of Figure 5.43 the deflection decreases with increasing V^* as in curve BDFI. Note that in Appendix E it was shown that when $N_{EC} = 1$, the energy maximum curve EF and the energy minimum curve BDF intersect at point F. That is, at F, the energy maximum and hence the energy barrier disappears, which leads to the jump discontinuity from point F to point G as V^* decreases. Here in curve HFDB, HF is an energy maximum and FDB is an energy minimum. Similarly for curve EFI, EF is an energy maximum and FI is an energy minimum. The existence of multiple closely spaced energy maxima and minima makes the energy contours shown in Figure 5.48 b) and d) very flat for drop sizes that result in multiple solutions which explains why energy appeared to be nearly continuous across the jump in Figure 5.47. Interestingly at point F, the deflection at the left meniscus is $w_1^* = 0.5$, which is close to the w_1^* for one of the equilibrium configurations seen in Figure 5.45, and Figure 5.46.

Now that we have seen considerable similarities between the branching diagrams of the simplified model and the behaviours seen in the full model we can use the branching diagrams to explain the jump discontinuity. Let us choose $V^* = 0.1$ and read the contour plot (Figure 5.43) as Λ is increased. First note that

unlike decreasing V^* in the quasi-static evaporation process (Appendix E), increasing Λ corresponds to decreasing N_{EC} , not movement on any of the branching diagrams in Figure 5.48. Before the jump we have $N_{EC} > 1$ and the DCB would be represented by the point associated with $V^* = 0.1$ on line CD in Figure 5.48e) which represents an equilibrium configuration with low w_2^* . In the bottom right corner of Figure 5.48e) there is another high deflection equilibrium solution at a local energy minimum. This energy minimum is separated from the low deflection energy minimum by an energy barrier (maxima also in bottom right corner). As N_{EC} gets closer to 1 (not shown) the higher deflection minima and maxima branch grows to exist at higher V^* and moves closer to the lower deflection curve. When $N_{EC} = 1$, Figure 5.48c), the high deflection energy minima and maxima coalesce to form an inflection point (point F); however, the low deflection minimum (point G) still exists, so the momentary disappearance of the energy maxima at $N_{EC} = 1$ cannot cause jump from point G to F in Figure 5.48c) analogous to the jump observed with increasing Λ in the free end deflection contours (Figure 5.43). In addition the $N_{EC} = 1$ jump described in the literature occurred only at one drop size (V^*) whereas in Figure 5.43 the jump is observed for a range of drops sizes and Λ (hence N_{EC}). Thus, the $N_{EC} = 1$ jump explanation presented by Mastrangelo *et al* [3] cannot explain the behaviour seen in Figure 5.43, however it has placed us on the right track as the behaviour can be explained by more closely studying how the branching diagrams evolve as N_{EC} is changed.

Shown in Figure 5.49 are branching diagrams for two intermediate N_{EC} not shown in Figure 5.48. As N_{EC} is decreased from Figure 5.48 e) a maxima forms in

line CDB which is shown by point E in Figure 5.49a) for $N_{EC} = 1.005$. This maximum leads to the creation of multiple solutions separated by an energy barrier for a small range of V^* (between parallel dashed lines $V^* = 0.1-0.13$). In Figure 5.48e) the entire curve BDC is an energy minimum, however in Figure 5.49a) curve BDF is a minimum, FE is a maximum and EGC is a minimum.

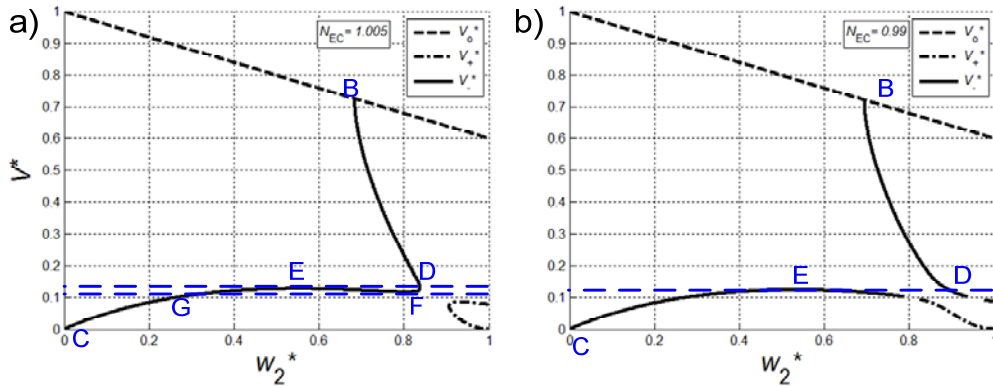


Figure 5.49: DCB branching diagrams for different values of the elastocapillary number.

Now use Figure 5.49 to see how changes in these curves with N_{EC} , can lead to the discontinuity observed when Λ is increased, by observing the position of point E as we increase Λ and move from Figure 5.49a), to Figure 5.48c), to Figure 5.49b) and finally to Figure 5.48a). Point E corresponds to the largest V^* for which the low deflection solution exists. As N_{EC} is decreased (with increasing Λ), point E moves to lower V^* ; this trend is subtle and most easily seen by comparing Figure 5.49b) to Figure 5.48a) where point E occurs at $V^* = 0.13$ and $V^* = 0.1$ respectively. Start with Figure 5.49a) and increase Λ to cause reduction in N_{EC} . Equilibrium for small drops would initially be on curve CE in Figure 5.49a). However as previously described, as we increase Λ point E moves to lower V^* resulting in a decrease in the maximum V^* for which the low deflection solution exists. As a result there is a jump and the system settles at the high deflection

equilibrium, point D in Figure 5.49b) (or equivalent figure), and proceeds to collapse when Λ is further increased. This is the behaviour seen in Figure 5.43 for $V^* > 0.0925$. For $V^* < 0.0925$, it can be seen from Figure 5.43 that the jump is directly associated with collapse of the DCB. This is because for such small V^* , once point E moves to a sufficiently low position, both the low deflection and high deflection solutions vanish for a range of V^* larger than point E, as demonstrated in Figure 5.48a) where there are no equilibrium solutions for V^* between points E and C ($V^* = 0.1 - 0.175$). The energy contours in Figure 5.48b) for these V^* (0.15 for example) slope down with increasing deflection. As a result the system proceeds to collapse directly from the low deflection solution. For smaller V^* , N_{EC} needs to be lower in order to cause the disappearance of the low deflection solution. This is why the value of Λ that corresponds to jump discontinuity (or direct collapse), shown in Figure 5.43, increases with decreasing V^* .

By demonstrating the existence of multiple solutions the branching diagram analysis illustrates the importance of the initial state on the equilibrium solution. It should be emphasized that Figure 5.43 was generated by increasing Λ and in the region of the discontinuity this figure can not be used to see how the solution would behave if Λ was instead decreased. Similarly to look at how the solution would behave due to increasing or decreasing V^* separate plots would again be needed. This point can be seen in Figure 5.50 where the contours were instead generated by decreasing V^* rather than increasing Λ as in Figure 5.43. Comparison of Figure 5.43 and Figure 5.50 clearly illustrates the existence of

multiple solutions for small drop sizes as within the discontinuity region different w_2^* are seen for fixed values of V^* and Λ . In each figure the initial condition is different in Figure 5.50 the initial state is the high deflection configuration whereas in Figure 5.43 the initial state is the low deflection configuration. Due to energy barriers the solution remains in its initial configuration until there is a reason for a jump to the other configuration to occur. Since the system of constraint equations is nonlinear the existence of multiple solutions is expected. However some of the solutions are not physical for example they may give $x_1^* < 0$ (the modified Newton-Raphson method described in Appendix A eliminates these possibilities). Compared with Figure 5.43 the slope of the band of discontinuity is different in Figure 5.50. In each case the cause of the discontinuity is different. Recall that in Figure 5.43 the jump is caused by the movement of point E (shown in Figure 5.49 b)) to lower V^* as Λ increases. To understand the discontinuity in Figure 5.50 consider the example of liquid drying in Figure 5.49c). As the liquid dries it follows curve BDF. However when V^* decreases below point F that equilibrium configuration ceases to exist and the solution will settle at the energy minimum point G. This transition represents a discontinuous jump in free end deflection from point F to G. Thus for decreasing V^* the system in Figure 5.48c) will follow path ABDFGC conversely if we considered increasing V^* in the same figure the system would follow CGEDBA (not CGFDAB). The result is for $V^* = 0.12$ we would have $w_2^* \approx 0.4$ for increasing V^* and $w_2^* \approx 0.9$ for decreasing V^* which is similar to the difference observed in Figure 5.43 and Figure 5.50 when the initial condition was changed. Furthermore, with decreasing $N_{EC} (> 1)$ point F

moves to lower V^* (not shown) causing the jump to occur at smaller V^* and larger Λ which is seen in Figure 5.50.

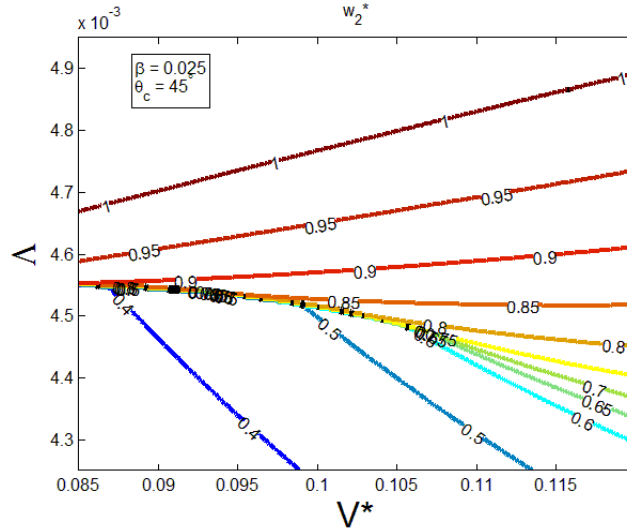


Figure 5.50: Contours for the free end deflection (w_2^*) focusing on a discontinuity. The contours are plotted with varying Λ and V^* . The other two governing parameters are fixed at $\theta_c = 45^\circ$ and $\beta = 0.025$. Generated by decreasing V^* .

Branching diagram analysis predicts jump at a small V^* for any combination of β and θ_c . However, due to the simplifying assumptions in the branching analysis the exact model does not always predict the presence of the jump. For example in the high contact angle regime it was observed that Laplace pressure decreased with deflection for small drops in which case it would be impossible for the jump to occur since there is no increase in the capillary force to compensate for the increased restoring force associated with the jump. Furthermore, as β was increased the low V^* contour spacing was observed to increase (Figure 5.14 vs. Figure 5.6); this behaviour was due to the competition between the effects of increases in w_1^* and ϕ_1 , which accompany deflection, on $|\alpha|$. The jump discontinuity is associated with converging contours so it will disappear as β is

increased. Increasing the contact angle and β both increase the degree of coupling between ϕ_1 and α . This coupling, not considered in the simplified branching diagram model, can prevent the occurrence of a jump. There are also quantitative differences between the jump predicted from the branching model and that observed from the exact model. Since the simplified model neglects MDISP, at a given Λ jumps were always observed at lower V^* than predicted by the branching model. Furthermore, at a given V^* , the jumps were always observed to occur for lower N_{EC} values than the branching model predicted. This can be most easily seen for the direct jump from the low deflection configuration to collapse (Figure 5.43, $V^* < 0.925$). Branching analysis only predicts this jump when $N_{EC} < 1$ ($\Lambda > 4.865 \times 10^{-3}$) however it was observed in Figure 5.43 for $N_{EC} > 1$. The reason for this discrepancy is the branching model neglects the surface tension force which increases DCB deflection allowing the jump to happen at higher N_{EC} (lower Λ).

5.7 Summary

In this chapter, by presenting the numerical solutions to the governing equations formulated in Chapter 3, we demonstrate how the governing parameters influence collapse and the role of nonlinear deflection coupling effects shown in Figure 5.5.

One of the most important nonlinear deflection coupling effects is the dependence of the Laplace pressure on w_1^* . This effect causes a significant increase in the Laplace pressure upon deflection, which enables smaller drops to

collapse the DCB more easily than larger V^* for small and moderate contact angles. The competing effect of ϕ_1 on the Laplace pressure, shown in Figure 5.5, comes into play at higher values of β . However, in the moderate and low contact angle regimes the effect of ϕ_1 is less important than that of w_1^* . In the high contact angle regime the opposite is true and ϕ_1 drives the deflection behaviour. In this regime, the collapse condition shows a non-monotonic variation with V^* ; the DCB is most easily collapsed by very small and very large drops.

Another important nonlinear deflection coupling effect is the deflection pushing the base meniscus closer to the base, thus decreasing x_1^* . This effect creates a relative decrease in both w_1^* and ϕ_1 which counteracts changes in the Laplace pressure. However, it increases the area the Laplace pressure acts on, and still contributes to the result that smaller drops collapse the DCB more easily in the low/moderate contact angle regimes. In addition for very large V^* , the final position of the base meniscus is so close to the base that it removes most of the nonlinear deflection coupling effects on the Laplace pressure. Changes in β , θ_c and ϕ_1 can also affect x_1^* through the liquid displaced by the meniscus (MDISP). Although the influence of MDISP on x_1^* is generally less than those of beam deflection and liquid volume it is of the same order of magnitude and should not be neglected.

The surface tension force, which has not been previously accounted for in the literature, was also found to contribute to collapse. Depending on the contact angle, the moment of the surface tension forces constitutes 15%-85% (from low to high contact angles) of the total moment on the beam, and should not be

neglected. Its influence for the high contact angle regime is especially important. Not only does it affect the load (Λ) needed to collapse the DCB, it also causes the collapse pattern (dependence of the collapse condition on V^*) to differ from the low/moderate contact angle regimes. In the low contact angle regime, as the beams deflect, the surface tension force at the free end shifts its direction from axial to transverse and has its maximum influence at collapse; however in this regime the solution is still largely driven by the Laplace pressure.

The governing parameter Λ has the most straight forward influence on the DCB deformation, in that higher Λ leads to higher DCB deflections. At a given V^* , higher values of Λ are needed to collapse DCBs with larger β and contact angles.

All the results so far are based on the linear beam formulation. The linear formulation allows us to obtain analytical expressions for the deflection and facilitates our understanding and interpretation of the numerical results. In the next chapter, the solutions for collapse based on the nonlinear formulation (Chapter 4) will be presented, which can be used to test the validity of the linear model. In addition, through the nonlinear model, a dimensionless number will be obtained which explicitly describes the condition for collapse in terms of the governing parameters.

Chapter 6 Results on Uncollapsed Configuration from Nonlinear Formulation

In this chapter, the results obtained from the nonlinear beam formulation (Chapter 4) pertaining to collapse are presented. Considerable discussion of the four governing parameters for the collapse of the DCB: β , θ_c , V^* , and Λ has been completed in Chapter 5. There are several objectives in this chapter: (1) to tie up any loose end in the discussion of the governing parameters; (2) to evaluate the need to use a beam model that accounts for geometric nonlinearity (3) to compare the findings of the model with results previously published in the literature; and (4) to obtain correlation equations describing the numerical results of the model.

6.1 Summary of Governing Equations

To look at the impact of geometric nonlinearity on the solution, the system of equations governing the deformation of the DCB is revisited below. As in Chapter 5 the discussion will be limited to negative α . The normalized equations from Chapter 4 pertinent to the discussion are listed below.

Dimensionless ODE relating moment and curvature:

$$\frac{d\phi}{ds^*} = M_R^* - Q_R^* x^* + M_{ST}^*(s^*) + M_P^*(s^*)$$

$$M_P^*(s^*) = \frac{-\Lambda}{2\alpha\beta} \left(\langle x^*(s^*) - x^*(s_1^*) \rangle^2 + \beta^2 \langle w^*(s^*) - w^*(s_1^*) \rangle^2 \right) \quad (6.1)$$

$$M_{ST}^*(s^*) = \Lambda \left(\sin(\phi(s_1^*) + \theta_c) \langle x^*(s^*) - x^*(s_1^*) \rangle - \beta \cos(\phi(s_1^*) + \theta_c) \langle w^*(s^*) - w^*(s_1^*) \rangle \right)$$

Dimensionless reaction moment and shear force at the clamped end:

$$Q_R^* = \Lambda \left[-\frac{1}{\alpha\beta} [x^*(1) - x^*(s_1^*)] + (\sin(\theta_c + \phi(s_1^*)) + \sin(\theta_2 - \phi(1))) \right]$$

$$M_R^* = M_P^* + M_{ST}^* \quad (6.2)$$

$$M_P^* = -\frac{\Lambda}{2\alpha\beta} \left(\beta^2 (w^*(1)^2 - w^*(s_1^*)^2) + (x^*(1)^2 - x^*(s_1^*)^2) \right)$$

$$M_{ST}^* = \Lambda(\sin(\theta_c + \phi(s_1^*))x^*(s_1^*) - \beta \cos(\theta_c + \phi(s_1^*))w^*(s_1^*)) \\ + \Lambda(\sin(\theta_2 - \phi(1))x^*(1) + \beta \cos(\theta_2 - \phi(1))w^*(1))$$

The shape of the deflected beam can be determined from :

$$\frac{dx^*}{ds^*} = \cos \phi \\ \frac{dw^*}{ds^*} = \frac{\sin \phi}{\beta} \quad (6.3)$$

Constant liquid volume constraint:

$$V^* = \int_{s_1^*}^{s_2^*=1} (1 - w^*(s^*)) \cos(\phi(s^*)) ds^* - \frac{\alpha^2 \beta}{2} \sum_{i=1}^2 \left[\cos^{-1}(l_i^*) - l_i^* \sqrt{1 - l_i^{*2}} \right] \quad (6.4)$$

The meniscus constraint equations from the linear case Eqs. (5.6), (5.7) and (5.8), continue to be valid.

6.2 Importance of nonlinear geometry

In the discussion of Chapter 5 considerable effort was spent addressing the nonlinear deflection coupling effects in the constraint equations. However, nonlinear geometrical effects in the beam equations were ignored which may seem contradictory. Therefore, it is desirable to solve the beam deformation using the nonlinear beam model coupled with the nonlinear constraint equations and compare the results with that of the linear model to gage the importance of the using a nonlinear beam model.

Again for collapse, the most important quantity is the free end deflection. Therefore the following function describing the difference between the free end deflection given by the linear and nonlinear models will be examined:

$$Discrepancy = \frac{\left| (w^*(s_2^*))_{nonlinear} - (w^*(s_2^*))_{linear} \right|}{(w^*(s_2^*))_{nonlinear}} \quad (6.5)$$

It was described in section 5.3.1 that if $\beta \rightarrow 0$ then $\phi \rightarrow 0$. In addition all of the nonlinear geometrical terms in the beam governing equations (6.1) and (6.2) are multiplied by β . So as $\beta \rightarrow 0$ the linear and nonlinear beam theories should coalesce. It would then be necessary to consider a range of β . In addition, based on Eqs. (6.1) and (6.2) the discrepancy may also depend on the magnitude of the deflection. Therefore to study the discrepancy Λ will be increased at each β to cause the deflection to increase till collapse. A plot of the discrepancy as a function of Λ and β is shown in Figure 6.1. Here the same contact angle ($\theta_c = 45^\circ$) from the moderate contact angle regime discussion (section 5.3) is used, and $V^* = 0.3$ is used since it is close to the middle of the V^* values discussed. In Figure 6.1, the free end deflection contours (thin solid black curves) are also shown to allow for comparison at constant values of w_2^* . For example following any line of constant w_2^* from $\beta = 0.025$ to $\beta = 0.25$ the magnitude of the discrepancy increases as was expected. Furthermore, if β is held fixed and the plot is read as Λ increases from 0.01 to 0.4 causing the deflection to increase towards collapse the discrepancy again increases. The most important information from Figure 6.1 is that the maximum discrepancy is only about 1% which occurs near collapse at $\beta = 0.25$. Furthermore, $\beta = 0.25$ is well above the maximum value ($\beta = 0.1$) deemed to be of practical importance for collapse [4]; at $\beta = 0.1$ the discrepancy is only about 0.3%. This suggests that for most engineering applications the linear theory is sufficient.

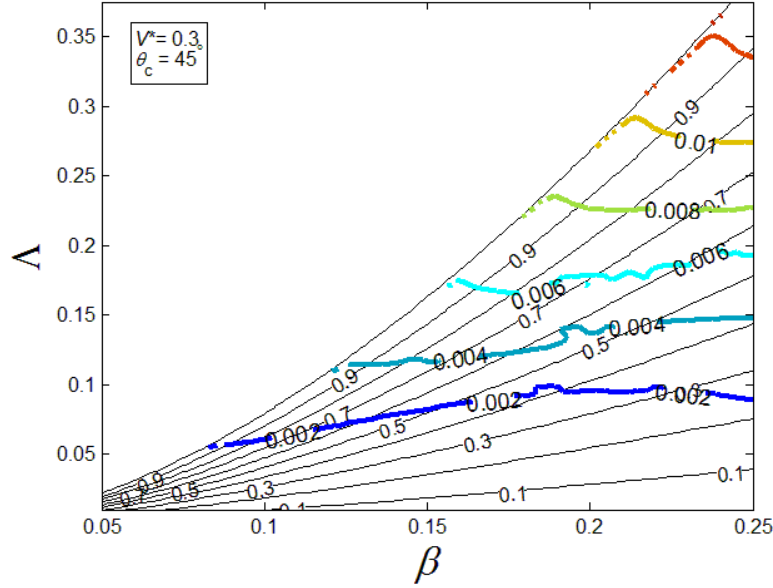


Figure 6.1: Contours for the discrepancy between linear and nonlinear beam theories. The contours are plotted with varying Λ and β . The other two governing parameters are fixed at $\theta_c = 45^\circ$ and $V^* = 0.3$.

Table 7: Maximum discrepancy between linear and nonlinear beam theories. For a range of θ_c and V^* . β is fixed at 0.1 to give maximum error.

	$V^* = 0.1$	$V^* = 0.3$	$V^* = 0.5$
$\theta_c = 2.5^\circ$	0.15%	0.30%	0.30%
$\theta_c = 45^\circ$	0.25%	0.30%	0.25%
$\theta_c = 80^\circ$	0.25%	0.18%	0.05%

6.3 Influence of β on collapse

In the linear discussion little consideration was given to the governing parameter β . In light of Section 6.2 this section may seem better placed within the linear discussion in Chapter 5 however the results of this section inspired an important analytical result Eq. (4.24) which is obtained from the nonlinear theory.

For the moderate contact angle regime, there were separate discussions for low β and high β showing how the increase in β results in increased influence of the deflection angles. From Figure 5.5 and Eq. (6.4) increasing β can also cause the liquid volume displaced by the menisci to increase, and potentially lead to a decrease in x_1^* . This was deemed to be a relatively unimportant effect when β was

increased from 0.025 to 0.1. To re-examine this point, shown in Figure 6.2 are the contours of x_1^* as a function of Λ and β . For the most part in this figure the x_1^* contours tend to follow the free end deflection contours, shown in black thin lines. This indicates that the influence of β on x_1^* is essentially through the deflection. The exception to this occurs at $\beta > 0.125$ and $w_2^* < 0.5$, where there is a drop in x_1^* with increasing β . However, for $w_2^* > 0.5$, the liquid volume displaced by the beam deflection, first term on RHS of Eq. (6.4), overpowers the effect of β on x_1^* , resulting in the x_1^* contours nearly following the w_2^* contours. Since our interest is primarily in predicting collapse for $\beta < 0.1$, the effect of β on x_1^* through the liquid volume displaced by the menisci is not as significant as liquid displaced by beam deflection.

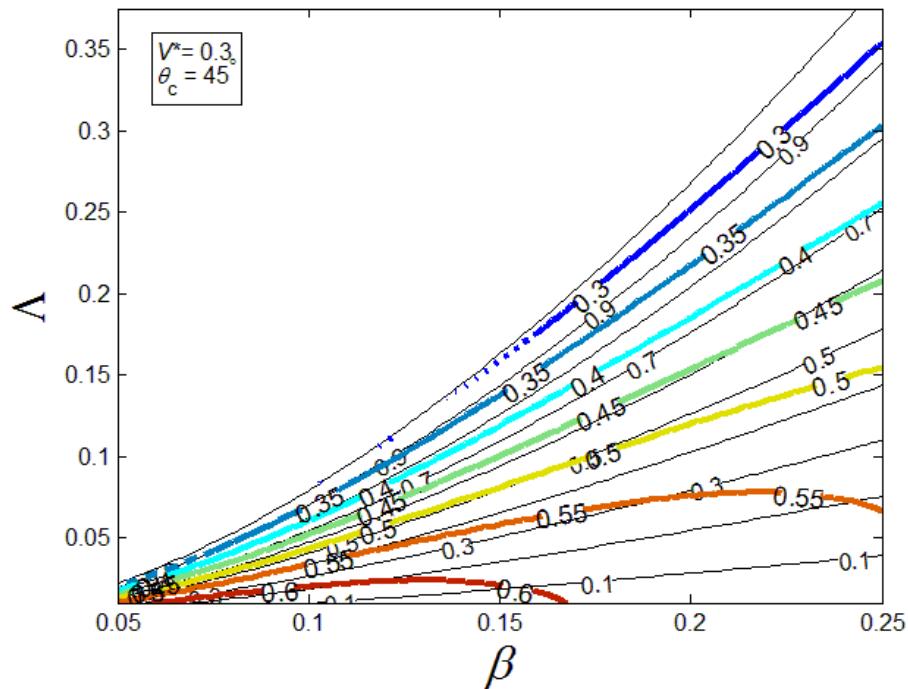


Figure 6.2: Contours for the base meniscus position (x_1^*). The contours are plotted with varying Λ and β . The other two governing parameters are fixed at $\theta_c = 45^\circ$ and $V^* = 0.3$.

Nevertheless, β does influence x_1^* through the deflection, and at a given Λ , the dependence of w_2^* on β can be clearly seen from Figure 6.2. Consider a contour plot showing w_2^* as a function of β and V^* shown in Figure 6.3. The features of this plot resemble Figure 5.14 but the higher w_2^* contours are now located at the lower part of the figure, i.e., for smaller β . This is because according to Eqs. (6.1) and (6.2), decreasing β increases M_p^* . Although Figure 6.3 and Figure 5.14 show similar characteristics for collapse, Figure 5.14 is more suitable for the initial discussion for several reasons. Firstly, since both the Laplace pressure and the surface tension force are directly proportional to Λ , changing Λ does not affect the relative importance of the two types of loading. On the contrary, changing β primarily influences the Laplace pressure which causes a change in the role of the Laplace pressure relative to the surface tension forces. Secondly, the normalization in β and V^* both involve the beam length L and DCB gap h , so if β is to be varied at a constant V^* , the physical volume of the liquid needs to be changed as well. Thirdly, as previously described the range of deflection angles scales with β . These features can make a plot such as Figure 6.3 difficult to interpret, and prevent an elucidation on the nonlinear deflection coupling effects. Because of this, previous discussions have been based on contour plots using Λ and V^* as the variables. On the other hand, plots such as Figure 6.3 have practical significance because once the materials of the beam and the liquid are specified so are the surface tension and contact angle. As a result plots like Figure 6.3 allow for determination of whether the given DCB geometry will collapse. Furthermore, experimentally varying surface tension or the beam's

flexural rigidity (EI) are more difficult than varying β which can be accomplished by varying the spacing or length of the beams (as in the experiments performed by Mastrangelo *et al.* [15]). One should, however, exercise care when trying to use Figure 6.3 for interpreting experimental data. For example if a drop of known volume is placed at the end of a DCB and spacing was decreased to cause the DCB to collapse, the system would not follow vertical lines (constant V^*) in Figure 6.3 since the normalized volume would increase as the spacing was decreased. As a result the system would follow a path such as the dashed black lines shown in Figure 6.3. In such situations, the experimental data should be normalized or the numerical result in Figure 6.3 should be converted into physical quantities before comparison.

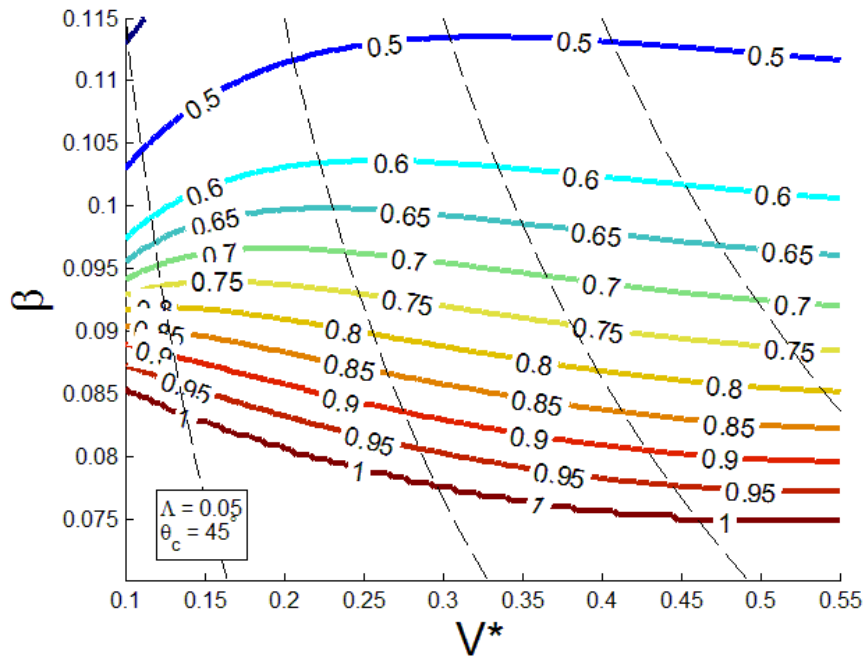


Figure 6.3: Contours for the free end deflection (w_2^*). The contours are plotted with varying β and V^* . The other two governing parameters are fixed at $\theta_c = 45^\circ$ and $\Lambda = 0.05$.

A particularly interesting observation is made when contours of the reaction moment M_R^* are plotted as a function of β and V^* , shown in Figure 6.4. It is clear from this figure that at collapse, the M_R^* contours are nearly parallel to the w_2^* contours. This suggests that at collapse M_R^* may not depend, or have weak dependence, on V^* or β . This is an extremely important observation because as was explained in the linear discussion M_R^* has a direct relationship with collapse; this is reinforced by Figure 6.4 where M_R^* greater than 0.28 is required for collapse. In fact, based on the nonlinear formulation, the reaction moment can be shown to be in the following closed form (see Eq. (4.24))

$$M_R^* = \sqrt{2\Lambda(\sin(\phi_2) + \cos(\theta_c))} \quad (\text{at collapse } w_2^* = 1) \quad (6.6)$$

where ϕ_2 is the free end deflection angle. This is an important result for several reasons. It establishes a direct correspondence between two of the governing parameters Λ and θ_c , and the collapsing M_R^* . It also shows that M_R^* depends on all other governing parameters through ϕ_2 . For most practical situations, ϕ_2 only ranges between 1° and 12° (obtained by considering extreme values of β). For the case of Figure 6.4 varying V^* from 0.1 to 0.55 only changes dw^*/dx^* at the free end from 0.0236 to 0.0233³; a difference of 2% indicating that ϕ_2 at collapse has only a slight dependence on V^* . Substituting $\Lambda = 0.05$ and $\theta_c = 45^\circ$ used for Figure 6.4 into Eq. (6.6), M_R^* is found to be 0.269 for $\phi_2 = 1^\circ$ and 0.302 for $\phi_2 = 12^\circ$, consistent with the M_R^* at collapse found in Figure 6.4. Based on Eq. (6.6), in

³ In light of $\tan(\phi) = \beta dw^*/dx^*$ for this example because β was varied to create collapse, dw^*/dx^* gives a better representation of the influence of V^* on ϕ_2 at collapse than directly looking at ϕ_2 .

Section 6.4 we will define a dimensionless number incorporating the four governing parameters to describe the condition for collapse in closed form.

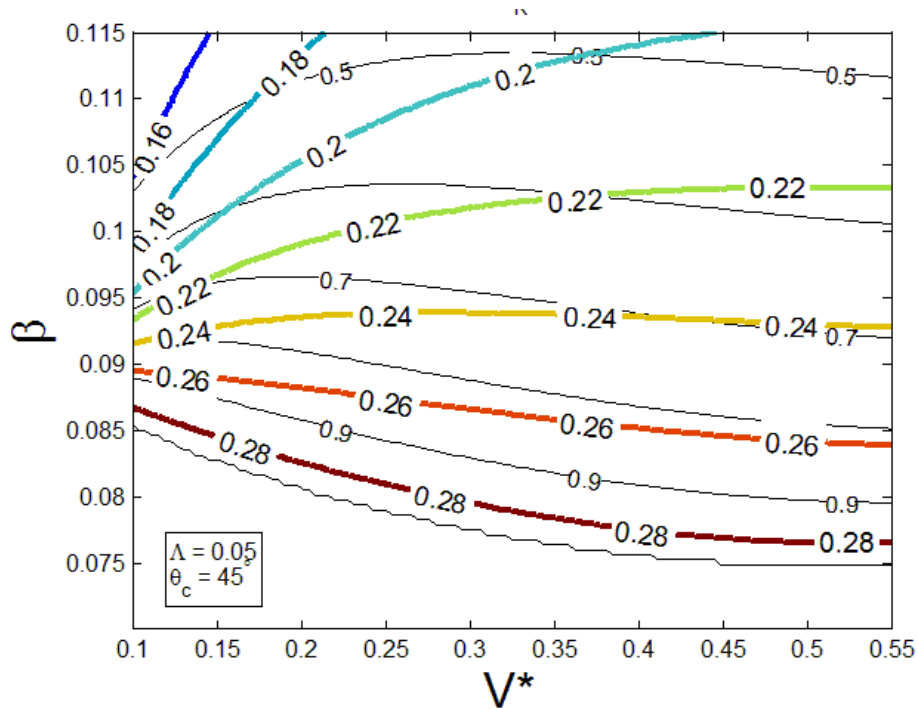


Figure 6.4: Contours for the reaction moment (M_R^*). The contours are plotted with varying β and V^* . The other two governing parameters are fixed at $\theta_c = 45^\circ$ and $\Lambda = 0.05$.

6.4 Collapse Correlation Equation

At the beginning of Chapter 5, we identified four governing parameters Λ , β , V^* and θ_c and expected that the collapse condition should be an equation in terms of these parameters. Detailed discussions were then performed to study the role of these governing parameters in causing deflection and collapse, and the collapse contour has been shown numerically for representative cases. Based on these studies, it is of interest to see whether a closed-form equation can be written explicitly for the condition of collapse.

To start, recall that in Chapter 5 when we studied collapse at several different contact angles it was noted that the reaction moment M_R^* at collapse had

only slight variation with V^* and appeared to be independent of contact angle θ_c . These observations suggest that it may be possible to fit a curve $M_R^*(\beta, V^*)$ to the numerical data, where it would be expected that the primary dependence would be on β . Contours of M_R^* at collapse for a wide range of V^* , and β are shown in Figure 6.5; here $\theta_c = 45^\circ$, and for each pair of (β, V^*) , Λ has been adjusted to cause collapse. The value of M_R^* at collapse is then calculated and plotted. Figure 6.5 gives several suggestion about the form of $M_R^*(\beta, V^*)$. First the contour spacing in the vertical direction is nearly constant which suggests that M_R^* depends linearly on β or $M_R^*(\beta, V^*) = \beta f(V^*)$. In addition the M_R^* contours are curved so a 2nd order polynomial would be an appropriate first guess for $f(V^*)$. Performing a regression using this form for the numerical data from Figure 6.5 gives the following relationship

$$M_R^*(w_2^* = 1) = \beta(3.156 + 2.3802V^* - 2.2091V^{*2}), \quad (6.7)$$

for $0.1 \leq V^* \leq 0.5$, $0.01 \leq \beta \leq 0.1$, $\theta_c = 45^\circ$.

Eq. (6.7) matches all of the data in Figure 6.5 with a maximum error of 4%.

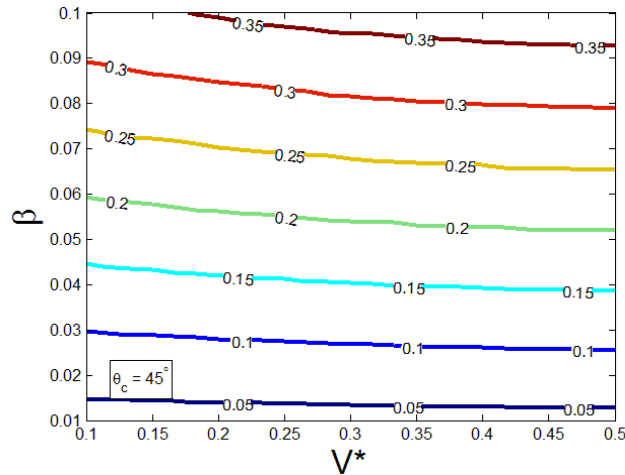


Figure 6.5: Contours for the reaction moment (M_R^*) at collapse. The contours are plotted with varying β and V^* and increasing Λ to create collapse ($w_2^* = 1$). The contact angle is fixed at $\theta_c = 45^\circ$.

Eq. (6.7) can be interpreted as the moment required to cause collapse, whereas Eq. (6.6) is the moment available to the beam at collapse. If we approximate $\sin(\phi_2)$ we can create an empirical formula for predicting collapse. For a linear cantilever beam with a uniform load q over its entire length L , $w_{\max} = qL^4 / 8EI$ and $\tan \phi_{\max} = qL^3 / 6EI$ [31]. Letting $w_{\max} = h$ these relationships can be combined to give $\tan \phi_{\max} = 4\beta / 3$, which provides a good approximation for ϕ_{\max} , i.e., ϕ_2 . The error can be reduced by using the same form for ϕ_2 and performing a regression against numerical data, which after using a small angle approximation ($\sin \phi_2 \approx \tan \phi_2$) gives

$$\sin \phi_2 \approx 1.382\beta . \quad (6.8)$$

For $0.1 \leq V^* \leq 0.5$, $0.01 \leq \beta \leq 0.1$ the maximum error associated with Eq. (6.8) is less than 2%. Therefore combining Eqs. (6.6), (6.7) and (6.8) allows us to define the following quantity

$$N = \frac{\beta(3.156 + 2.3802V^* - 2.2091V^{*2})}{\sqrt{2\Lambda(1.382\beta + \cos(\theta_c))}} . \quad (6.9)$$

If $N \leq 1$ the DCB is expected to collapse otherwise it is expected to be free. The contours of N are compared with the free end deflection contours from Figure 5.14 (black thin lines) in Figure 6.6. Ideally the $N = 1$ contour should be coincident with the $w_2^* = 1$ contour. Despite some small discrepancies at large V^* , N defined from (6.9) does an excellent job in predicting collapse.

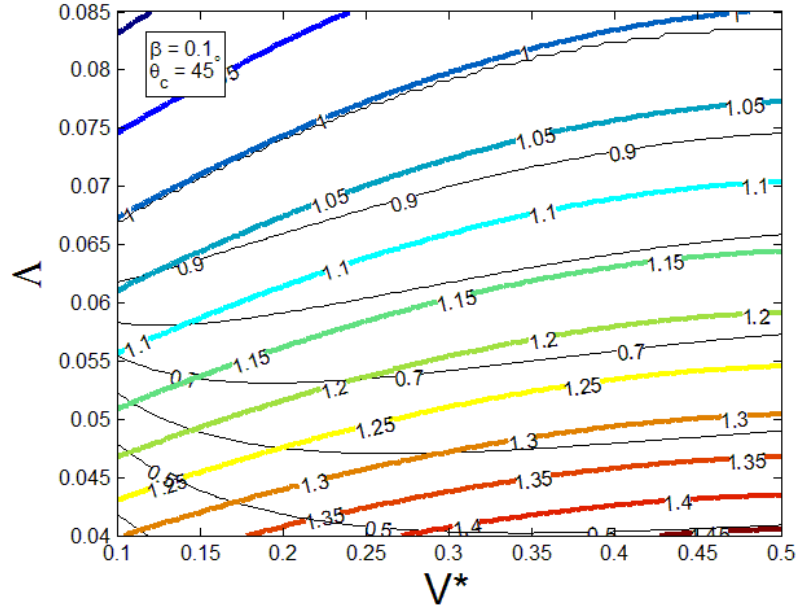


Figure 6.6: Contours for the nondimensional number N for comparison with free end deflection (w_2^*). Ideally the 1 contours of each would be coincident. The contours are plotted with varying Λ and V^* . The other two governing parameters are fixed at $\theta_c = 45^\circ$ and $\beta = 0.1$.

As mentioned in Section 5.6 another normalized number exists in the literature, the so-called elastocapillary number N_{EC} , which predicts collapse when $N_{EC} < 1$ [3], [40]. For a cantilever suspended above a substrate the elastocapillary number is given as follows [3],[40]

$$N_{EC} = \frac{8EIh^2}{3\gamma_{LA} \cos \theta_c L^4 D(1+t/D)} = \frac{8\beta^2}{3\Lambda \cos \theta_c (1+t/D)}. \quad (6.10)$$

where t is the thickness of the beam. Here the t/D term is a “suitable meniscus correction” [3] which is somehow related to the thickness of the beam⁴. This relationship is approximate and is obtained from energy considerations. There are two problems with the existing N_{EC} (i) its approximate nature in that it neglects surface tension forces, liquid displaced by the menisci and uses simplified test functions, (ii) it provides no indication of what V^* leads to collapse. As will be shown (see Chapter 7) the latter is a significant deficiency because as drop size

⁴ $N_{EC} = 5.504\beta^2/\Lambda \cos(\theta_c)$ was obtained for a DCB in Appendix E

decreases it can pull more of the DCB into s-shaped adhesion. This results in greater adhesion energy (Eq. (3.50)) which is important for determining stiction failure [18]. Because of the similarities in the definitions of N and N_{EC} it is of interest to compare the form of Eq. (6.9) and Eq. (6.10). If angles ($\sin \phi_2 \approx 1.382\beta$) are neglected Eq. (6.9) has the following form

$$N^2 = \frac{\beta^2 f(V^*)}{2\Lambda \cos(\theta_c)}, \quad (6.11)$$

which is similar to that of Eq. (6.10).

Although Eq. (6.9) does a good job in Figure 6.6, the contact angle in the figure has been fixed at 45° and β has been fixed at 0.1. Additional numerical calculations show M_R^* has a slight nonlinear dependency on β and θ_c . As a result for a range of contact angles from $0^\circ \leq \theta_c \leq 80^\circ$ the maximum error for Eq. (6.7) can be more than 10%. Particularly the $N = 1$ contour can show significant deviation from the $w_2^* = 1$ contour at both low β and high θ_c . At $\theta_c = 0^\circ$ there is almost no deviation; however as the contact angle is increased N becomes too high. Similarly, as β is decreased N becomes too low. In addition, as shown in Figure 6.6 the deviations increase with V^* . Correction terms are added to the assumed form of M_R^* (Eq. (6.7)) to give the regression the freedom to correct these errors. The correction terms are assumed to be in the form of $\beta(A\beta + (B+C\beta)/\cos(\theta_c))V^{*2}$, where A , B and C are to be determined from regression. To explain the choice of the correction terms, it is noted that because the deviation in Figure 6.6 appears to grow quadratically with V^* the correction terms are assumed to be proportional to V^{*2} . Introduction of β^2 terms allows the regression to capture the slight nonlinear dependence in β . Finally, multiplication by

$1/\cos(\theta_c)$ allows the solution to capture the variation in contact angle. $1/\cos(\theta_c)$ was chosen because it is one at low contact angles, in which case there is little deviation in the original curve fit, also it increases at higher contact angles which helps to reduce the increase in N in its original form. The result from regression is as follows.

$$M_R^* = \beta \left(3.1458 + 2.4041V^* - \left(1.3147 + 6.4924\beta + \left(\frac{0.1485 + 1.0870\beta}{\cos(\theta_c)} \right) \right) V^{*2} \right), \quad (6.12)$$

$$w_2^* = 1, \quad 0.125 \leq V^* \leq 0.5, \quad 0.01 \leq \beta \leq 0.1, \quad 0^\circ \leq \theta_c \leq 80^\circ$$

The maximum deviation of Eq. (6.12) from the numerical data in this range is about 2.5%. It is important to note that the most important term in Eq. (6.12) is the first one as it has the highest magnitude. Furthermore, the linear and quadratic V^* terms have opposite signs and partially cancel each other out to fine tune the expression. Now a new expression for N can be obtained as follows

$$N = \frac{\beta \left(3.1458 + 2.4041V^* - \left(1.3147 + 6.4924\beta + \left(\frac{0.1485 + 1.0870\beta}{\cos(\theta_c)} \right) \right) V^{*2} \right)}{\sqrt{2\Lambda(1.382\beta + \cos(\theta_c))}}. \quad (6.13)$$

Note that improving our estimate of ϕ_2 was found to have little effect on the N contours. Eq. (6.13) is compared with each case studied in Chapter 5 in Figure 6.7 - Figure 6.10. All together, these figures cover a broad range of the four governing parameters. In each case the $N = 1$ contour closely matches the $w_2^* = 1$ contour. Therefore, Eq. (6.13) provides an excellent measure for predicting collapse.

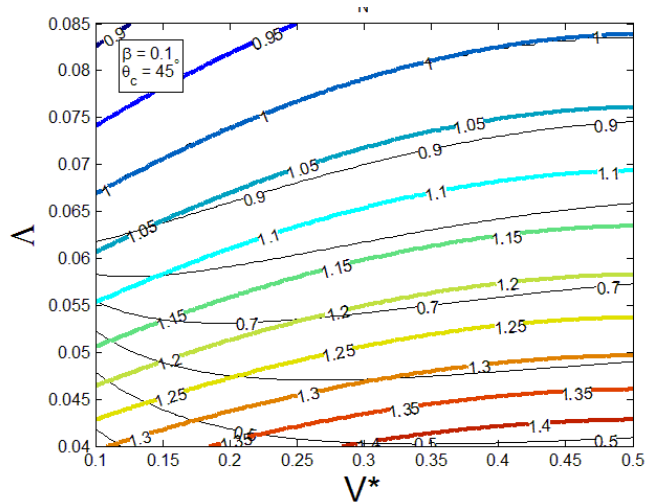


Figure 6.7 Contours for the nondimensional number N for comparison with free end deflection (w_2^*). Ideally the 1 contours of each would be coincident. The contours are plotted with varying Δ and V^* . The other two governing parameters are fixed at $\theta_c = 45^\circ$ and $\beta = 0.1$.

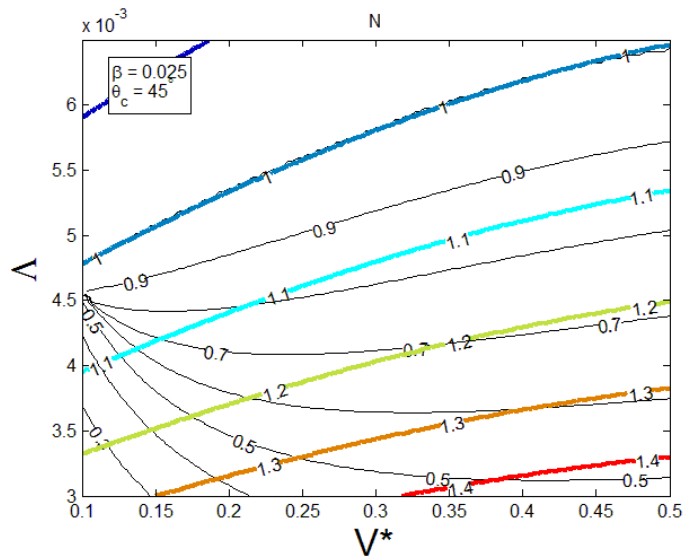


Figure 6.8: Contours for the nondimensional number N for comparison with free end deflection (w_2^*). Ideally the 1 contours of each would be coincident. The contours are plotted with varying Δ and V^* . The other two governing parameters are fixed at $\theta_c = 45^\circ$ and $\beta = 0.025$.

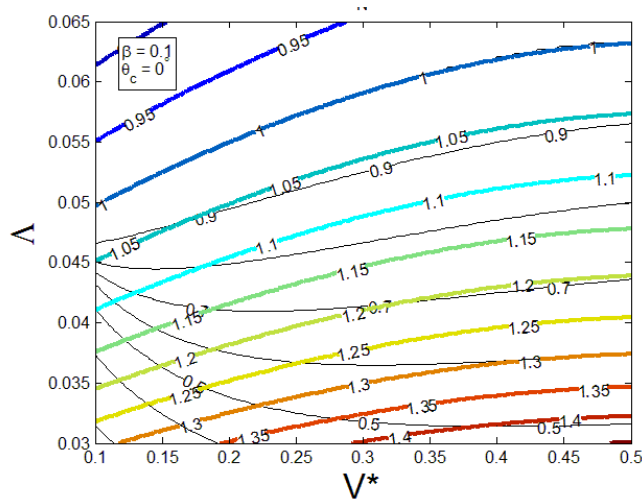


Figure 6.9 Contours for the nondimensional number N for comparison with free end deflection (w_2^*). Ideally the 1 contours of each would be coincident. The contours are plotted with varying Δ and V^* . The other two governing parameters are fixed at $\theta_c = 0^\circ$ and $\beta = 0.1$.

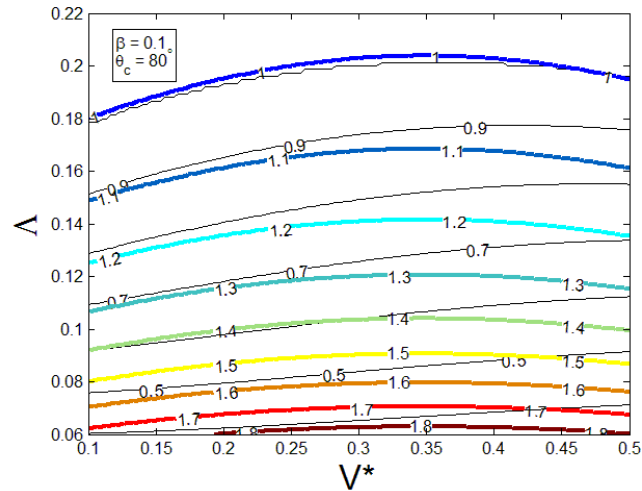


Figure 6.10 Contours for the nondimensional number N for comparison with free end deflection (w_2^*). Ideally the 1 contours of each would be coincident. The contours are plotted with varying Δ and V^* . The other two governing parameters are fixed at $\theta_c = 80^\circ$ and $\beta = 0.1$.

6.5 Comparison with Previous Works

As previously mentioned the problem of collapse where the DCB is completely filled with liquid has been studied [4],[6],[11],[12]. For this problem, Tanaka *et al.* proposed the following equation for free end deflection [4]

$$w_2^* = \frac{2h - \gamma_{LA} L^3 D \sin \theta_c / 3EI - \sqrt{(2h - \gamma_{LA} L^3 D \sin \theta_c / 3EI)^2 - 2\gamma_{LA} L^4 D \cos \theta_c / EI}}{4h} \quad (6.14)$$

This equation does not depend on the volume of the liquid because it was assumed that the liquid completely fill the gap between the DCB. Although the problem studied in this dissertation is for a liquid drop located at the free end, the volume of the liquid can be increased so that the base meniscus touches the base, which then resembles the situation of liquid-filled DCB. Kotera *et al.* [6] applied the model of Tanaka *et al.* [4] to a system with, $E = 5.9\text{GPa}$, $\gamma_{\text{LA}} = 72.28\text{dyn/cm}$, $L = 1000\text{nm}$, $h = 100\text{nm}$, $D = 500\text{nm}$, $I = 3.333 \times 10^8 \text{nm}^4$, and $\theta_c = 0^\circ$, using these data the result of Eq. (6.14) is shown in Figure 6.11. Normalizing this data for use with our model gives $\Lambda = 0.0184$ and $\beta = 0.1$ and from Figure 6.9 collapse is not expected for any V^* . Also plotted in Figure 6.11 are the free end deflections obtained from our model for a range of V^* . With increasing V^* , w_2^* predicted from our models increases and ultimately reaches a plateau when the base meniscus approaches the clamped end. The plateau value obtained from our model and the value obtained from Eq. (6.14) are of the same order of magnitude; however the completely filled DCB model gives a higher deflection, even though in both cases the Laplace pressure acts over the entire area of the beam. The reason is that in the completely filled DCB model the Laplace pressure is controlled by the meniscus at the free end, whereas in our model there are two menisci, and the one closer to the base controls the Laplace pressure because the angle at the free end meniscus is allowed to adjust (isobaric drop condition). Since the meniscus at the free end has higher deflection it gives rise to higher Laplace pressure and thus higher deflections in the completely filled DCB model.

It should also be pointed out that in Eq. (6.14), the surface tension forces are neglected, so it may not be appropriate at a high contact angles. A comparison of w_2^* for $\theta_c = 50^\circ$ is shown in Figure 6.12. Clearly, at this contact angle surface tension forces are important, and our model which accounts for surface tension forces now predicts higher deflection.

One final note about Eq. (6.14) is that it cannot predict deflections from zero to collapse. For example consider $\theta_c = 0^\circ$ in Eq. (6.14); for any $w_2^* > 0.5$ the term in the square root becomes negative and not meaningful. The occurrence of negative term under the square root was interpreted as the criterion for collapse in previous works, [4], [6], which we find unconvincing.

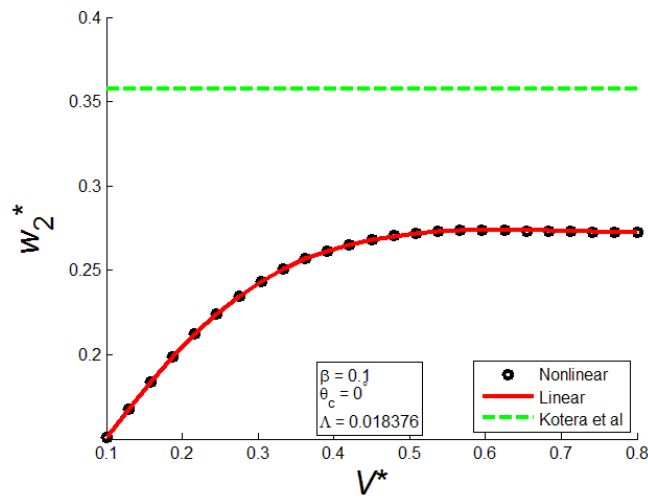


Figure 6.11: Comparison of free end deflection (w_2^*) with completely filled DCB models [4],[6] using data from [6].

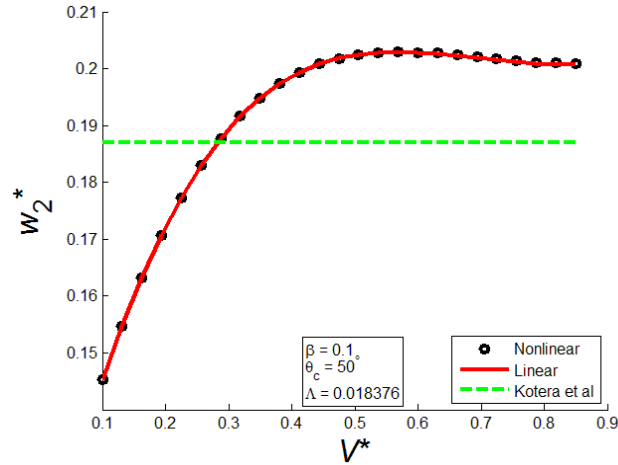


Figure 6.12: Comparison of free end deflection (w_2^*) with completely filled DCB models [4],[6] using data from [6] with contact angle changed to 50°

6.6 Summary

For the range of governing parameters deemed to be of practical interest it was shown that it is acceptable to neglect geometrical nonlinearity in the beam equations. Doing so introduced an error of less than 1%. In the nonlinear discussion the influence of governing parameter β was focused on because it was given the least attention in the linear discussion. Decreasing β increases the Laplace pressure which may lead to DCB collapse much like increasing Λ , however varying β would be more practical experimentally. Changing β also influences the base meniscus position through the liquid displaced by the menisci, however for the range of β of interest this effect is relatively unimportant compared to the changes caused by liquid displaced by beam deflection. Finally, the nonlinear formulation allows the total moment on the beam to be written in a closed form. This further allows a dimensionless quantity to be defined, as a function of the four governing parameters, which accurately predicts collapse for a large range of governing parameter values.

Chapter 7 Results on Adhered Configuration

In the discussion of the uncollapsed configuration it was shown how the governing parameters Λ , β , V^* , and θ_c influenced the beam's deflection. In the adhered case the free end meniscus and its associated constraint equations have been removed and replaced with two essential boundary conditions at the tip of the contact zone (crack tip) between the two beams. Because many of the governing equations remain the same the parameters Λ , β , V^* , and θ_c will continue to impact the solution in a similar way. As these parameters were addressed in detail during the discussions in previous chapters, this chapter will focus on the effect of the new natural boundary conditions at the crack tip. These boundary conditions introduce an additional governing parameter Λ_{SL} related to adhesion, and an additional unknown Q_2^* related to the contact force. Results from both linear and nonlinear formulations on the adhered configuration will be discussed in this chapter. Since bending the DCB to form an s-shaped adhered configuration takes considerable energy, for this configuration to exist small values of β will typically be required; therefore there is expected to be little difference between the linear and nonlinear results. There are several objectives of this chapter. Firstly the discussion will partially mirror existing works which looked at the detachment beam length experimentally [14]-[18], i.e., for what values of β it is possible to have the adhered configuration in equilibrium; for $s_2^* > 1$ the s-shaped adhered configuration is no longer possible. However, in past studies the detachment length was investigated only when the liquid had completely dried or equivalently by taking the limit as $V^* \rightarrow 0$; in this work we

will look at how a decrease in V^* influences the length of the DCB in adhesion. The second objective will be to look at how the adhesion energy Λ_{SL} influences the solution; in particular its effect on the value of β required for detachment. Finally, we will compare the results of our model with similar models found in the literature.

7.1 Summary of Governing Equations

We wish to study how the new essential boundary conditions and the additional governing parameter Λ_{SL} influence the problem as well as study the impact of geometric nonlinearity. The system of equations governing the deformation of the DCB with both linear and nonlinear beam models is revisited below. Keeping mind that these equations are nearly identical to the uncollapsed case it is helpful to focus on how the adhesion natural boundary conditions influence the moment. As in Chapter 5 and Chapter 6 the discussion will be limited to negative α . The normalized equations from Chapter 3 and Chapter 4 pertinent to the discussion are listed below starting with the linear case.

Dimensionless linear ODE relating moment and curvature Eq. (5.2):

$$\beta \frac{d^2 w^*}{dx^{*2}} = M^* = \Lambda \left(-\frac{\langle x^* - x_1^* \rangle^2}{2\alpha\beta} + \sin(\theta_c) \langle x^* - x_1^* \rangle^1 \right) - Q_R^* x^* + M_R^* \quad (7.1)$$

Dimensionless clamped end reaction moment and shear force from Eq. (3.38):

$$\begin{aligned} Q_R^* &= Q_R L^2 / EI = -\Lambda (x_2^* - x_1^*) / \alpha\beta + \Lambda \sin \theta_c - Q_2^* \\ M_R^* &= M_P^* + M_{ST}^* - \sqrt{2\Lambda_{SL}} - Q_2^* x_2^* \\ M_P^* &= -\Lambda (x_2^{*2} - x_1^{*2}) / 2\alpha\beta \\ M_{ST}^* &= \Lambda \sin(\theta_c) x_1^* \end{aligned} \quad (7.2)$$

The deflection and slope at an arbitrary position x^* along the beam Eq. (5.4):

$$\beta w^*(x^*) = \Lambda \left(-\frac{\langle x^* - x_1^* \rangle^4}{24\alpha\beta} + \sin(\theta_c) \frac{\langle x^* - x_1^* \rangle^3}{6} \right) - \frac{Q_R^*}{6} x^{*3} + \frac{M_R^*}{2} x^{*2} \quad (7.3)$$

$$\tan(\phi) = \beta \frac{dw^*}{dx^*} = \Lambda \left(-\frac{\langle x^* - x_1^* \rangle^3}{6\alpha\beta} + \sin(\theta_c) \frac{\langle x^* - x_1^* \rangle^2}{2} \right) - \frac{Q_R^*}{2} x^{*2} + M_R^* x^*$$

Constant liquid volume constraint from Eq. (3.41):

$$V^* = \int_{x_1^*}^{x_2^*} (1 - w^*(x^*)) dx^* - \frac{\alpha^2 \beta}{2} \left(\cos^{-1}(l_1^*) - l_1^* \sqrt{1 - l_1^{*2}} \right) \quad (7.4)$$

Condition for the defections at the location of the base meniscus:

$$1 = l_1^{*2} + \alpha^{-2} (w^*(x_1^*) - 1)^2 \quad (7.5)$$

Condition for the slope at the location of the base meniscus:

$$\theta_c = \sin^{-1}(l_1^*) - \phi_1 \quad (7.6)$$

In the nonlinear case we have dimensionless ODE relating moment and curvature:

$$\frac{d\phi}{ds^*} = M_R^* - Q_R^* x^* + M_{ST}^*(s^*) + M_P^*(s^*)$$

$$M_{ST}^*(s^*) = \Lambda \left(\sin(\phi(s_1^*) + \theta_c) \langle x^*(s^*) - x^*(s_1^*) \rangle - \beta \cos(\phi(s_1^*) + \theta_c) \langle w^*(s^*) - w^*(s_1^*) \rangle \right) \quad (7.7)$$

$$M_P^*(s^*) = -\Lambda \left(\langle x^*(s^*) - x^*(s_1^*) \rangle^2 + \beta^2 \langle w^*(s^*) - w^*(s_1^*) \rangle^2 \right) / 2\alpha\beta$$

Dimensionless clamped end moment and shear force from Eqs. (4.30) and (4.31):

$$Q_R^* = \Lambda \left[-\langle x^*(s_2^*) - x^*(s_1^*) \rangle / \alpha\beta + \sin(\theta_c + \phi(s_1^*)) \right] - Q_2^*$$

$$M_R^* = M_P^* + M_{ST}^* - \sqrt{2\Lambda_{SL}} - Q_2^* x^*(s_2^*) \quad (7.8)$$

$$M_P^* = -\Lambda \left(\beta^2 (1 - w^*(s_1^*)^2) + (x^*(s_2^*)^2 - x^*(s_1^*)^2) \right) / 2\alpha\beta$$

$$M_{ST}^* = \Lambda \left(\sin(\theta_c + \phi(s_1^*)) x^*(s_1^*) - \beta \cos(\theta_c + \phi(s_1^*)) w^*(s_1^*) \right)$$

The deflected beam can be located as follows:

$$\frac{dx^*}{ds^*} = \cos \phi \quad (7.9)$$

$$\frac{dw^*}{ds^*} = \frac{\sin \phi}{\beta}$$

Constant liquid volume constraint:

$$V^* = \int_{s_1^*}^{s_2^*} (1 - w^*(s^*)) \cos(\phi(s^*)) ds^* - \frac{\alpha^2 \beta}{2} \left(\cos^{-1}(l_1^*) - l_1^* \sqrt{1 - l_1^{*2}} \right) \quad (7.10)$$

It will be shown that for the cases discussed there is negligible difference between the linear and nonlinear models. Therefore, unless otherwise stated the results and figures are from the nonlinear model.

7.2 Basic considerations

In the uncollapsed case the discussion centered around w_2^* which determined whether the DCB would collapse; in the case of s-shaped adhesion the discussion will center around s_2^* which for the nonlinear model will show how much of the DCB length is in contact. If the solution finds $s_2^* > 1$ then this configuration is not possible. A representative s-shaped deflected curve is shown in Figure 7.1. The meniscus location is indicated by the blue line.

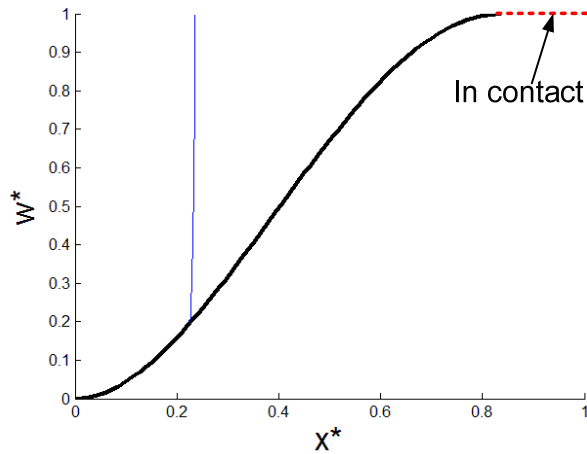


Figure 7.1: Elastic curve and meniscus location for $V^* = 0.2$. The other four governing parameters are fixed at $\theta_c = 30^\circ$, $\Lambda = 0.01$, $\Lambda_{SL} = 0.01$, $\beta = 0.02$.

To begin the investigation consider a contour plot of s_2^* as a function of β and V^* shown in Figure 7.2. Because it takes considerable energy to bend the DCB to form a finite contact area, higher Λ and/or lower β are needed. As a result this configuration does not exist near the upper range of β ($\beta \approx 0.1$) discussed in Chapter 5, so β in this plot is in its low range ($\beta < 0.025$). To allow for comparisons the same contact angle $\theta_c = 45^\circ$ is chosen. Although β in Figure 7.2 is less than in Figure 5.6, Λ needed to be set to 0.02 to have s-shaped adhesion. This value of Λ is more than three times larger than what was required to cause collapse in Figure 5.6. One reason for this is that Λ_{SL} has been set to 0 for this

figure which means that it does not take any energy to separate the adhered surfaces. This observation shows that forming the s-shaped adhered configuration is considerably harder than just causing the two free ends of the DCB to touch (defined as collapse). Returning to Figure 7.2, the s_2^* contours are nearly parallel arcs with the top right portion of the plot representing detachment. Reading the plot at a constant value of V^* , s_2^* increases as β is increased indicating a smaller adhered DCB length. Once β is increased so that $s_2^* > 1$ the s-shaped configuration is no longer possible. This behaviour is similar to what was seen in the detachment length experiments as the beam length decreased (β increased) the beams became detached.

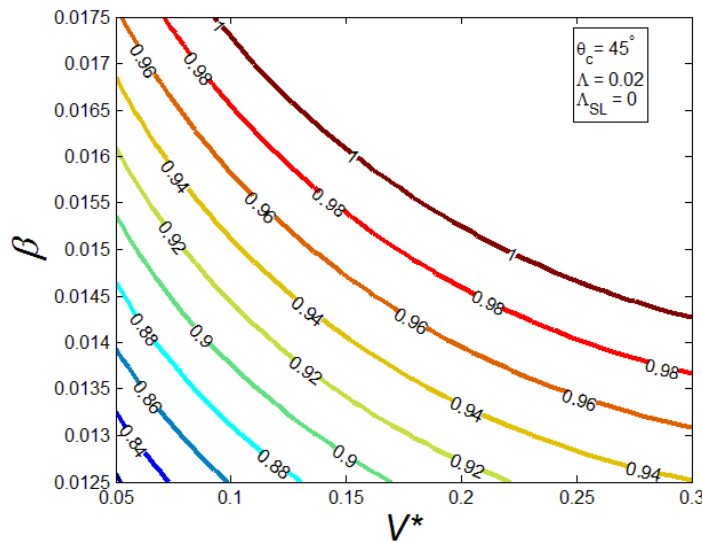


Figure 7.2: Contours for the normalized length of DCB not in contact (s_2^*). The contours are plotted with varying β and V^* . The other three governing parameters are fixed at $\theta_c = 45^\circ$, $\Lambda = 0.02$, and $\Lambda_{SL} = 0$.

As previously mentioned a number of papers [14]-[17] sought to obtain the adhesion energy experimentally by creating an array of cantilevers with different length (hence different β), and measuring the detachment length or the longest cantilever that would not remain attached. However, for cantilevers detachment

length experiments use a shear deformation correction to estimate adhesion energy [14] and are inherently associated with arc-shaped stiction failures [18]. Later studies use interferometry to measure beam deflection and obtain the crack length for an s-shaped adhered configuration [18], [19]. The adhesion energy then follows from the crack length, strain energy and the strain energy release rate⁵ [18], [19], [38]. These studies let $V^* \rightarrow 0$ in their models and then used the detachment or crack length to estimate the adhesion energy. In Figure 7.2 V^* is retained as a variable for two reasons. Firstly, for this figure $\Lambda_{SL} = 0$, i.e., it takes zero energy to separate the adhered DCB, so if V^* is set to zero from the beginning of the calculation there would be no force exerted on the DCB to form the adhered configuration. On the other hand, a non-trivial solution can be obtained by considering $V^* \rightarrow 0$ from Figure 7.2 however Laplace pressure becomes infinite at $V^* = 0$. Secondly, retaining V^* as a variable allows for a study of how V^* influences the adhered beam length $(1 - s_2^*)$. Consider reading Figure 7.2 at a constant value of β , for example $\beta = 0.0125$ and imagine a drying process where V^* decreases. As V^* decreases so does s_2^* , indicating that the adhered beam length $(1 - s_2^*)$ increases during the drying process. This may seem odd at first, but can be explained by the nonlinear deflection coupling effects. Since there is a deflection boundary condition at the crack tip ($w_2^* = 1$), decreasing V^* causes the base meniscus to move closer to the crack tip or s_1^* increases as shown in Figure 7.3; here s_2^* contours are also shown by the thin black curves so that

⁵ If reformulated without liquid and for a cantilever over a substrate our linear model gives the same adhesion energy based on a measured crack length (x_2^*)

comparisons can be made at constant values of adhered beam length. This increases the base meniscus deflection (w_1^*) resulting in a decrease in $|\alpha|$ shown in Figure 7.4 which promotes adhesion. This is consistent with experimental procedure of Leseman *et al.* [19] where liquid was evaporated to pull cantilevers into s-shaped adhered configurations to study adhesion energy. This observation is valid at other contact angles as well since decreasing V^* increases w_1^* and decreases ϕ_1 (if V^* is small enough) both increase the Laplace pressure and promote adhesion. In Figure 7.4 the α contours are nearly vertical indicating dependence primarily on V^* . Specifically, $|\alpha|$ decreases with decreasing V^* which results in an increase in the Laplace pressure, consistent with the corresponding increase in adhered length. If Figure 7.4 is read at a constant V^* there is a slight increase in $|\alpha|$ with decreasing β , which appears inconsistent with the increase in adhered length; however, the increase in Laplace pressure (see from M_p^* Eq. (7.7) by ignoring pressure area and moment arm) created by decreasing β is larger than the decrease in Laplace pressure caused by the slight increase in $|\alpha|$. The slight increase in $|\alpha|$ as β is decreased is caused by meniscus movement towards the base. The nonlinear deflection coupling effect through s_1^* can be seen in its contour plot for s_1^* shown in Figure 7.3, where the contours display the same patterns as the α contours. At constant values of V^* , s_1^* is smaller at lower values of β ; lower β increases M_p^* resulting in a larger adhered length which displaces the meniscus towards the clamped end decreasing s_1^* . As in Chapter 5 this causes a reduction in w_1^* and larger $|\alpha|$.

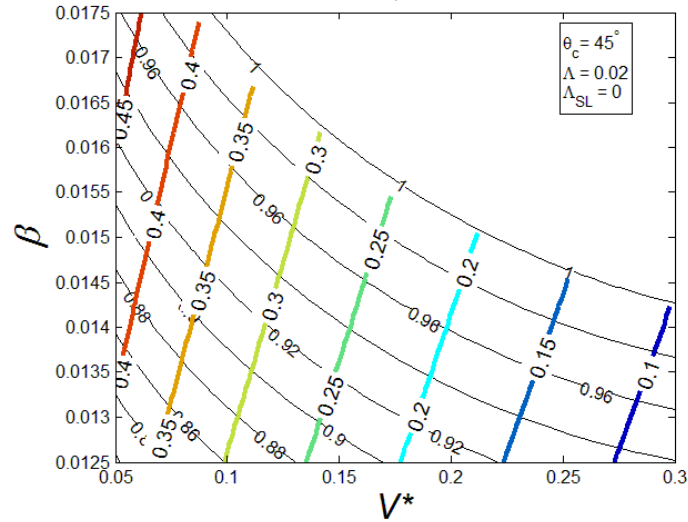


Figure 7.3: Contours for the normalized base meniscus position (s_1^*). The contours are plotted with varying β and V^* . The other three governing parameters are fixed at $\theta_c = 45^\circ$, $\Lambda = 0.02$, and $\Lambda_{SL} = 0$.

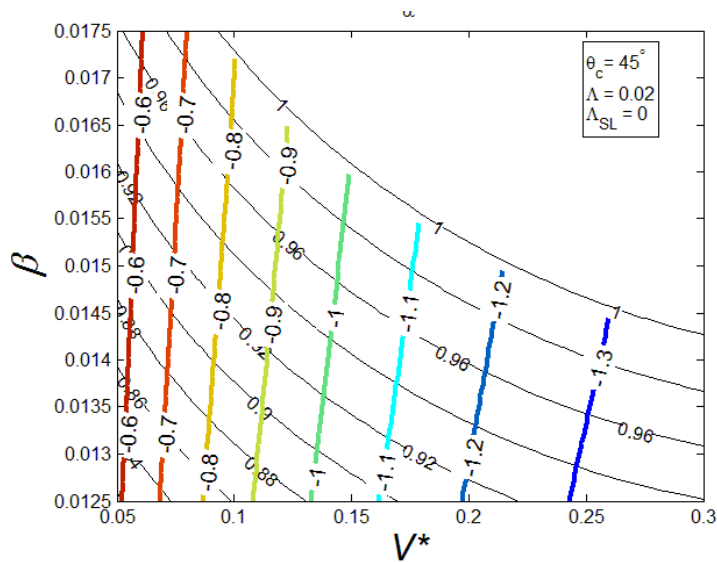


Figure 7.4: Contours for the normalized meniscus radius (α) contours. The contours are plotted with varying β and V^* . The other three governing parameters are fixed at $\theta_c = 45^\circ$, $\Lambda = 0.02$, and $\Lambda_{SL} = 0$.

It should be noted that unlike in the discussion of Chapter 5, the decrease in s_1^* as β is decreased does not create an increase in Laplace pressure area since the corresponding decrease in s_2^* is greater. This effect combined with the decreased moment arm associated with decreasing s_1^* and s_2^* result in a slight decrease in

M_p^* as β decreases, as seen in Figure 7.5, even though there is an increase in the Laplace pressure. To understand this behaviour it is important to note that the mechanic of adhesion is different from that of DCB collapse discussed in Chapter 5. For DCB collapse when the Laplace pressure was increased it led to an increase in M_p^* , which increased M_R^* and caused increased deflection. However, in the adhered problem increasing Laplace pressure will not necessarily increase M_p^* since, we derived a closed form equation for the reaction moment M_R^* in Eq. (4.32)

$$M_R^* = \sqrt{2(\Lambda_{SL} + \Lambda \cos(\theta_c))}. \quad (7.11)$$

In other words when we vary β and V^* , M_R^* is fixed and the moments which contribute to M_R^* must be balanced; i.e. we must satisfy Eq. (7.2) or $\sqrt{2(\Lambda_{SL} + \Lambda \cos(\theta_c))} = M_p^* + M_{ST}^* - \sqrt{2\Lambda_{SL}} - Q_2^* x_2^*$. Here $\sqrt{2\Lambda_{SL}}$ is constant and for this range of β , M_{ST}^* is small thus we must satisfy

$$C \approx M_p^* - Q_2^* x_2^*. \quad (7.12)$$

where C is a constant. Let's consider the case of decreasing β , which as previously mentioned increases the Laplace pressure and would tend to increase both the capillary force and M_p^* . To satisfy Eq. (7.12), the shear reaction at the crack tip Q_2^* would have to increase. However it is not possible to balance Eq. (7.12) by simply increasing Q_2^* . From force equilibrium, the increase in capillary force (first and second terms on RHS of first equation in (7.2)) would be carried not only by increased Q_2^* but also by an increase in reaction shear Q_R^* . How the

capillary force is divided between Q_R^* and Q_2^* cannot be determined from force equilibrium alone, rather it requires a compatible deflection which satisfies all essential boundary conditions. Hence Q_R^* and Q_2^* depend on how the load is distributed along the DCB and more of the capillary force will be carried by the support closer to where the load is applied. Since decreasing β increases the Laplace pressure which would tend to increase the capillary force but hardly change how it is distributed along the beam, the ratio Q_2^*/Q_R^* will need to remain nearly constant in order to satisfy essential boundary conditions at both the base and the crack tip. This can be seen in the $G = Q_2^*/Q_R^*$ contours shown in Figure 7.6 where the contours are nearly vertical indicating the ratio changes little with decreases in β . Thus if the surface tension force is neglected the contact force can be expressed as $Q_2^* = HF_p^*$ where $H = G/(G + 1)$ is a constant which depends on how the load is distributed. Substituting this relation into Eq. (7.12) and using $M_p^* = F_p^*(x_2^* + x_1^*)/2$ gives

$$C \approx F_p^* \left(\frac{x_2^* + x_1^*}{2} - Hx_2^* \right). \quad (7.13)$$

Decreasing β will increase the Laplace pressure and hence the Laplace pressure force F_p^* while from Figure 7.6 G , and therefore H , remains nearly constant. Since C and H are fixed when changing β , Eq. (7.13) cannot be satisfied for different F_p^* without changing adhered length. Instead, to satisfy Eq. (7.12) when the Laplace pressure increases the expected increase in M_p^* is counteracted by a decrease in x_2^* (and x_1^*). Increasing the adhered DCB length or decreasing x_2^*

reduces the moment arm thus decreasing M_p^* . The behaviour explains why M_p^* decreases as β is decreased in Figure 7.5. Also as a result, Q_2^* shown in Figure 7.7, shows only a slight increase with decreasing β rather than a drastic increase in order to compensate for increases Laplace pressure.

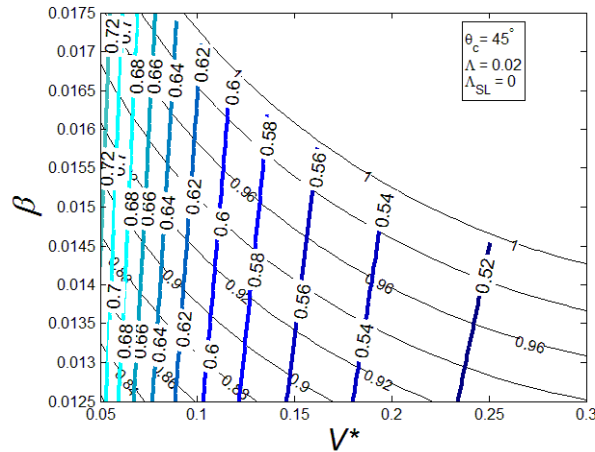


Figure 7.5: Contours for the pressure moment (M_p^*) contours. The contours are plotted with varying β and V^* . The other three governing parameters are fixed at $\theta_c = 45^\circ$, $\Lambda = 0.02$, and $\Lambda_{SL} = 0$.

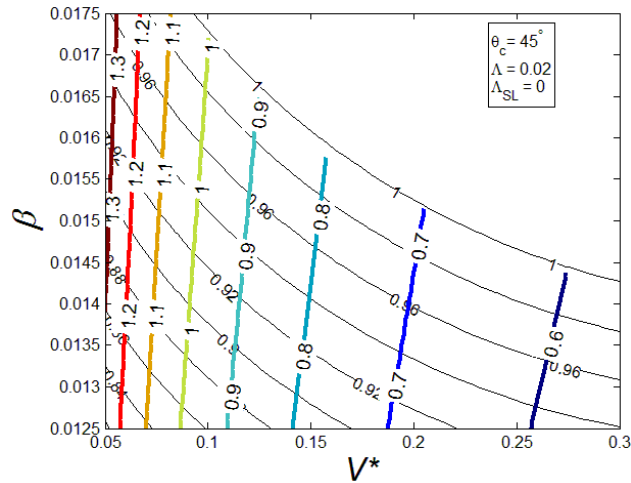


Figure 7.6: Contours for the ratio G of normalized shear reaction at adhered end to base (Q_2^*/Q_R^*). The contours are plotted with varying β and V^* . The other three governing parameters are fixed at $\theta_c = 45^\circ$, $\Lambda = 0.02$, and $\Lambda_{SL} = 0$.

It can also be observed in Figure 7.5 that when V^* decreases M_p^* increases. To understand why M_p^* still increases when V^* is decreased we need to look at contours of Q_2^* shown in Figure 7.7. Here Q_2^* increases with decreasing V^* . Decreasing V^* causes the base meniscus to move closer to the crack tip simultaneously decreasing $|\alpha|$ and increasing the moment arm, both of which tend to increase M_p^* . From Figure 7.7, the increase in Q_2^* with decreasing V^* is more pronounced. This can be explained by Eq. (7.12) since accompanying the increase in M_p^* there is a decrease in s_2^* and hence x_2^* . Furthermore, for smaller drops the distribution of Laplace pressure and the surface tension force will be relatively closer to the crack tip as a result a greater fraction of the total capillary force will be balanced by Q_2^* rather than Q_R^* . As a result Q_R^* does not sharply increase with the increased capillary force and drastic reduction in x_2^* is not needed to satisfy Eq. (7.12) for a given increase in Laplace pressure. To quantify the last statement consider the contours of normalized Laplace pressure ($F_p^*/(x_2^* - x_1^*)$) shown in Figure 7.8. Consider $V^* = 0.075$ when β is decreased from 0.0175 to 0.0125, the normalized Laplace pressure increases from 1.7 to 2.1, a 24% increase, while x_2^* decreases from 0.985 to 0.845 a 14% reduction. While for $\beta = 0.0135$ as V^* is decreased from 0.3 to 0.05 the normalized Laplace pressure increases from 1.1 to 2.6, a 136% increase, while x_2^* decreases from 0.97 to 0.84, a 13% reduction. Clearly a much larger increase in Laplace pressure is required to cause a given change in x_2^* if the increase in Laplace pressure is caused by decreasing V^* rather than by decreasing β .

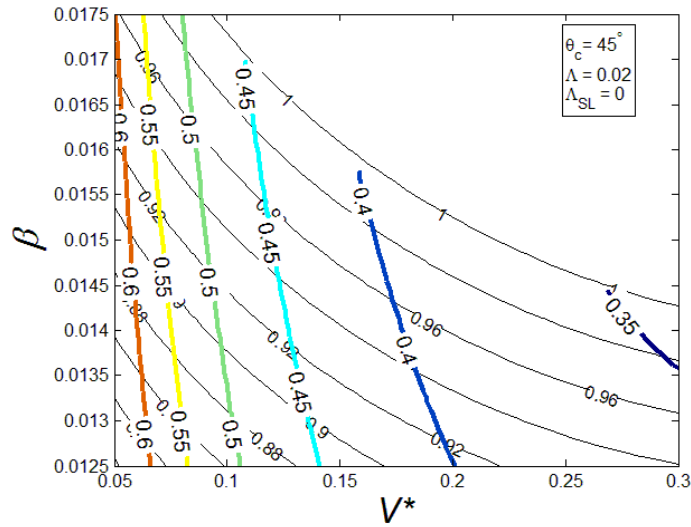


Figure 7.7: Contours for the normalized shear reaction at adhered end of DCB (Q_2^*). The contours are plotted with varying β and V^* . The other three governing parameters are fixed at $\theta_c = 45^\circ$, $\Lambda = 0.02$, and $\Lambda_{SL} = 0$.

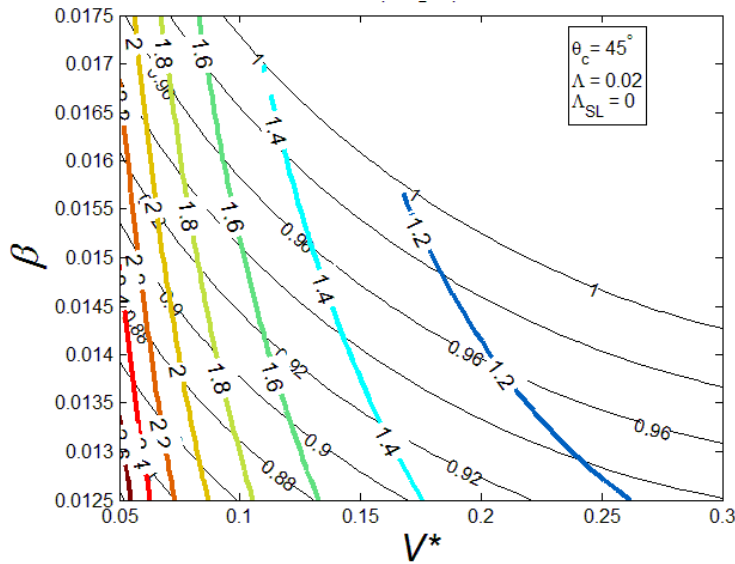


Figure 7.8: Contours for the normalized Laplace pressure ($F_p^*/(x_2^* - x_1^*)$). The contours are plotted with varying β and V^* . The other three governing parameters are fixed at $\theta_c = 45^\circ$, $\Lambda = 0.02$, and $\Lambda_{SL} = 0$.

To summarize the results of this section, while free end deflection or w_2^* was the focal point of discussion for the uncollapsed case, the point of contact or s_2^* is the focus of the adhesion discussion. Increasing β decreases the adhered

DCB length eventually leading to detachment ($s_2^* > 1$). Decreasing V^* increases the Laplace pressure which causes more beam deformation, resulting in a larger adhered length. Unlike in the unadhered configuration; where a strong correlation between M_R^* and w_2^* is found, M_R^* in the adhered configuration is a constant once Λ_{SL} , Λ and θ_c are specified. Changes that would tend to increase M_R^* such as decreasing V^* or decreasing β must be balanced by an increase in contact shear Q_2^* and/or an increase in adhered length. The increased capillary force cannot be balanced by increases in Q_2^* alone since a compatible beam deformation would require the reaction shear Q_R^* to increase as well; changing Q_R^* influences the moment distribution which generates the deflected curve which must satisfy essential boundary conditions at the crack tip. As a result when Laplace pressure increases there must be a decrease in s_2^* to satisfy compatibility and equilibrium.

7.3 Effect of Λ_{SL}

Results previously presented are for $\Lambda_{SL} = 0$, this parameter (Λ_{SL}) quantifies the adhesion strength of the solid-solid interface relative to the liquid-solid interface, and it is desirable to know how it impacts the adhered length. Ideally, we would have Λ_{SL} as one of the variables for a contour plot. However, for each Λ_{SL} there is only a narrow range of parameters (V^* , Λ , β , θ_c) that will give rise to convergent equilibrium solutions. For a given range of the other four parameters increase Λ_{SL} too much and the meniscus will be pushed to the base; decrease Λ_{SL} too much and the adhered configuration does not exist. For this reason contour plots at different values of Λ_{SL} , using β and V^* as variables, will be compared.

It is expected that Λ_{SL} will impact the s_2^* contours but what other quantities will be of interest? Λ_{SL} only factors into the boundary conditions and not the governing equations; therefore, if comparing at constant values of s_2^* we would not expect to see any differences in solution parameters previously discussed such as s_1^* and α . On the other hand from Eq. (7.11) increasing Λ_{SL} also increases M_R^* . Also note that in Eq. (7.2), $M_R^* = M_P^* + M_{ST}^* - \sqrt{2\Lambda_{SL}} - Q_2^* x_2^*$, M_P^* and M_{ST}^* are caused by the liquid and if Λ_{SL} is increased they will only experience changes due to differences in deflection. Which implies that increasing Λ_{SL} would tend to decrease M_R^* which contradicts Eq. (7.11). The most logical explanation is that an increase in Λ_{SL} should be accompanied by a decrease in Q_2^* . This may be expected since without adhesion Q_2^* must be a contact pressure (positive Q_2^*); however with adhesion then Q_2^* could pull the beams together (negative Q_2^*). Return to the plot for Q_2^* for the case previously discussed (Figure 7.7) in which $\Lambda_{SL} = 0$, as expected Q_2^* is positive indicating a contact pressure between the DCB beams.

Now consider what happens when Λ_{SL} is increased to 0.01, the resulting Q_2^* contour plot is shown Figure 7.9. As hypothesized the increase in Λ_{SL} results in a decrease in Q_2^* . In fact in most regions of this plot, Q_2^* is negative, corresponding to adhesive force between the two beams. Furthermore, the slope of the negative Q_2^* contours in Figure 7.9 is opposite to those in Figure 7.7. Specifically, the magnitude of the adhesive force ($|Q_2^*|$) increases with decreasing β and increasing

V^* (same as adhered length). We again use Eq. (7.12) to explain the coupled response of Q_2^* and s_2^* to changes in β and V^* . As described before the decrease in M_p^* caused by increasing V^* is primarily balanced by a decrease in Q_2^* , seen in both Figure 7.7 and Figure 7.9. On the other hand, the increase in M_p^* that would be caused by a decrease in β cannot be balanced by an increase in Q_2^* since it would lead to Q_r^* causing the deflected curve to not satisfy crack tip essential boundary conditions. Thus a greater DCB length is pulled into adhesion to reduce M_p^* and satisfy equilibrium. The net result is actually a slight reduction in M_p^* and Q_2^* is adjusted by Eq. (7.12) so that the product $Q_2^*x_2^*$ balances the change in M_p^* . This behaviour tends to give higher $|Q_2^*|$ when the length of DCB in contact $1 - s_2^*$ is larger. In Figure 7.7 $Q_2^* > 0$ and Q_2^* increases as β decreases while in Figure 7.9 $Q_2^* < 0$ and Q_2^* decreases as β decreases; in each case changes in M_p^* are slight so the product $Q_2^*x_2^*$ must remain nearly constant. Note that in Figure 7.9 the $Q_2^* = 0$ contour appears jagged because the shooting method has difficulty converging to the desired residual when the sign of Q_2^* is changing.

Comparing the s_2^* contours in Figure 7.9 to those in Figure 7.7 also provides valuable information. Firstly the range of β in Figure 7.9 is much larger indicating that by adding adhesion the DCB can be adhered for shorter beams relative to the gap. Secondly, the s_2^* contours in Figure 7.9 are flatter indicating less dependence on the drop volume V^* . In this case some of the moment required to hold the beam in this configuration is supplied by adhesion so the DCB is less sensitive to

the forces supplied by the drop. In fact, in some situations the adhesive force and moment may be sufficient to cause s-shaped adhesion without the presence of liquid on the beam's free span (crack); this is the case for the adhesion energy measurement experiments [18], [19].

If Λ_{SL} is again increased this time to $\Lambda \cos \theta_c = 0.01414$ (which is to approximate capillary adhesion to be discussed in section 7.5) the Q_2^* contours are shown in Figure 7.10. Further increasing Λ_{SL} continues to create the same patterns: Q_2^* decreases, the maximum β for which the configuration can exist increases, and the s_2^* contours become flatter.

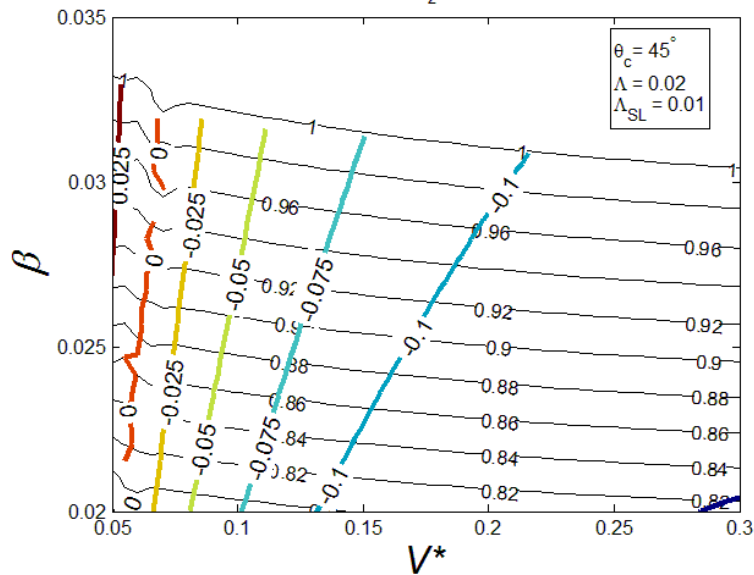


Figure 7.9: Contours for the normalized shear reaction at adhered end of DCB (Q_2^*). The contours are plotted with varying β and V^* . The other three governing parameters are fixed at $\theta_c = 45^\circ$, $\Lambda = 0.02$, and $\Lambda_{SL} = 0.01$.

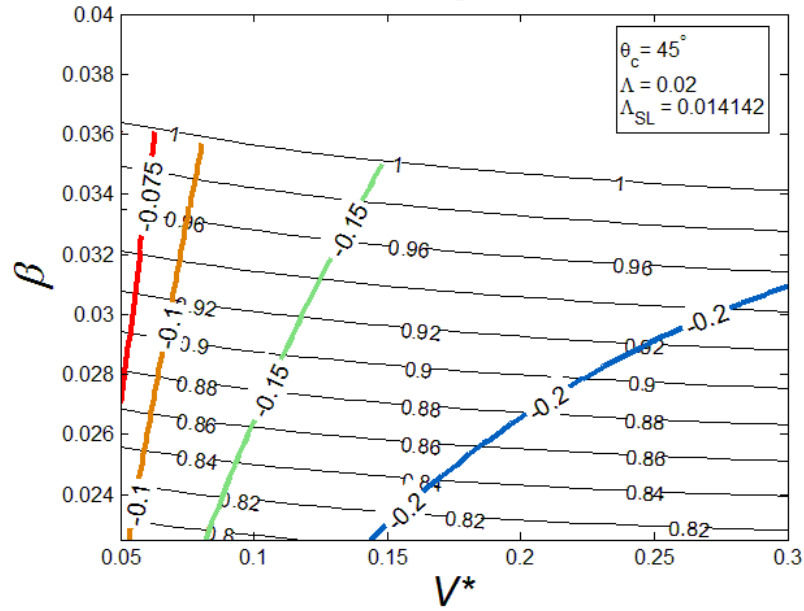


Figure 7.10: Contours for the normalized shear reaction at adhered end of DCB (Q_2^*). The contours are plotted with varying β and V^* . The other three governing parameters are fixed at $\theta_c = 45^\circ$, $\Lambda = 0.02$, and $\Lambda_{SL} = \Lambda \cos \theta_c = 0.01414$.

The bending moment distribution along the DCB is shown in Figure 7.11. Here the thick red dashed line corresponds to $\Lambda_{SL} = 0$ and the thick solid black line corresponds to $\Lambda_{SL} = 0.01$. Figure 7.11 can be used to highlight several of the points made in this section. First the M^* intercept is equal to M_R^* given by Eq. (7.11) which is higher for the $\Lambda_{SL} = 0.01$ case. Second, as previously described increasing Λ_{SL} decreases Q_2^* , as a result to maintain force balance the reaction Q_R^* must increase; This is represented by the $\Lambda_{SL} = 0.01$ curve having a more negative slope at $s^* = 0$. Finally the $\Lambda_{SL} = 0.01$ curve does not end at $M^* = 0$ because there is a moment applied at the crack tip due to adhesion. In the adhered case M^* may not monotonically decrease from M_R^* to zero as it did in the uncollapsed case; as a result M_R^* does not have the same impact on the beam deflection as it did in the uncollapsed case.

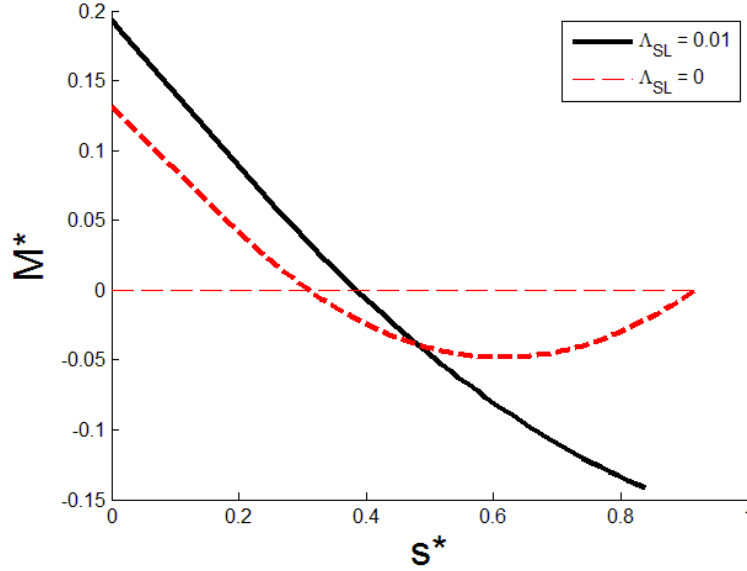


Figure 7.11: Comparing bending moment diagrams for $\Lambda_{SL} = 0.01$ $\beta = 0.02$, and for $\Lambda_{SL} = 0$, $\beta = 0.01$. With governing parameters $V^* = 0.2$, $\theta_c = 30^\circ$, and $\Lambda = 0.01$.

7.4 Discrepancy between the Linear and Nonlinear Models

As in the uncollapsed case we would like to know the discrepancy between the results given by the linear and nonlinear theories to judge if the linear theory provides sufficient accuracy. In this case define the discrepancy between the models as follows

$$Discrepancy = \left| (x^*(s_2^*))_{nonlinear} - (x_2^*)_{linear} \right|. \quad (7.14)$$

The discrepancy compares the x -coordinate of the crack tip predicted from both models. A contour plot for this variable is shown in Figure 7.12. This plot corresponds to $\Lambda_{SL} = 0.01414$ previously discussed, and it had a relatively large range of β for which adhered configuration exists. Therefore, this case is expected to have a relatively large discrepancy. In Figure 7.12 the largest error magnitude is 7×10^{-4} which is negligible considering that it is of the same order as the residuals used to determine convergence. Again for the range of β relevant to collapse and adhesion the linear model provides sufficient accuracy.

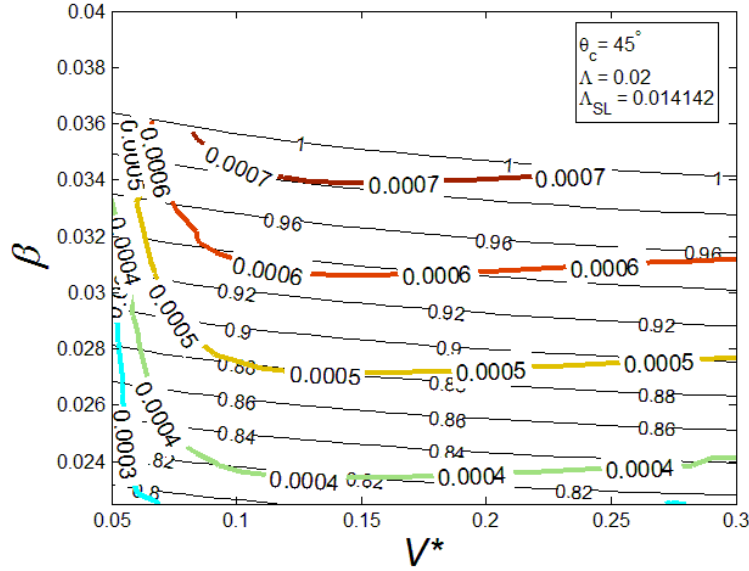


Figure 7.12: Contours for the discrepancy between linear and nonlinear beam theories. The contours are plotted with varying β and V^* . The other three governing parameters are fixed at $\theta_c = 45^\circ$, $\Lambda = 0.02$, and $\Lambda_{SL} = \Lambda \cos \theta_c = 0.01414$.

7.5 Comparison with Previous Works

Several previous works studied the adhesion of beams or hairs dipped in liquid [1], [24], [25]. The typical procedure was to submerge the free end of the beams in liquid causing the beams to clump together and measure the “dry” beam length. These works were each accompanied by an energy analysis comparing strain energy to adhesion energy. The result transformed to our normalized parameters⁶

$$\left(\frac{L_{dry}}{L}\right)^4 = \frac{9}{2} \frac{\beta^2}{\Lambda \cos \theta_c}. \quad (7.15)$$

In these works adhesion was modeled as capillary pressure caused by a thin film of interstitial liquid between the hairs; cohesion between the two solid beams in contact is ignored. The thickness of the film is on the order of the surface roughness of the beams. In addition, these works used $L - L_{dry}$ as the length to

⁶ In [1],[24] $\cos \theta_c$ does not appear making the equations in these works only valid for perfectly wetting liquids

determine the adhesion energy and L_{dry} as the length to determine the strain energy. That is, the transition zone from the dry part of the beams to adhered part of the beams was completely neglected. This may be appropriate if the transition zone is significantly smaller than the dry area and the adhered area. However, it is clear from the photographs shown in [1], [24] that there is a noticeable transition zone, occupying about 10% of the beam's length, between the end of the dry area (s_1^* in this work) and the beginning of the adhered area (s_2^* in this work). It appears that experimentally s_1^{*7} was the quantity being measured for L_{dry} , which was used to calculate the adhesion energy, but the strain energy of the beam is obtained based on $L_{dry} = s_2^*$. In other words, to calculate the beams' deflection, there is assumed to be no liquid in the transition zone, while to calculate the adhesion energy, the beams are assumed to be in contact in the transition zone. This is an apparent contradiction. Furthermore, from the results presented previously, the meniscus geometry in the transition zone can play an important role in determining the capillary forces on the beam and hence the adhered length, and should be considered carefully.

Since L_{dry} / L given by Eq. (7.15) is neither s_1^* nor s_2^* , we compare both s_1^* and s_2^* predicted from our work to Eq. (7.15) and the experimental results from Liu *et al.* [25]. When determining what to use for the adhesion energy some care is needed because the other works used a different energy reference state without liquid between the hairs. As a result they obtained the following adhesion energy

⁷ There is some ambiguity as to whether the meniscus peak or point of contact with the beam was measured

$(\Lambda_S - \Lambda_{SL})(1 - s_2^*)$. Physically this is the energy required to separate the solid-liquid interface and then remove the area of liquid (cohesively join it with other liquid) that was created by separating the interface $(1 - s_2^*)$ (See Dupree Equation Eq. (2.23)). Using Young's Equation (Eq. (2.3)) this can be simplified to $\Lambda \cos \theta_c (1 - s_2^*)$. Therefore, to compare with Eq. (7.15), in the result of the "J-integral", Eq. (3.37), we should replace Λ_{SL} with $\Lambda \cos \theta_c$. Following the data from Liu *et al.* [25] we set $\theta_c = 0^\circ$, $E = 4.512$ GPa, $\gamma_{SL} = 20.6$ mN/m, $D = 25$ mm, $I = 2.083 \times 10^{-3} \text{ mm}^4$ and vary h from 2 mm to 7 mm. The total length of the hairs was not listed, however as long as the beams are adhered it is not a factor. So $L = 70$ mm, which is sufficient for the adhered configuration to form, was chosen. Furthermore, a small drop size $V^* = 0.02$ was chosen to try to mirror the experiments. The comparison is shown in Figure 7.13. The black circles represent the experimental measurement of L_{dry} from Liu *et al.* [25] and the solid green curve represents Eq. (7.15); both have been normalized to be consistent with the results given by our model. The black dashed line represents s_2^* and the red dot-dash line represents s_1^* , both predicted by our model. Clearly Eq. (7.15) is between s_1^* and s_2^* from our model which would be expected and provides verification for our model. As previously mentioned, the derivation of Eq. (7.15) involves an apparent contradiction. In addition, in its derivation, the limit of $V^* = 0$ has been taken whereas the photographs in [1], [24]⁸ clearly show non-negligible V^* , and are similar to the configuration from our simulation shown in

⁸ Note that it is valid to compare the experimental data from Liu *et al.* [25], with the photographs from Roman *et al.* [1], Bico *et al.* [24] since it was a duplication of this experiment.

Figure 7.14. Therefore it may have been reasonable to expect that Eq. (7.15) would not provide a good fit to the experimental data. Nevertheless, with the exception of one point⁹ Eq. (7.15) fits the measured data well, which remains to be puzzle.

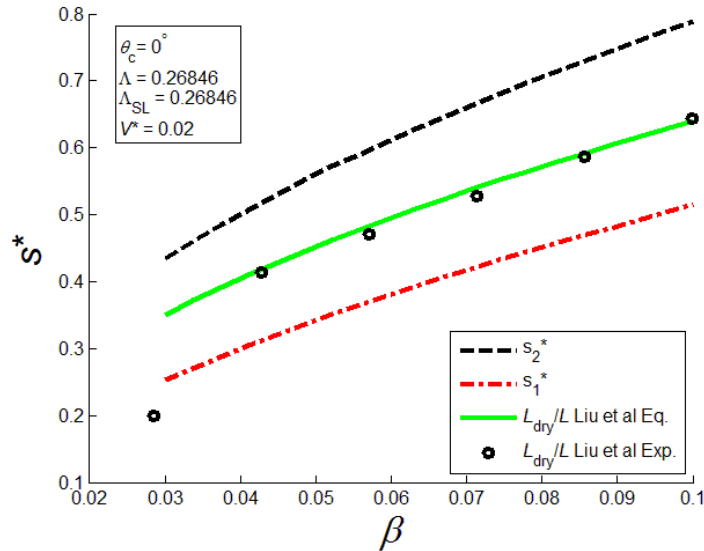


Figure 7.13: Comparison of s_1^* and s_2^* with results from Lui *et al.* [25]. β varied the other four governing parameters are fixed at $\theta_c = 0^\circ$, $\Lambda = 0.2685$, $\Lambda_{SL} = 0.2685$, $V^* = 0.02$.

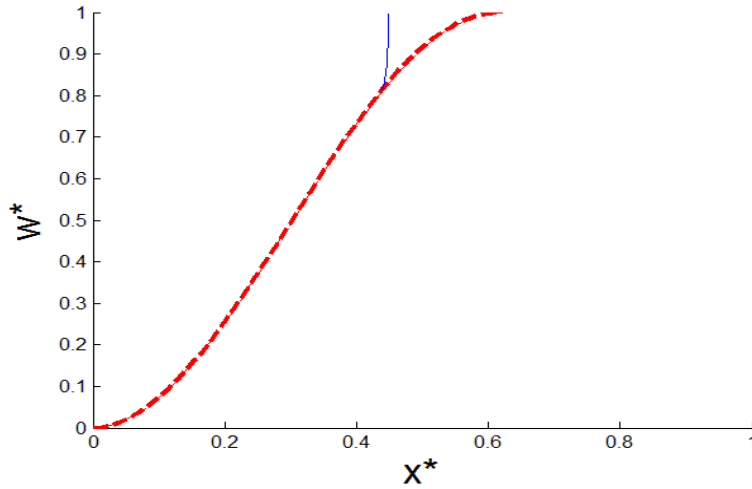


Figure 7.14: Elastic curve and meniscus location of s-shaped adhered hair for $V^* = 0.02$. The other four governing parameters are fixed at $\theta_c = 0^\circ$, $\Lambda = 0.2685$, $\Lambda_{SL} = 0.2685$, $\beta = 0.06$.

⁹ While it was not mentioned in [25] this discrepancy could have been caused by increased capillary rise due to the decreased hair spacing in this case.

7.6 Summary

Generating the s-shaped adhered configuration takes considerably more energy than initiating the collapse of the DCB. As a result its existence requires a combination of higher Λ and lower β . Decreases in β increase the adhered length of the DCB; the same can be said for decreases in V^* . Increasing Λ_{SL} has several effects. First it allows the configuration to exist at higher values of β . Second it dampens the dependency of the adhered length on V^* . Third, it alters the nature of the contact force from being a contact pressure at low Λ_{SL} to eventually becoming adhesive at larger Λ_{SL} . Similarly to the uncollapsed configuration it is deemed acceptable to neglect geometrical nonlinearity in the beam model.

Chapter 8 Conclusions and Future Work

In this work, the collapse and adhesion of a double cantilever beam (DCB) with a free end liquid droplet are studied. Justification for only considering a free end droplet is based on pressure gradients within the drop driving it to the free end. Both Laplace pressure and surface tension forces are considered as beam loadings generated by the presence of liquid. The Laplace pressure is found to be extremely dependent on the beam's deflection, which often results in smaller drops collapsing the DCB more easily. The surface tension force, which has been previously neglected in the literature, is found to be important unless both the contact angle and the ratio of beam gap to length are small. Allowing the base meniscus to move towards the base as the DCB deflects to maintain a constant liquid volume introduces an important nonlinear coupling effect. It changes the area on which the Laplace pressure acts and the moment created by one of the surface tension forces. There are a number of other coupled nonlinear effects due to the interrelationship between the constraint and beam equations, however variation of Laplace pressure and base meniscus movement due to deflection are found to be the most important. Four dimensionless parameters governing DCB collapse are identified Λ , β , θ_c , and V^* , which are the ratio of surface tension to beam bending stiffness, ratio of beam length to half of the gap spacing, contact angle, and normalized liquid drop volume. How each parameter influences DCB collapse has been accurately described by the nondimensional number N . Collapse is predicted when N given by

$$N = \frac{\beta \left(3.1458 + 2.4041V^* - \left(1.3147 + 6.4924\beta + \left(\frac{0.1485 + 1.0870\beta}{\cos(\theta_c)} \right) \right) V^{*2} \right)}{\sqrt{2\Lambda(1.382\beta + \cos(\theta_c))}}. \quad (8.1)$$

is less than 1. Finally, comparison of the linear beam model with one accounting for nonlinear geometrical effects shows that within the practical range of governing parameters the linear model provided sufficient accuracy.

DCB adhesion in an s-shaped configuration takes considerably more energy than merely DCB collapse. As a result this configuration is more likely to exist at small values of β where the discrepancy between the linear and nonlinear models is negligible. Within this configuration decreases in β increase the length of the DCB in contact; the same can be said for decreases in V^* . In previous works the former behaviour had been widely studied experimentally whereas the latter behaviour has been experimentally observed but not analyzed. Decreasing V^* also increases the crack tip contact force which lessens the increase in adhered length decreasing V^* would otherwise cause. For this case the governing equations are similar to those in the uncollapsed case; however an importance difference is the adhesion natural boundary conditions which influence the beam's internal moment by influencing the reaction shear and moment required for equilibrium. These boundary conditions introduce an additional governing parameter Λ_{SL} representing the ratio of the energy to separate the adhered beams (and introduce the liquid to the interface) to the beam's bending rigidity. Increasing Λ_{SL} has several effects most importantly it allows the configuration to exist at higher values of β ; furthermore, increasing Λ_{SL} also causes the crack tip contact force to eventually become adhesive.

Future work could include, modelling the transition from collapse to s-shaped adhesion, and extending the analysis to the situation where the liquid drop has 3-D geometry. Because of the limited symmetry (if any) and the presence of edge effects considering 3-D drop geometry present a considerable increase in the difficulty of the problem. As an example, Appendix F illustrates a rigorous treatment for the case of an axisymmetric drop sandwiched between undeformable solids. Experimental work could also be done to verify the collapse relation as well as use the adhesion model to measure adhesion energies.

Bibliography

- [1] Roman, B., Bico, J., “Elasto-capillary: deforming an elastic structure with a liquid droplet”, *J. Phys.: Condens. Matter*, 22 (2010), 16pp.
- [2] Mastrangelo, C., “Suppression of Stiction in MEMS”, *Materials Research Society Symposium-Proceedings*, v 605 (2000) p 105-116,
- [3] Mastrangelo, C., Hsu, C. “Mechanical Stability and Adhesion of Microstructures Under Capillary Forces-Part I: Basic Theory”, *Journal of Microelectromechanical Systems*, Vol. 2 (1993), pp. 33-43
- [4] Tanaka, T., Morigami, M., Atoda, N., “Mechanism of Resist Pattern Collapse during Development Process”, *Jpn. J. Appl. Phys.*, Vol. 32 (1993), pp.6059-6064.
- [5] Hui, Y., Yang, K., Jiao, B., Jing, Y., Chen, D., “Simple Sticking Models and Adhesion Criterion to Predict Sticking Effects of Fixed-Fixed Beams in RF MEMS Switch Design”, *Proceedings of the 2010 5th IEEE International Conference on Nano/Micro Engineered and Molecular Systems*, 2010
- [6] Kotera, M., Ochiai, N., “Three-dimensional simulation of resist pattern deformation by surface tension at the drying process”, *Microelectronic Engineering*, 78-79 (2005), pp. 515-520.
- [7] Abe T., Reed M., “Control of liquid bridging induced stiction of micromechanical structures”, *J. Micromech. Microeng.*, 6 (1996), pp.213-217.
- [8] Ouakad, H., Younis, M., “Modeling and Simulations of Collapse Instabilities of Microbeams due to Capillary Forces”, *Mathematical Problems in Engineering*, Vol. 2009. (2009)
- [9] Peng, Y., Li, X., Kui, W., “Capillary Adhesion between the Microcantilever and the Substrate”, *Key Engineering Materials*, Vols. 353-358 (2007) p 770-773
- [10] Rose, F., Hattori, M., Kobayashi, D., Toshiyoshi, H., Fujita, H., Kawakatsu, H., “Application of capillary forces and stiction for lateral displacement, alignment, suspension and locking of self-assembled microcantilevers”, *J. Micromech. Microeng.*, 16 (2006) pp 2077-2085
- [11] Lee, H.J., Park, J.T, Yoo, J.Y, An, I., Oh, H.K., “Resist Pattern Collapse Modeling for Smaller Features”, *Journal of the Korean Physical Society*, Vol. 42 (2003) pp. S202-S206.
- [12] Yoshimoto, K., Stoykovich, M.P., Cao, H.B., de Pablo, J.J., Nealey, P.F., Drugan, W.J., “A two-dimensional model of the deformation of photoresist structures using elastoplastic polymer properties”, *Journal of Applied Physics*, Vol. 96 Number 4 (2004) pp. 1857-1865.
- [13] Yeh, W.-M., Noga, D., Lawson, R., Tolbert, L., Henderson, C., “Comparison of positive tone versus negative tone resist pattern collapse behaviour”, *J. Vac. Sci. Technol. B* 28 (2010) C6S6-C6S11
- [14] Mastrangelo, C.H., Hsu, C.H., “A simple experimental technique for the measurement of the work of adhesion of microstructures”, *IEEE Solid-State*

- Sensor and Actuator Workshop, Hilton Head Island, South Carolina, June 22-25, 1992, IEEE, 1992, pp. 208-212
- [15] Mastrangelo, C., Hsu, C., “Mechanical Stability and Adhesion of Microstructures under Capillary Forces-Part II: Experiments”, *Journal of Microelectromechanical Systems*, Vol. 2, NO. I (1993), pp. 44-55
- [16] Wu, D., Fang, N., Sun, C., Zhang, X., “Stiction problems in releasing of 3D microstructures and its solution”, *Sensors and Actuators A* 128 (2006) 109–115
- [17] Raccurt, O., Tardif, F., D'Avitaya, F.A., Vareine, T., “Influence of liquid surface tension on stiction of SOI MEMS”, *Journal of Micromechanics and Microengineering*, 14 (2004) pp. 1083-1090.
- [18] de Boer, M. P., Michalske, T. A., “Accurate method for determining adhesion of cantilever beams”, *J. Appl. Phys.* 86 (1999) pp 817-827
- [19] Leseman, Z.C., Carlson, S.P., Mackin, T.J., “Experimental measurements of the strain energy release rate for stiction-failed microcantilevers using a single-cantilever beam peel test”, *Journal of Microelectromechanical Systems* 16 (2007), pp. 38-43.
- [20] Legtenberg, R., Tilmans, H.A.C.; Elders, J.; Elwenspoek, M., “Stiction of surface micromachined structures after rinsing and drying: model and investigation of adhesion mechanisms”, *Sensors and Actuators A* 43(1994) p 230-238
- [21] Tas, N., Sonnenberg, T., Jansen, H., Legtenberg, R., Elwenspoek, M., “Stiction in surface micromachining”, *Journal of Micromechanics and Microengineering* 6 (1996) p 385-397
- [22] van Spengen, W. M., Puers, R., De Wolf, I., “A physical model to predict stiction in MEMS”, *J. Micromech. Microeng.* 12 (2002) 702-713
- [23] Delrio, F. W., de Boer, M. P., Knapp, J. A., Reedy, E. D. Jr, Clews, P. J., Dunn, M. L., “The role of van der Waals forces in adhesion of micromachined surfaces”, *Nature Mater.* 4 (2005) pp. 629-634
- [24] Bico, J., Roman, B., Moulin, L., Boudaoud, A., “Elastocapillary coalescence in wet hair”, *Nature*, Vol432 (2004) pp. 690
- [25] Liu, J.L., Feng, X.Q., Xia, R., Zhao, H.P., “Hierarchical capillary adhesion of microcantilevers or hairs”, *J. Phys. D: Appl. Phys.* 40 (2007) 5564–5570
- [26] Liu, J.L., Feng, X.Q., “Capillary Adhesion of Microbeams: Finite deformation analysis”, *Chin. Phys. Lett.* VOL24, No.8 (2007) 2349-2352
- [27] Cengel, Y.A., Cimbala, J.M., *Fluid Mechanics Fundamentals and Applications*, McGraw-Hill, New York, 2006, pp. 287
- [28] Israelachvili, J., *Intermolecular and Surface Forces*, 2nd Ed, Academic Press Limited, San Diego, 1992, pp. 312-318
- [29] Butt, H.J., Graf, K., Kappl, M., *Physics and Chemistry of Interfaces*, Wiley-VCH, Weinheim, 2003, pp. 8-12, 118-120
- [30] Adamson, A., Gast, A., *Physical Chemistry of Surfaces*, Sixth Edition, Wiley, 1997
- [31] Hibbeler, R.C., *Mechanics of Materials*, SI second ed., Pearson Prentice Hall, Singapore, 2005, pp 607-614

- [32] Stewart, J., *Calculus Early Transcendentals*, 5th Ed, Thomson Brooks/Cole, 2003, Pg. 668
- [33] Glassmaker, N., Hui, C., “Elastica solution for a nanotube formed by self-adhesion of a folded thin film”, *J. of Appl. Phys.* Vol. 96 No. 6 (2004), 3429–3434
- [34] Tang, T., Glassmaker, N., “On the Inextensible Elastic Model for the Collapse of Nanotubes”, *Mathematics and Mechanics of Solids*, 15 (2010), 591–606
- [35] Ugural, A.C., Fester, S.K., *Advanced Strength and Applied Elasticity*, Fourth ed., Prentice Hall, New Jersey, 2003, pp. 187,198-9,205
- [36] Love, A., *A treatise on the mathematical theory of elasticity Volume II*, Cambridge: at the university press, 1893. pp.24-28
- [37] Ding, J., Wen, S., Meng, Y., “Theoretical study of the sticking of a membrane strip in MEMS under the Casimir effect”, *Journal of Micromechanics and Microengineering*, 11 (2001) pp 202-208
- [38] Gdoutos, E.E., *Fracture Mechanics and Introduction*, 2nd ed, Springer, 2005, Pp. 161-168
- [39] Meseguer, J., Slobozhanin, L. A., Perales, J. M., “A review on the stability of liquid bridges”, *Adv. Space. Res.*, Vol. 16, No. 7 (1995), pp. (7)5-(7)14
- [40] Zhao, Y., “Stiction and Anti-Stiction in MEMS and NEMS”, *Acta Mechanica Sinica (English Series)*, Vol. 19 No.1 (2003), 10pp
- [41] Reddy, J.N., *An Introduction to Nonlinear Finite Element Analysis*, Oxford University Press, 2004, pp 88-95
- [42] Gilat, A., Subramaniam, V., *Numerical Methods for Engineers and Scientists: An Introduction with Applications using MATLAB*, Wiley, 2008, pp 62-67, 127-130,334, 353-354
- [43] Chini, S. F., Amirfazli, A., “Understanding Pattern Collapse in Photolithography Process Due to Capillary Forces”, *Langmuir*, 26 (2010), 13707-13714
- [44] Myshkis, A.D., Babskii, V.G., Kopachevskii, N. D., Slobozhanin, L.A., Tyuptsov, A.D., *Low-Gravity Fluid Mechanics*, Springer-Verlag, Berlin, 1987, pp 31

Appendix A *Details of Modified Newton-Raphson Method*

Write the n constraint equations in the following form

$$f_i(x_j) = f_i(x_1, \dots, x_n) = 0, i, j = 1 \dots n$$

Where each f_i represent a constraint equation and each x_j represents an unknown variable to be determined. For the linear uncollapsed case f_i would consist of Eqs. (3.24), (3.25), (3.26), (3.28), and (3.29); x_j would corresponds to α , x_1^* , θ_2 , l_1^* , and l_2^* . The associated Jacobian is given by

$$J_{ij} = \frac{\partial f_i}{\partial x_j}.$$

To solve guess values for each x_j then calculate the change in each x_j as

$$\Delta x_j = -(J_{ij})^{-1} f_i,$$

where J_{ij} and f_i are evaluated at the guess value x_j . The new guess is then

$$(x_j)_{new} = x_j + \omega \Delta x_j,$$

where ω is a relaxation factor used to decrease fluctuation although it slows convergence. Next each $(x_j)_{new}$ would be checked for physicality; if the obtained value is outside of physical bounds it would be recalculated. Each constraint equation was assigned to one x_j , rearranging the equation gives

$$(x_j)_{new} = g_j((x_1)_{new} + \dots (x_{j-1})_{new} + x_j + \dots x_n)$$

where g_i represents a constraint equation rearranged to have the j th unknown variable x_j on the left side (Note: this variable may also appear on the right side).

Convergence was measured using L2 norms of f as well as the absolute and relative changes in x_j from iteration to iteration. The solution was considered converged when the L2 of f was less than 5×10^{-4} and the L2 norm of either the absolute or relative x_j residuals was less than 5×10^{-4} .

Appendix B Details of Runge-Kutta Shooting Method

From the beam governing Eqs. (4.7), (4.8) and (4.9) dropping the * from all variables for simplicity, to solve these equations using 4th order Runge-Kutta [42] we can write the following

$$\begin{aligned}\frac{d\phi}{ds} &= f_\phi(s, \phi, x, w) & f_\phi(s, \phi, x, w) &= M & \phi(0) &= 0 \\ \frac{dx}{ds} &= f_x(s, \phi, x, w) & f_x(s, \phi, x, w) &= \cos \phi & x(0) &= 0 \\ \frac{dw}{ds} &= f_w(s, \phi, x, w) & f_w(s, \phi, x, w) &= \frac{\sin \phi}{\beta} & w(0) &= 0.\end{aligned}\tag{B.1}$$

where $M = d\phi/ds = M_R - Q_R x + M_{ST}(s) + M_P(s)$. The first values of x, w, ϕ are obtained from the $s = 0$ boundary conditions and the subsequent values are obtained using the following relationship

$$\begin{aligned}\phi_{i+1} &= \phi_i + \frac{1}{6}(K_{\phi,1} + 2K_{\phi,2} + 2K_{\phi,3} + K_{\phi,4})h_i \\ x_{i+1} &= x_i + \frac{1}{6}(K_{x,1} + 2K_{x,2} + 2K_{x,3} + K_{x,4})h_i \\ w_{i+1} &= w_i + \frac{1}{6}(K_{w,1} + 2K_{w,2} + 2K_{w,3} + K_{w,4})h_i.\end{aligned}\tag{B.2}$$

where h_i is the i th step width and the remaining quantities are determined as follows

$$\begin{aligned}K_{\phi,1} &= f_\phi(s_i, \phi_i, x_i, w_i) \\ K_{x,1} &= f_x(s_i, \phi_i, x_i, w_i) \\ K_{w,1} &= f_w(s_i, \phi_i, x_i, w_i) \\ K_{\phi,2} &= f_\phi\left(s_i + \frac{1}{2}h_i, \phi_i + \frac{1}{2}K_{\phi,1}h_i, x_i + \frac{1}{2}K_{x,1}h_i, w_i + \frac{1}{2}K_{w,1}h_i\right) \\ K_{x,2} &= f_x\left(s_i + \frac{1}{2}h_i, \phi_i + \frac{1}{2}K_{\phi,1}h_i, x_i + \frac{1}{2}K_{x,1}h_i, w_i + \frac{1}{2}K_{w,1}h_i\right) \\ K_{w,2} &= f_w\left(s_i + \frac{1}{2}h_i, \phi_i + \frac{1}{2}K_{\phi,1}h_i, x_i + \frac{1}{2}K_{x,1}h_i, w_i + \frac{1}{2}K_{w,1}h_i\right) \\ K_{\phi,3} &= f_\phi\left(s_i + \frac{1}{2}h_i, \phi_i + \frac{1}{2}K_{\phi,2}h_i, x_i + \frac{1}{2}K_{x,2}h_i, w_i + \frac{1}{2}K_{w,2}h_i\right) \\ K_{x,3} &= f_x\left(s_i + \frac{1}{2}h_i, \phi_i + \frac{1}{2}K_{\phi,2}h_i, x_i + \frac{1}{2}K_{x,2}h_i, w_i + \frac{1}{2}K_{w,2}h_i\right)\end{aligned}\tag{B.3}$$

$$K_{w,3} = f_z(s_i + \frac{1}{2}h_i, \phi_i + \frac{1}{2}K_{\phi,2}h_i, x_i + \frac{1}{2}K_{x,2}h_i, w_i + \frac{1}{2}K_{w,2}h_i)$$

$$K_{\phi,4} = f_\phi(s_i + h_i, \phi_i + K_{\phi,3}h_i, x_i + K_{x,3}h_i, w_i + K_{w,3}h_i)$$

$$K_{x,4} = f_x(s_i + h_i, \phi_i + K_{\phi,3}h_i, x_i + K_{x,3}h_i, w_i + K_{w,3}h_i)$$

$$K_{w,4} = f_w(s_i + h_i, \phi_i + K_{\phi,3}h_i, x_i + K_{x,3}h_i, w_i + K_{w,3}h_i)$$

For this problem M_R and Q_R are not known beforehand so it is necessary to use a shooting method where M_R and Q_R are guessed then the solution is compared with boundary conditions at the end. Note that even in the adhered case where we have an expression for M_R , the derivation of the expression used end boundary conditions which we must force the Runge-Kutta solution to obey. Residuals measuring how well the Runge-Kutta solution satisfies the end conditions are calculated; if the L2 norm of these residuals is less than 1×10^{-4} then the solution is considered converged. Note that since the values from the Runge-Kutta solution are used in the Newton-Raphson iteration it is necessary to use stricter convergence criteria for Runge-Kutta. If the convergence criteria are not met new estimates for M_R and Q_R are obtained using secant interpolation and a new Runge-Kutta solution is obtained.

The quality of the Runge-Kutta solution depends on the step spacing and hence the number of steps. A convergence study was conducted to determine what spacing was necessary to obtain the desired solution accuracy. Two variables were studied, the free end deflection and the strain energy, the latter requiring numerical integration of the Runge-Kutta solution. The free end deflection shown in Figure B.1 converges within 1×10^{-5} if 4 or more steps are used, however the strain energy, Figure B.2, requires 12 steps to converge to the third significant figure (strain energy is not used for subsequent calculations so it is not needed to a

high degree of accuracy). Because the method is 4th order it converges quickly as the point spacing is decreased. In the analysis the minimum number of steps used was 16. Note that there are some complications because we will force a point to be at the base meniscus and will adjust the divisions to give roughly uniform mesh on both sides. Generally similar mesh spacing would be used on each side of the meniscus; however, a minimum number of steps are enforced on both sides (4) for cases when the meniscus is close to either end.

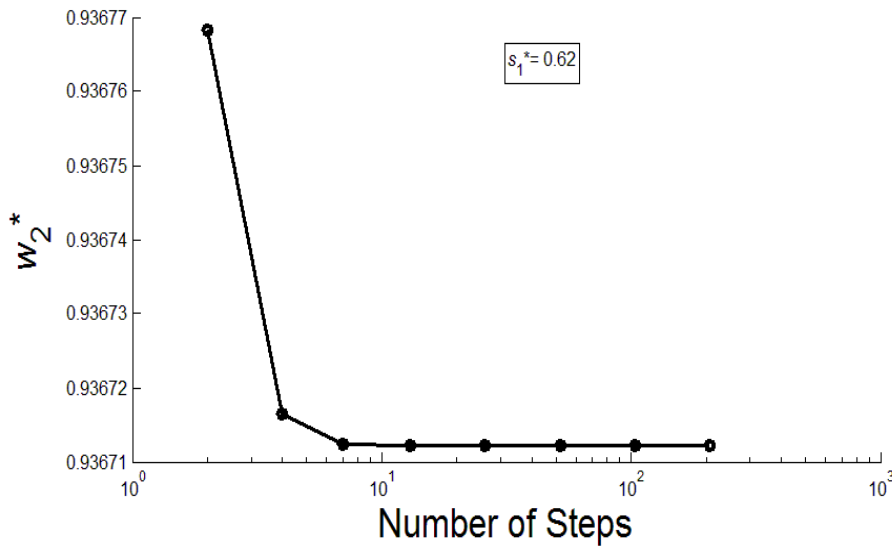


Figure B.1: Free end deflection convergence

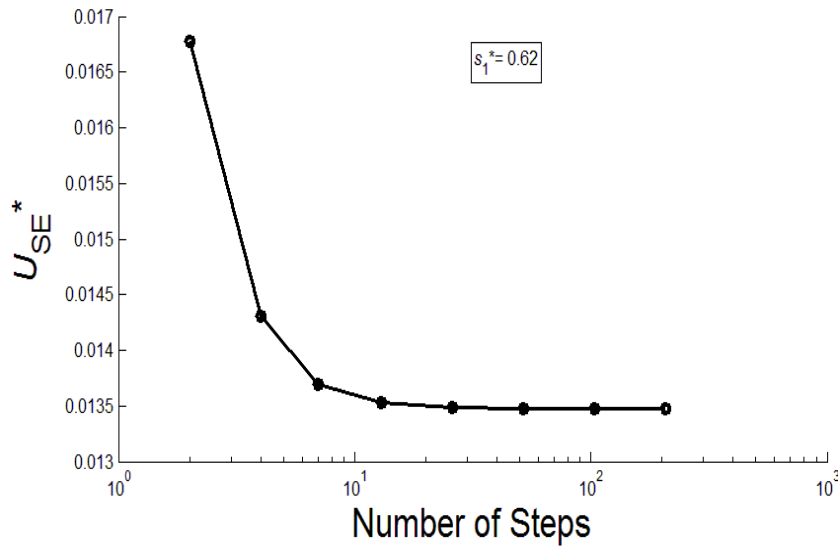


Figure B.2: Strain energy convergence

Appendix C Analytical Result for Nonlinear Beam Theory

The nonlinear beam governing equations can be manipulated with the objective of determining a simplified formula for M_R^* at collapse where $w^*(s_2^*) = 1$. First differentiate Eq. (4.7) and apply Eq. (4.8) and trigonometric identities to give

$$\frac{d^2\phi}{ds^{*2}} = -Q_R^* \underbrace{\frac{dx^*}{ds^*}}_{\cos\phi} + \frac{dM_{ST}^*}{ds^*} + \frac{dM_P^*}{ds^*} \quad (C.1)$$

$$\frac{dM_{ST}^*}{ds^*} = \Lambda \sin(\phi(s_1^*) + \theta_c - \phi(s^*)) \langle s^* - s_1^* \rangle^0$$

$$\frac{dM_P^*}{ds^*} = \frac{-\Lambda}{\alpha\beta} \left(\langle x^*(s^*) - x^*(s_1^*) \rangle \cos\phi + \beta \langle w^*(s^*) - w^*(s_1^*) \rangle \sin\phi \right).$$

Now integrating Eq. (C.1) with respect to ϕ over the length of the beam gives

$$\int_{\phi(0)=0}^{\phi(s_2^*)} \frac{d^2\phi}{ds^{*2}} d\phi = \underbrace{\int_{\phi(0)=0}^{\phi(s_2^*)} -Q_R^* \cos\phi d\phi}_{I_1} + \underbrace{\int_{\phi(0)=0}^{\phi(s_2^*)} \frac{dM_{ST}^*}{ds^*} d\phi}_{I_2} + \underbrace{\int_{\phi(0)=0}^{\phi(s_2^*)} \frac{dM_P^*}{ds^*} d\phi}_{I_3}, \quad (C.2)$$

where each integral will be evaluated separately. The left side of Eq. (C.2) can be integrated by changing the variable of integration as follows

$$\int_{\phi(0)=0}^{\phi(s_2^*)} \frac{d^2\phi}{ds^{*2}} d\phi = \int_0^{s_2^*} \frac{d^2\phi}{ds^{*2}} \frac{d\phi}{ds^*} ds^* = \frac{1}{2} \int_0^{s_2^*} \frac{d}{ds^*} \left[\left(\frac{d\phi}{ds^*} \right)^2 \right] ds^* = \frac{1}{2} \left((M_2^*)^2 - (M_R^*)^2 \right), \quad (C.3)$$

where M_2^* is the moment at s_2^* . The integral I_1 is easily integrated giving

$$\int_{\phi(0)=0}^{\phi(s_2^*)} -Q_R^* \cos\phi d\phi = -Q_R^* \sin(\phi(s_2^*)). \quad (C.4)$$

Similarly I_2 can easily be integrated however recall that due to the definition of the Macaulay Function Eq. (2.50) the integration from 0 to s_1^* is zero, thus

$$\int_{\phi(0)=0}^{\phi(s_2^*)} \frac{dM_{ST}^*}{ds^*} d\phi = \int_{\phi(s_1^*)}^{\phi(s_2^*)} \Lambda \sin(\phi(s_1^*) + \theta_c - \phi(s^*)) d\phi = \Lambda [\cos(\phi(s_1^*) + \theta_c - \phi(s_2^*)) - \cos(\theta_c)]. \quad (C.5)$$

The final integral I_3 ,

$$\int_{\phi(0)=0}^{\phi(s_2^*)} \frac{dM_P^*}{ds^*} d\phi = \frac{-\Lambda}{\alpha\beta} \int_{\phi(s_1^*)}^{\phi(s_2^*)} [\langle x^*(s^*) - x^*(s_1^*) \rangle \cos\phi + \beta \langle w^*(s^*) - w^*(s_1^*) \rangle \sin\phi] d\phi, \quad (C.6)$$

is more difficult and integration by parts must be used as follows

$$\int_{\phi(s_1^*)}^{\phi(s_2^*)} (x^*(s^*) - x^*(s_1^*)) \cos \phi d\phi = (x^*(s_2^*) - x^*(s_1^*)) \sin(\phi(s_2^*)) - \int_{\phi(s_1^*)}^{\phi(s_2^*)} \frac{\sin \phi \cos \phi}{M^*} d\phi$$

$$\int_{\phi(s_1^*)}^{\phi(s_2^*)} \beta (w^*(s^*) - w^*(s_1^*)) \sin \phi d\phi = -\beta (1 - w^*(s_1^*)) \cos(\phi(s_2^*)) + \int_{\phi(s_1^*)}^{\phi(s_2^*)} \frac{\sin \phi \cos \phi}{M^*} d\phi. \quad (\text{C.7})$$

Note: $\frac{dx^*}{d\phi} = \frac{dx^*}{ds^*} \frac{ds^*}{d\phi} = \frac{\cos \phi}{M^*}$, $\frac{dw^*}{d\phi} = \frac{dw^*}{ds^*} \frac{ds^*}{d\phi} = \frac{\cos \phi}{\beta M^*}$

Thus substituting Eq. (C.7) into Eq. (C.6) and applying Eq. (4.17) yields

$$\int_{\phi(0)=0}^{\phi(s_2^*)} \frac{dM_P^*}{ds^*} d\phi = -\Lambda \cos(\theta_c + \phi_1) \cos(\phi(s_2^*)) - \frac{\Lambda}{\alpha\beta} (x^*(s_2^*) - x^*(s_1^*)) \sin(\phi(s_2^*)) \quad (\text{C.8})$$

Finally substituting all the evaluated integrals Eq. (C.3), Eq. (C.4), Eq. (C.5), and

Eq. (C.8) back into Eq. (C.2) gives

$$\frac{1}{2} \left((M_2^*)^2 - (M_R^*)^2 \right) = -Q_R^* \sin(\phi(s_2^*)) + \Lambda \left[\cos(\phi(s_1^*) + \theta_c - \phi(s_2^*)) - \cos(\theta_c) \right]$$

$$- \Lambda \cos(\phi(s_1^*) + \theta_c) \cos(\phi(s_2^*)) - \frac{\Lambda}{\alpha\beta} (x^*(s_2^*) - x^*(s_1^*)) \sin(\phi(s_2^*)), \quad (\text{C.9})$$

this can be simplified by applying trigonometric identities as follows

$$\frac{1}{2} \left((M_2^*)^2 - (M_R^*)^2 \right) = -Q_R^* \sin(\phi(s_2^*)) + \Lambda \left[\sin(\phi(s_1^*) + \theta_c) \sin(\phi(s_2^*)) - \cos(\theta_c) \right]$$

$$- \frac{\Lambda}{\alpha\beta} (x^*(s_2^*) - x^*(s_1^*)) \sin(\phi(s_2^*)). \quad (\text{C.10})$$

Appendix D *MDISP Nonlinear Deflection Coupling ($\theta_c = 0$)*

Contours of MDISP are shown in Figure D.1. Note that changes in MDISP due to deflection may also influence x_1^* and this influence is most pronounced at low contact angles and deflections. For large V^* there are only small changes to MDISP with deflection, whereas for small V^* there are sharp changes with deflection at first, however these changes become more gradual near collapse. This behaviour is shown for $V^* = 0.1$ in Figure D.2. Also shown as comparison is the change of x_1^* with deflection. Here the initial drop in MDISP with deflection slows down the decrease of x_1^* with deflection. However, once the MDISP curve levels off x_1^* decreases sharply. This behaviour explains some of the trends observed in Figure 5.36 in the small V^* regime. Specifically, for $V^* < 0.15$, the contours are nearly vertical (small variation of x_1^* with increasing deflection) at small deflection but bend towards horizontal (rapid reduction of x_1^* with increasing deflection) near collapse.

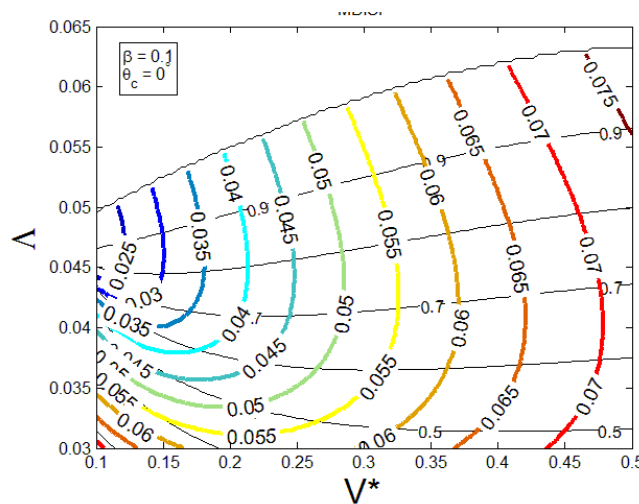


Figure D.1: Contours of normalized volume of liquid displaced by menisci (MDISP). The contours are plotted with varying Δ and V^* . The other two governing parameters are fixed at $\theta_c=0^\circ$ and $\beta=0.1$.

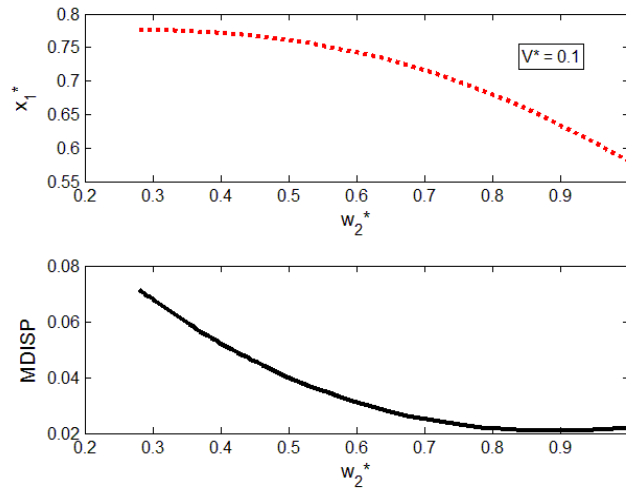


Figure D.2: Influence of MDISP on x_1^* . $V^* = 0.1$ with $\theta_c = 0^\circ$, $\beta = 0.1$

Knowing that MDISP can play a role on the position of the base meniscus it is desirable to understand the relative importance of the factors that influence its value. As shown in Eq. (5.5), for a given β , MDISP depends on the meniscus curvature (α) and the two terms in the summation, referred to earlier as the meniscus displacement factor (MDF) and shown in Figure 5.4. $MDF = \pi/2$ at $l_i^* = 0$ which corresponds to semicircular meniscus and decreases as l_i^* increases until $MDF = 0$ at $l_i^* = 1$ which corresponds to a cap height of zero. Each meniscus has a MDF and both contribute to the determination of x_1^* .

The MDF for the base meniscus is a function of l_1^* which has been discussed in section 5.2.1.2. In particular, from Eq. (5.8) l_1^* depends on the contact angle and the deflected angle ϕ_1 at the base meniscus. Because the slope of the sine function is maximized when its argument is 0, in the small contact angle regime, the same change in ϕ_1 will cause a larger change in l_1^* than it would in the moderate contact angle regime. Contours of l_1^* for the low contact angle case are

shown in Figure D.3. These contours display the same trends as the moderate contact angle contours (Figure 5.17) however as expected the change in the values of the contours with deflection are greater in the low contact angle case. This is clearer from the numerical example for $V^* = 0.1$ shown in Table 8. In both cases ($\theta_c = 45^\circ$ and $\theta_c = 0^\circ$), with increasing deflection, l_1^* increases, which will cause a decrease in MDF, as shown in Figure 5.4. This in turn tends to increase x_1^* . From Table 8, the larger increase in l_1^* with deflection for smaller θ_c is expected to cause more pronounced increases in x_1^* with deflection. Nevertheless the overall x_1^* value is still smaller for smaller θ_c since at the same deflection l_1^* is less in the low θ_c case which results in larger MDF and MDISP.

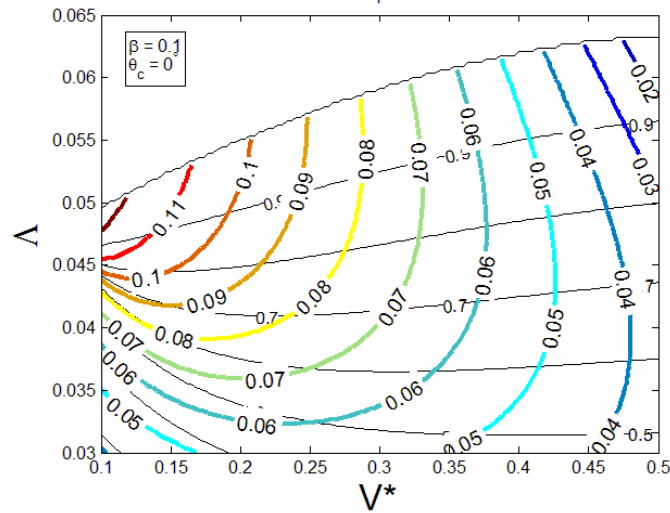


Figure D.3: Contours of base meniscus geometry factor (l_1^*). The contours are plotted with varying Δ and V^* . The other two governing parameters are fixed at $\theta_c=0^\circ$ and $\beta=0.1$.

Table 8: Change in l_1^* for $V^* = 0.1$ as deflection increases from $w_2^* = 0.6$ to collapse

	$\theta_c = 45^\circ$	$\theta_c = 0^\circ$
$w_2^* = 0.6$	$l_1^* \approx 0.765$	$l_1^* \approx 0.08$
$w_2^* = 1$	$l_1^* \approx 0.79$	$l_1^* \approx 0.12$
Change	$\Delta l_1^* \approx 0.025$	$\Delta l_1^* \approx 0.04$

l_2^* and hence the MDF of the free end meniscus are extremely dependent on the deflection, which can be shown by considering the geometric relationships for each meniscus Eq. (5.6) and Eq. (5.7), rewritten as follows

$$\alpha = \frac{w_2^* - 1}{\cos(\theta_2 - \phi_2)} = \frac{w_1^* - 1}{\cos(\theta_c + \phi_1)}. \quad (\text{D.1})$$

This equation determines θ_2 , the angle at the free end, needed to maintain equilibrium. At collapse, because $w_2^* = 1$ while $w_1^* \neq 1$, this relationship requires that $\cos(\theta_2 - \phi_2) = 0$, and therefore, $l_2^* = \sin(\theta_2 - \phi_2) = 1$, which implies that the MDF at the free end is zero; this is clearly consistent with the physical situation. Furthermore, before deformation $l_1^* = l_2^* = \sin(\theta_c)$ so in the $\theta_c = 0^\circ$ case l_2^* varies from 0 before deformation to 1 at collapse; this may potentially create a larger change in the base meniscus position. A contour plot of l_2^* is shown in Figure D.4. As expected the contours increase with increasing deflection. However, the rate of increase slows down considerably near collapse, represented by the increased spacing in the contours for large Λ . As a result the change in x_1^* due to this effect occurs primarily at low deflections. This behaviour is due to the fact that the sine function that determines l_2^* (Eq. (5.8)) has its smallest slope then when its value approaches 1.

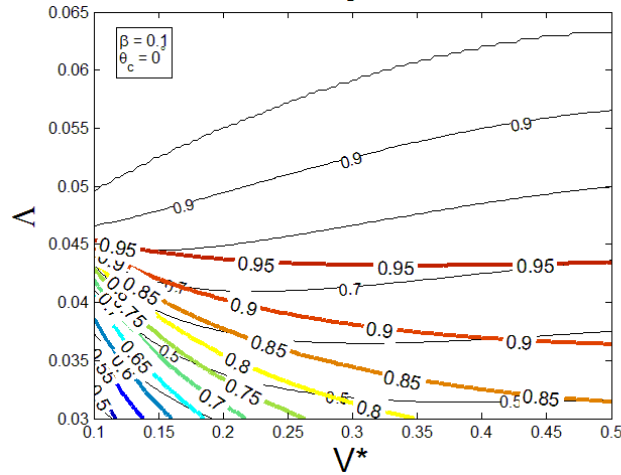


Figure D.4: Contours of free end meniscus geometry factor (l_2^*). Contours are plotted with varying Δ and V^* . The other governing parameters are fixed at $\theta_c=0^\circ$ and $\beta=0.1$.

Contour plots for the sum of the two meniscus displacement factors (SMDF) are shown in Figure D.5. This plot takes on the behaviour of l_2^* at low deflection, and that of l_1^* at high deflection once l_2^* has stabilized. First let us examine the contours in the low V^* area. In this region, the drop in SMDF with increasing deflection at low deflection causes the drop in MDISP which was shown in Figure D.2. The decrease in MDISP counteracts the decrease in x_1^* caused by beam deflection. Once deflection is near collapse the SMDF spacing increases; this indicates that the changes in SMDF, which had been driven in large part by the sharp increase in l_2^* at the free end meniscus, have stabilized due to the levelling off of l_2^* at higher deflections. This is a driving force for the MDISP contours at small V^* (Figure D.1), bending to become vertical as deflection increases. At higher V^* and deflections the SMDF contours begin to show an increasing trend as deflection is increased which would tend to push the meniscus closer to the base.

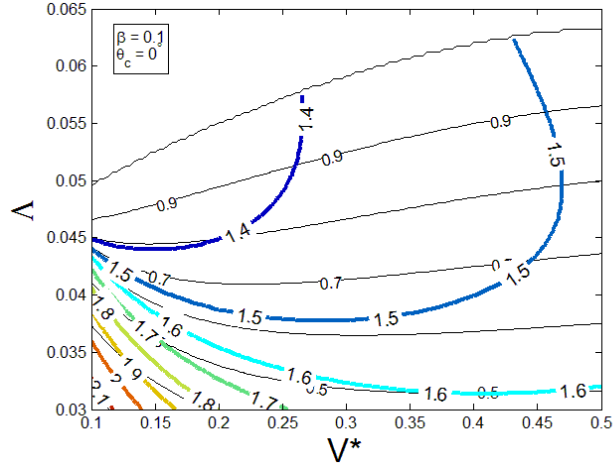


Figure D.5: Contours of sum of meniscus displacement factors (SMDF). Contours are plotted with varying Δ and V^* . The other governing parameters are fixed at $\theta_c=0^\circ$ and $\beta=0.1$.

The contours of SMDF do not fully explain the trends in MDISP for example MDISP (Figure D.1) has much greater V^* dependence than SMDF ((Figure D.5)); from Eq. (5.5) this suggests that the meniscus curvature α also plays a role. Contours of α are shown in Figure D.6. Patterns of these contours are similar to the moderate contact angle contours Figure 5.15. A notable difference is the overall lower value of $|\alpha|$ for the small θ_c case, which can be easily explained by Eq. (5.9). Since from Eq. (5.5) $\text{MDISP} \propto \alpha^2$, changes in α with deflection may overpower the changes in SMDF with deflection. The behaviour of MDISP, (Figure D.1), is influenced by α , Figure D.6, and SMDF, (Figure D.5), both of which vary with the deflection. By comparing these figures conclusions can be drawn about the relative importance of each factor on MDISP. First of all, in the low V^* regime, at lower deflections where SMDF changes sharply with deflection, MDISP is strongly influenced by SMDF. However, near collapse SMDF levels off and MDISP is driven primarily by α rather than SMDF. It should also be noted that near collapse MDISP no longer changes significantly with deflection and changes in x_1^* are driven primarily by the liquid displaced by the

beams deflection. Secondly, in the high V^* regime, the magnitude of α is closer to 1 and changes very little with deflection. As a result MDISP is driven primarily by SMDF. However, in this region the changes in MDISP with deflection are small and do not cause significant changes in x_1^* .

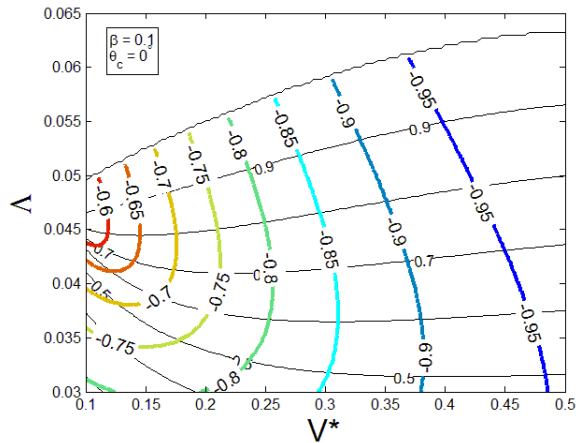


Figure D.6: Contours for the normalized meniscus radius (α). The contours are plotted with varying Λ and V^* . The other governing parameters are fixed at $\theta_c=0^\circ$ and $\beta=0.1$.

Appendix E *DCB Branching*

We wish to generate branching diagrams for a DCB, like the ones shown for the spring-plate-drop system, to help understand the jump in deflection observed. However, doing so with the existing system is too complex. Instead the analysis will be carried out to mirror the analysis of the doubly clamped beam presented by Mastrangelo and Hsu [3]. The analysis makes several simplifications. Surface tension forces and the liquid displaced by the meniscus curvature are neglected; which was shown in this work to be a reasonable assumption if $\beta \ll 1$. Furthermore, we will use an approximate 4th order polynomial test function for the deflection, which is needed to account for a uniform pressure in the Bernoulli-Euler beam theory. Forcing this test function to satisfy the essential boundary conditions at $x = 0$ gives the following form

$$w = Ax^2 + Bx^3 + Cx^4. \quad (\text{E.1})$$

Forcing this test function to satisfy the natural boundary conditions at the free end, i.e., zero moment ($w''(L) = 0$) and zero shear ($w'''(L) = 0$) gives the following form

$$w = A \left(x^2 - \frac{2}{3L} x^3 + \frac{1}{6L^2} x^4 \right). \quad (\text{E.2})$$

Neglecting liquid displaced by meniscus curvature the constant volume constraint, Eq. (5.5) simplifies to

$$V^* = \frac{V}{2LDh} = \int_{x_1^*}^1 (1 - w^*(x^*)) dx^*, \quad (\text{E.3})$$

where $x_1^* = x_1 / L$ and $w^* = w / h$. The undetermined constant A can be obtained from Eq. (E.2) and Eq. (E.3)

$$A = \frac{h}{L^2} \frac{(1 - x_1^* - V^*)}{P(x_1^*)}; \quad (\text{E.4})$$

where $P(x_1^*)$ is given by

$$P(x_1^*) = \frac{1}{3}(1 - x_1^{*3}) - \frac{1}{6}(1 - x_1^{*4}) + \frac{1}{30}(1 - x_1^{*5}). \quad (\text{E.5})$$

From Eq. (E.2) and Eq. (E.4) the normalized free end deflection can be obtained

$$w_2^* = \frac{w_2}{h} = \frac{w(L)}{h} = \frac{1 - x_1^* - V^*}{2P(x_1^*)}. \quad (\text{E.6})$$

The normalized deflection can then be written as follows

$$w^*(x^*) = 2w_2^* \left(x^{*2} - \frac{2}{3}x^{*3} + \frac{1}{6}x^{*4} \right). \quad (\text{E.7})$$

Using symmetry the strain energy of one of the beams in the DCB is given by

$$U_{SE} = \int_0^L \frac{M^2}{2EI} dx = \frac{EI}{2} \int_0^L (w'')^2 dx = \frac{2EIh^2}{5L^3} \left(\frac{(1 - x_1^* - V^*)}{P(x_1^*)} \right)^2 = \frac{8EIh^2}{5L^3} w_2^{*2}. \quad (\text{E.8})$$

The surface energy is given by

$$U_S = \gamma_{SA}A_{SA} + \gamma_{LA}A_{LA} + \gamma_{SL}A_{SL}. \quad (\text{E.9})$$

Neglecting the area of the liquid meniscus (A_{LA}) and using Young's Equation (Eq.

(2.3)) to eliminate γ_{SA} gives

$$U_S = U_{S_0} + \gamma_{LA}LDx_1^* \cos \theta_c, \quad (\text{E.10})$$

where $U_{S_0} = \gamma_{SL}LD$ is a constant which we will denote as the reference surface energy. Similarly the reference state for strain energy is when the beam is undeflected. Thus the total energy of the system, $U_T = U_{SE} + U_S$, measured relative to the respective reference, can be normalized to

$$U_T^* = \frac{U_T}{\gamma_{LA}LD \cos \theta_c} = 2N_C \left(\frac{(1 - x_1^* - V^*)}{P(x_1^*)} \right)^2 + x_1^*. \quad (\text{E.11})$$

where N_C is a nondimensional number given by

$$N_C = \frac{EIh^2}{5\gamma_{LA}DL^4 \cos \theta_c}. \quad (\text{E.12})$$

A necessary condition for equilibrium solutions is as follows

$$\frac{dU_T^*}{dw_2^*} = \frac{\partial U_T^*}{\partial x_1^*} \frac{dx_1^*}{dw_2^*} = 0. \quad (\text{E.13})$$

From Eq. (E.6) $dx_1^*/dw_2^* = 0$ only when $x_1^* = 1$ (no liquid) so the following can be used in place of Eq. (E.13)

$$\frac{\partial U_T^*}{\partial x_1^*} = 0 = 4N_C \left(\frac{(1-x_1^*-V^*)}{P(x_1^*)} \right) \left(\frac{-P(x_1^*) - (1-x_1^*-V^*)dP(x_1^*)/dx_1^*}{P^2(x_1^*)} \right) + 1, \quad (\text{E.14})$$

where

$$\frac{dP(x_1^*)}{dx_1^*} = -x_1^{*2} + \frac{2}{3}x_1^{*3} - \frac{1}{6}x_1^{*4}. \quad (\text{E.15})$$

Applying the quadratic formula gives, after rearrangement

$$V^* = 1 - x_1^* + \frac{P(x_1^*)}{2dP(x_1^*)/dx_1^*} \left(1 \pm \sqrt{1 + N_C^{-1}P(x_1^*)dP(x_1^*)/dx_1^*} \right). \quad (\text{E.16})$$

Solutions of Eq. (E.16) may give a maximum or minimum energy whereas stable solutions only occur at energy minima. Note that if $1 + N_C^{-1}P(x_1^*)dP(x_1^*)/dx_1^* = 0$,

Eq. (E.16) gives a double root which corresponds to a bifurcation point [3].

Attaining this condition will depend on the value of N_C and the maximum of

$g(x_1^*) = -P(x_1^*)dP(x_1^*)/dx_1^*$. A plot of $g(x_1^*)$ is shown in Figure E.1. The

maximum value of 0.036338 occurs at about $x_1^* = 0.67632$. It is helpful to define

the following nondimensional number

$$N_T = \max(-P(x_1^*)dP(x_1^*)/dx_1^*) \approx 0.036338. \quad (\text{E.17})$$

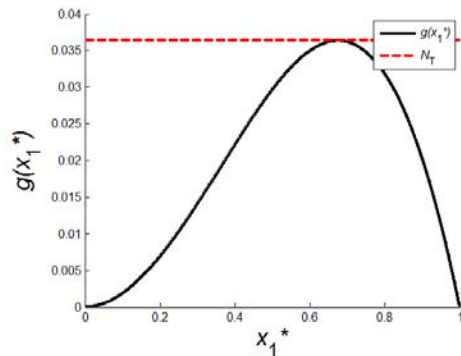


Figure E.1: Variation of the function g with x_1^* . Maximum value gives N_T .

Thus the elastocapillary number can be obtained as follows

$$N_{EC} = \frac{N_C}{N_T} = \frac{5.504EIh^2}{\gamma_{LA}DL^4 \cos \theta_c}. \quad (\text{E.18})$$

For $N_{EC} < 1$ the DCB is expected to collapse as $V^* \rightarrow 0$. The reason for this behaviour will be elucidated when we subsequently discuss branching diagrams; however, note that for $N_{EC} < 1$ imaginary (nonphysical) roots appear in Eq. (E.16) for some x_1^* values. This behaviour prevents the transition from high deflection roots of Eq. (E.16) to low deflection roots of Eq. (E.16) as V^* decreases. Note N_{EC} in Eq. (E.18) is roughly double the one presented by Mastrangelo and Hsu [3] for a cantilever above a substrate. Note that Mastrangelo and Hsu only presented the final result for a cantilever unfortunately the intermediate results which we require were not presented.

It is desirable to place bounds on the solution. If $x_1^* = 0$, From Eq. (E.6),

$$V^* = 1 - \frac{2}{5}w_2^*, \quad (\text{E.19})$$

this may not correspond to a local extreme value of energy. If equilibrium is to

exist at $x_1^* = 0$ then from Eq. (E.14), V^* must satisfy

$$V^* = 1 - \frac{1}{100N_C}. \quad (\text{E.20})$$

The energy Eq. (E.11) of the $x_1^* = 0$ configuration simplifies to

$$U_{T_0}^* = 50N_C(1 - V^*)^2. \quad (\text{E.21})$$

Branching and energy diagrams are shown for the DCB in Figure E.2. In the branching diagrams Figure E.2a),c),e) the dashed line represent the limiting case of $x_1^* = 0$ and the other two lines represent the “roots” of Eq. (E.16). The solid line corresponds to subtraction of the square root term, and the dash-dot line corresponds to addition of the square root term. We consult the energy curves

Figure E.2b),d),f) to see if the portion of the root of interest corresponds to a energy maximum or minimum.

Consider what happens to a DCB initially filled with liquid ($V^* = 1$) as the liquid is evaporated. The response of the system will depend on N_{EC} . For $N_{EC} < 1$ the DCB is expected to collapse during the evaporation process. As liquid is first evaporated w_2^* increases, however because there are no local energy minima the system follows the $x_1^* = 0$ path in Figure E.2 a) given by Eq. (E.19) from A to B (similarly the energy path is the dashed red line in Figure E.2 b) given by Eq. (E.21)). At point B, the volume V^* is given by Eq. (E.20), and a local energy minima appears. The system attains equilibrium at this point and begins to follow curve BC in Figure E.2 a) which represents the root with subtraction of the square root term in Eq. (E.16); for $N_{EC} < 1$ two curves appear for this root to Eq. (E.16) since for some x_1^* the roots are imaginary and unphysical. The solution follows curve BC until collapse at point C. At the same time the energy curves, Figure E.2 b), follow a path through the local minima. For this N_{EC} there are no local energy minima for $0.1 < V^* < 0.15$, based on the slope of the energy contours these drops sizes will all lead to collapse.

For $N_{EC} = 1$ the DCB is not expected to collapse. Again as liquid is first evaporated w_2^* increases, however because there are no local energy minima the system follows the $x_1^* = 0$ path in Figure E.2 c) given by Eq. (E.19) from A to B (similarly the energy path is the dashed red line in Figure E.2 d) given by Eq. (E.21)). At point B, the volume V^* is given by Eq. (E.20), and a local energy minima appears and the system attains equilibrium at this point now following the

curve in Figure E.2 c) given by Eq. (E.16) with subtraction of the square root term in. The solution follows this curve until point F. Note that at point D a second local energy minima appears as represented by curve EC however it is not immediately obtainable due to the energy barrier represented by curve EF. At point F, the square root in Eq. (E.16) is zero and the two roots coalesce, and the energy minima that the system had previously been following (BF) changes into a maxima (FH). As a result the system experiences a jump decrease in deflection from point F to point G. As liquid continues to evaporate the system then follows curve GC and finishes at a state of zero deflection. Note that for this N_{EC} there are multiple possible equilibrium solutions for some values of V^* , for example the initial condition could cause the system to reach equilibrium on curve EG rather than DF. Furthermore, the initial condition may also lead the system to reach equilibrium on curve FI or even collapse (anything above curve FH and below point I) rather than on curve GC.

For $N_{EC} > 1$ the DCB is again not expected to collapse. Again as liquid is first evaporated w_2^* increases, however because there are no local energy minima the system follows the $x_1^* = 0$ path in Figure E.2 e) given by Eq. (E.19) from A to B (similarly the energy path is the dashed red line in Figure E.2 f) given by Eq. (E.21)). At point B, the volume V^* is given by Eq. (E.20), and a local energy minima appears. The system attains equilibrium at this point and begins to follow the curve in Figure E.2 e) given by Eq. (E.16) with subtraction of the square root term in. The solution follows this curve until point C and finishes at a state of zero deflection. Note that at point D there is a change in solution behaviour from

deflection increasing as drop size is decreased to deflection decreasing as drop size is decreased. Also note that for very small drop sizes with initial deflections near collapse the DCB may remain stable or collapse (bottom right corner of Figure E.2 e)).

From Figure E.2 it can be seen that collapse is not possible for $V^* > 0.6$, which is close to the upper limit used in this study of $V^* = 0.5-0.55$.

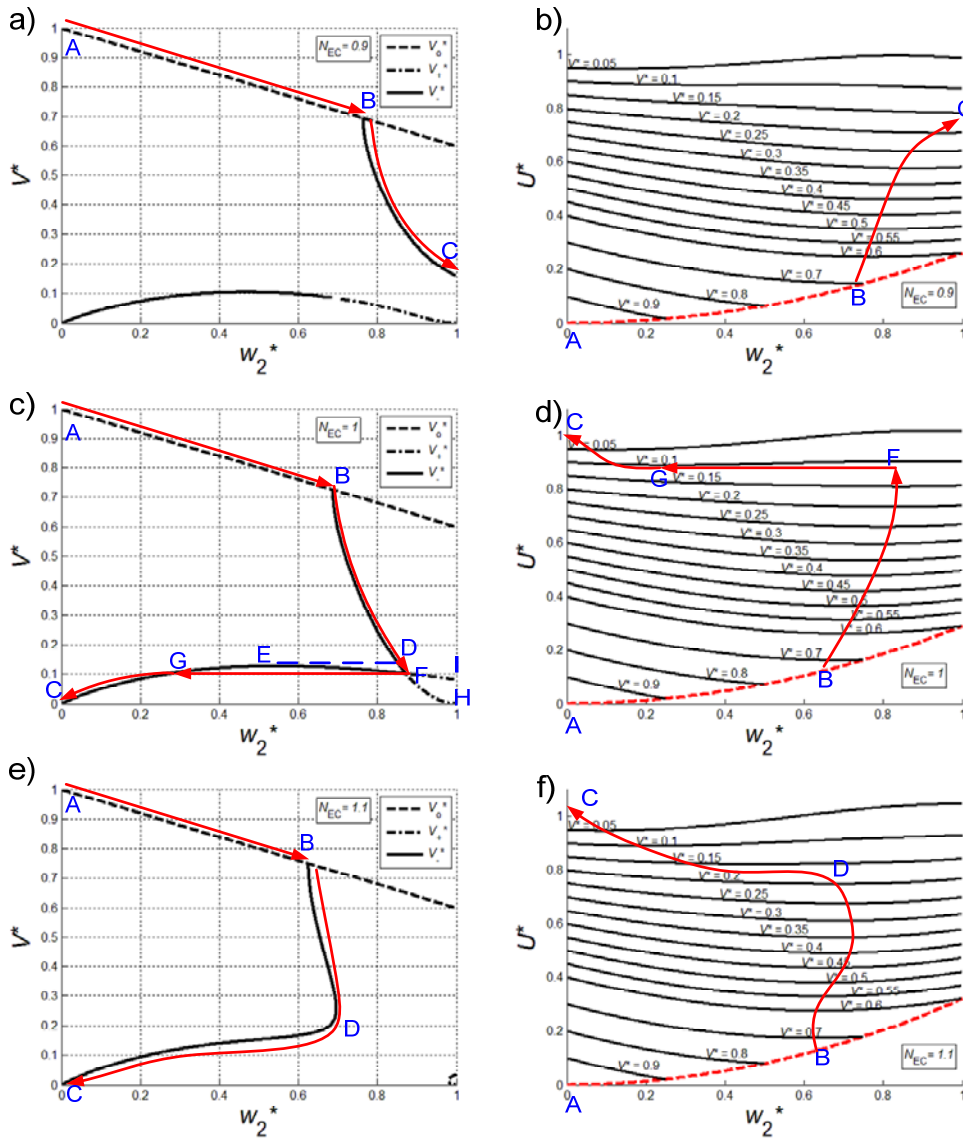


Figure E.2: DCB branch and energy diagrams showing equilibrium path of a quasistatic evaporation process a) Branch diagram $N_{EC} = 0.9$ b) Branch diagram $N_{EC} = 1$ c) Branch diagram $N_{EC} = 1.1$ d) Energy diagram $N_{EC} = 0.9$ e) Energy diagram $N_{EC} = 1$ f) Energy diagram $N_{EC} = 1.1$

Appendix F *Axisymmetric Meniscus Calculation*

In this Appendix the influence of including both principal radii of curvature in the Young-Laplace equation is considered for the case of an axisymmetric drop. For simplicity the analysis is carried out for a drop sandwiched between two rigid circular plates. The objective is to compare the Laplace pressures given from this more rigorous approach with the result of a simplified energy approach presented by Mastrangelo *et al.* [3] and evaluate when the simplified approach can be used.

We will first use the simplifications adopted by Mastrangelo *et al.* [3] for plate bending but look at the simplified problem of calculating the force an axisymmetric liquid drop exerts on two parallel rigid plates. The total surface energy of the system is first written as

$$U_S = \gamma_{LA}A_{LA} + \gamma_{SL}A_{SL} + \gamma_{SA}A_{SA}. \quad (\text{F.1})$$

Our system consists of a plate of radius R filled axisymmetrically with liquid of radius r_{lit} . In the work of Mastrangelo *et al.* [3] the energy of the liquid-air area (A_{LA}) is neglected. Thus Eq. (F.1) can be written as

$$U_S = \gamma_{SL}\pi r_{lit}^2 + \gamma_{SA}\pi(R^2 - r_{lit}^2). \quad (\text{F.2})$$

Using Young's equation Eq. (2.3), Eq. (F.2) can be rewritten as

$$U_S = U_{So} + \gamma_{LA}\cos(\theta_c)\pi(R^2 - r_{lit}^2). \quad (\text{F.3})$$

Mastrangelo *et al.* [3] uses a simplified cylindrical representation for the liquid volume (V_L)

$$V_L = \pi r_{lit}^2 h . \quad (F.4)$$

where h is the spacing between plates. Rearranging Eq. (F.4) gives the liquid radius

$$r_{lit} = \sqrt{\frac{V_L}{\pi h}} . \quad (F.5)$$

The liquid force pulling the plates together can be calculated as follows

$$F = \frac{dU_S}{dh} = \frac{\gamma_{LA} \cos(\theta_c) \pi r_{lit}^2}{h} = -\Delta P_{lap} A_{SL} . \quad (F.6)$$

where $A_{SL} = \pi r_{lit}^2$, and $\Delta P_{lap} = \gamma_{LA} q_{lit}$. In the context of the Young-Laplace equation (Eq. (2.4)) q_{lit} is twice the mean curvature of the meniscus from Eq.

(F.6) q_{lit} obtained using the energy approach of Mastrangelo *et al.* [3] is

$$q_{lit} = -\frac{\cos \theta_c}{h} . \quad (F.7)$$

This result may seem odd since the drop is axisymmetric but the radius of the drop does not factor into the obtained curvature. So Eq. (F.7) will only be valid if r_{lit} is large enough to generate negligible curvature. In addition, the curvature from Eq. (F.7) is neglected in the volume representation Eq. (F.4). For convenience introduce the following nondimensional parameters

$$r^* = \frac{r}{R}, \quad z^* = \frac{z}{h}, \quad V_L^* = \frac{V_L}{\pi R^2 h}, \quad q^* = \frac{qh}{\cos \theta_c}, \quad \xi = \frac{h}{R} . \quad (F.8)$$

The surface energy (Eq. (F.3)) normalizes as follows

$$U_{lit}^* = \frac{U_S - U_{So}}{\gamma_{LA} \pi R^2} = \cos(\theta_c) (1 - r_{lit}^{*2}) . \quad (F.9)$$

Wetted plate radius(Eq. (F.5)) normalizes as follows

$$r_{lit}^* = \sqrt{V_L^*} . \quad (F.10)$$

Force (Eq. (F.6)) normalizes as follows

$$F_{lit}^* = \frac{F}{\gamma_{LA} \cos(\theta_c) \pi R} = -\frac{q_{lit}^* r_{lit}^{*2}}{\xi} . \quad (F.11)$$

Thus curvature Eq. (F.7) normalizes as follows.

$$q_{lit}^* = -1. \quad (F.12)$$

We will now more rigorously calculate the curvature of an axisymmetric drop using equilibrium requirements. Starting with the Young-Laplace Equation (Eq. (2.4))

$$\Delta P_{lap} = \gamma_{LA} q = \gamma_{LA} \left(\frac{1}{R_1} + \frac{1}{R_2} \right). \quad (F.13)$$

where q is twice the mean curvature of the meniscus. At the length scales of MEMS devices the Bond number is small and gravity can be neglected. In the absence of gravity fluid equilibrium requires the drop to be isobaric. Therefore, q must be constant and can be determined by evaluating principal radii of curvature from meniscus geometry shown in Figure F.1 [44]

$$q = \frac{1}{R_1} + \frac{1}{R_2} = \frac{\sin(\beta(s))}{r} + \frac{d\beta}{ds}. \quad (F.14)$$

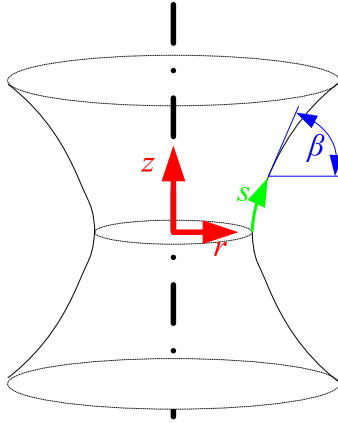


Figure F.1: Schematic of axisymmetric drop

If we adopt the following parametric representation for the meniscus surface

$$\begin{aligned} r' &= \frac{dr}{ds} = \cos(\beta(s)), \\ z' &= \frac{dz}{ds} = \sin(\beta(s)), \end{aligned} \quad (F.15)$$

Eq. (F.14) can be rewritten as follows

$$\beta' = \frac{d\beta}{ds} = q - \frac{z'}{r}. \quad (\text{F.16})$$

From Figure F.1 we have the following boundary conditions

$$\begin{aligned} z(0) = 0, \quad r(0) = r_o, \quad \beta(0) = \pi / 2 \\ z(l) = h, \quad r(l) = r_l, \quad \beta(l) = \theta_c. \end{aligned} \quad (\text{F.17})$$

where r_o is the drop radius at $s = 0$, l is the length of the meniscus from $s = 0$ to the plate, and r_l is the drop radius at $s = l$. r_o , r_l , l , and q are unknown and must be determined from the solution. Furthermore, the solution must enforce the following liquid volume condition

$$V_L = \int_0^h \pi r^2 dz = \int_0^l \pi r^2 \sin(\beta) ds. \quad (\text{F.18})$$

In order to include the energy of the liquid-air surface neglected by Mastrangelo *et al.* [3] we calculate the meniscus surface area as follows.

$$A_{LA} = \int_0^h 2\pi r \sqrt{1 + \left(\frac{dr}{dz}\right)^2} dz = \int_0^l 2\pi r ds. \quad (\text{F.19})$$

Introduce the normalization Eq. (F.8) with additional parameters

$$s^* = \frac{s}{h}, \quad A_{LA}^* = \frac{A_{LA}}{2\pi R h}, \quad (\text{F.20})$$

Eqs. (F.15) and (F.16) transform as follows

$$\begin{aligned} \frac{dr^*}{ds^*} &= \xi \cos(\beta(s)), \\ \frac{dz^*}{ds^*} &= \sin(\beta(s)), \\ \frac{d\beta}{ds^*} &= q^* \cos \theta_c - \xi \frac{\sin \beta}{r^*}. \end{aligned} \quad (\text{F.21})$$

The boundary conditions Eq. (F.17) transform as follows

$$\begin{aligned} z^*(0) = 0, \quad r^*(0) = r_o^*, \quad \beta(0) = \pi / 2 \\ z^*(l^*) = 1, \quad r^*(l^*) = r_l^*, \quad \beta(l^*) = \theta_c. \end{aligned} \quad (\text{F.22})$$

The normalized liquid volume condition Eq. (F.18) is

$$V_L^* = \int_0^{l^*} r^{*2} \sin(\beta) ds^*. \quad (\text{F.23})$$

The solution procedure will be the shooting method: guess q^* , l^* and r_o^* then use the 4th order Runge-Kutta method (RK4) to solve for β , z^* and r^* . These results are

compared with the l^* boundary conditions $z^*(l^*) = 1$ and $\beta(l^*) = \theta_c$ in Eq. (F.22) and Eq. (F.23); if these conditions are not satisfied to the desired accuracy a new guess is obtained using secant interpolation and the procedure is repeated. r_i^* is an additional unknown which is determined for use in force and energy calculations.

The normalized meniscus surface area is calculated from the RK4 solution by numerically integrating the normalized version of Eq. (F.19)

$$A_{LA}^* = \int_0^{l^*} r^* ds^* . \quad (F.24)$$

The normalized energy for the axisymmetric case is then

$$U^* = \frac{U_S - U_{So}}{\gamma_{LA} \pi R^2} = U_{LS}^* + U_{LA}^* = \cos(\theta_c) (1 - r_i^{*2}) + 2A_{LA}^* \xi . \quad (F.25)$$

This expression differs from Eq. (F.9) in two ways: the inclusion of the energy of the meniscus and differences in wetted radius denoted as r_i^* in the exact model and r_{lit}^* in the simplified model. A difference between r_i^* and r_{lit}^* results due to the more rigorous approach of the volume condition Eq. (F.23) as opposed to the cylindrical approximation Eq. (F.10).

The resulting force on the plates is given by

$$F^* = \frac{F}{\gamma_{LA} \cos(\theta_c) \pi R} = F_P^* + F_{ST}^* = -\frac{q^* r_i^{*2}}{\xi} + 2r_i^* \tan(\theta_c) , \quad (F.26)$$

where the last term represents surface tension of the meniscus; the simplifications to the energy method present by Mastrangelo *et al.* [3] result in this term being missing.

Our objective will be to compare the force exerted on the plates from Eq. (F.11) and Eq. (F.26) for a range of governing parameters: ξ , θ_c and V_L^* .

Comparison of these two forces will provide insight as to when the simplified and much more convenient approach of Mastrangelo *et al.* [3] can be used with sufficient accuracy. There are three important differences between Eq. (F.11) and Eq. (F.26) that will enter into the discussion. Firstly, as mentioned earlier Eq. (F.26) accounts for the surface tension force. Secondly, the magnitude of the curvature $q^* > q_{lit}^* = -1$ so the pressure pulling the plates together will be less in the exact model; this is caused by the consideration of the second principal curvature which has opposite sign. Finally, $r_l^* > r_{lit}^*$ due to the more rigorous treatment of the constant liquid volume condition. The net result on F^* is unknown since in the axisymmetric case we have a smaller pressure which acts on a larger area plus the addition of the surface tension force.

Be aware that in order to make differences more visible values of ζ larger than would be encountered in most MEMS applications are considered. A representative axisymmetric equilibrium surface is shown in Figure F.2; here the meniscus is shown in blue and the plate is shown in red. Recall that in Mastrangelo *et al.* [3] this surface is treated as a right circular cylinder when constraining drop size however when calculating curvature the axisymmetric curvature ($q_2^* = \xi \sin \beta / r^*$) is ignored and the other principal curvature $q_1^* = d\beta / ds^*$ is treated as a constant. The surface shown in Figure F.2 illustrates that these assumptions will not always be valid. Here the drop radius decreases as distance from the plate is increased and the need to consider two curvatures is evident. Shown in Figure F.3a) is the variation of each of these curvatures with position along the meniscus s^* ; also shown in Figure F.3a) is twice the mean

curvature q^* and the curvature obtained using the assumptions of Mastrangelo *et al.* [3] q_{lit}^* . There are several important trends in this figure that should be discussed. Firstly, because the liquid bridge has a smaller radius at $s^* = 0$, q_2^* is highest at $s^* = 0$ and decreases with increasing s^* . Since $q^* = q_1^* + q_2^*$ must be constant for the liquid bridge to be isobaric, q_1^* increases with increasing s^* ; however, it is interesting to note that the average value of q_1^* is close to the value of q_{lit}^* . In addition because the axisymmetric model considers contributions from both principal curvatures and these curvatures have opposite signs, we observe $q^* > q_{lit}^* = -1$ in Figure F.3a).

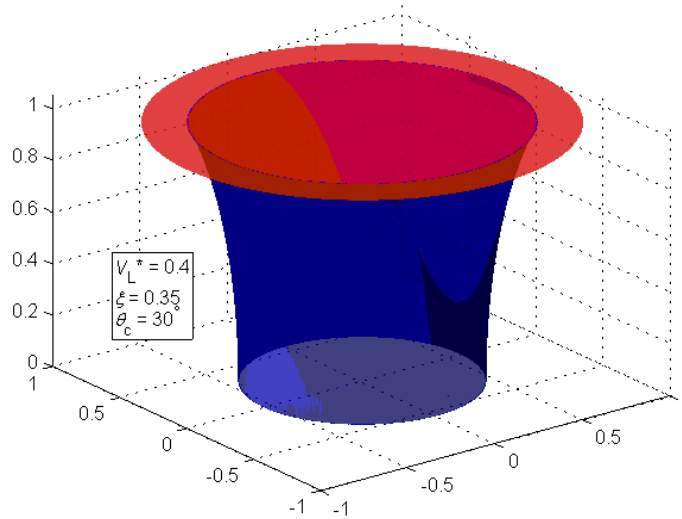


Figure F.2: An example of an axisymmetric equilibrium surface. Meniscus is shown in blue plate is shown in red.

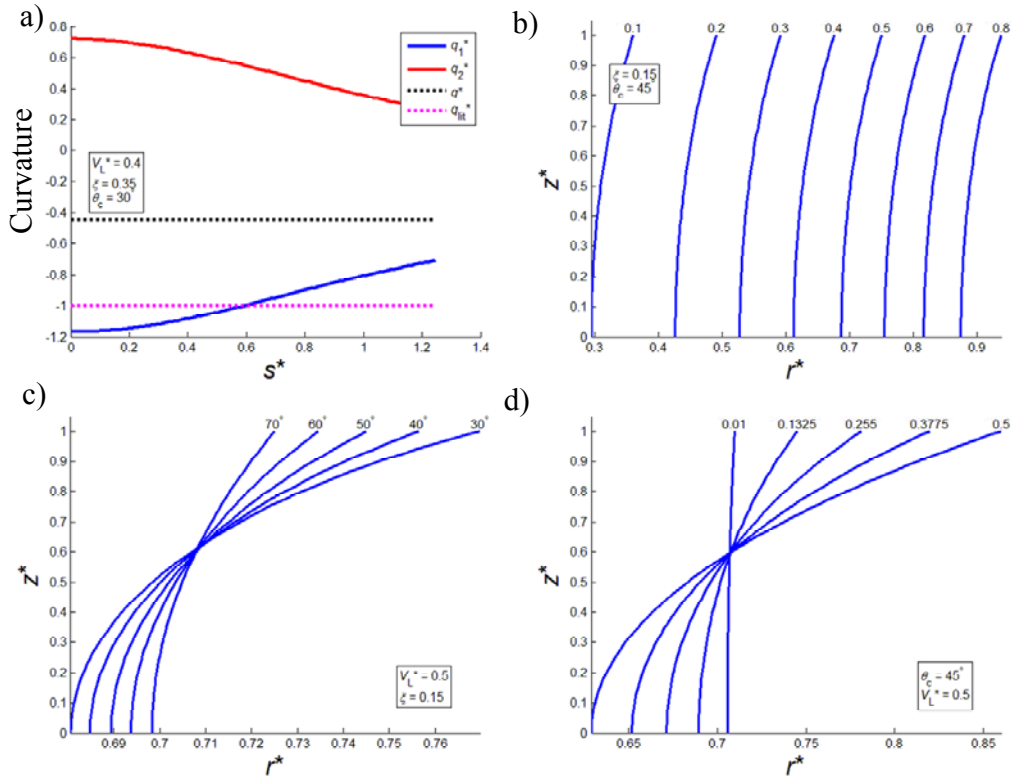


Figure F.3: a) Variation in each principal curvature with position along meniscus. Also shown are the mean curvature and the value obtained using the method of Mastrangelo *et al.* [3] b) Variation of equilibrium surface shape (z^* vs. r^*) with V_L^* c) Variation of equilibrium surface shape (z^* vs. r^*) with θ_c * d) Variation of equilibrium surface shape (z^* vs. r^*) with ζ .

The curvature variations in Figure F.3a) show how meniscus shape can impact the Laplace pressure. Figure F.3b)-d) shows how the meniscus shape (z^* vs. r^*) changes when one of the governing parameters (ζ , θ_c , V_L^*) is varied. In Figure F.3b) the meniscus shape is plotted for a range of V_L^* ; it is interesting to note that the shape of the meniscus appears to be insensitive to drop volume; however based on the spacing of the curves the magnitude of r^* depends nonlinearly on V_L^* ; in fact from Eq. (F.23) r^* is expected to be proportional to the square root of V_L^* (which agrees with curve spacing Figure F.3b)). In Figure F.3c) the meniscus shape is plotted for a range of θ_c in this case the shapes differ showing larger variation in r^* at lower contact angles which is not surprising considering the geometry in Figure F.1 and the boundary conditions Eq. (F.22).

Finally, in Figure F.3d) the meniscus shape is plotted for a range of ζ ; in this case the shapes differ showing larger variation in r^* at higher ζ . ζ is the ratio between the plate spacing to the plate radius thus based on the normalization Eq. (F.8) the curves in Figure F.3d) are stretched in the vertical direction by different amounts depending on ζ . For $\zeta = 0.01$ the curve has been stretched in the vertical direction by a factor of 100 resulting in the nearly vertical appearance of the curve. One final interesting note is that in Figure F.3c) and d) the curves intersect at $r_{lit}^* = \sqrt{V_L^*}$.

With knowledge of how the meniscus shapes vary with the three governing parameters we can now look at how the variables of interest vary. A justification for the simplified model is often that the dimensions of the structure are much larger than the spacing [18]; with our normalization this assumption corresponds to small ζ . In Figure F.4a) the curvature q^* is plotted against ζ while keeping the other two parameters fixed. The relationship is linear and q^* approaches $q_{lit}^* = -1$ as $\zeta \rightarrow 0$. In Figure F.4b) the wetted radius r_i^* is plotted against ζ while keeping the other two parameters fixed; also shown in this plot is the minimum radius r_o^* . Again the relationship is linear and both r_i^* and r_o^* approach r_{lit}^* as $\zeta \rightarrow 0$. These results seem to suggest that for small ζ the simplified approach and the axisymmetric model coalesce; however it will be demonstrated in Figure F.4c)-f) that small ζ is a necessary but not sufficient condition to use the simplified model.

In Figure F.4c) the curvature q^* is plotted against V_L^* while keeping the other two parameters fixed. The relationship is nonlinear and the deviation of q^*

from $q_{lit}^* = -1$ grows sharply as drop size decreases. The reason for this is q^* and hence the Laplace depend on the radius of the drop ($q_2^* = \xi \sin \beta / r^*$) not the radius of the plate so $\xi \rightarrow 0$ is not sufficient because the drop may not fully wet the plate area; the minimum (r_o^*) and wetting (r_l^*) liquid bridge radius are shown in Figure F.4d) here we see essentially the same behaviour as in Figure F.3b) the radius decreases nonlinearly with V_L^* however the shape (hence the distance between curves in Figure F.4d)) remains unchanged. Also shown is the radius from the simplified model r_{lit}^* which is between the minimum and wetting radii. These results are important because the classical analysis uses the simplified model to define the elastocapillary number N_{EC} which predicts when two elastic structures will be brought into contact by Laplace pressure [3]. In this analysis N_{EC} is defined such that contact occurs as the liquid dries or V_L^* decreases. Based on there result of Figure F.4c) caution should be used when applying N_{EC} results because the discrepancy in Laplace pressure grows as V_L^* decreases which may make the result invalid. Unfortunately N_{EC} provides no indication as to what V_L^* causes contact so based on the above observations it is impossible to know if the simplifications used in deriving N_{EC} will be valid.

In Figure F.4e) the curvature q^* is plotted against θ_c while keeping the other two parameters fixed. The relationship is nonlinear and the deviation of q^* from $q_{lit}^* = -1$ grows sharply as contact angle increases. The reason for this behaviour is q^* depends on the sum of the two radii of curvature. If $\xi \rightarrow 0$ and V_L^* is sufficiently large then $q_2^* = \xi \sin \beta / r^*$ will be small; however as the contact angle approaches 90° the liquid bridge approaches a right circular cylinder. For a

right circular cylinder the other principal curvature ($q_1^* = d\beta / ds^*$) is zero. Thus q_1^* becomes small as $\theta_c \rightarrow 90^\circ$ so q_2^* will not be negligible even if $\zeta \rightarrow 0$ and V_L^* is sufficiently large. In these cases the Laplace pressure can often be in the opposite direction to that predicted using q_{lit}^* . In Figure F.4f) the wetted radius r_l^* and minimum radius r_o^* are plotted against θ_c while keeping the other two parameters fixed. The relationship is nearly linear and both r_l^* and r_o^* approach r_{lit}^* as $\theta_c \rightarrow 90^\circ$. One interesting point from comparing Figure F.4e) and f) is that the largest discrepancy in Laplace pressure occurs as $\theta_c \rightarrow 90^\circ$ however the largest discrepancy in Laplace pressure area occurs as $\theta_c \rightarrow 0^\circ$.

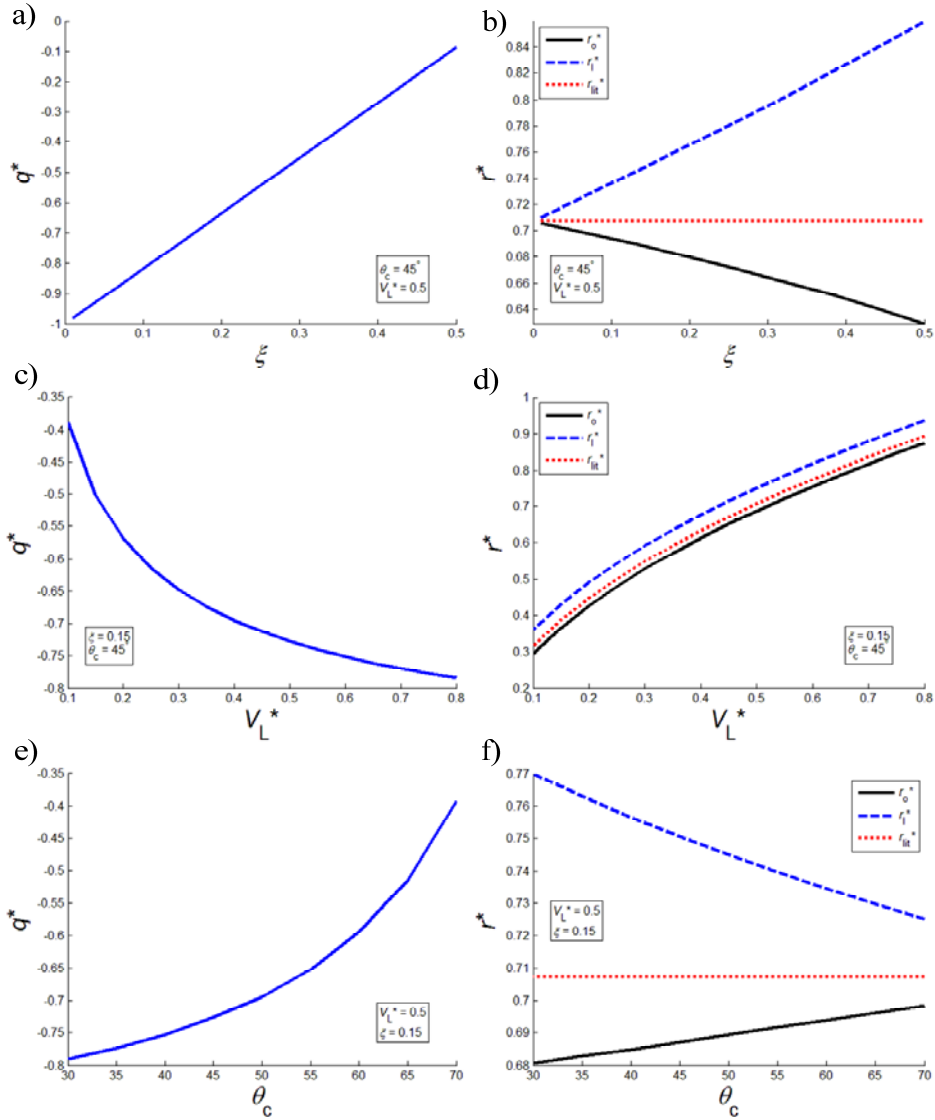


Figure F.4: Dependency of q^* and r_l^* on ξ , θ_c , and V_L^* . r_o^* and r_{lit}^* are also shown in b), d), f).
a) q^* vs. ξ b) r_l^* vs. ξ c) q^* vs. V_L^* d) r_l^* vs. V_L^* e) q^* vs. θ_c f) r_l^* vs. θ_c

Shown in Figure F.5 are some example plots for how the trends previously described can cause the energy U^* and force F^* as well as their components to deviate from the values obtained with the simplified model. The results of Figure F.5 are by no means comprehensive since for each subfigure several variables are held fixed. Therefore, generalizations about the total U^* and force F^* relative to the simplified model should not be made from the figure. For example in Eq. (F.26) F_P^* is inversely proportional to ξ whereas F_{ST}^* does not depend on ξ thus

at lower ζ values F_P^* will become larger relative to F_{ST}^* . Recall that the simplified model F_{ST}^* is neglected and the force is due entirely to Laplace pressure; on the other hand, the Laplace pressure and Laplace pressure area are also different in the simplified model. Starting with Figure F.5a) which shows the surface energy of the system U^* and its components due to plate wetting U_{LS}^* and due to meniscus area U_{LA}^* as ζ is varied. In the literature U_{LA}^* is neglected based on an argument that this area will be small if ζ is small; this trend is observed in Figure F.5a) and U^* approaches U_{lit}^* since U_{LA}^* tends to zero as $\zeta \rightarrow 0$. Furthermore, due to differences in wetted area U_{LS}^* diverges from U_{lit}^* as ζ increases. Figure F.5b) shows the total force F^* and its components due to pressure F_P^* and due to surface tension F_{ST}^* as ζ is varied. From Eq. (F.26) F_P^* increases sharply as $\zeta \rightarrow 0$; as a result the constant difference F_{ST}^* between the simplified and axisymmetric models becomes negligible. Figure F.5c) again shows surface energy U^* and its components this time as V_L^* is varied. Here we see the energy of the neglected area U_{LA}^* increases with increasing V_L^* . U_{LS}^* follows a similar trend to U_{lit}^* however it diverges slightly as V_L^* increases. Variations in the total force F^* and its components as V_L^* is varied are shown in Figure F.5d). Here all force components increase with increasing V_L^* since from Figure F.4c)-d) this corresponds to an increase in both Laplace pressure and Laplace pressure area which increases F_P^* . Furthermore the increase in r_l^* increases the contact line length on which the surface tension force acts which increases F_{ST}^* . F_P^* follows the same behaviour as F_{lit}^* although it diverges slightly as V_L^* increases. Figure F.5e) again shows surface energy U^* and its

components this time as θ_c is varied. Here we see the energy of the neglected area U_{LA}^* decreases with increasing θ_c . U_{LS}^* asymptotes to U_{lit}^* as θ_c increases. Variations in the total force F^* and its components as θ_c is varied are shown in Figure F.5f). Here the pressure force (F_P^*) diverges from F_{lit}^* as the contact angle is increases due to the discrepancy in curvature shown in Figure F.4e). Furthermore since the surface tension force F_{ST}^* is proportional to $\tan(\theta_c)$ it increases with increasing contact angle.

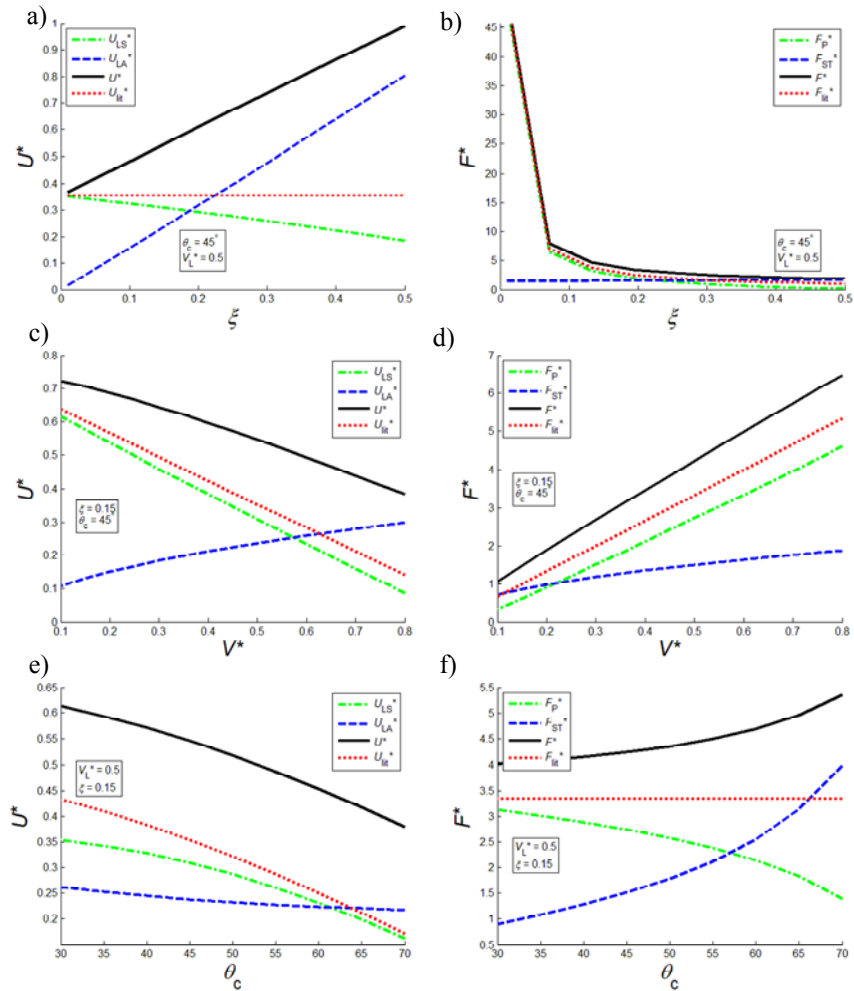


Figure F.5 Dependency of U^* and F^* on ζ , θ_c , and V_L^* . In a) c) e) contributions from the wetted plate U_{SL}^* and meniscus U_{LA}^* are also shown along with the energy obtained using the method of Mastrangelo *et al.* [3] U_{lit}^* . In b), d), f) contributions from the pressure force F_P^* and surface tension force F_{ST}^* are also shown along with the force obtained using the method of Mastrangelo *et al.* [3] F_{lit}^* . a) U^* vs. ζ b) U^* vs. ζ c) U^* vs. V_L^* d) F^* vs. V_L^* e) F^* vs. θ_c f) F^* vs. θ_c